ACTIVATED CARBON/CARBON NANOCOMPOSITE MATERIALS FOR ADSORPTION AND CATALYTIC OXIDATION OF ORGANIC POLLUNTS: AN EXPERIMENTAL AND THEORETICAL STUDY

by

SOREMO L EZUNG

Registration No.: 790/2017

Submitted to

NAGALAND UNIVERSITY

In Partial Fulfillment of the Requirements for Award of the Degree

of

DOCTOR OF PHILOSOPHY IN CHEMISTRY

DEPARTMENT OF CHEMISTRY
NAGALAND UNIVERSITY
LUMAMI-798627
NAGALAND, INDIA
2022

DEDICATED

To

My Family

DECLARATION

I, **Mr. Soremo L Ezung** bearing Ph.D. Registration No. **790/2017** with effect from **30th August 2016**, hereby declare that the subject matter of my Ph.D. thesis entitled "**Activated Carbon/Carbon Nanocomposite Materials for Adsorption and Catalytic Oxidation of Organic pollutants: An Experimental and Theoretical Study**" is the record of work done by me and also that the contents of this thesis did not comprise the basis for the award of any previous degree/diploma to me or to anybody else in any other University/Institution, to the best of my knowledge.

This Ph.D. thesis is submitted in compliance with the UGC Regulation 2016 dated May 05, 2016 (Minimum Standard and Procedure for Award of M. Phil./Ph.D. Degree) to the Nagaland University for the degree of Doctor of Philosophy in Chemistry

(**Soremo L Ezung**)

(**Prof. Upasana Bora Sinha**)
Head
Department of Chemistry
Nagaland University

(**Prof. Dipak Sinha**)
Supervisor

Department of Chemistry

CERTIFICATE

This is to certify that **Mr. Soremo L Ezung**, a registered Research Scholar for Ph.D. degree in Chemistry under Nagaland University has carried out his research work under my guidance and supervision. His thesis entitled "**Activated Carbon/Carbon Nanocomposite Materials for Adsorption and Catalytic Oxidation of Organic pollutants: An Experimental and Theoretical Study**" embodies the original research work and has fulfilled all the requirements according to the rules/regulations of Nagaland University.

Further, to the best of my knowledge, the present research work has not been submitted to any University/Institution for the award of any degree or diploma.

17/2/23

(Prof. Dipak Sinha)
Supervisor

ACKNOWLEDGEMENTS

"Alone we can do so little, together we can do so much".

I take this moment to extend my appreciation and gratitude to every individual for their help and support through the course of my Ph.D. journey. THANK YOU.

Firstly, I would like to thank our almighty God for blessing me with wisdom, good health, and guidance throughout my research journey.

I extend my heartfelt and profound gratitude to **Prof. Dipak Sinha**, my research supervisor, for allowing me to work under him in the first place. His constant and patient guidance, enthusiastic motivation, and encouragement have always been the fuel to move one step further. His valuable and constructive critiques have always been the pillar, without which the completion of this work would not have been possible. The years spent under his guidance have been a worthy experience that has molded me into the person I am today. His consistency in discussing creative and brilliant ideas has been a catalyst which has elevated my interest and confidence in science more than ever before.

I would also like to thank **Prof. Upasana Bora Sinha** (Head of Department), Department of Chemistry, Nagaland University, for her thoughtful advice and constructive recommendations. Her ever-ready attitude and excellent caliber to proofread my manuscripts whenever I approach, despite her busy schedule have contributed significantly to the success of my research work.

I also would acknowledge a deep sense of gratitude to all the teaching faculties of the Chemistry department, Nagaland University: **Prof. M. Indira Devi**, **Dr. I. Tovishe Phucho**, **Dr. M. Prabhakar**, **Dr. Nurul Alam Choudhury**, and **Dr. Seram Dushila Devi**, for their useful suggestions and assistance that helped me to keep my progress on track.

My sincere gratitude to **Nagaland University**, for providing the basic facilities to conduct my research. I am also grateful to the University Grant Commission (PF/RDC/NNF-72/2018-2912) for providing financial assistance.

I extend my sincere gratitude to **Prof. Nikhil Guchhait**, Department of Chemistry, Calcutta University for extending computational facility.

Sl. No. : 16- **59084**

NAGALAND UNIVERSITY

STATEMENT OF MARKS
Ph. D COURSE WORK EXAMINATION, 2017

DEPARTMENT OF ____CHEMISTRY____

The following are the marks secured by _____Soremo L. Ezung_____

Roll No. ____11/16____ of Ph.D Course Work Examination held in ____2017____

Subject(s)/Paper(s)	Max. Marks	Minimun Qualifying Marks	Marks Secured
Paper No. Chem-601 Research Methodology	100	35	**75**
Paper No. Chem-602 (D) Advance in Chemistry	100	35	**64**
Paper No. Chem-603 Literature Review, Report Writing and Presentation	100	35	**72**
Total Aggregate Marks			**211**
Average Pass Mark – 55 %			

Result	Division	Percentage
Passed	**I Division**	**70 %**

Marks compared by

COE/Dy. Reg./AR (Exams)

NAGALAND UNIVERSITY

HEAD QUARTERS : LUMAMI

Ph. D COURSE WORK EXAMINATION

This is to certify that Mr/Ms. _____Soremo L. Ezung_____

of Nagaland University bearing Roll No. ____11/16____ is qualified in the Ph.D Course Work Examination

in the Department of ____Chemistry____ Nagaland University held in the Year 20__17__

Head of Department
Head
Department of Chemistry
Nagaland University

Dean Dean
School of ____Science____
School of Sciences
Nagaland University
HQ. Lumami Nagaland

CONTENTS

CHAPTER 3: Experimental and theoretical insight into the adsorption of 2,4-dichlorophenol on low-cost bamboo sheath activated carbon   61-89

CHAPTER 4: Photocatalytic degradation of the organophosphorus insecticide chlorpyrifos in aqueous suspensions using a novel activated carbon ZrO_2-ZnO nanocomposite under UV light   90-120

CHAPTER 5: Photocatalytic degradation of chlorpyrifos using Fe-doped ZnO/activated carbon nanocomposite

CHAPTER 6: 2,4,6-Trichlorophenol adsorption using activated carbon: A DFT analysis of the role of functional groups on the carbonaceous surface

CHAPTER 7: Summary and Conclusion   **159-162**

Appendix 1   *Ph.D. Thesis Certificate on Plagiarism check*

List of Figures

List of Tables

CHAPTER 1

INTRODUCTION

This chapter represents a brief introduction of activated carbon, carbon nanocomposite, and Density Functional Theory simulations of activated carbon, its structure, and properties. The chapter also discusses the raw precursors used for the synthesis of activated carbon and carbon nanocomposite, different types of synthesis methods, and modification techniques. The applications of the activated carbon and carbon nanocomposite materials for adsorption and catalytic oxidation of aqueous organics are also discussed.

1.1. Introduction

Water contamination is rising at an alarming rate, and the entire planet is in its malignant grip [1]. Water contaminants at various concentrations in water (including drinking water, groundwater, and surface water) represent a significant danger to the environment and human health. The advent of the industrial revolution, continued economic expansion, population growth, and climate change have contributed immensely to poor water quality leading to scarcity of clean water. As a result, providing clean, safe water, particularly drinking water, becomes increasingly challenging and vital in developing countries. The majority of water pollution is caused by the discharge of organic and inorganic pollutants from the textile industries, chemical sectors, pharmaceutical sectors, and domestic household applications [2-4]. The use of harmful chemicals in various industrial operations pollutes water, posing a significant threat to the ecosystem [5]. While certain hazardous organic compounds are easily biodegradable by microbes in water, synthetic chemicals cannot be eliminated from water by natural phenomena [6]. Chemicals that are very persistent in the environment include phenolic compounds, insecticides, synthetic dyes from the textile industry, nitroaromatics, polycyclic aromatic hydrocarbons, organochlorines, polychlorinated biphenyls, polymers, and among others [7-10].

Since organic pollutants have several negative side effects and are carcinogenic, they cause a serious threat to human health and the environment [11]. As a result, removing hazardous organic contaminants from water is critical in the current situation.

Several techniques for treating organic pollutants in wastewater are currently available, including biological treatments, ion exchange, reverse osmosis, adsorption, microbial and enzymatic breakdown, and catalytic oxidation, among others. The development of a suitable approach for the removal of water pollutants is dependent on various aspects, including treatment efficiency, economic efficiency, pollutant type, pollutant concentration, and environmental compatibility [12]. Figure 1.1 shows some of the common physicochemical techniques for wastewater treatment.

Among this method, adsorption is regarded as one the finest water waste treatment technology for the removal of organic contaminants due to its easy operation, lack of pre-treatment requirements, eco-friendliness, lack of harmful byproducts, and low cost. Adsorption is defined as the accumulation of a substance at a surface or interface. In the case of water treatment, the process takes place at the interface of solid adsorbent and contaminated water. Adsorbate refers to the pollutant that is being adsorbed, and adsorbent refers to the adsorbing phase [13].
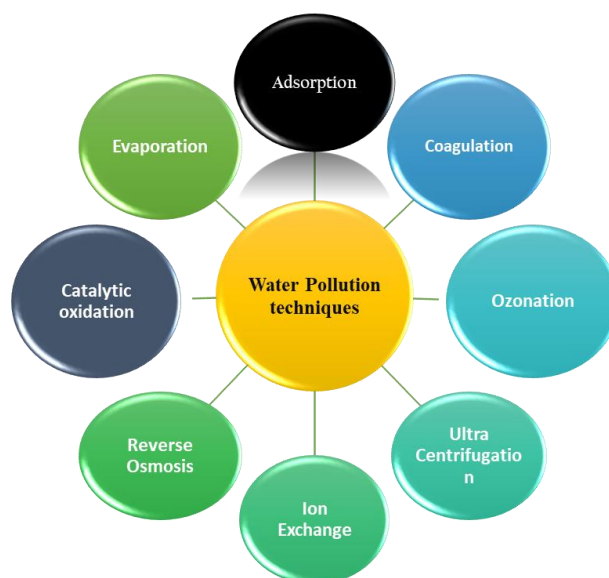
Figure 1.1. Wastewater treatment methods.

Adsorption through activated carbon is most commonly used as a successful method for the removal of various organic pollutants from aqueous solutions due to its highly developed pore structure, large surface area, and surface chemical functional groups [14,15]. Despite the fact that (or although) activated carbon has such capabilities, its use is restricted due to its short service life and difficulty in separation/recovery from polluted water [16]. As a result, it is important to develop more capable and cost-effective adsorbents with the minimal contact time, greater adsorption capacity, and the ability to perform in neutral conditions, with a focus on real-world application. Specifically, biomass-derived activated carbon has emerged as a viable substitute for expensive commercial activated carbon since biomass resources are abundant, renewable, and inexpensive.

Activated carbon is a type of co-adsorbent that is widely used as a key support for the photocatalyst in wastewater treatment via the photocatalytic degradation method [17]. The interesting use of AC as catalytic support materials arises from their large surface area, high aspect ratio, and ability to disperse catalytically active metal particles, which are important in catalytic applications. The often-employed techniques for wastewater purification, such as coagulation, membrane filtration, flotation, ion exchange on resins, adsorption, chemical precipitation, etc., transform pollutants into harmful byproducts and produce sludge, whose removal imposes more expense and steps [18]. However, each procedure has its efficiency and limitations. Photocatalysis is one of the most promising advanced oxidation processes (AOPs) and has attracted a lot of interest in the last two decades since it may mineralize refractory or hazardous organic molecules to carbon dioxide, water, and mineral acids at room temperature

[19]. The majority of photocatalytic studies employ metal oxides such as TiO_2 (Titanium dioxide), ZnO (Zinc oxide), WO_3 (Tungsten trioxide), CuO (Copper oxide), and ZrO_2 (Zirconium dioxide), etc [20].

In addition, for any removal studies, it is essential to understand the mechanism involved in the process which is a prerequisite for designing a treatment plant. In this regard, numerous researchers have studied the mechanism through theoretical approaches of which density functional theory (DFT) is one strong tool for investigating the mechanism involved during the removal process (adsorption, absorption process, etc.). Li *et al.* [21] investigated transition metals (Ti, Mn, Fe, Co, Ni, Cu, Ag)-doped graphene and their adsorption capabilities find good candidates for selective AsH_3 adsorption rather than CO by DFT method. Al-Kahtani *et al.* [22] studied the photocatalytic degradation mechanism of bisphenol- A (BPA) by ZnS/NSDC nanocomposite and supported the experimental results with theoretical calculations via, density functional theory (DFT). These efforts suggested that the fabricated ZnS/NSDC nanocomposite exhibits excellent properties and can be used as a reusable photocatalyst for the degradation of BPA in an aqueous solution. Thus, in this proposed work, mechanisms involved during the removal processes will be calculated using the Gaussian 09 program package implementation of DFT method. Shen *et al.* [23] reported a systematic theoretical analysis on activated carbon for the adsorption of hydrogen sulfide (H_2S) . The study was performed using the DFT method to provide a molecular-level understanding of the adsorption mechanism, shown in Figure 1.2. Both zigzag and armchair edge sites of benzene ring models were considered as possible active sites of activated carbon and the zigzag edge sites appeared to provide a stronger force to attract H_2S than the arm chair edge sites.

Zigzag (Zg)   **Armchair (Am)**
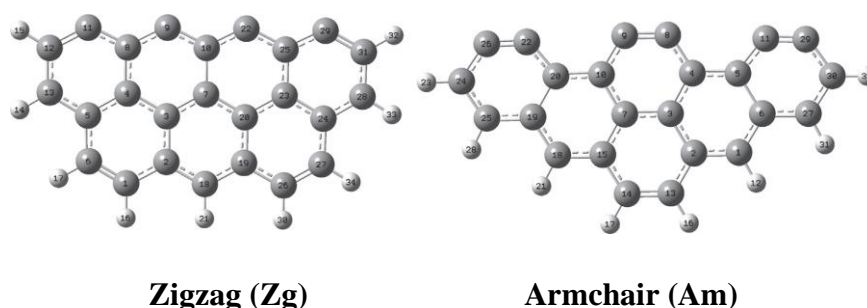
Figure 1.2. Activated carbon surface models [23].

Given the importance of wastewater treatment, it is considered worthwhile to describe the activated carbon and photocatalysis for the removal of organic pollutants.

1.2. Activated carbon (AC)

Carbonaceous materials with high porosity, high physicochemical stability, numerous functional groups, strong adsorptive capacity, and a high degree of surface reactivity are referred to as activated carbon [24].

Activated carbon (AC) is a flavorless, amorphous, microcrystalline, non-graphite form of carbon and black solid material that resembles powdered or granular charcoal. The term "activated carbon" refers to carbonaceous materials that have high porosity, high physicochemical stability, high adsorptive capacity, high mechanical strength, strong surface reactivity, and a well-developed pore structure [25]. In many cases, the presence of heteroatoms including oxygen, sulphur, hydrogen, nitrogen, halogen, and other elements has been linked to activated carbon [26,27], in the form of functional groups that were chemically attached to the structure. The functional groups on the AC surface are either produced by carbonization of biomass or modified by chemical agents during the activation process. AC surfaces can be oxidized or modified by adding nitrogen-containing groups to form nitrogen and oxygen enriched carbons. Using potassium hydroxide, NaOH, and H_2SO_4, oxygen can be produced in the form of functional groups such as carboxyl, carbonyl, phenols, lactones, and others during the activation process [28] while nitrogen-containing functional groups such as amide, amine, pyridine, and pyrrole can be generated during the activation process utilizing ammonia, urea, and melamine solution in ethyl alcohol [29]. Figure 1.3 represents some of the functional groups that might be available on the surface of activated carbon.
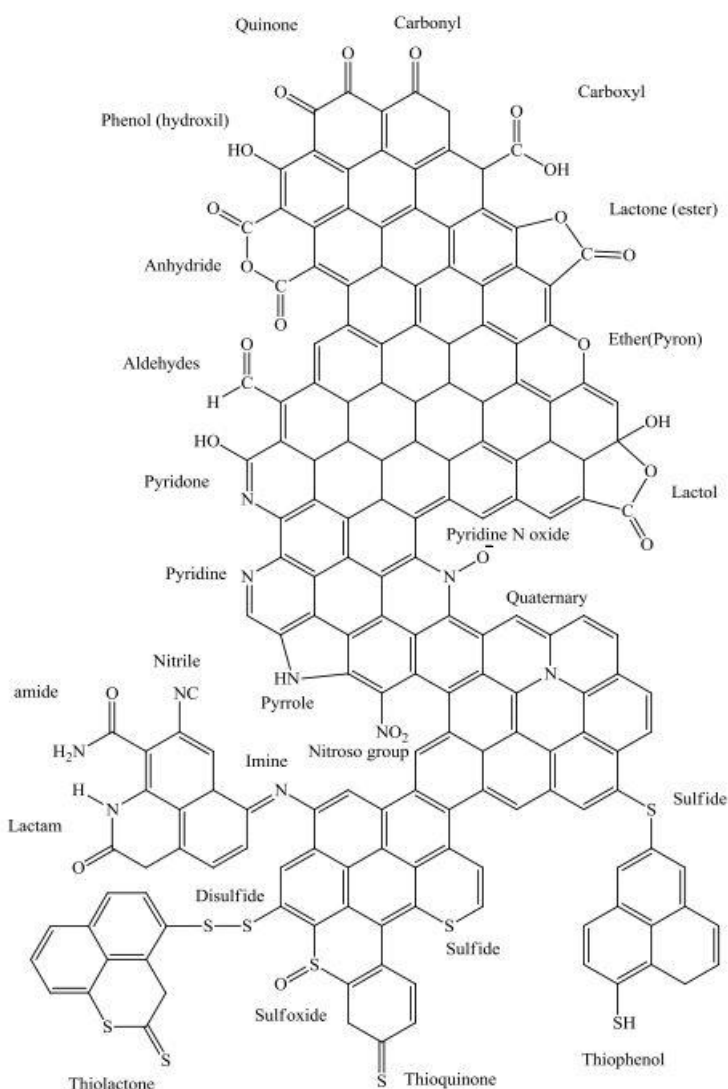
Figure 1.3. Oxygen, sulfur, and nitrogen functional groups on the surface of activated carbon [30].

According to Cuhadaroglu and Uygun [31] AC does not have a particular chemical formula. Depending upon its physical properties, activated carbon can be divided into several categories, including powdered AC, granulated AC, extracted AC [32], fibrous AC [33], AC cloths [34], and others. Based on these attractive features, activated carbon is regarded as a remarkable and adaptable carbon material with a wide range of useful applications in supercapacitors, batteries, gas separation, wastewater treatment, energy storage, air purification, medicine, and catalytic processes, among many other things.

Over the last few years, it has been widely employed for environmental pollution protection, and antipollution regulations have increased the sales of AC for air and water pollution control.

AC is a broad-spectrum agent that successfully eliminates harmful and bio-refractive chemicals found in many water sources, including pesticides, herbicides, chlorinated hydrocarbons, heavy metal ions, and phenols [35]. AC is a common adsorbent with an excellent capacity for pollutant removal; however, desorption and reuse are difficult under normal conditions, and the overall process is expensive [36]. The production of low-cost adsorbents from waste materials was effectively employed for the removal of water contaminants utilising adsorption technology that included batch procedures and column operations [37]. The ongoing improvement and optimization of the activated carbon production process, as well as the use of novel raw materials, have resulted in the creation of higher-quality carbon that is currently in use.

1.2.1. Raw material for the synthesis of activated carbon

AC can be synthesized using both naturally occurring and synthesised carbonaceous solid materials, according to Girgis *et al.* [38]. Depending on the raw materials, it has been categorised. The starting material or precursor used has a significant impact on the quality, features, and qualities of the produced activated carbon [39,40]. Cagnon *et al.* [41] have highlighted that the structure of the starting material may also have an impact on the characteristics of AC**.** Commercially AC uses precursors such as petroleum residues, wood, coal, peat, and lignite which are very expensive and non-renewable [42]. Therefore, in recent years, researchers have been focusing on the preparation of AC based on agricultural waste and lignocelluloses materials which are effective and low cost, such as corn cob, hazelnut shell, pruning mulberry shoot, olive stone, Jojoba seed, Chinese fir sawdust, coconut shell, wood, hazelnut bagasse, kenaf fiber, bamboo, rice husk, petai, groundnut shell, paper mill sludge, prosopis (Prosopis juliflora), coconut husk, Jatropha husk, tamarind wood, pistachio-nut, sugarcane bagasse, jackfruit peel, and many others [43].

In contrast to their availability, renewability, and cost-effectiveness, these biomass sources have a high proportion of volatile matter, which is excellent for producing a highly porous structure of activated carbon. Most biomass resources are discarded as trash without suitable usage from a marketing perspective. As a result, converting agro-waste or biomass resources into value-added products such as activated carbon can eventually reduce waste disposal costs and the negative environmental effect [44].

1.2.2. Preparation of activated carbon

The activation process creates or increases porosity on the AC surface as shown in Figure 1.4. AC can be synthesized either directly from dried raw materials or using a two-step activation

process that includes carbonization of the raw precursor followed by activation [45]. Based on the type of activation method. AC are commonly synthesized in two ways: (i) Physical or gas activation method, and (ii) Chemical activation.

Before Activation   **After Activation**

Pores
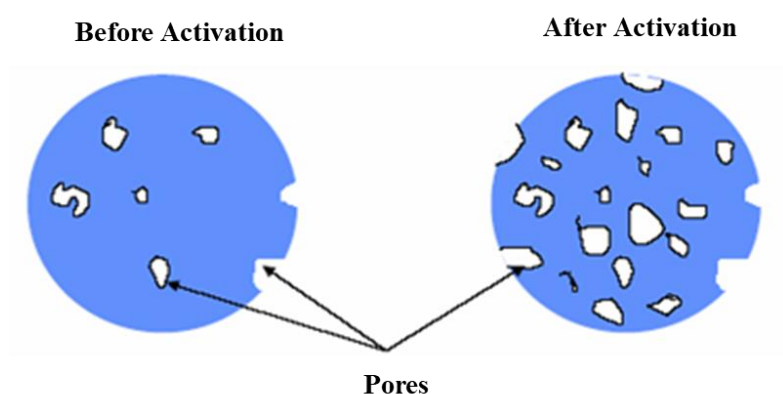
Figure 1.4. Two-dimensional representation of carbon activation [46].

Physical activation

Physical activation consists of two steps: first, pyrolyzing raw material in an inert environment at temperatures above 400 °C to remove the majority of the volatile matter, followed by activating the carbonised sample using oxidising gases like steam, nitrogen, carbon dioxide, or their mixtures at temperatures between 600 to 1200 °C [47-49]. This process can synthesize activated carbon with an excellent porous structure as well as physical strength and is regarded as a low-cost green approach due to the lack of chemicals [50,51]. Physical activation, on the other hand, has drawbacks which include a long activation period, high energy consumption, and a limited adsorption capacity of the resulting AC [52].

Chemical activation

Chemical activation or wet oxidation can be accomplished in one or two steps. In the one-step method, the dried raw material is immediately impregnated with oxidising and highly dehydrating chemicals and activated at high temperatures for a predetermined period [53]. In the two-step process, the dried raw material is first carbonised at temperatures ranging from 400 to 600 °C to generate char, and then the char is impregnated with chemical agents and heated at high temperatures [52]. Finally, AC is generated by repeatedly washing the activated sample. In this process, the activated carbon is washed with acid or alkali, depending on the chemical reagents employed in the synthesis, and then rinsed with water. The components in the activated carbon would be eliminated during the washing process. The pores of the produced

AC are largely occupied by the chemicals in the carbon structure. As a result, the washing phase is one of the most essential processes in the chemical activation process for developing porosity in AC [54].

The most common chemicals used as an activating agent include metal salts like $FeCl_3$, $ZnCl_2$, and $MgCl_2$ [55-57], alkaline groups like Na_2CO_3, K_2CO_3, NaOH, and KOH, and acidic groups like HNO_3, HCl, H_3PO_4, and H_2SO_4. A porous structure is created when these chemical agents interact with the carbon matrices of the precursor and release gas products [58]. Furthermore, they operate as oxidizing or dehydrating agents, which promote pyrolytic breakdown and increase the generation of activated carbon by lowering tar and ash formation [59,60]. Activating agents serve critical roles in the development of surface chemical groups or pores during activation. Among the several chemical activating agents, potassium hydroxide (KOH) is one of the most effective for creating AC with an extraordinarily high specific surface area [61].

In comparison to physical activation, Chemical activation is preferred because it creates AC with a greater surface area and better-developed pore structures [62]. Furthermore, the lower activation temperature and shorter activation time make the procedure economically viable [63].

1.2.3. Effect of activating agents

The improvement of AC surface area and pore volume can be done by using different chemical activating agents. The most often employed chemical activating agents for improving the textural qualities of activated carbon are H_3PO_4, $ZnCl_2$, and KOH [64,65]. The use of Zinc chloride increases the inter- and intra-voids, resulting in the development of activated carbon with a large surface area and porosity [66,67]. H_3PO_4 enhances the yield of carbon and creates higher pore volumes with both micro- and mesopores [68]. On the other hand, the use of KOH causes AC to create well-developed micropores, which results in the creation of a large surface area [69-71].

1.2.4. Effect of impregnation ratio

The impregnation ratio is the weight ratio of the activating agent to the precursor. It has been recognized as one of the most important factors in the process of chemical activation. Giraldo and Moreno-Pirajan, have reported that the impregnation ratio has a substantial impact on the development of porosity [72]. The use of $ZnCl_2$ and KOH as activating agents, by varying the activating agent/precursor ratio between 2:1 and 3:1. The surface area and total pore volumes

increase as the ratio increased from 2 to 3. The increase in porosity was related to the release of tars from the cross-linked framework, which occurred as a result of the chemical reagents. Singh *et al.* investigated chemical impregnation with KOH and found that activation at 600 °C with an impregnation ratio of 1:2 generated AC with the maximum surface area and degree of porosity [73]. Akpen *et al.* [74] investigated the removal of colour from wastewater using activated carbon derived from the seeds of two types of mangos, local and dausha. They utilized anhydrous $ZnCl_2$ as a chemical activating agent. The impregnation ratios were 1:2 and 1:3. The efficiency of AC was in the sequence of local 1:2>local 1:3>dausha 1:2>dausha 1:3. They observed that the impregnation ratio might influence the efficacy of AC. The study on grape industrial processing waste using $ZnCl_2$ as an activating agent done by Sagili *et al.* [75] found that a larger impregnation ratio resulted in mesopore production whereas a lower impregnation ratio results in micropore creation. This is because a larger impregnation ratio causes more swelling and a stronger release of volatile matter contents, causing pores to widen [76]. Meanwhile, a low impregnation ratio increases the release of volatile matter contents while inhibiting tar deposition, resulting in the creation of more micropores. Similarly, several investigations have found that the impregnation ratio has a significant influence on the surface area and pore volume of AC [77,78].

1.2.5. Effect of temperature on surface area and pore volume

The activation temperature is an important parameter that influences the textural properties of AC. The ideal temperature range is determined by the type of precursor, activation agent, heating source, mixing procedure, and other factors. A high activation temperature may reduce specific surface area and carbon production. This might be owing to the increased conversion of cross-linked compounds in the solid phase to volatile chemicals in the gas phase [79,80]. Also, a low activation temperature might lead to a poor porous structure since the activation energy is insufficient to start pyrolysis, which would produce an incomplete reaction [81]. Therefore, to create AC with a relatively large surface area and pore volume, an ideal temperature range must be identified for each activation procedure. The optimal activation temperature when employing acidic activating agents usually ranges between 400 and 500 °C, whereas the optimal activation temperature when using alkaline and self-activating agents usually ranges between 750 and 850 °C [82,83].

1.2.6. Applications of activated carbon

AC is a superior and adaptable adsorbent with numerous uses in a variety of industries includ-

ing the removal of colour, odour, and undesirable inorganic and organic chemicals from water, solar cells, gas-phase adsorptions, solvent recovery, separation and purification technologies, catalytic processes, biomedical applications, pollution control, spill clean-up, supercapacitors, energy storage, batteries, etc [84-88].

The enormous surface area, well-developed porosity, and high surface reactivity of AC are primarily responsible for their exceptional adsorbent qualities. Additionally, the adaptability of AC in the alteration of its physical and chemical features has made it possible for its use in a wide range of fields [89]. AC is one of the most used for the removal of different biological, organic, and inorganic contaminants from wastewater. Several researches have described the use of biomass-derived AC for the removal of such contaminants from water. For example, AC prepared from distillers' grains with an adsorption capacity of 934.57 mg/g was used by Wang *et al.* to remove methylene blue from an aqueous solution [90]. Nasser *et al.* [91] investigated the capacity of palm fruit bunch particles to absorb basic dye (BR18) over a range of initial dye concentrations with adsorbent particle sizes ranging from 106 to 300 mm. The highest dye adsorption capacity q_{max} of palm bunch was determined to be 242 mg/g. The removal of bisphenol A using AC generated from argan nutshells material has a maximum adsorption capacity of 1250 mg/g at 293 K [92]. Supong *et al.* [93] investigated both experimental and theoretical studies on the adsorption of phenol and dinitrophenol on *Tithonia diversifolia* activated carbon. It was found that removal efficiency of phenol was 99.98% and dinitrophenol was 97.81% respectively. The removal of methylene blue (MB) and hexavalent chromium (Cr (VI)) from an aqueous solution using AC derived from biosludge of natural rubber waste, was first reported by Mahapatra *et al.* [94]. Khalil *et al.*, developed AC from sugarcane bagasse, and the results reveal that it has good adsorption properties for the adsorptive removal of phenolic compounds [95]. Bhomick *et al.* [96] investigated the production of activated biocarbon from *Pinus kesiya* cone by $ZnCl_2$ activation and reported that its effectiveness in the elimination of Alizarin Red S (ARS) dye was 89%. The capacity of AC obtained from waste newspaper (WNAC) to remove the herbicide glyphosate from aqueous solution is investigated by Nourouzi *et al.* [97].

1.3. Photocatalysis

Photocatalysis is the process of altering the rate of a chemical reaction when it is exposed to light (ultraviolet/visible/infrared radiation) in the presence of a photocatalyst [98]. The development of the photocatalytic process is one of the most promising procedures for the degradation of organic pollutants due to its ease of use, high efficiency, absence of secondary

pollution, and cheap cost [99]. Photocatalysis occurs when photocatalyst materials expose to light, it produce highly reactive hydroxyl radicals ($\cdot$OH) [100]. These active hydroxyl radicals may easily oxidize pollutants and mineralize them to H_2O and CO_2 [101]. Based on the photocatalyst phase with regard to the reactants, photocatalysis can be divided into two types: homogeneous photocatalysis and heterogeneous photocatalysis [102].

A homogeneous photocatalyst forms reactive hydroxyl radicals when exposed to light in the presence of reactant molecules and photocatalyst molecules. The two most widely utilized homogeneous photocatalysis methods are Photo-Fenton systems ($UV/Fe^{2+}/H_2O_2$) and ozone photolysis ($UV/O_3/H_2O_2$) [103].

During the heterogeneous photocatalysis process, the reactants and photocatalysts coexist either in the solid-gas or solid-liquid phases [104]. This approach is an effective destructive technology for photocatalytic degradation of contaminants because of its ease of removal from the reaction mixture, lower operating costs, and reusability [105]. In this process, semiconductor metal oxides are employed to degrade harmful organic contaminants by using easily available atmospheric oxygen and light as the source of oxidant and energy [106]. As a result, our current study focuses on the production of heterogeneous semiconductor metal oxide catalysts and their use in pollutant degradation.

1.3.1. Mechanism of heterogeneous photocatalysis

The heterogeneous photocatalysis mechanism used for the photo degradation of highly toxic and hazardous pollutants to carbon dioxide (CO_2) and water (H_2O) are explained below [107].

(i) Excitation of the semiconductor

A semiconductor metal oxide's structure includes a conduction band (CB) and a valence band (VB), and the electrons are present in the valence band [108]. The energy that exists between the two bands is referred to as bandgap energy. When the semiconductor metal oxide is exposed to light with an energy equivalent to or greater than the bandgap energy, electrons (e^-) present in the VB are excited to the CB, leaving a hole (h^+) in the VB (equation 1.1). Photo-induced electrons at the bottom of the CB participate in reduction activities, whereas holes at the top of the VB participate in oxidation processes [109].

$$\text{Metal oxide} + h\nu \longrightarrow \text{Metal oxide } e^-_{CB} + h^+_{CB} \qquad 1.1$$
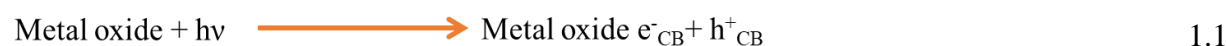
(ii) Formation of hydroxyl radical

In a photoreduction reaction, the excited electron (e^-_{CB}) can combine with the oxygen (O_2) that is adsorbed on the surface of MO to produce the reactive superoxide radical ($^.O_2^-$) given in equation 1.2.

$$e^-_{CB} + O_2 \longrightarrow O_2^{.-} \qquad\qquad 1.2$$

The superoxide radical continues to interact with water molecules to generate H_2O_2, which ultimately breaks down and releases the $^.OH$ radical (equation 1.3) [110].

The O_2^- radical further reacts with water molecules to form H_2O_2 which eventually decomposes with the liberation of $^.OH$ radical (equation 1.3).

$$O_2^{.-} + H^+ \longrightarrow HOO^.$$

$$HOO^. + HOO^. \longrightarrow H_2O_2 + O_2^.$$

$$H_2O_2 + HOO^. \longrightarrow {}^.OH + {}^.OH \qquad\qquad 1.3$$
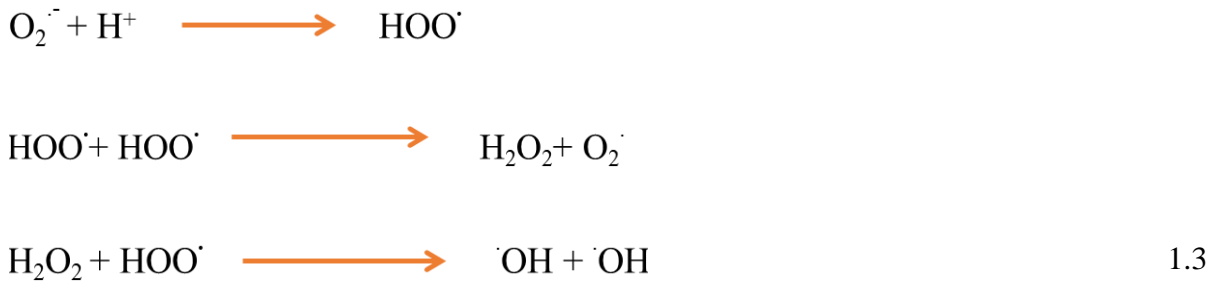
Now the hole (h^+_{VB}) can photo oxidize with water to generate the reactive hydroxyl radical ($^.OH$) (equation 1.4) [111].

$$h^+_{VB} + OH^- \longrightarrow {}^.OH \qquad\qquad 1.4$$

(iii) Recombination reaction

The produced hole (h^+_{VB}) and electron (e^-_{CB}) can also recombine without participating in photoreaction as well as releases the absorbed light energy as heat [112].

(iv) Photodegradation of organic pollutants

The adsorbed organic pollutants on the surfaces of semiconductors get oxidized by generating $^.OH$ radical. This extremely reactive $^.OH$ radical can oxidize organic contaminants to the mineralization products, producing CO_2 and H_2O, since it has an oxidation potential that is similar to that of a normal hydrogen electrode (2.8 V) [113]. Organic pollutants adsorbed on

semiconductor surfaces are oxidized by the generated $\cdot$OH radical. Because of the highly reactive $\cdot$OH radical, the organic pollutants can be oxidized into mineralized products, yielding CO_2 and H_2O (equation 1.5).

$$\text{Organic Pollutant} + \cdot OH \longrightarrow CO_2 + H_2O \qquad\qquad 1.5$$
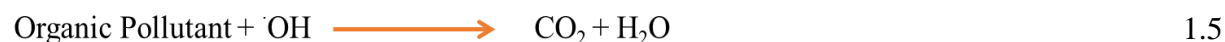
The schematic representation of the photocatalysis mechanism is shown in Figure 1.5:
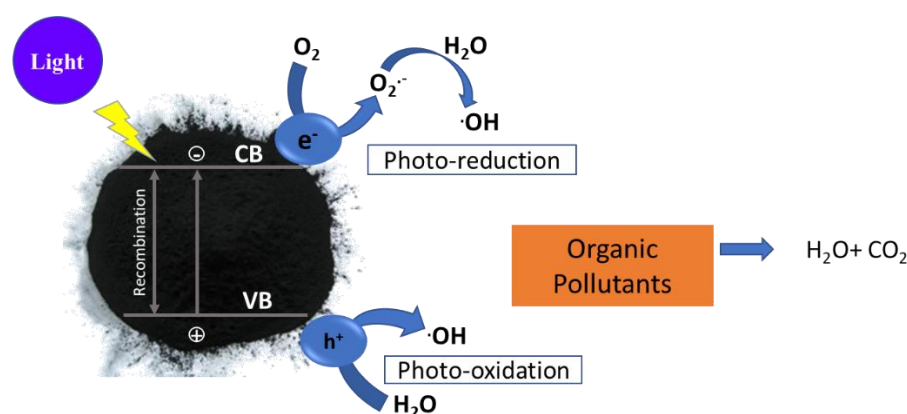
Figure 1.5. Photocatalytic degradation mechanism.

1.3.2. Semiconductor materials as photocatalysts

Several semiconductors (metal oxides) photocatalysts and their characteristics have been studied in recent years. Metal oxide photocatalysts should be photostable, physiologically and chemically inert, non-toxic, able to utilize UV and visible light energy, and have acceptable bandgap energies for catalyzing processes [112,114].

Table 1.1 provides a summary of the most common semiconductor metal oxides used as photocatalysts together with their bandgap energies (E_g) and appropriate wavelengths [115].

Table 1.1. Bandgap energy and wavelength of photocatalysts.

Semiconductor	Bandgap (eV)	Wavelength (nm)
ZnO	3.37	362
TiO_2	3.20	413
WO_3	2.80	443
Bi_2O_3	2.80	400
Fe_2O_3	2.20	539
CdS	2.40	514
CuS	2.20	570

ZnS	3.60	344
CuO	2.00	570
BiVO$_4$	2.40	500
Ag$_3$PO$_4$	2.45	365
g-C$_3$N$_4$	2.70	450
TaON	2.30	532
Ta$_3$N$_5$	2.10	473

A semiconductor must have the following characteristics to function as a photocatalyst effectively: a semiconductor metal oxide must absorb photons, generate electron-hole pairs, have minimal recombination of the electron-hole pairs, be stable over a long time, and have oxidation-reduction potential of the $\cdot$OH and H$_2$O pairs within the semiconductor material's bandgap domain [116].

Photocatalysis mainly uses different semiconductor metal oxides (TiO$_2$, SnO$_2$, Bi$_2$O$_3$, ZrO$_2$, ZnO, etc.) or metal sulphides (ZnS, PbS, CdS) for the degradation of pollutants using easily available solar light and atmospheric oxygen (O$_2$) as the source of energy and oxidant, respectively [117]. Among all the metal oxides used in photocatalysis, Zinc dioxide (ZnO) is considered to be a benchmark photocatalyst that is superior to others due to its good photoactivity, strong oxidizing power, low cost, active at ambient temperature, and non-toxic nature [118]. Therefore, in our present study, we used ZnO as a photocatalyst for photodegradation studies, a brief description of its characteristics, structures, etc. is provided in the following section.

1.3.3. Zinc oxide (ZnO) as a photocatalyst

Since Zn and O are grouped into groups 2 and 6 of the periodic table, respectively, ZnO is referred to as an II-VI semiconductor. Due to its distinct optical, chemical sensing, semiconducting, electric conductivity, and piezoelectric capabilities, it is one of the most thoroughly studied oxides [119]. Figure 1.6 illustrates the three phases of zinc oxide (ZnO) found in nature: cubic wurtzite, hexagonal zincblende, and rock salt. The thermodynamically most stable phase at room temperature is wurtzite. It possesses tetrahedral geometry, with each Zn atom tetrahedrally bound to four oxygen atoms and vice versa [120]. ZnO is an n-type semiconductor with a large band gap (3.37 eV), high excitation binding energy (60 meV), and deep violet/near ultraviolet (UV) absorption at room temperature. However, when lowered to the nanoscale and doped with other elements, its value may vary. ZnO has garnered a lot of attention in the degradation and total mineralization of water contaminants due to its incredible

benefits such as low cost and high quantum efficiency, as well as a favorable bandgap, high redox potential, and photocatalytic mechanisms [121]. The physical and chemical properties of wurtzite ZnO is shown in Table 1.2.
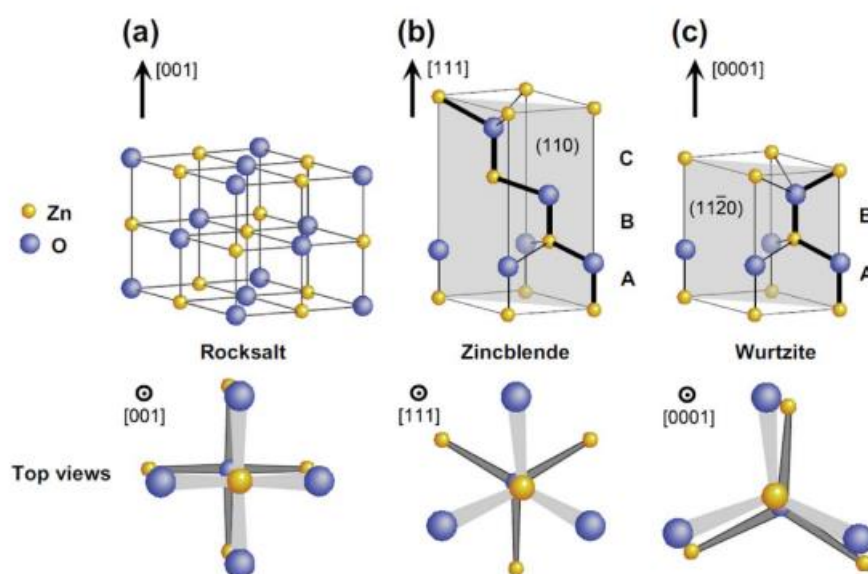
Figure 1.6. Different crystals forms of ZnO [122].

Table 1.2. Physical and chemical properties of wurtzite ZnO.

Properties	ZnO nanoparticles
Molar mass (g mol^{-1})	81.4
Light absorption (nm)	<320
Atoms per unit cell (Z)	4
Lattice parameters	a = 3.25Å, c = 5.205Å
Color	White solid
Odor	Odorless
Density (gcm^{-3})	5.6
Melting point (K)	2248
Flash point (K)	1709
Solubility	Insoluble in water
Refractive index	2.0041
Ti-O bond length (Å)	1.91 (monolayer)
	2.01 (bulk)
Thermal Conductivity (W m^{-1} K^{-1})	38-116

1.3.4. Limitations in ZnO photocatalysis

ZnO has a few limitations despite being widely utilised as an antibacterial agent in wastewater treatment, antifouling applications, and radiation-assisted breakdown of organic pollutants. One of the significant drawbacks of ZnO nanocomposite is its photo-instability in aqueous solution and high recombination rate of photogenerated electron-hole pairs, which considerably reduces the photocatalytic activity of pure photocatalysts [121]. Another disadvantage of pure ZnO is nanomaterial aggregation at high concentrations, a limited specific surface area of traditional bulk ZnO, and increased colloidal stability in water, making it more difficult to separate and recover after usage [123].

Researchers have incorporated hybrid foreign materials (metal/metal oxide, ceramic, or polymer) on ZnO semiconductors to further increase efficiency. The purpose of using these materials is:

I. To capture photoexcited electrons and then transfer them to a semiconductor surface. The recombination of photoinduced electron-hole pairs could be reduced by manipulating metal oxide-metal oxide heterostructures using ZnO hybrid [121].

II. An appropriate work function value would be one of the essential characteristics needed for the foreign substance. The major factors determining the work function of a hybrid system are its energy level, location, and efficiency of electron transfers in the semiconductor's conduction bands toward adsorbed electrolytes [124].

III. The matrix should have a large surface area and a high capacity for the adsorption of the contaminants to be degraded. This reduces the number of intermediates generated during photocatalytic degradation.

IV. The matrix should enable easy and quick photocatalyst recovery and re-use of photocatalyst with or without regeneration.

Supporting material

To get around the limitations of ZnO photocatalysis, activated carbon (AC) has been employed extensively as a support. AC modified with Zinc oxide has a larger surface area, cation exchange capacity, and porosity than the pristine material [125]. AC is a highly porous material with hydrophilic surface functional groups and a hydrophobic graphene layer used for both sorption and catalytic applications [126]. It has a good degree of porosity, a large surface area (500-2000 m^2g^{-1}), and a high rate of surface reactivity. As a result, in the current work, photocatalytic degradation of pollutants has been accomplished using a nanocomposite of ZnO with AC as a support system.

AC when combined with ZnO solves problems such as aggregation of ZnO particles in suspension, difficulties applying ZnO to continuous flow systems, and difficulty removing the powder from the solution after the reaction is complete. The introduction of AC in addition to ZnO significantly improved the photocatalytic capacity of the bare semiconductor [127].

The main advantages of using AC for ZnO support are:

i. It provides a high surface area and increases charge separation between CB and VB, allowing these species to diffuse into the surface and then react with pre-adsorbed redox species on the surface.

ii. The intermediates produced by photocatalysis can be successfully absorbed by AC for the subsequent degradation cycle, increasing the photocatalyst's availability [128].

iii. The photocatalytic activity of nanocomposite can be increased by combining semiconductors with AC, which can partially prevent the combination of photogenerated electron-hole pairs [129].

iv. ZnO/AC has a larger electron transfer capacity, is more readily dispersible, has smaller crystallite sizes, and is less likely to aggregate and passivate.

1.3.5. Modification of ZnO photocatalyst

ZnO is a promising semiconductor photocatalyst due to many appealing features. However, the photocatalytic activities of ZnO are limited. The fundamental disadvantage of ZnO photocatalysts is they undergo photo corrosion and shows instability when exposed to light. Also, a high recombination rate of photogenerated holes and electrons renders the photocatalytic process ineffective [130]. Another drawback of ZnO photocatalysts is their huge band gap, which is only effective when exposed to UV light and is ineffective when exposed to visible light, which limits the efficiency of using sunlight [131]. It is critical to minimize the bandgap energy to enable photodegradation in the visible light area. To overcome this limitation, researchers devised several techniques, including metal/nonmetal atom doping, noble metal deposition, and coupling with other semiconductors or carbon materials. The incorporation of this substance serves to capture and then transport photoexcited electrons on the semiconductor surface [132].

In recent years, there has been a lot of interest in ZnO/metal hybrid photocatalysis because it not only combines the unique properties of metals and semiconductors but also generates novel optical, electrical, and catalytic properties due to the synergistic interaction between metal and ZnO semiconductor. To improve the efficiency of ZnO as a photocatalyst, significant efforts are now being undertaken to synthesize ZnO-based nanocomposites. Many novel

nanocomposites, such as ZnO-CuO, ZnO-Fe$_2$O$_3$, ZnO-NiO, Zn-ZrO$_2$, and other novel nanocomposites have all been effectively produced. These efforts can increase photocatalytic activity by improving the photo response range and enhancing the efficiency of electron-hole pair separation [133,134]. The transfer of photogenerated electrons from the conduction band of ZnFe$_2$O$_4$ to ZnO, which reduces charge carrier recombination, might be a possible explanation for the enhanced visible photocatalytic activity of the produced Fe/ZnO catalyst as shown in Figure 1.7 [135].

The crystal's band edge positions were altered by the insertion of a metal ions dopant to the crystal lattice [136]. The cations that have been utilised for doping include rare earth metals (Th, Sc, Y) [137], transition metals (Fe, Co, Ni) [138], noble metals (Pd, Os, Ru) [139], poor metals (Al, Ga, Sn), non-metals (C, N, S) [140] and halogens (F, Cl, Br) [141]. Doping metal or non-metal atoms can successfully reduce the band gap of semiconductors altering the photoelectric characteristics of ZnO to expand its spectrum sensitivity to the visible light area. Doped metal/non-metal atoms alter the coordination environment of Zn atoms and modify the electronic structure of ZnO by introducing localised electronic energy levels in the band gap. The dopant energy level is briefly situated below the CB, trapping photogenerated charge carriers and increasing photocatalytic activity. Metals doped into ZnO are likely to broaden their visible light response and improve their quantum efficiency. Thus, doping ZnO with metals may enhance its photocatalytic activity.
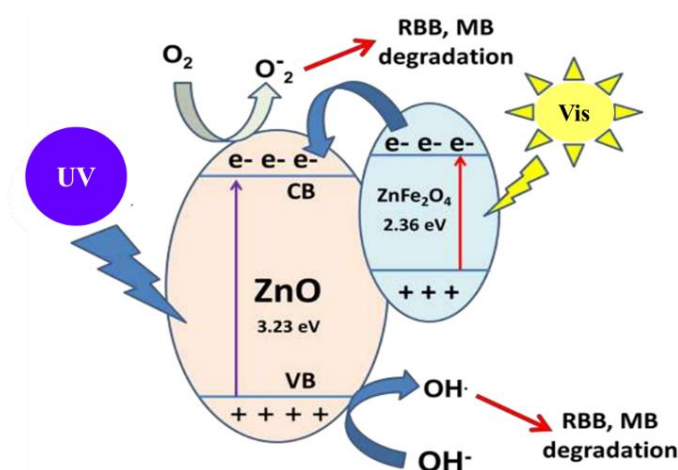
Figure 1.7. Mechanism for photocatalytic degradation of MB and RBB in the presence of ZnFe$_2$O$_4$/ZnO composite.

1.3.6. Applications of ZnO photocatalysis

The photocatalytic degradation of organophosphorus insecticides like chlorpyrifos (CPs) was

investigated in this study. CPs are commonly used in agriculture to increase production and protect crops from insects. The presence of chlorpyrifos in water can cause skin irritation, headaches, nausea, respiratory failure, stomach cramps, and even death in humans. Therefore, the elimination of these pollutants from water sources has become a prime concern for researchers. A brief description of the water pollutants studied in this thesis is given below:

Degradation of chlorpyrifos

Water containing polyaromatic, aromatic compounds is a major concern due to their highly toxic effects on nontarget organisms, including humans [142]. Chlorpyrifos penetrates freshwater and saltwater habitats mostly by spray drift and degraded soil particles. Surface water may be affected if soil containing absorbed chlorpyrifos is carried by storm water runoff [143]. These are highly toxic as they are not readily soluble in water and easily comes out of solution, and slow biodegradation capability. Thus, the removal of this hazardous substance from water is a high concern in the environment. The present study planned to utilize metal oxide photocatalysts supported on the surface of activated carbon nanocomposite for the degradation of chlorpyrifos from water and the result are discussed in Chapter 4 and 5.

1.4. Density functional theory study (DFT)

Quantum chemical calculations have become a significant technique for studying the structure and characteristics of molecules in recent years. Quantum chemical calculations may provide extensive information on molecular energy, charge, dipole moment, chemical bond, and other properties for most small and medium molecule systems. The calculated results have important implications for the investigation of adsorption mechanisms and the advancement of experimental research [144]. Even though the experimental studies provide valuable information, there are phenomena and system insights that cannot be observed through pure experimental methods. Furthermore, because of the complexity of the system and the coupling of various interactions, some experimental data are difficult to interpret. For instance, experiments cannot provide information on orbital and electronic charge distributions or molecular bonding. Experiments cannot anticipate the strength of interactions or the relative stabilities between various structures. As a result, a strategy that goes beyond experimentation is required to forecast the unobservable features and enhance the interpretation of the experimental results [145].

Quantum mechanics methods can be utilized to tackle issues that experimental approaches have failed to solve. The majority of molecular behavior may be predicted using various theoretical

approaches. For instance, the relative energy and stability of molecules or solids can be expected [146]. There are numerous sorts of computational approaches depending on the quantum theory used: ab initio method, semi-empirical/empirical method, molecular mechanics, and molecular dynamics [147]. The present work have considered density functional theory (DFT), which belongs to ab initio category since it provides a good balance between accuracy and computational cost [146]. Ab initio is commonly referred to as the first principle method because it allows people to determine many system properties by providing only basic structural information and no adjustable parameters [147]. It offers an alternative method for investigating systems to the traditional experimental and pure theoretical approaches based on quantum (field) theory.

All results are obtained directly from theoretical principles since the ab initio approach does not incorporate any empirical or semi-empirical parameters in their equation to solve the molecular Schrödinger equation. However, this does not indicate that the solution is precise; rather, it implies that the specific approximation is strictly specified on first principles, with a qualitatively expected error margin [147].

It is becoming a valuable tool for experimentalists and theorists to understand material properties, make specific predictions of experimentally observable phenomena for real materials, and design new materials [146].

DFT method uses Hamiltonian approximation and total electron density expression approximation to solve the Schrödinger equation. Hohenberg-Kohn and Kohn-Sham originally proposed it in two seminar papers in the 1960s [148,149]. From the 1960s to the 1980s, the lack of powerful computers severely limited electronic structure calculations based on density functional theory. The last few decades have witnessed the prevailing applications of the DFT method-especially after the 90s, the usage of the technique has increased exponentially owing to the advancement of computer technology. Nowadays, a single personal computer can perform such calculations for small and medium systems [147].

As of now, DFT is the most successful and promising method for computing the electronic structure of matter. It also calculates various molecular aspects, including molecular structures and energies, vibrational frequencies, electric and magnetic properties, reaction routes, etc. [150,151].

The density functional theory has been implemented in several computer programs such as VASP, Quantum Espresso, SIESTA, Gaussian, etc. In my research, I employed Gaussian to perform DFT calculations.

Gaussian 09

Gaussian is a popular and widely used computing program due to its user-friendly interface. As input coordinates, both Cartesian and Z-matrix are supported. The software includes a good number of basis sets. In addition to optimizing geometry and calculation of energies of systems, it can also be used to compute Raman and NMR spectrums, locate transition states, and so on (Gaussian).

The GAUSSIAN input consists of the following lines discussed below (Gaussian):

Link 0 commands: This line should contain the path to the "Checkpoint" file. The "Checkpoint" file is machine-readable and holds the results of the calculations (optimized structure and orbital information). It is advantageous when one calculation's results are used as the starting point for another calculation. This will save time in the computation (Gaussian).

Route section (lines which begin with #): The desired calculation type and iop parameters are mentioned in this section. This line specifies the task type (e.g. optimization, frequency, IRC, NMR, or ADMP), computational technique (e.g. ground state, TD-DFT, HF, DFT, CCSD, or MP2), and basis set. Internal settings can also be specified on this line to override the system defaults (Gaussian).

Title section: A summary of the calculation is specified here. In this section, a blank line is also acceptable (Gaussian).

Molecule specification: The molecular system to be studied is specified in this section. It is generally a line of spin and charge information accompanied by atom species and their coordinates. Both Z-matrix and Cartesian coordinates are valid formats (Gaussian).

Optional additional sections: Any other input required for specific job types is specified in this section (Gaussian).

1.5. Present study

Activated carbon is a well-known versatile adsorbent that is used in a variety of water-related applications. Another interesting feature of activated carbon is that it can be incorporated with photocatalyst and improves the removal efficiency of organic pollutants. However, its practical application is often limited due to the expensive cost and non-renewability of the precursor. Further, single semiconductor photocatalysts like Zinc oxide have certain limitations, such as photo corrosion and instability when exposed to light. Also, a high recombination rate of photogenerated holes and electrons renders the photocatalytic process ineffective. Another drawback of ZnO photocatalysts is their huge band gap, which is only effective when exposed

to UV light and is ineffective when exposed to visible light, which limits the efficiency of using visible light.

Therefore, keeping this in mind, the present study aimed to prepare activated carbon and activated carbon nanocomposite materials. The activated carbon was prepared from locally available waste material using KOH as an activating agent whilst the photocatalyst supported on activated carbon was prepared using the hydrothermal method. The physicochemical characterization was done using various analytical techniques. The synthesized activated carbon was then applied for the adsorption of 2,4-dichlorophenol whereas the prepared activated carbon nanocomposite was used for the degradation of chlorpyrifos from wastewater. The photocatalytic activity of a single photocatalyst such as ZnO can be increased by coupling or doping with metal/metal oxides, which may significantly improve photocatalytic performance via electron-hole separation and improved light absorption, as well as strengthen thermomechanical and chemical stability of ZnO. The well-known metal oxide zirconium dioxide (ZrO_2) has high thermal stability, and excellent corrosion resistance which helps to strengthen the thermo-mechanical and chemical stability of ZnO. Thus, ZrO_2/ZnO supported on activated carbon nanocomposite was applied for the degradation of chlorpyrifos from an aqueous solution under UV light.

To achieve visible light response photocatalysis, bandgap energy narrowing and lowering electron-hole recombination rate are the most important factors. Narrowing bandgap energy and lowering electron-hole recombination are the most important factors to achieve visible light active photocatalysis. Therefore, modification of nanocomposite by doping with transition metal was done to increase the visible light photocatalytic efficiency of nanocomposite towards the degradation of water pollutants. The modification of the prepared nanocomposite was done by doping transition metal through the hydrothermal synthesis method. The Fe-doped ZnO supported on activated carbon nanocomposite was applied for the degradation of chlorpyrifos from an aqueous solution under visible light. The mechanism of degradation of chlorpyrifos was studied using LC-MS analysis. The effect of different interfering ions in the degradation of pollutant molecules was also studied. The reusability of the nanocomposite for the photocatalytic degradation of pollutant molecules was also studied up to the sixth cycle. Besides, theoretical studies were also conducted to understand the mechanism involved in the adsorption process. The outline of the work undertaken in this thesis is shown in Figure 1.8.
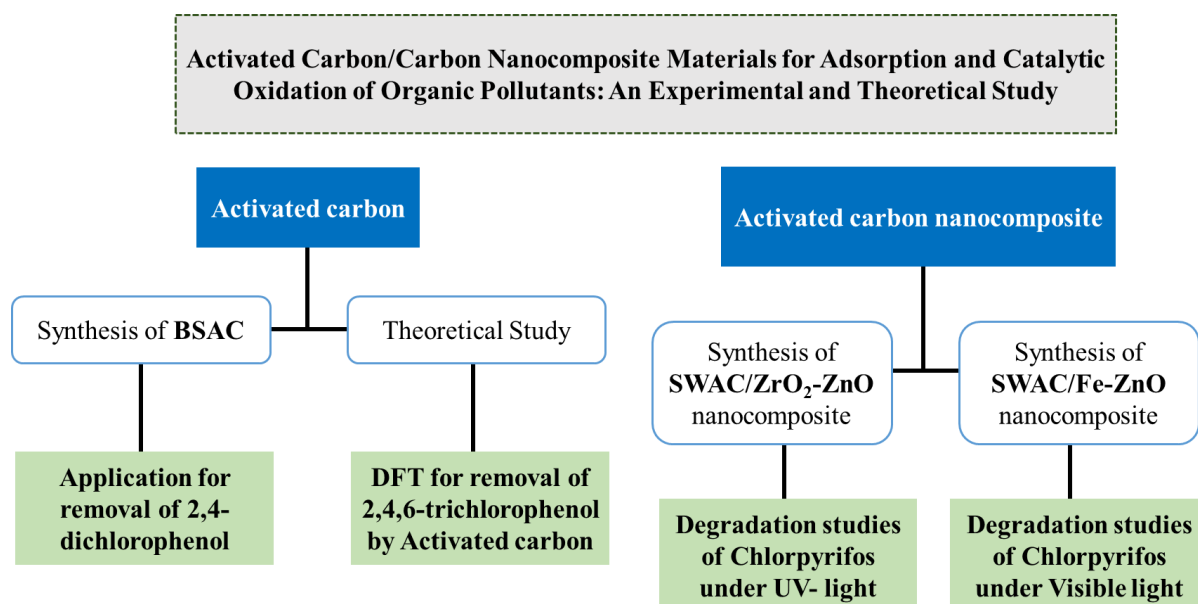
Figure 1.8. Scheme of the present study.

1.6. Aims and objectives of the work

The objectives of the present work are as follows:

1. To develop activated carbon adsorbent from locally available biomass material.

2. To develop activated carbon support nanocomposite using metal oxides for catalytic oxidation.

2. Reducing the band gap of nanocomposite materials by doping with transition metal thereby, shifting the oxidation process in the visible region.

3. Application of density functional theory to comprehend interaction processes between target pollutant and activated carbon surface.

The outline of the thesis is presented in Figure 1.9.

Chapter 1	Introduction
Chapter 2	Materials and methods
Chapter 3	Experimental and theoretical insight into the adsorption of 2,4-dichlorophenol on low-lost bamboo sheath activated carbon
Chapter 4	Photocatalytic degradation of the organophosphorus insecticide chlorpyrifos in aqueous suspensions using a novel activated carbon ZrO_2-ZnO nanocomposite under UV light
Chapter 5	Photocatalytic degradation of chlorpyrifos using Fe-doped ZnO/Activated carbon nanocomposite
Chapter 6	2,4,6-Trichlorophenol adsorption using activated carbon: A DFT analysis of the role of functional groups on the carbonaceous surface
Chapter 7	Summary and Conclusion

Figure 1.9. Outline of the thesis.

References

[1]   P. O. Ukaogo, U. Ewuzie, C. V. Onwuka, Environmental pollution: causes, effects, and the remedies, *in: Microorg. Sustain. Environ. Heal*., 21 (**2020**) 419-430.

[2]   S. D. Noel, M. R. Rajan, Impact of dyeing industry effluent on groundwater quality by water quality index and correlation analysis, *Res. J. Biotechnol.*, 2 (**2014**) 2-5.

[3]   M. El Khames Saad, R. Khiari, E. Elaloui, Y. Moussaoui, Adsorption of anthracene using activated carbon and Posidonia oceanica, *Arab. J. Chem*., 7 (**2014**) 109-113.

[4]   F. Lu, D. Astruc, Nanocatalysts and other nanomaterials for water remediation from organic pollutants, *Coord. Chem. Rev*., 408 (**2020**) 213180.

[5]   A. S. Ayangbenro, O. O. Babalola, A new strategy for heavy metal polluted environments: a review of microbial biosorbents, *Int. J. Environmetal Res. Public Heal*., 14 (**2017**) 1-16.

[6]   F. R. Deleo, H. F. Chambers, Reemergence of antibiotic-resistant Staphylococcus aureus in the genomics era, *J. Clin. Investig*., 119 (**2009**) 2464-2474.

[7]   H. Harms, D. Schlosser, L. Y. Wick, Untapped potential: exploiting fungi in bioremediation of hazardous chemicals, *Nat. Rev. Microbiol*., 9 (**2011**) 177-192.

[8]   K. Azam, N. Shezada, I. Shafiq, P. Akhter, F. Akhtar, F. Jamil, S. Shafique, Y. K. Park, M. Hussain, A review on activated carbon modifications for the treatment of wastewater containing anionic dyes, *Chemosphere*, 306 (**2022**) 135566.

[9]   M. Ahmaruzzaman, Adsorption of phenolic compounds on low-cost adsorbents: A review, *Adv. Colloid Interface Sci*., 143 (**2008**) 48-67.

[10]   A. Dąbrowski, P. Podkościelny, Z. Hubicki, M. Barczak, Adsorption of phenolic compounds by activated carbon - a critical review, *Chemosphere*, 58 (**2005**) 1049-1070.

[11]   M. Yang, A current global view of environmental and occupational cancers. *J. Environ. Sci. Health Part. C*, 29 (**2011**) 223-249.

[12]   M. T. Amin, A. A. Alazba, U. Manzoor, A review of removal of pollutants from water/ wastewater using different types of nanomaterials, *Adv. Mater. Sci. Eng*., 2014 (**2014**) 1-24.

[13]   Imran Ali, Mohd. Asim, Tabrez A. Khan, Low cost adsorbents for the removal of organic pollutants from wastewater, *J. Environ. Manage*., 113 (**2012**) 170-183.

[14]   H. Nourmoradi, A.R. Ghiasvand, Z. Noorimotlagh, Removal of methylene blue and acid orange 7 from aqueous solutions by activated carbon coated with zinc oxide (ZnO) nanoparticles: equilibrium, kinetic, and thermodynamic study. *Desalin. Water Treat.*, 55 (**2015**) 253-263.

[15] A. Kumar, H. M. Jena, Removal of methylene blue and phenol onto prepared activated carbon from fox nutshell by chemical activation in batch and fixed-bed column, *J. Clean. Prod.*, 137 (**2016**) 1246-1259.

[16] S. Alhan, M. Nehra, N. Dilbaghi, N. K. Singhal, K. Kim, S. Kumar, Potential use of ZnO@activated carbon nanocomposites for the adsorptive removal of Cd^{2+} ions in aqueous solutions, *Environ. Res.*, 173 (**2019**) 411-418.

[17] J. Matos, J. Laine, J. M. Herrmann, Effect of the type of activated carbons on the photocatalytic degradation of aqueous organic pollutants by UV-irradiated titania, *J. Catal.*, 200 (**2001**) 10-20.

[18] A. M. Ahmad, Green synthesis of Xanthan gum/Methionine-bentonite nanocomposite for sequestering toxic anionic dye, *Surf. Interfaces.*, 2 (**2013**) 65-72.

[19] R. Ahmad, P. K. Mondal, Adsorption and photodegradation of methylene blue by using PAni/TiO_2 nanocomposite. *J. Dispers. Sci. Technol.*, 33 (**2012**) 380-386.

[20] K. Byrappa, A. S. Dayananda, C. P. Sajan, B. Basavalingu, M. B. Shayan, K. Soga, M. Yoshimura, Hydrothermal preparation of ZnO: CNT and TiO_2: CNT composites and their photocatalytic applications, *J. Mater. Sci.*, 43 (**2008**) 2348-2355.

[21] Y. Li, X. Sun, L. Zhou, P. Ning, L. Tang, Density functional theory analysis of selective adsorption of AsH_3 on transition metal-doped graphene, *J. Mol. Model.*, 25 (**2019**) 1-12.

[22] A. A. Al-Kahtani, S. M. Alshehri, M. Naushad, Ruksana, T. Ahamad, Fabrication of highly porous N/S doped carbon embedded with ZnS as highly efficient photocatalyst for degradation of bisphenol, *Int. J. Biol. Macromol.*, 121 (**2019**) 415-423.

[23] F. Shen, J. Liu, Z. Zhang, Y. Dong, C. Gu, Density functional study of hydrogen sulfide adsorption mechanism on activated carbon, *Fuel Process. Technol.*, 171 (**2018**) 258-264.

[24] Z. Heidarinejad, M. H. Dehghani, M. Heidari, G. Javedan, I. Ali, M. Sillanpää, Methods for preparation and activation of activated carbon: a review, *Environ. Chem. Lett.*, 18 (**2020**) 393-415.

[25] M. A. Yahya, Z. Al-Qodah, C. W. Zanariah Ngah, Agricultural bio-waste materials as potential sustainable precursors used for activated carbon production: A review. *Renew. Sustain. Energy Rev.*, 46 (**2015**) 218-235.

[26] H. L. Chiang, C.P. Huang, P. C. Chiang, The surface characteristics of activated carbon as affected by ozone and alkaline treatment, *Chemosphere*, 47 (**2002**) 257-265.

[27] A. M. Puziy, O. I. Poddubnaya, R. P. Socha, J. Gurgul, M. Wisniewski, XPS and NMR studies of phosphoric acid activated carbons, *Carbon*, 46 (**2008**) 2113-2123.

[28] K. László, P. Podkościelny, A. Dąbrowski, Heterogeneity of polymer-based active carbons in adsorption of aqueous solutions of phenol and 2,3,4-trichlorophenol. *Langmuir*, 19 (**2003**) 5287-5294.

[29] M. Seredych, D. Hulicova-Jurcakova, G. Q. Lu, T. J. Bandosz, Surface functional groups of carbons and the effects of their chemical character, density and accessibility to ions on electrochemical performance, *Carbon*, 46 **(2008)** 1475-1488.

[30] F. G. Jahromi, A. Ghahreman, Effect of surface modification with different acids on the functional groups of AF 5 catalyst and its catalytic effect on the atmospheric leaching of enargite, *Colloids Interfaces*, 3 **(2019)** 45.

[31] D. Cuhadaroglu, O. A. Uygun, Production and characterization of activated carbon from a bituminous coal by chemical activation. *Afr. J. Biotechnol.*, 7 **(2008)** 3703-3710.

[32] L. I. Onyeji, A. A. Aboje. Removal of heavy metals from dye effluent using activated carbon produced from coconut shell, *Int. J. Eng. Sci. Technol.*, 3 **(2011)** 8238-8246.

[33] K. Tahvildari, T. Bigdeli, S. N. Esfahani, M. Farshchi, Optimization of activated carbon preparation from peach stone, *J. Appl. Chem. Res.*, 11 **(2009)** 47-55.

[34] J. M. Dias, M. C. M. Alvim-Ferraza, M. F. Almeida, J. Rivera-Utrilla, M. Sanchez-Polo, Waste materials for activated carbon preparation and its use in aqueous phase treatment: a review, *J Environ. Manag.*, 85 **(2007)** 833-46.

[35] A. Mohammad-Khah, R. Ansari, Activated charcoal: Preparation, characterization and applications: A review article, *Int. J. Chem Tech Res.*, 1 **(2009)** 859-864.

[36] S. S. Ray, D. Sangeetha, R. Vijayaraghavan, Enhanced activity and reusability of ZnO loaded magnetic activated carbon for the removal of organic pollutants under sunlight, *J. Chem. Pharm. Res.*, 7 **(2015)** 157-173.

[37] M. E. Gamal, H. A. Mousa, M. H. El-Naas, R. Zacharia, S. Judd, Bio-regeneration of activated carbon: A comprehensive review, *Sep. Purif. Technol.*, 197 **(2018)**, 345-359.

[38] B. S. Girgis, S. S Yunis, A. M. Soliman. Characteristics of activated carbon from peanut hulls in relation to conditions of preparation, *Mater. Lett.*, 57 **(2002)** 164-72.

[39] Y. A. Alhamed, Activated carbon from dates' stone by $ZnCl_2$ activation, *JKAU: Eng Sci.*, 17 **(2006)** 75-100.

[40] L. Li, P. A. Quinlivan, D. R. U. Knappe. Effects of activated carbon surface chemistry and pore structure on the adsorption of organic contaminants from aqueous solution, *Carbon*, 40 **(2002)** 2085-2100.

[41] B. Cagnon, X. Py, A. Guillot, F. Stoeckli, G. Chambat, Contributions of hemicellulose, cellulose and lignin to the mass and the porous properties of chars and steam activated carbons from various lignocellulosic precursors, *Bioresour. Technol.*, 100 **(2009)** 292-298.

[42] S. Altenor, B. Carene, E. Emmanuel, J. Lambert, J. J. Ehrhardt, S. Gaspard, Adsorption studies of methylene blue and phenol onto vetiver roots activated carbon prepared by chemical activation. *J. Hazard. Mater.*, 165 **(2009)** 1029-1039.

[43] M. A. Yahya, Z. Al-Qodah, C.W. Z. Ngah, Agricultural bio-waste materials as potential sustainable precursors used for activated carbon production: A review, *Renew. Sustain. Energy Rev.*, 46 **(2015)** 218-235.

[44] R. Yan, T. Chin, Y. L. Ng, H. Duan, D. T. Liang, J. H. Tay, Influence of surface properties on the mechanism of H_2S removal by alkaline activated carbons, *Environ. Sci. Technol.*, 38 **(2004)** 316-323.

[45] Z. Heidarinejad, M. H. Dehghani, M. Heidari, G. Javedan, I. Ali, M. Sillanpää, Methods for preparation and activation of activated carbon: a review, *Environ. Chem. Lett.*, 18 **(2020)** 393-415.

[46] N. B. Amari, Preparation of activated carbons from waste tyres char impregnated with potassium hydroxide and carbon dioxide gasification, *Master's thesis*, University Sains Malaysia **(2008)**.

[47] N. Radenahmad, A. T. Azad, M. Saghir, J. Taweekun, M. S. A. Bakar, M. S. Reza, A. K. Azad, A review on biomass derived syngas for SOFC based combined heat and power application, *Renew. Sustain. Energy Rev.*, 119 **(2020)** 109560.

[48] A. U. Rajapaksha, M. Vithanage, M. Ahmad, D. C. Seo, J. S. Cho, S. E. Lee, S. S. Lee, Y. S. Ok, Enhanced sulfamethazine removal by steam-activated invasive plant-derived biochar, *J. Hazard. Mater.*, 290 **(2015)** 43-50.

[49] T. Zhang, W. P. Walawender, L. T. Fan, M. Fan, D. Daugaard, R. C. Brown, Preparation of activated carbon from forest and agricultural residues through CO_2 activation, *Chem. Eng. J.*, 105 **(2004)** 53-59.

[50] J. Pallarés, A. González-Cencerrado, I. Arauzo, Production and characterization of activated carbon from barley straw by physical activation with carbon dioxide and steam, *Biomass and Bioenergy*, 115 **(2018)** 64-73.

[51] N. Byamba-Ochir, W. G. Shim, M. S. Balathanigaimani, H. Moon, Highly porous activated carbons prepared from carbon rich Mongolian anthracite by direct NaOH activation, *Appl. Surf. Sci.*, 379 **(2016)** 331-337.

[52] W. Ao, J. Fu, X. Mao, Q. Kang, C. Ran, Y. Liu, H. Zhang, Z. Gao, J. Li, G. Liu, J. Dai, Microwave assisted preparation of activated carbon from biomass: a review, *Renew. Sustain. Energy Rev.*, 92 **(2018)** 958-979.

[53] G. Jolly, L. Dupont, M. Aplincourt, J. Lambert, Improved Cu and Zn sorption on oxidized wheat lignocellulose, *Environ. Chem. Lett.*, 4 **(2006)** 219-223.

[54] C. Pongener, P. Bhomick, S. Upasana Bora, R. L. Goswamee, A. Supong, D. Sinha, Sand-supported bio-adsorbent column of activated carbon for removal of coliform bacteria and *Escherichia coli* from water, *Int. J. Environ. Sci. Technol.*, 14 **(2017)** 1897-1904.

[55] J. M. Ketcha, D. J. D. Dina, H. M. Ngomo, N. J. Ndi, Preparation and characterization of activated carbons obtained from maize cobs by zinc chloride activation, *Am.Chem. Sci. J.*, 2 **(2012)** 136-160.

[56] B. Wanassi, I. B. Hariz, C. M. Ghimbeu, C. Vaulot, M. B. Hassen, M. Jeguirim, Carbonaceous adsorbents derived from textile cotton waste for the removal of Alizarin S dye from aqueous effluent: kinetic and equilibrium studies, *Environ. Sci. Pollut. Res.*, 24 (**2017**) 10041-10055.

[57] Z. Xu, Z. Yuan, D. Zhang, W. Chen, Y. Huang, T. Zhang, D. Tian, H. Deng, Y. Zhou, Z. Sun, Highly mesoporous activated carbon synthesized by pyrolysis of waste polyester textiles and $MgCl_2$: physiochemical characteristics and pore-forming mechanism, *J. Clean. Prod.*, 192 (**2018**) 453-461.

[58] M. Molina-Sabio, F. Rodríguez-Reinoso, Role of chemical activation in the development of carbon porosity, *Colloids Surf. A Physicochem. Eng. Asp.*, 241 (**2004**) 15-25.

[59] M. K. B. Gratuito, T. Panyathanmaporn, R. A. Chumnanklang, N. Sirinuntawittaya, A. Dutta, Production of activated carbon from coconut shell: optimization using response surface methodology, *Bioresour. Technol.*, 99 (**2008**) 4887-4895.

[60] Y. Gao, Q. Yue, B. Gao, A. Li, Insight into activated carbon from different kinds of chemical activating agents: a review, *Sci. Total Environ.*, 746 (**2020**) 141094.

[61] X. Y. Cui, F. Jia, Y. X. Chen, J. Gan, Influence of single-walled carbon nanotubes on microbial availability of phenanthrene in sediment, *Ecotoxicology*, 20 (**2011**) 1277-1285.

[62] N. Rambabu, B. V. S. K. Rao, V. R. Surisetty, U. Das, A. K. Dalai, Production, characterization, and evaluation of activated carbons from de-oiled canola meal for environmental applications, *Ind. Crops Prod.*, 65 (**2015**) 572-581.

[63] J. M. Ketcha, D. J. D. Dina, H. M. Ngomo, N. J. Ndi, Preparation and characterization of activated carbons obtained from maize cobs by zinc chloride activation, *Am. Chem. Sci. J.*, 2 (**2012**) 136-160.

[64] J. Wang, S. Kaskel, KOH activation of carbon-based materials for energy storage, *J. Mater. Chem.*, 22 (**2012**) 23710-23725.

[65] G. Singh, K. S. Lakhi, I. Y. Kim, P. Srivastava, R. Naidu, A. Vinu, Highly efficient method for the synthesis of activated mesoporous biocarbons with extremely high surface area for high pressure CO_2 adsorption, *ACS Appl. Mater. Interfaces*, 9 (**2017**) 29782-29793.

[66] A. Bin Noor, M. Asri, B. Mohd, Textural characteristics of activated carbons prepared from oil palm shells activated with $ZnCl_2$ and pyrolysis under nitrogen and carbon dioxide, *J. Phys. Sci.*, 19 (**2008**) 93-104.

[67] S. M. Yakout, G. S. El-Deen, Characterization of activated carbon prepared by phosphoric acid activation of olive stones, *Arab. J. Chem.*, 9 (**2016**) 1155-1162.

[68] G. Singh, K. S. Lakhi, I. Y. Kim, P. Srivastava, R. Naidu, A. Vinu, Highly efficient method for the synthesis of activated mesoporous biocarbons with extremely high surface

area for high pressure CO_2 adsorption, *ACS Appl. Mater. Interfaces,* 9 **(2017)** 29782-29793.

[69] H. Deng, G. Li, H. Yang, J. Tang, J. Tang, Preparation of activated carbons from cotton stalk by microwave assisted KOH and K_2CO_3 activation, *Chem. Eng. J*., 163 **(2010)** 373-381.

[70] D. Lozano-Castelló, J. M. Calo, D. Cazorla-Amorós, A. Linares-Solano, Carbon activation with KOH as explored by temperature programmed techniques, and the effects of hydrogen, *Carbon N. Y.*, 45 **(2007)** 2529-2536.

[71] X. Liu, G. Yu, Combined effect of microwave and activated carbon on the remediation of polychlorinated biphenyl-contaminated soil, *Chemosphere*, 63 **(2006)** 228-235.

[72] L. Giraldo, J. C. Moreno-Pirajan, Synthesis of activated carbon mesoporous from coffee waste and its application in adsorption zinc and mercury ions from aqueous solution, *E Journal Chem*., 9 **(2012)** 938-948.

[73] G. Singh, I. Y. Kim, K. S. Lakhi, P. Srivastava, R. Naidu, A. Vinu, Single step synthesis of activated bio-carbons with a high surface area and their excellent CO_2 adsorption capacity, *Carbon N. Y.*, 116 **(2017)** 448-455.

[74] G. D. Akpen, I. L. Nwaogazie, T. G. Leton. Optimum conditions for the removal of colour from waste water by mango seed shell based activated carbon, *Indian J. Sci. Technol*., 4 **(2011)** 890-894.

[75] H. Sayłili, F. Güzel, Y. Önal, Conversion of grape industrial processing waste to activated carbon sorbent and its performance in cationic and anionic dyes adsorption, *J. Clean. Prod.*, 93 **(2015)** 84-93.

[76] S. Timur, I. C. Kantarli, E. Ikizoglu, J. Yanik, Preparation of activated carbons from Oreganum stalks by chemical activation, *Energy and Fuels*, 20 **(2006)** 2636-2641.

[77] A. Kumar, H. M. Jena, High surface area microporous activated carbons prepared from Fox nut (Euryale ferox) shell by zinc chloride activation, *Appl. Surf. Sci.*, 356 **(2015)** 753-761.

[78] S. Uçar, M. Erdem, T. Tay, S. Karagöz, Preparation and characterization of activated carbon produced from pomegranate seeds by $ZnCl_2$ activation, *Appl. Surf. Sci*., 255 **(2009)** 8890-8896.

[79] G. A. Adebisi, Z. Z. Chowdhury, P. A. Alaba, Equilibrium, kinetic, and thermodynamic studies of lead ion and zinc ion adsorption from aqueous solution onto activated carbon prepared from palm oil mill effluent, *J. Clean. Prod*., 148 **(2017)** 958-968.

[80] Q. Liang, Y. Liu, M. Chen, L. Ma, B. Yang, L. Li, Q. Liu, Optimized preparation of activated carbon from coconut shell and municipal sludge, *Mater. Chem. Phys*., 241 **(2020)** 122327.

[81] A. Nayak, B. Bhushan, V. Gupta, P. Sharma, chemically activated carbon from lignocellulosic wastes for heavy metal wastewater remediation: Effect of activation conditions, *J. Colloid Interface Sci.*, 493 **(2017)** 228-240.

[82] R. T. Ayinla, J. O. Dennis, H. M. Zaid, Y. K. Sanusi, F. Usman, L. L. Adebayo, A review of technical advances of recent palm bio-waste conversion to activated carbon for energy storage, *J. Clean. Prod.*, 229 **(2019)** 1427-1442.

[83] E. Redondo, J. Carretero-González, E. Goikolea, J. Ségalini, R. Mysyk, Effect of pore texture on performance of activated carbon supercapacitor electrodes derived from olive pits, *Electrochim. Acta.*, 160 **(2015)** 178-184.

[84] H. Treviño-Cordero, L. G. Juárez-Aguilar, D. I. Mendoza-Castillo, V. HernándezMontoya, A. Bonilla-Petriciolet, M. A. Montes-Morán, Synthesis and adsorption properties of activated carbons from biomass of Prunus domestica and Jacaranda mimosifolia for the removal of heavy metals and dyes from water, *Ind. Crops Prod.*, 42 **(2013)** 315-323.

[85] R. H. Gumus, I. Okpeku, production of activated carbon and characterization from snail shell waste (*Helix pomatia*), *Adv. Chem. Eng. Sci.*, 5 **(2015)** 51-61.

[86] D. O. Cooney, Activated charcoal in medical applications, 2nd ed., *CRC* Press, Boca Raton, Florida, (**1995**).

[87] A. Dobashi, Y. Shu, T. Hasegawa, J. Maruyama, S. Iwasaki, Y. Shen, H. Uyama, Preparation of activated carbon by KOH activation from *Amygdalus pedunculata* shell and its application for electric double-layer capacitor, *Electrochemistry*, 83 **(2015)** 351-353.

[88] X. Li, W. Xing, S. Zhuo, J. Zhou, F. Li, S. Z. Qiao, G. Q. Lu, Preparation of capacitor's electrode from sunflower seed shell, *Bioresour. Technol.*, 102 **(2011)** 1118-1123.

[89] H. Treviño-Cordero, L. G. Juárez-Aguilar, D. I. Mendoza-Castillo, V. Hernández-Montoya, A. Bonilla-Petriciolet, M. A. Montes-Morán, Synthesis and adsorption properties of activated carbons from biomass of *Prunus domestica* and *Jacaranda mimosifolia* for the removal of heavy metals and dyes from water, *Ind. Crops Prod.*, 42 **(2013)** 315-323.

[90] H. Wang, R. Xie, J. Zhang, J. Zhao, Preparation and characterization of distillers' grain based activated carbon as low-cost methylene blue adsorbent: Mass transfer and equilibrium modeling, *Adv. Powder Technol.*, 29 **(2018)** 27-35.

[91] M. M. Nasser, The kinetics of basic dye removal using palm fruit bunch, *Adsorp. Sci. Technol.*, 15 **(1997)** 609-617.

[92] M. Zbair, K. Ainassaari, A. Drif, S. Ojala, M. Bottlinger, M. Pirilä, R. L. Keiski, M. Bensitel, R. Brahmi, Toward new benchmark adsorbents: preparation and characterization of activated carbon from argan nut shell for bisphenol A removal, *Environ. Sci. Pollut. Res.*, 25 **(2018)** 1869-1882.

[93] A. Supong, P. C. Bhomick, R. Karmaker, S. L. Ezung, L. Jamir, U.B. Sinha, D. Sinha, Experimental and theoretical insight into the adsorption of phenol and 2,4-dinitrophenol onto *Tithonia diversifolia* activated carbon, *Appl. Surf. Sci.*, 529 (**2020**) 147046.

[94] U. Mahapatra, A. Chatterjee, C. Das, A. Kumar, Environmental Technology & Innovation Adsorptive removal of hexavalent chromium and methylene blue from simulated solution by activated carbon synthesized from natural rubber industry biosludge, *Environ. Technol. Innov.*, 22 (**2021**) 101427.

[95] K. M. S. Khalil, M. Khairy, O. A. S. Allam, M. K. Khalil, Formation of improved activated carbons from sugarcane bagasse as environmental materials for adsorption of phenolic pollutants, *Int. J. Environ. Sci. Technol.*, 19 (**2022**) 3103-3116.

[96] P. C. Bhomick, A. Supong, M. Baruah, C. Pongener, Pine cone biomass as an efficient precursor for the synthesis of activated biocarbon for adsorption of anionic dye from aqueous solution: Isotherm, kinetic, thermodynamic and regeneration studies, *Sustain. Chem. Pharm.*, 10 (**2018**) 41-49.

[97] M. Mohsen Nourouzi, T. G. Chuah, T. S. Y. Choong, Adsorption of glyphosate onto activated carbon derived from waste newspaper, *Desalin. Water Treat.*, 24 (**2010**) 321-326.

[98] S. W. Verbruggen, TiO_2 photocatalysis for the degradation of pollutants in gas phase: from morphological design to plasmonic enhancement, *J. Photochem. Photobiol. C Photochem.*, 24 (**2015**) 64-82.

[99] D. Pathania, A. Sharma, S. Kumar, A. Kumar, Bio-synthesized Cu-ZnO hetro-nanostructure for catalytic degradation of organophosphate chlorpyrifos under solar illumination, *Chemosphere*, 277 (**2021**) 130315.

[100] A. Buthiyappan, A. Raman Abdul Aziz, W. Mohd Ashri Wan Daud, Recent advances and prospects of catalytic advanced oxidation process in treating textile effluents, *Rev. Chem. Eng.*, 32 (**2016**) 1-47.

[101] L. Lin, W. Jiang, L. Chen, P. Xu, H. Wang, Treatment of produced water with photocatalysis: recent advances, affecting factors and future research prospects, *Catalysts*, 10 (**2020**) 1-18.

[102] A. Kumar, G. Pandey, A review on the factors affecting the photocatalytic degradation of hazardous materials, *Mater. Sci. Eng. Int. J.*, 1 (**2017**) 106-114.

[103] M. Muruganandham, R. P. S. Suri, S. Jafari, M. Sillanpää, G. Lee, J. J. Wu, M. Swaminathan, Recent developments in homogeneous advanced oxidation processes for water and wastewater treatment, *Int. J. Photoenergy*, 2014 (**2014**) 1-21.

[104] D. Chen, M. Sivakumar, A. K. Ray, Heterogeneous photocatalysis in environmental remediation, *Dev. Chem. Eng. Miner. Process.*, 8 (**2000**) 505-550.

[105] O. Carp, C. L. Huisman, A. Reller, Photoinduced reactivity of titanium dioxide, *Prog. Solid State Chem.*, 32 (**2004**) 33-177.

[106] A. Omo Ibhadon, P. Fitzpatrick, heterogeneous photocatalysis: recent advances and applications, *Catalysts*, 3 **(2013)** 189-218.

[107] M. M. Mahlambi, C. J. Ngila, B. B. Mamba, Recent developments in environmental photocatalytic degradation of organic pollutants: the case of titanium dioxide nanoparticles- a review, *J. Nanomater*., 2015 **(2015)** 1-29.

[108] W. Wang, J. C. Yu, P. Keung Wong, Photocatalysts for solar-induced water disinfection: new developments and opportunities, *Mater. Sci. Forum*., 734 **(2013)** 63-89.

[109] O. Legrini, E. Oliveros, A. M. Braun, Photochemical processes for water treatment, *Chem. Rev*., 93 **(1993)** 671-698.

[110] W. H. Glaze, J. W. Kang, Advanced oxidation processes. Description of a kinetic model for the oxidation of hazardous materials in aqueous media with ozone and hydrogen peroxide in a semibatch reactor, *Ind. Eng. Chem. Res*., 28 (1989) 1573-1580.

[111] J. Carlos Colmenares, R. Luque, Heterogeneous photocatalytic nanomaterials: prospect and challenges in selective transformations of biomass-derived compounds, *Chem Soc Rev*., 43 **(2014)** 765-778.

[112] R. Daghrir, P. Drogui, D. Robert, Modified TiO_2 for environmental photocatalytic applications: a review, *Ind. Eng. Chem. Res*., 52 **(2013)** 3581-3599.

[113] E. M. Cuerda-correa, M. F. Alexandre-franco, C. Fernández-González, Advanced oxidation processes for the removal of antibiotics from water. An overview, *Water*, 12 **(2020)** 1-51.

[114] L. A. C. Santiago, A. L. M. Salazar, J. V. Moreno, O. R. Hernánde, B. P. Martínez, Fe–Zn–Ti combined systems as photocatalysts for hydroxyl radicals production in sunlight, *Int. J. Hydrog. Energy*, 47 **(2022)** 31888-31902.

[115] G. Mamba, A. K. Mishra, Graphitic carbon nitride (g-C_3N_4) nanocomposites: A new and exciting generation of visible light driven photocatalysts for environmental pollution remediation, *Appl. Catal. B Environ*., 198 **(2016)** 347-377.

[116] L. Yang, H. Zhou, T. Fan, D. Zhang, Semiconductor photocatalysts for water oxidation: current status and challenges, *Phys. Chem. Chem. Phys*., 16 **(2014)** 6810-6826.

[117] C. Han, M. Yang, B. Weng, Y. J. Xu, Improving the photocatalytic activity and anti-photocorrosion of semiconductor ZnO by coupling with versatile carbon, *Phys. Chem. Chem. Phys.*, 16 **(2014)** 16891-16903.

[118] X. Gu, C. Li, S. Yuan, M. Ma, Y. Qiang, J. Zhu, ZnO based heterojunctions and their application in environmental photocatalysis, *Nanotechnology*, 27 **(2016)** 1-21.

[119] G. K. Weldegebrieal, Synthesis method, antibacterial and photocatalytic activity of ZnO nanoparticles for azo dyes in wastewater treatment: a review, *Inorg. Chem. Commun*., 120 **(2020)** 108140.

[120] C. B. Ong, L. Y. Ng, A. W. Mohammad, A review of ZnO nanoparticles as solar photocatalysts: synthesis, mechanisms and applications, *Renew. Sustain. Energy Rev*., 81 (**2018**) 536-551.

[121] S. S. Kumar, P. Venkateswarlu, V. R. Rao, G. N. Rao, Synthesis, characterization and optical properties of zinc oxide nanoparticles, *Int. Nano Lett*., 3 (**2013**) 1-6.

[122] S. Mustapha, M. M. Ndamitso, A. S. Abdulkareem, J. O., Tijani, D. T. Shuaib, A. O. Ajala, A. K. Mohammed, Application of TiO_2 and ZnO nanoparticles immobilized on clay in wastewater treatment: a review, *Appl. Water Sci*., 10 (**2020**) 1-36.

[123] R. Darvishi Cheshmeh Soltani, Gh. Shams Khoramabadi, H. Godini & Z. Noorimotlagh, The application of ZnO/SiO_2 nanocomposite for the photocatalytic degradation of a textile dye in aqueous solutions in comparison with pure ZnO nanoparticles, *Desalin. Water Treat*., 56 (**2015**) 2551-2558.

[124] K. Qi, B. Cheng, J. Yu, W. Ho. Review on the improvement of the photocatalytic and antibacterial activities of ZnO, *J. Alloys Compd*., 727 (**2017**) 792-820.

[125] M. Baruah, A. Supong, P. Chandra, B. Rituparna, K. Chubaakum, Batch sorption-photodegradation of Alizarin Red S using synthesized TiO_2/activated carbon nanocomposite: an experimental study and computer modelling, *Nanotechnol. Environ. Eng*., 3 (**2020**) 1-13.

[126] M. J. Sweetman, S. May, N. Mebberson, P. Pendleton, K. Vasilev, S. E. Plush, J. D. Hayball, Activated carbon, carbon nanotubes and graphene: materials and composites for advanced water purification, *J. Carbon Res*., 3 (**2017**) 1-29.

[127] S. Alhan, M. Nehra, N. Dilbaghi, N. K. Singhal, K. H. Kim, S. Kumar, Potential use of ZnO@activated carbon nanocomposites for the adsorptive removal of Cd^{2+} ions in aqueous solutions, *Environ. Res.*, 173 (**2019**) 411-418.

[128] J. Ge, Y. Zhang, S. J. Park, Recent advances in carbonaceous photocatalysts with enhanced photocatalytic performances: a mini review, *Materials*, 12 (**2019**) 1-26.

[129] F. Khan, M. S. Kahan, S. Kamal, M. Arshad, S. I. Ahmad, S. A. A. Nami, Recent advances on graphene oxide and reduced graphene oxide based nanocomposites for photodegradation of dyes, *J. Mater. Chem. C.*, 8 (2020) 15940-15955.

[130] O. Benton, S. Apollo, B. Naidoo, A. Ochieng, Photodegradation of molasses wastewater using tio_2-zno nanohybrid photocatalyst supported on activated carbon, *Chem. Eng. Commun*., 203 (**2016**) 1443-1454.

[131] K. Qi, B. Cheng, J. Yu, W. Ho, Review on the improvement of the photocatalytic and antibacterial activities of ZnO, *J. Alloys Compd*., 727 (**2017**) 792-820.

[132] M. A. M. Adnan, N. M. Julkapli, S. B. Abd Hamid, Review on ZnO hybrid photocatalyst: impact on photocatalytic activities of water pollutant degradation, *Rev. Inorg. Chem*., 36 (**2016**) 77-104.

[133] Y. Liu, L. Sun, J. Wu, T. Fang, R. Cai, A. Wei, Preparation and photocatalytic activity of ZnO/Fe$_2$O$_3$ nanotube composites, *Mater. Sci. Eng. B*, 194 (**2015**) 9-13.

[134] A. I. Vaizoğullar, ZnO/ZrO$_2$ composites: synthesis characterization and photocatalytic performance in the degradation of oxytetracycline antibiotic, *Mater. Technol*., 34 (**2019**) 433-443.

[135] M. Zouhier, K. Tanji, J. A. Navio, M. C. Hidalgo, C. Jaramillo-Paez, A. Kherbeche, Preparation of ZnFe$_2$O$_4$/ZnO composite: effect of operational parameters for photocatalytic degradation of dyes under UV and visible illumination, *J. Photochem. Photobiol. A: Chem*., 390 (**2020**) 11230.

[136] H. Benhebal, M. Chaib, A. Leonard, S. D. Lambert, M. Crine, Photodegradation of phenol and benzoic acid by sol-gel-synthesized alkali metal-doped ZnO, *Mater. Sci. Semicond. Proc.*, 15 (**2012**) 264-269.

[137] J. C. Sin, S. M. Lam, K. T. Lee, A. R. Mohamed, Preparation of rare earth-doped ZnO hierarchical micro/nanospheres and their enhanced photocatalytic activity under visible light irradiation, *Ceram. Int.*, 40 (**2014**) 5431-5440.

[138] D. Schelonka, J. Tolasz, V. Štengl, Doping of zinc oxide with selected first row transition metals for photocatalytic applications, *Photochem. Photobiol*., 91 (**2015**) 1071-1077.

[139] Y. Lin, Y. Cao, Q. Yao, O. Jin Huang Chai, J. Xie, Engineering noble metal nanomaterials for pollutant decomposition, *Ind. Eng. Chem. Res*., 59 (**2020**) 20561-20581.

[140] M. Zheng, J. Wu, One-step synthesis of nitrogen-doped ZnO nanocrystallites and their properties, *Appl. Surf. Sci*., 255 (**2009**) 5656-5661.

[141] J. Xie, H. Wang, M. Duan, L. Zhang, Synthesis and photocatalysis properties of ZnO structures with different morphologies via hydrothermal method, *Appl. Surf. Sci*., 257 (**2011**) 6358-6363.

[142] M. M. Jacob, M. Ponnuchamy, A. Kapoor, P. Sivaraman, Bagasse based biochar for the adsorptive removal of chlorpyrifos from contaminated water, *J. Environ. Chem. Eng.,* 8 (**2020**) 103904.

[143] D. Pathania, A. Sharma, S. Kumar, A. Kumar, Bio-synthesized Cu-ZnO hetro-nanostructure for catalytic degradation of organophosphate chlorpyrifos under solar illumination, *Chemosphere*, 277 (**2021**) 130315.

[144] Q. Yin, L. Si, R. Wang, Z. Zhao, H. Li, Z. Wen, DFT study on the effect of functional groups of carbonaceous surface on ammonium adsorption from water, *Chemosphere*, 287 (**2022**) 132294.

[145] S. L. Ezung, M. Baruah, A. Supong, S. Sharma, D. Sinha, Experimental and theoretical insight into the adsorption of 2,4-dichlorophenol on low-cost bamboo sheath activated carbon, *Sustain. Chem. Pharm*., 26 (**2022**) 100643.

[146] S. Kumar, S. Sharma, R. Karmaker, D. Sinha, DFT study on the structural, optical and electronic properties of platinum group doped graphene, *Mater. Today Commun*., 26 **(2021)** 101755.

[147] P. Deglmann, A. Schäfer, C. Lennartz, Application of quantum calculations in the chemical industry- an overview, *Int. J. Quantum Chem.*, 115 **(2015)** 107-136.

[148] P. Hohenberg, W. Kohn, In homogeneous electron gas, *Phys. Rev.*, 136 **(1964)** 864.

[149] W. Kohn, L. J. Sham, Self-consistent equations including exchange and correlation effects, *Phys. Rev.*, 140 **(1965)** 1133-1138.

[150] P. He, X. Zhang, X. Peng, X. Jiang, J. Wu, N. Chen, Interaction of elemental mercury with defective carbonaceous cluster, *J. Hazard Mater.*, 300 **(2015)** 289-297.

[151] C. Lee, W. Yang, R. G. Parr, Development of the Colle-Salvetti correlation-energy into a function of the electron density, *Phys. Rev.*, 37 **(1988)** 785-789.

CHAPTER 2

MATERIALS AND METHODS

This chapter describes the materials and methods used in the present research work. The procedure used for the synthesis of the activated carbon/carbon nanocomposite is also highlighted in this chapter. This chapter also includes a brief discussion of the various analytical techniques used for this study. The adsorption isotherm models, kinetic models, and thermodynamic parameters used to understand the adsorption process are also described in detail. The photocatalytic kinetic model and thermodynamic parameters used to understand the photocatalytic degradation process are also briefly described. The effects of activated carbon with various functional groups on the adsorption process were studied using DFT simulations.

2.1. Raw precursor for the preparation of activated carbon

The raw materials for the current study were chosen based on their availability, abundance, and eco-friendly nature. The local biomass materials bamboo sheath of *Dendrocalamus hamiltonii* and *Schima wallichii* were chosen as the raw precursors for the preparation of activated carbon. The biomasses were then cut into small pieces, rinsed, and dried at 110 °C in a hot air oven for 48 hours. The dried biomasses were subsequently treated to chemical activation for the preparation of activated carbon. The biomasses used in this study are described below.

2.1.1. Bamboo sheath biomass *(Dendrocalamus hamiltonii)*

Dendrocalamus hamiltonii (family, Poaceae), also known as Hamilton's bamboo, is a species of bamboo that grows up to 15-18 m in height and 12-15 cm in diameter [1]. It is a tall, dull green bamboo species with drooping tops that grow in dense thickets of a few closely growing stems. Sheaths on the stem are long and gradually taper upward from a flattened base. They are green when young and turn yellowish brown when mature. The sheath itself measures 15-28 cm in width and 18-45 cm in length and the blade is 8 to 20 cm long. There are no auricles. The lower surfaces of the sheaths are hairless, while the upper surfaces are covered in patches of blackish-brown hair. Sheaths fall off prematurely [2,3]. Sheaths from bamboo are a potential source of lignocellulose waste that are commonly discarded without being properly used [4]. The plant grows wild or in cultivation in India's tropical and subtropical regions. The North-East of India is recognised as one of India's bamboo reserves [5]. As a result, the present study explored the use of locally accessible waste material bamboo sheaths *(Dendrocalamus hamiltonii)* (Figure 2.1) as a raw precursor for the production of activated carbon. The raw material bamboo sheath of *Dendrocalamus hamiltonii* (26°28'29" N, 94°50'58" E) utilized for this experiment was obtained from the vicinity of Nagaland University, Lumami campus.

Figure 2.1. Picture showing bamboo sheath biomass
(Dendrocalamus hamiltonii).

2.1.2. *Schima wallichii*

Schima wallichii (family, Theaceae) is a luxurious evergreen tree that grows in warm temperate to subtropical climates. It can be found throughout southern and Southeast Asia, stretching from Nepal's Eastern Himalaya to India's Eastern Himalaya, as well as Southern China, Indo-china, the Ryukyu Islands, and Taiwan. It is commonly known as a needle wood tree and can grow to a height of 10-20 m tall [6,7]. The tree's wood is relatively resistant to dry-wood termites, so it is used for medium to heavy construction, and its bark is used for dyeing. The population of these trees are currently not known. However, the regeneration of this tree is considered to be an excellent, particularly in degraded areas, despite the fact that its seed cover is frequently discarded without being used [8]. Therefore, in this study the fruit of *Schima wallichii* (Figure 2.2) was used as an optional precursor for activated carbon synthesis. The raw material of *Schima wallichii* (26°13' 29.60" N, 94° 28' 35.0" E) utilized for this experiment was obtained from the vicinity of Nagaland University, Lumami campus.
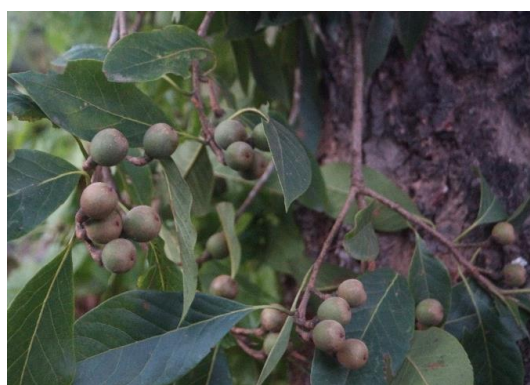
Figure 2.2. Picture showing *Schima wallichii* fruit.

2.2. Synthesis of activated carbon

Activated carbons are commonly synthesized through physical and chemical activation methods. In physical activation, the raw materials are carbonized using O_2, CO_2, or steam in an inert atmosphere and heated at temperatures around 600-1200 °C. In the chemical activation process, raw materials are activated by applying chemical activating agents such as acids (HCl, H_2SO_4, H_3PO_4), alkali metals (KOH, NaOH, Na_2CO_3), metal salts ($ZnCl_2$, $AlCl_3$, $FeCl_3$), and heating the materials at 400-900 °C.

In the present study, activated carbon were prepared using the chemical activation method by applying activating agent KOH (potassium hydroxide). This approach produces more porous material with a higher yield and larger surface area. The details of the synthesis of activated carbon are given in Chapters 3 and 4.

2.3. Synthesis of photocatalysts

The synthesis method and operating conditions are the primary factors that influence the structure, particle size, electrical, optical, and stoichiometry of any nanomaterial [9]. As a result, selecting an appropriate technique is an essential requirement for the synthesis of a highly active photocatalyst. In the current work, photocatalysts Zirconium dioxide -Zinc oxide (ZrO_2-ZnO), Iron doped zinc oxide (Fe-ZnO), and Zirconium dioxide-Zinc oxide and Iron doped nanocomposite supported on activated carbon were employed for photocatalytic degradation experiments.

2.3.1. Synthesis of ZrO_2-ZnO and Fe-ZnO nanocomposite supported on activated carbon

There are several approaches for preparing metal oxide nanocomposite, including the co-precipitation method [10], microemulsion [11], polyol method [12] and reverse micelle method [13]. These approaches, however, have a low efficiency, significant agglomeration, poor crystallinity, and a wide particle size distribution [14]. As a result, in the current work, hydrothermal synthesis were employed to produce highly pure, uniform, and narrow particle size distribution ZrO_2-ZnO and Fe-ZnO nanocomposite. The next sections describe the synthetic procedures used to synthesize ZrO_2-ZnO and Fe-ZnO nanocomposite supported on activated carbon.

2.3.1.1. Hydrothermal method for synthesis of ZrO_2-ZnO, Fe-ZnO nanocomposite supported on activated carbon

Hydrothermal synthesis is one of the most used methods for preparing metal oxide nanocom-

posites [15]. In the process of hydrothermal synthesis, high pressure and temperature are produced within the hydrothermal autoclave, which influences the physicochemical characteristics of water and thereby changes the mobility and solubility of reactant molecules to undergo crystallization reactions [16]. Hydrothermal synthesis is a promising method for producing nanomaterials due to its simplicity, low-temperature reaction conditions, and one-step reaction processing [17].

In this work, ZrO_2-ZnO and Fe-ZnO nanocomposite supported on activated carbon were synthesized using the hydrothermal method and the details regarding ZrO_2-ZnO/activated carbon and Fe-ZnO/activated carbon nanocomposite synthesis are presented in Chapters 4 and 5.

2.4. Analytical instruments used for characterization

The synthesized activated carbon, ZrO_2-ZnO/activated carbon and Fe-ZnO/activated carbon nanocomposite were characterized by Fourier Transform Infra-Red (FT-IR) Spectroscopy, Brunauer-Emmett-Teller (BET) Surface Area Analyser, Scanning Electron Microscopy (SEM), X-Ray Diffraction (XRD), Transmission Electron Microscopy (TEM), Energy Dispersive X-ray analysis (EDX), X-ray Photoelectron Spectroscopy (XPS), UV-Visible Diffuse Reflectance Spectroscopy (UV-DRS), Photoluminescence (PL), and Zero-point charge (pH_{zpc}) at different pH values. Brief descriptions of the different instruments used in the present study are given below.

Fourier Transform Infra-Red Spectroscopy

Fourier Transform Infra-Red Spectroscopy is an important technique to identify the surface chemical functional groups in any material [18]. Thus, the FT-IR spectra of the carbon samples were used to identify the various functional groups. To record the FT-IR spectra of the samples, pellets were made by mixing activated carbon with KBr in a 1:100 ratio, followed by pressing with a hydraulic pellet press. The FT-IR spectra of the sample pellets were then recorded using a FT-IR spectrometer (Model: Spectrum Two, Made: Perkin Elmer) with a spectral range of 4000 to 400 cm^{-1} and a spectral resolution of 4 cm^{-1}.

Scanning Electron Microscopy

The surface morphological characteristics of any material can be determined using scanning electron microscopy. In the present investigation, Scanning Electron Microscopy (Model: JSM 6390LV, Made: JEOL, Japan) was used to examine the morphological structure of the activated

carbon since the surface morphology of the material has a significant effect on the interaction between the adsorbent and adsorbate.

BET Surface Area and total pore volume

The Brunauer, Emmett, and Teller analyser is a device that determines a sample's specific surface area, including their pore size distribution. BET utilises multilayer gas adsorption to measure the surface area. In the current study, a BET Surface Area Analyzer (Model: Autosorb iQ MP-AG (2 STAT) Anton Paar) was used to investigated the total surface area and total pore volume by N_2 adsorption-desorption isotherm studies along with the Barrett-Joyner-Halenda model (BJH) pore size distribution of activated carbon.

X-Ray Diffraction

X-Ray Diffraction analysis is a useful technique for determining the degree of crystallinity of a material based on its diffraction pattern. The process is carried out by directing an X-ray beam at the sample and then measuring the intensities and scattering angles of the X-rays that leave the sample. The average value of the crystal sizes was determined by using Debye-Scherrer's equation [19].

$$D = \frac{\kappa\lambda}{\beta cos\theta} \tag{2.1}$$

where k = Scherer constant (0.9), λ = wavelength of the CuK_α X-ray radiation (0.15418 nm), θ = diffraction angle, and β = full-width at half-maximum (FWHM) of highest intensity peak [20].

In this research, Powder X-Ray Diffractometry was used to determine the diffraction pattern from a prepared sample. Based on a database of diffraction patterns, the diffraction patterns were used to determine whether the sample was crystalline or amorphous. Powder X-Ray Diffraction was performed using an XRD diffractometer (Rigaku, Model: Micromax-007HF). using CuK_α radiation at a scan rate of 0.2 degrees per minute.

Transmission Electron Microscopy

Transmission Electron Microscopy is a method that provides much higher resolution than light-based imaging methods by using an electron beam to scan a sample of nanoparticles. TEM is the primary technology for directly measuring nanoparticle size, grain size, size distribution, and morphology. Thus, in the present study, the morphologies and surface texture of the

nanocomposite were studied using a Transmission Electron Microscopy (Model: JEM-2100, Made: JEOL, JAPAN).

Energy-Dispersive X-Ray Spectroscopy

Energy-Dispersive X-Ray Spectroscopy is an efficient analytical method for analysing the elemental composition of the desired sample [21]. The spectra generated with EDX are easy to interpret and also give a high spatial resolution. In the present study, the elemental composition of the prepared sample was analysed using Energy-Dispersive X-Ray Spectroscopy.

X-Ray Photoelectron Spectroscopy

X-Ray Photoelectron Spectroscopy is a surface characterisation method that uses binding energies to measure a material's elemental composition, electrical/chemical states, and stoichiometry. The XPS spectra are obtained when a high-energy photon (X-ray) ejects an electron from the core orbital of an atom. In the present research work, X-ray photoelectron spectroscopy (Model: ESCALAB Xi+ Make: Thermo Fisher Scientific Pvt. Ltd., UK) was used to determine the valence state and elemental composition of photocatalyst.

UV-Visible Diffuse Reflectance Spectroscopy (DRS)

UV-Visible Diffuse Reflectance Spectroscopy is the most efficient tool for investigating the bandgap energy of any photocatalyst. It is determined by the reflection of electromagnetic radiation by a powder sample. It is determined by the amount of electromagnetic radiation reflected by a powder sample [22]. A UV-Visible Diffuse Reflectance Spectrophotometer (Shimadzu UV-2600) was used to measure the bandgap energy of the photocatalysts.

Photoluminescence (PL)

Photoluminescence is a non-destructive analytical process that absorbs a photon into a material by transferring its energy to a ground-state electron and driving it to an excited state in femtoseconds [23]. This approach was utilized in the present study to determine the photocatalyst's bandgap and to investigate the recombination process of the electron-hole pair of semiconductor material [24]. The photoluminescence spectra of the photocatalyst were determined using a photoluminescence spectrophotometer (Horiba Fluoromax-4CP spectrofluorometer, 150 W Xenon Lamp).

Zero-point charge (pH_{zpc})

The pH at which the net electrical charge of the activated carbon/carbon nanocomposite (photo-

catalyst) is zero is known as zero-point charge (pH$_{zpc}$) [25]. The surface of activated carbon/carbon nanocomposite would acquire a positive charge if the pH of a solution is less than the zero-point charge, whereas if the pH is greater than the zero-point charge, the surface would be occupied by negative charges (pH>pH$_{zpc}$) [26]

The batch equilibrium method was used to measure the zero-point charge of the prepared activated carbon samples [27]. For this measurement, 0.1 g of activated carbon/carbon nanocomposite was added to different sets of Erlenmeyer flask containing 50 ml of 0.1 M potassium nitrate (KNO$_3$) solution. The initial pH values of the mixtures were adjusted between 2 and 12 with 0.1N HNO$_3$ or 0.1N KOH. The mixture was then sealed and agitated on a shaker for 24 hours after which the final pH values were measured. The difference between the initial pH and final pH values (ΔpH= pH$_{initial}$ - pH$_{final}$) were plotted against the pH$_{initial}$. The pH$_{zpc}$ occurred when there was no change in the pH after adsorption. The pH$_{zpc}$ is the point where the plot of ΔpH *vs pH$_{initial}$* crosses the baseline in the graph.

2.5. Application of the activated carbon for the removal of 2,4-dichlorophenol from wastewater by adsorption

The batch adsorption approach was used to study activated carbon adsorption studies for the removal of as 2,4-dichlorophenol from wastewater. The influence of important operational variables such activated carbon dosage, initial 2,4-dichlorophenol concentration, contact time, temperature, and pH on removal efficiency was investigated. A 250 mL Erlenmeyer flask was filled with 50 mL 2,4-dichlorophenol solution at varying initial concentrations and the requisite activated carbon dose in each experiment. After that, the mixtures were then shaken for a fixed time at 180 rpm in a rotary shaker at 298 K. After filtering the solution, the residual 2,4-dichlorophenol solution was determined by using UV-Visible spectroscopy (Lambda 365, Perkin Elmer) at 284 nm absorbance. Each set of adsorption investigations was performed in triplicate, with the average of the three measurements given. The following equation was used to calculate 2,4-dichlorophenol adsorption capacity (q$_e$) and removal efficiency (R%):

$$q_e = \frac{(C_0 - C_e)}{M} \times V \tag{2.2}$$

$$R\% = \frac{C_0 - C_e}{C_e} \tag{2.3}$$

where the quantity of DCP adsorbed per unit mass at equilibrium is represented by *q$_e$* (mg/g),

the initial DCP concentration is represented by C_0 (mg/L), the equilibrium concentration is represented by C_e (mg/L) represents, the mass of the BSAC is represented by M (g), and the volume of the solution is represented by V (L).

The detailed experimental set up for the removal of 2,4-dichlorophenol is described in Chapter 3.

2.6. Photocatalytic degradation of chlorpyrifos by activity of activated carbon/ ZrO₂-ZnO nanocomposite and activated carbon/ Fe-ZnO nanocomposite

In the present study, the synthesized nanocomposite was used for the photocatalytic degradation of water pollutants such as pesticides from water. The pesticides under study was the organophosphorus insecticide chlorpyrifos (CPs). Batch mode degradation experiments were conducted within a reactor for the degradation of organic pollutants [27,28]. The photocatalytic degradation was performed by utilizing a continuous flow of water at room temperature throughout the reaction process. A stock solution of 1000 ppm was first prepared by dissolving 1 g (5 mL of 20 % of chlorpyrifos) of CPs in 1000 ml double-distilled water. Furthermore, dilutions were prepared to obtain the working solution of various concentration. In the present work, the required amount of activated carbon nanocomposite was dispersed in a 50 ml aqueous solution of varied CPs concentrations by vigorous stirring under dark conditions for 30 minutes to achieve adsorption-desorption equilibrium. After reaching equilibrium, the pollutant concentration was measured and used as the initial concentration so that the adsorption of the pollutant due to the activated carbon nanocomposite did not hinder the study of the overall photocatalytic effect. Later, the light was switched on to start the photocatalytic reaction, and then after 10 minutes intervals, 3 mL of sample was withdrawn and centrifuged for 10 minutes. The concentration of residual CPs was determined using a UV-Vis (PerkinElmer UV/Vis -365) spectrophotometer at λ_{max} of 221 nm. Using equations 2.3 the degradation efficiency (R %) of CPs concentration was calculated.

A batch mode study was conducted for photocatalytic degradation of water pollutants by varying different parameters are described in Chapters 4 and 5.

2.6.1. Photocatalytic reactor

For the present study, photocatalytic reactions were performed inside a photocatalytic device, as described in the schematic diagram (Figure 2.3).
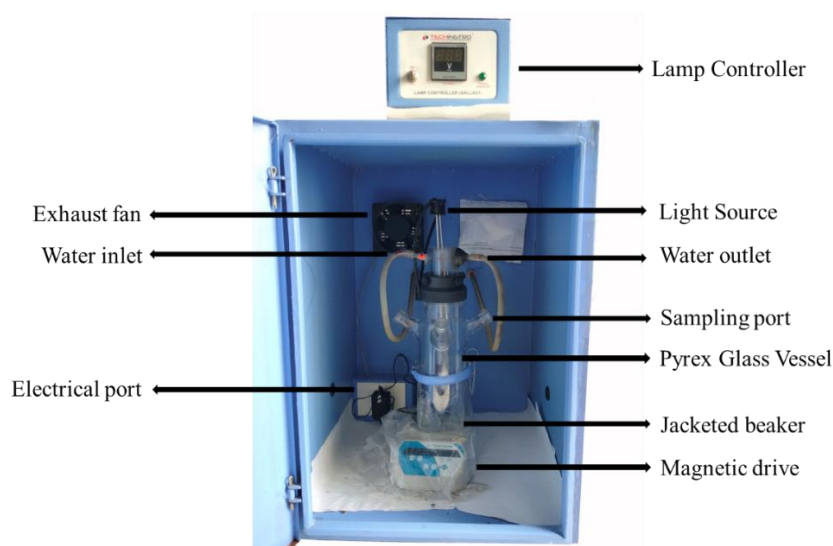
Figure 2.3. Schematic experimental setup for UV-light photocatalytic device.

2.6.2. Liquid chromatography–mass spectrometry (LC-MS) analysis to identify end products of photocatalysis

Liquid Chromatography-Mass Spectrometry is a technique that couple for identifying of degradation intermediates in aqueous solution [29]. Liquid Chromatography (LC) separates multicomponent mixtures, whereas Mass Spectrometry (MS) reveals the structural identification of individual components with high molecular specificity and detection sensitivity [30]. In this study, Liquid Chromatography-Mass Spectrometry (LC-MS) spectra (Make: INKAR, Model: Expression-S) is utilized to identify the degraded products after the photocatalytic reaction.

2.7. Description of pollutants considered for the present study

A brief description of the different pollutants considered for the current work is presented in the following section.

2,4-dichlorophenol

Chlorophenols (CPs) are phenol derivatives with one or more covalently linked chlorine atoms (Figure 2.4). These are organic contaminants found in soils, sediments, surface and ground waters. Chlorophenols are often used as preservatives or disinfectants for wood, paints, natural fibres, and leather because of their antibacterial properties [31]. It is one of the 65 pollutants identified by the US Environmental Protection Agency (EPA) as the most hazardous to human health [32]. 2,4-dichlorophenol is one of the most prevalent chlorophenols and a crucial intermediate in the synthesis of highly chlorinated phenols, pharmaceuticals, and insecticides

[33]. These pollutants are commonly found in effluents from industries such as pharmaceutical, petrochemical refineries, herbicide, pesticide, and coal conversion etc [34]. 2,4- DCP could constitute a significant concern to the ecosystem and public health due to their retention in the environment, high toxicity, and detrimental consequences on the kidney, liver, lungs, skin, etc. The general symptoms associated with exposure to these pollutants include overall weakness, fatigue, headaches, anorexia, nausea, hyperpyrexia, abdominal discomfort, and terminal spasm, among others [35]. As a result, the maximum permissible concentration of 2,4-DCP in drinking water, as recommended by World Health Organization (WHO) and EPA is 40 μgL^{-1}.
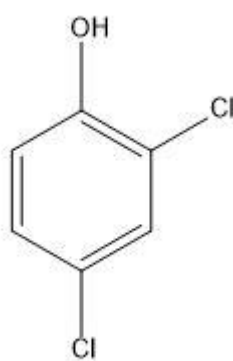
Figure 2.4. Molecular structure of 2,4-dichlorophenol.

Chlorpyrifos

Pesticides, which include fungicides, insecticides, bactericides, and herbicides, have improved agricultural yield for several decades. When used appropriately, pesticides greatly benefit mankind by controlling weeds, insects, pests, and mites that feed on crops [36]. Pesticides and insecticides in particular are used extensively, posing risks to the environment and public health because of their toxic, non-biodegradable and persistent nature. Some examples of typical pesticides are chlorpyrifos (CPs), cypermethrin, methamidophos, atrazine, chlorothalonil, etc. Among them, chlorpyrifos (O, O-diethyl O-3,5,6-trichloro-2-pyridyl phosphorothionate) a broad-spectrum organophosphate substance, is frequently used to control Diptera, Homoptera, and Lepidoptera on grain, cotton, fruit, nut, and vegetable crops etc [37]. CPs (Figure 2.5) has been identified as one of the substances hazardous to humans due to its persistent presence in soil and ground water. It enters running water by runoff and leaching from soil erosion, causing water contamination. In humans, CPs has a negative impact on the central nervous system, endocrine system, and cardiovascular system. The most commonly reported side effects of

chlorpyrifos poisoning are nausea, headache, salivation, dizziness, blurred vision, excessive perspiration, stomach cramps, muscle weakness, and, in extreme circumstances even death [38].
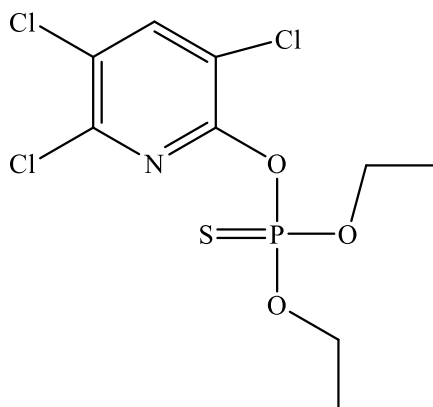
Figure 2.5. Molecular structure of chlorpyrifos.

2,4,6-trichlorophenol

2,4,6-trichlorophenol is an organic aromatic compound containing a benzene ring that carries a single hydroxyl group and three chloro groups (Figure 2.6). It appears as yellow-whitish solid with the chemical formula $C_6H_3Cl_3O$ and 197.4 g/mol molecular weight. 2,4,6-trichlorophenol is mainly used in producing preservatives for wood, pesticides, herbicides, and defoliants [39]. Among the chlorinated phenols, 2,4,6-trichlorophenol (TCP) is one of the chlorophenolic pollutants commonly found in wastewater [40,41]. The continued use of these compounds in numerous applications causes an increase in the level of a contaminant in soil and water, which has an adverse effect on public health [42].
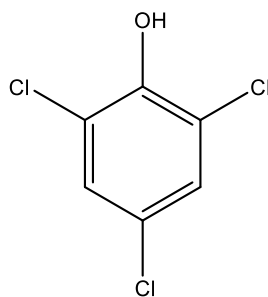
Figure 2.6. Molecular structure of 2,4,6-trichlorophenol.

2.8. Description of different models used for the present study

Adsorption models are important for determining an adsorbent's efficiency, the rate at which it removes a target pollutant, and the thermodynamics of the adsorption system [43]. The

mechanism of an adsorption process can also be determined with the use of these models. In order to understand the adsorption process, experimental adsorption data were fitted to various established mathematical equations and models in the current work. The various isotherm models, kinetic models, and thermodynamic equations that were employed are detailed below.

2.8.1. Adsorption isotherms

Adsorption isotherms are important for describing the interaction of pollutants with adsorbent surfaces and are helpful to optimize the design of the adsorption system for the removal of pollutants from aqueous solutions [44]. Adsorption isotherms are invaluable tools for determining adsorption processes, adsorption affinities, and adsorbent surface characteristics. The equilibrium concentration of an adsorbate on the surface of an adsorbent (q_e) is represented by an adsorption isotherm depending on the concentration of the adsorbate in solution (C_e). Normally, the relationship between these 'q_e' and 'C_e' is fitted to one or more equilibrium isotherm models. There are several isotherm models available for analysing experimental adsorption characteristics, and the most frequent isotherm models utilised for the application of activated carbon in water include the Langmuir, Freundlich, and Temkin models.

Langmuir isotherm model

Langmuir isotherm model, proposed by Irving Langmuir assumes that adsorption takes place on a homogeneous active site and no interactions occur between two adsorbate molecules on adjacent sites [45]. It corresponds to monolayer coverage of the adsorbate at the surface of the adsorbent and indicates chemisorption. The linear form of the Langmuir isotherm model is given by equation 2.4.

$$\frac{C_e}{q_e} = \frac{1}{q_m} C_e + \frac{1}{q_m K_L} \tag{2.4}$$

where C_e is the adsorbate concentration at equilibrium (mg L^{-1}), q_e is the quantity of adsorbate per gram of adsorbent at equilibrium (mg g^{-1}), K_L is the Langmuir isotherm constant (L mg^{-1}), and q_m is the maximum adsorption capacity of the adsorbent (mg g^{-1}).

Another important parameter of Langmuir isotherm is the dimensionless separation factor (R_L), which determines the favourability of the adsorption process [46]. The R_L is given by equation 2.5.

$$R_L = \frac{1}{1 + K_L \, C_O} \tag{2.5}$$

The value of R_L indicates whether the adsorption process is favourable ($0 < R_L < 1$), linear ($R_L = 1$), irreversible ($R_L = 0$), or unfavourable ($R_L > 1$) [47].

Freundlich isotherm model

Freundlich model describes a heterogeneous system with non-uniform distribution of adsorption heat on the surface of the adsorbent and applies to multilayer adsorption processes [48]. The linear form of the Freundlich adsorption isotherm model is given by equation 2.6.

$$log \, q_e = log \, K_F + \frac{1}{n} log \, C_e \tag{2.6}$$

where C_e = adsorbate concentration at equilibrium (mg L^{-1}), q_e = amount of adsorbate per gram of adsorbent at equilibrium (mg g^{-1}), and K_F = Freundlich adsorption capacity constant (mg g^{-1}) (L mg^{-1}), '$1/n$' and 'n' indicating Freundlich adsorption intensity.

The adsorption intensity is described by the Freundlich adsorption intensity 'n'. The greater the 'n' value, the greater the adsorption intensity. Additionally, the adsorption process is said to follow a typical Langmuir isotherm if the value of '$1/n$' is less than unity, while the cooperative nature of the adsorption process is specified if the value of "$1/n$" is greater than unity [48].

Temkin isotherm model

Temkin isotherm suggests that due to adsorbate-adsorbent interaction, the adsorption heat reduces linearly with surface coverage and the adsorption is characterised by a homogeneous distribution of binding energies [49]. Equation 2.7 provides the linear form of the Temkin isotherm model.

$$q_e = \frac{RT}{b_T} ln \, C_e + \frac{RT}{b_T} ln \, A_T \tag{2.7}$$

where b_T denotes the Temkin constant related to the heat of sorption (kJ mol^{-1}), A_T denotes the Temkin isotherm equilibrium binding constant (L mg^{-1}), R denotes the universal gas constant (8.314 J mol^{-1} K^{-1}) and T denotes the temperature at 298 K.

2.8.2. Adsorption kinetics

Adsorption kinetic studies help in evaluating adsorption mechanisms in terms of order and rate constants, as well as providing necessary information on potential rate-controlling steps [50]. In the current study, two kinetic models were used to investigate the kinetics of adsorption processes namely pseudo-first-order, and pseudo-second-order.

Pseudo-first-order model

The pseudo-first-order kinetic model proposed by Lagergren gives a simple kinetic evaluation of the adsorption of adsorbate from a liquid phase to a solid phase [51]. The pseudo-first-order model assumes that physical interactions such as van der Waals forces, π–π type of interactions and hydrogen bonding are the rate-limiting step [52]. The linear form of the pseudo-first-order model is given by equation 2.8.

$$log(q_e - q_t) = log\, q_e - \frac{k_1}{2.303}t \qquad\qquad (2.8)$$

where q_e denotes the equilibrium adsorption capacity (mg g^{-1}), q_t denotes the adsorption capacity at time t (mg g$^{-1)}$ and k_1 denotes the pseudo-first-order rate constant (min^{-1}).

Pseudo-second-order model

The pseudo-second-order model illustrates the chemisorptive behaviour of the adsorption process and is based on adsorption equilibrium capacity. The pseudo-second-order model suggests that the rate constant is proportional to the number of occupied active adsorption sites [53]. Equation 2.9 expresses the linear version of the pseudo-second-order rate model.

$$\frac{t}{q_t} = \frac{1}{k_2 q_e^2} + \frac{1}{q_e}t \qquad\qquad (2.9)$$

where q_e is the equilibrium adsorption capacity (mg g^{-1}), q_t is the adsorption capacity at time t (mg g^{-1}), and k_2 is the pseudo-second-order rate constant (min^{-1}).

2.8.3. Thermodynamic studies

The effect of temperature on the adsorption process are investigated through thermodynamic studies. The adsorption thermodynamics study improves our understanding of the internal energy changes that occur throughout the adsorption process. The thermodynamic parameters like entropy ($\Delta S°$) and enthalpy ($\Delta H°$) change were determined using the intercept and slope

of the plot of lnK_d vs $1/T$ of equation 2.10, however, the Gibbs free energy change ($\Delta G°$) at various temperatures was determined by equation 2.11.

$$lnK_d = \frac{\Delta S^o}{R} - \frac{\Delta H^o}{RT}$$ (2.10)

$$\Delta G^o = -RTlnK_d$$ (2.11)

where K_d = distribution adsorption coefficient, T = absolute temperature (K), $\Delta S°$ = entropy change (J/mol/K), $\Delta H°$ = enthalpy change (J/mol), $\Delta G°$ = gibbs free energy change, and R = universal gas constant (8.314 J/mol K).

2.8.4. Validation of the adsorption models

Chi-squared test

A chi-squared test (χ^2) is a statistical hypothesis that is used to examine if the calculated and experimental data differ significantly. The chi-squared test (χ^2) was employed in this work to examine the fitness of the isotherm and kinetics adsorptions models to the experimental result. Equation 2.12 is the mathematical formula for chi-square analysis.

$$\chi^2 = \sum_{i=1}^{n} = \frac{(q_{e(exp)} - q_{e(cal)})^2}{q_{e(cal)}}$$ (2.12)

The calculated data using various isotherm and kinetic models agrees with the experimental result in a small χ^2 value. However, the variation between calculated and experimental data will result in a high χ^2 value. As a result, it is essential to use χ^2 to evaluate the data and select the best-fitting adsorption isotherm and kinetics models for the adsorbate on the adsorbents.

2.8.5. Photodegradation kinetics

Langmuir Hinshelwood kinetic model

The most prevalent kinetic model employed in the heterogeneous catalytic process for the photocatalytic destruction of organic contaminants in solution is the Langmuir Hinshelwood kinetic. According to this model, the two reacting species are chemisorbed on the surface of the catalyst before the reaction occurs [54]. Furthermore, the limiting reaction rate is the rate of

oxidation at maximum catalyst coverage. The Langmuir Hinshelwood kinetic model is expressed as follows:

$$R = -\frac{Dc}{dt} = \frac{k_{ap}C}{1+K_eC}$$

(2.13)

where C is the pollutant concentration (mg L^{-1}), k_e is the equilibrium constant for pollutant adsorption on the photocatalyst surface (L mg^{-1}), and k_{ap} is the apparent rate coefficient (min^{-1}) [55].

As the concentration of pollutant is generally very small for standard photocatalytic reactions, k_eC in equation 2.13 is much lower than 1, and therefore equation 2.14 changes to:

$$-\frac{Dc}{dt} = k_{ap}C$$

(2.14)

Another form of the L-H model can be determined by integrating equation 2.10 from 0 to t:

$$ln\frac{C_i}{C_e} = k_{ap}t$$

(2.15)

where C_i denotes initial concentration of pollutant, and C_e denotes concentration of a pollutant at equilibrium. The k_{ap} value of various photocatalytic processes can be determined by using equation 2.15 [56].

where C_i denotes the pollutant's initial concentration and C_e denotes the pollutant's equilibrium concentration.

Half-life time reaction

The first-order kinetics reaction rate is determined using a half-life time reaction. Equation 2.16 is used to calculate the half-life time ($t_{1/2}$).

$$t_{\frac{1}{2}} = \frac{ln\,2}{K_{app}} = \frac{0.6931}{K_{ap}}$$

(2.16)

where ($t_{1/2}$) represents the half-life of reactions as determined by k_{ap} (minute) [57].

2.9. Density functional theory (DFT) studies

To understand the potential interaction between adsorbate and activated carbon, theoretical sim-

ulations using the density functional theory (DFT) approach were employed. Density functional theory has been applied because of its simplicity and computational effectiveness.

The Gaussian 09/16 [58,59] programme package was used to perform all geometry optimizations, frequency calculations, and energy calculations using the B3LYP hybrid functional at the basis set 6-31G/LanL2DZ level of theory in a dielectric medium of $\varepsilon = 80$ (corresponding to water). Different models of activated carbon were taken into consideration, and Gauss View 05/06 was utilised for building all the structures that were optimised in their electronic ground states. Equation 2.17 was used to determine the adsorption energy (E_{Ads}) of an adsorbate on the carbon surface.

$$E_{Ads} = E_{ab} - (E_a + E_b) \tag{2.17}$$

where E_a denotes the total energy of the adsorbate, E_b denotes the total energy of the activated carbon, and E_{ab} denotes the total energy of the adsorbate and activated carbon in equilibrium. In general, if E_{Ads} is lower than -30 kJ/mol, interactions are regarded to be physisorption; if E_{Ads} is larger than -50 kJ/mol, the interactions are termed chemisorption. Furthermore, a greater negative E_{Ads} value indicates more adsorption [60].

The use of DFT method in adsorption investigations would provide a thorough knowledge of the adsorption phenomenon under investigation. Such research could assist in the development of an efficient adsorbent for a particular adsorbate removal as well as increase our understanding of the bonding and reactivity between the adsorbate and adsorbent.

Further to understand the chemical reactivity and to get a better insight into the adsorption and degradation process, quantum chemical parameters such as η (chemical hardness), H (HOMO-LUMO energy gap), μ (chemical potential), S (chemical softness), and ω (electrophilicity index) were used to comprehend the chemical reactivity of SWAC/ZrO_2-ZnO nanocomposite.were calculated using the formulas given below:

HOMO-LUMO energy gap

The chemical reactivity of a molecule is determined by the HOMO-LUMO energy gap (H); thus, a high value of the HOMO-LUMO energy gap signifies that the molecule is less reactive and more stable. Equation 2.18 gives the HOMO–LUMO energy gap [61].

$$H = E_{LUMO} - E_{HOMO} \tag{2.18}$$

where E_{LUMO} represents the energy of the lowest unoccupied molecular orbital, whereas E_{HOMO} represents the energy of the highest occupied molecular orbital.

Chemical hardness (η) and chemical softness (S)

The concepts of hardness (η) and softness (S) are important in understanding the behaviour of chemical systems. The molecular stability increases as hardness increases and thereby its reactivity decreases. The chemical hardness (η) of a molecule is given by equation 2.19. The molecular stability increases as its softness decreases and thereby its reactivity increases. Equation 2.20 gives the chemical softness (S) of a molecule [62].

$$\eta = \frac{E_{LUMO} - E_{HOMO}}{2} \tag{2.19}$$

$$S = \frac{1}{2\eta} \tag{2.20}$$

Chemical potential and electronegativity

The reactivity of a molecule is determined by chemical potential (μ) and electronegativity (X) which are represented by the equations 2.21 and 2.22 respectively [63].

$$\mu = \frac{E_{HOMO} + E_{LUMO}}{2} \tag{2.21}$$

$$X = \frac{-(E_{HOMO} + E_{LUMO})}{2} \tag{2.22}$$

Electrophilicity index

The electrophilicity index (ω) is a measurement of energy loss caused by maximum electron flow between donor and acceptor. The higher the electrophilicity index, the molecule becomes more reactive. Electrophilicity index is calculated using equation 2.23 [64].

$$\omega = \frac{\mu^2}{2\eta} \tag{2.23}$$

when ω *is* greater than 1.5 eV, it has a high electrophilicity, ω less than 0.8 eV is considered marginal, and when ω is greater than 0.8 and less than 1.5 eV is considered moderate.

References

[1]   C. M. A. Stapleton, The bamboos of Nepal and Bhutan part I: *Bambusa, Dendrocalamus*, *Melocanna*, *Cephalostachyum*, *Teinostachyum*, and *Pseudostachyum* (Gramineae: Poaceae, Bambusoideae), EDINB. J. BOT., 51 **(1994)** 1-32.

[2]   K. K. Sarma, K. C. Pathak, leaf and culm sheath morphology of some important bamboo species of Assam, *J. Bamboo and Rattan*, 3 **(2004)** 265-281.

[3]   P. Chaowana, Bamboo: an alternative raw material for wood and wood-based composites, *J. Mater. Sci.*, 2 **(2013)** 90-102.

[4]   G. Juliana, J. Vanderley, Sheath bamboo leaves used at high pressure architect, *Key Eng. Mater.*, 668 **(2015)** 92-99.

[5]   M. Walling, N. Puro, Bamboo diversity and utilization in Mokokchung District, Nagaland, *EPH - Int. j. environ. agric. res.,* 4 **(2018)** 14-25.

[6]   G. C. Jagetia, K. Lalhminghlui, assessment of anticancer potential of Chilauni, *Schima wallichi* (D.C) korth. In mice transplanted with Dalton's Lymphoma Ascite Tumor, *SAJ Cancer Sci.*, 5 **(2018)** 201.

[7]   M. Bhattacharjee, Y. V. Sema, M. Ratimsarma, Study on multipotent medicinal aspects of *Schima wallichii* (bark) from Nagaland, NE India, *Asian J. Pharm. Clin. Res.*, 12 **(2019)** 155-158.

[8]   P. C. Bhomick, A. Supong, M. Baruah, C. Pongener, C. Gogoi, D. Sinha, Alizarin Red S adsorption onto biomass-based activated carbon: optimization of adsorption process parameters using Taguchi experimental design, *Int. J. Environ. Sci. Technol.*, 7 **(2020)** 1137-1148.

[9]   J. Kumar Patra, K.-H. Baek, Green nanobiotechnology: factors affecting synthesis and characterization techniques, *J. Nanomater.*, 2014 **(2014)** 219.

[10] Y. Li, G. P. Demopoulos, Precipitation of nanosized titanium dioxide from aqueous titanium (IV) chloride solutions by neutralization with MgO, *Hydrometallurgy.*, 90 **(2008)** 26-33.

[11] G. S. Falk, M. Borlaf, M. J. López-Muñoz, J. C. Fariñas, J. B. Rodrigues Neto, R. Moreno, Microwave-assisted synthesis of TiO_2 nanoparticles: photocatalytic activity of powders and thin films, *J. Nanoparticle Res.*, 20 **(2018)** 1-10.

[12] H. -Hsin Tseng, M. -Chi Wei, S. -Fan Hsiung, C. -Wei Chiou, Degradation of xylene vapor over Ni-doped TiO_2 photocatalysts prepared by polyol-mediated synthesis, *Chem. Eng. J.,* 150 **(2009)** 160-167.

[13] T. Tatarchuk, N. Danyliuk, A. Shyichuk, W. Macyk, M. Naushad, Photocatalytic degradation of dyes using rutile TiO_2 synthesized by reverse micelle and low temperature methods: real-time monitoring of the degradation kinetics, *J. Mol. Liq.*, 342 **(2021)** 1-17.

[14] T. Dippong, E. Andrea Levei, O. Cadar, Recent advances in synthesis and applications of MFe$_2$O$_4$ (M = Co, Cu, Mn, Ni, Zn) Nanoparticles, *Nanomaterials*., 11 (**2021**) 1-33.

[15] Y. X. Gan, A. H. Jayatissa, Z. Yu, X. Chen, M. Li, Hydrothermal synthesis of nanomaterials, *J. Nanomater*., 2020 (**2020**) 1-3.

[16] A. Querejeta, A. Varela, M. Parras, F. del Monte, M. Garcia-Hernandez, J. M. Gonzalez-Calbet, Hydrothermal synthesis: a suitable rute to elaborate nanomanganites, *Chem.Mater*., 21 (**2009**) 1898-1905.

[17] S. Feng, R. Xu, New materials in hydrothermal synthesis, Acc. *Chem. Res*., 34 (**2001**) 239-247.

[18] M. Zainal Abidin, M. Paula Junqueira-Gonçalves, V. V. Khutoryanskiy, K. Niranjan, Intensifying chitin hydrolysis by adjunct treatments – an overview, *J. Chem. Technol. Biotechnol.,* 92 (**2017**) 2787-2798.

[19] M. Obaidullah, T. Furusawa, I. A. Siddiquey, N. M. Bahadur, M. Sato, N. Suzuki, A fast and facile microwave irradiation method for the synthesis of ZnO@ZrO$_2$ core-shell nanocomposites and the investigation of their optical properties, *Adv. Powder Technol*., 29 (**2018**) 1804-1811.

[20] A. A. Bunaciu, H.Y. Aboul-enein, X-ray diffraction: instrumentation and applications, *Crit. Rev. Anlytical Chem*., 45 (**2015**) 289-299.

[21] P. D. Ngo, Energy dispersive spectroscopy, *in: Fail. Anal. Integr. Circuits*, (**1999**) 205-215.

[22] G. Kortüm, W. Braun, G. Herzog, Principles and techniques of diffuse-reflectance spectroscopy, *Angew. Chemie Int. Ed. English*., 2 (**1963**) 333-341.

[23] T. Aoki, Photoluminescence spectroscopy, in: E. N. Kaufmann (Ed.), *Charact. Mater*., (**2012**) 681-688.

[24] A. Erbe, S. Nayak, Y. H. Chen, F. Niu, M. Pander, S. Tecklenburg, C. Toparli, How to probe structure, kinetics, and dynamics at complex interfaces in situ and operando by optical spectroscopy, *in: Encycl. Interfacial Chem. Surf. Sci. Electrochem*., (**2018**) 199-219.

[25] T. Mahmood, M. Tahir Saddique, A. Naeem, P. Westerho, S. Mustafa, Comparison of different methods for the point of zero charge determination of NiO, *Ind. Eng. Chem. Res*., 50 (**2011**) 10017-10023.

[26] M. A. Qhalandari, S. Fozooni, E. Darezereshki, Magnetic pine leaf waste-cl-MBA/modified kaolinite nanocomposite: synthesis, characterization, and optimization by response surface methodology for Pb^{2+} and Cd^{2+} ion adsorption, *J. Aust. Ceram. Soc.*, 58 (**2022**) 705-724.

[27] B. M. Babic, S. K. Milonjic, M. J. Polovina, B. V. Kaludierovic, Point of zero charge and intrinsic equilibrium constants of activated carbon cloth, *Carbon N. Y.*, 37 (**1999**) 477-481.

[28] M. Baruah, A. Supong, P. C. Bhomick, R. Karmaker, C. Pongener, D. Sinha, Batch sorption–photodegradation of Alizarin Red S using synthesized TiO_2/activated carbon nanocomposite: an experimental study and computer modelling, *Nanotechnol. Environ. Eng.*, 5 (**2020**) 1-13.

[29] C. Medana, P. Calza, C. Baiocchi and Ezio Pelizzetti, Liquid chromatography tandem mass spectrometry as a tool to investigate pesticides and their degradation products, *Curr. Org. Chem.*, 9 (**2005**) 859-873.

[30] J. J. Pitt, Principles and applications of liquid chromatography mass spectrometry in clinical biochemistry, *Clin. Biochem. Rev.*, 30 (**2009**) 19-34.

[31] X. Zhang, X. Yu, X. Yu a, M. Kamali, L. Appels, B. Van der Bruggen, D. Cabooter, R. Dewil, Efficiency and mechanism of 2,4-dichlorophenol degradation by the UV/IO^{4-} process, *Sci. Total Environ.*, 782 (**2021**) 146781.

[32] E. Taheri, M. M. Amin, A. Fatehizadeh, E. C. Lima, Fabrication of high surface area acid-treated activated carbon from pomegranate husk for 2,4-dichlorophenol adsorption, *Res. Sq.*, (**2021**) 1-14.

[33] S. Contreras, M. Rodriguez, F. Al Momani, C. Sans, S. Esplugas, Contribution of the ozonation pre-treatment to the biodegradation of aqueous solution of 2,4-dichlorophenol, *Water Res.*, 37 (**2003**) 3164-3171.

[34] C. Namasivayam, D. Kavitha, Adsorptive removal of 2,4-dichlorophenol from aqueous solution by low-cost carbon from an agricultural solid waste: coconut coir pith, *Sep. Sci. Technol.*, 39 (**2004**) 1407-1425.

[35] R. Subha, C Namasivayam, Zinc chloride activated coir pith carbon as low cost adsorbent for removal of 2,4-dichlorophenol: equilibrium and kinetic studies, *Indian J. Chem. Technol.*, 16 (**2009**) 471-479.

[36] D. Pathania, A. Sharma, S. Kumar, A. K. Srivastava, A. Kumar, L. Singh, Bio-synthesized Cu-ZnO hetro-nanostructure for catalytic degradation of organophosphate chlorpyrifos under solar illumination, *Chemosphere*, 277 (**2021**) 130315.

[37] V. Mahdavi, F. Taghadosi, F. Dashtestani, S. Bahadorikhalili, M. M. Farimani, L. Ma'mani, A. M. Khaneghah, Aminoguanidine modified magnetic graphene oxide as a robust nanoadsorbent for efficient removal and extraction of chlorpyrifos residue from water, *J. Environ. Chem. Eng.*, 9 (**2021**) 106117.

[38] A. Saljooqi, T. Shamspur, A. Mostafavi, Synthesis and photocatalytic activity of porous ZnO stabilized ny TiO_2 and FeO_3 nanoparticles: investigation of pesticide degradation reaction in water treatment, *Environ. Sci. Pollut. Res.*, 28 (**2021**) 9156-9156.

[39] C. E. Enyoh and B. O. Isiuku, 2,4,6-Trichlorophenol (TCP) removal from aqueous solution using *Canna indica* L.: kinetic, isotherm and thermodynamic studies, *Chem Ecol.*, 37 (**2020**) 64-82.

[40] S. Sahnoun, M. Boutahala, H. Zaghouane-Boudiaf, L. Zerroual, Trichlorophenol removal from aqueous solutions by modified halloysite: kinetic and equilibrium studies. *Desalin. Water Treat.*, 57 (**2016**)15941-15951.

[41] U. I. Gaya, A. H. Abdullah, M. Z. Hussein, Z. Zainal, Photocatalytic removal of 2,4,6-trichlorophenol from water exploiting commercial ZnO powder. *Desalination*, 263 (**2010**) 176-182.

[42] S. Chaliha, K. G.Bhattacharyya, Wet oxidative method for removal of 2,4,6-trichlorophenol in water using Fe(III), Co(II), Ni(II) supported MCM41 catalysts, *J. Hazard. Mater.,* 150 (**2008**) 728-736.

[43] E. I. Unuabonah, M. O. Omorogie, N. A. Oladoja, Modeling in adsorption: fundamentals and applications, *in: Compos. Nanoadsorbents*, (**2018**).

[44] R. K. Gautam, M. C. Chattopadhyaya, Kinetics and equilibrium isotherm modeling: graphene-based nanomaterials for the removal of heavy metals from water, in: Nanomater, *Wastewater Remediat.*, (**2016**)**.**

[45] I. Langmuir, The adsorption of gases on plane surfaces of glass, mica and platinum, *J. Am. Chem. Soc.*, 40 (**1918**) 1361-1403.

[46] K. R. Hall, L. C. Eagleton, A. Acrivos, T. Vermeulen, Pore- and solid-diffusion kinetics in fixed-bed adsorption under constant-pattern conditions, *Ind. Eng. Chem. Fund.*, 5 (**1966**) 212-223.

[47] O. S. Amuda, A. A. Giwa, I. A. Bello, Removal of heavy metal from industrial wastewater using modified activated coconut shell carbon, *Biochem. Eng. J.*, 36 (**2007**) 174-181.

[48] H. M. Freundlich, Over the adsorption in solution, *J. Phys. Chem.*, 57 (**1906**) 385-470.

[49] M. I. Temkin, Adsorption equilibrium and the kinetics of processes on nonhomogeneous surfaces and in the interaction between adsorbed molecules, *Zh. Fiz. Khim.*, 15 (**1941**) 296-332.

[50] D. Gialamouidis, M. Mitrakas, M. Liakopoulou-Kyriakides, Equilibrium thermo-dynamic and kinetic studies on biosorption of Mn(II) from aqueous solution by *Pseudomonas* sp., *Staphylococcus xylosus* and *Blakeslea trispora* cells, *J. Hazard. Mater.*, 182 (**2010**) 672-680.

[51] S. K. Lagergren, About the theory of so-called adsorption of soluble substances, *Sven. Vetenskapsakad. Handingarl*, 24 (**1898**) 1-39.

[52] J. Chang, J. Ma, Q. Ma, D. Zhang, N. Qiao, M. Hu, H. Ma, Adsorption of methylene blue onto Fe_3O_4/activated montmorillonite nanocomposite, *Appl. Clay Sci.*, 119 (**2015**) 132-140.

[53] Y. S. Ho, G. McKay, Pseudo-second order model for sorption processes, *Process Biochem.*, 34 (**1999**) 451-465.

[54] R. J. Baxter, P. Hu, Insight into why the Langmuir–Hinshelwood mechanism is generally preferred, *J. Chem. Phys.*, 116 (**2002**) 4379-4381.

[55] N. G. Asenjo, R. Santamarı, C. Blanco, M. Granda, Pa. Alvarez, R. Menendez, Correct use of the Langmuir-Hinshelwood equation for proving the absence of a synergy effect in the photocatalytic degradation of phenol on a suspended mixture of titania and activated carbon, *Carbon N. Y.*, 5 (**2012**) 62-69.

[56] S. A. Ayon, M. M. Billah, , S. S. Nishat, A. Kabir, Enhanced photocatalytic activity of Ho^{3+} doped ZnO NPs synthesized by modified sol-gel method: an experimental and theoretical investigation, *J. Alloys Compd.*, 856 (**2021**) 158217.

[57] N. Guettai, H. A. Amar, Photocatalytic oxidation of methyl orange in presence of titanium dioxide in aqueous suspension. Part II: kinetics study, *Desalination*, 185 (**2005**) 439-448.

[58] M. J. Frisch, G. W. Trucks, H. B. Schlegel, G. E. Scuseria, M. A. Robb, J. R. Cheeseman, G. Scalmani, V. Barone, B. Mennucci, G. A. Petersson, H. Nakatsuji, M. Caricato, X. Li, H. P. Hratchian, A. F. Izmaylov, J. Bloino, G. Zheng, J. L. Sonnenberg, M. Hada, M. Ehara, K. Toyota, R. Fukuda, J. Hasegawa, M. Ishida, T. Nakajima, Y. Honda, O. Kitao, H. Nakai, T. Vreven, J. A. Jr. Montgomery, J. E. Peralta, F. Ogliaro, M. Bearpark, J. J. Heyd, E. Brothers, K. N. Kudin, V. N. Staroverov, R. Kobayashi, J. Normand, K. Raghavachari, A. Rendell, J. C. Burant, S. S. Iyengar, J. Tomasi, M. Cossi, N. Rega, J. M. Millam, M. Klene, J. E. Knox, J. B. Cross, V. Bakken, C. Adamo, J. Jaramillo, R. Gomperts, R. E. Stratmann, O. Yazyev, A. J. Austin, R. Cammi, C. Pomelli, J. W. Ochterski, R. L. Martin, K. Morokuma, V. G. Zakrzewski, G. A. Voth, P. Salvador, J. J. Dannenberg, S. Dapprich, A. D. Daniels, O. Farkas, J. B. Foresman, J. V. Ortiz, J. Cioslowski, D. J. Fox, Gaussian 09, Revision A.02-SMP, Gaussian, Inc., Wallingford, CT. (**2009**).

[59] Q. Yin, L. Si, R. Wang, Z. Zhao, H. Li, Z. Wen, DFT study on the effect of functional groups of carbonaceous surface on ammonium adsorption from water, *Chemosphere*, 287 (**2022**) 132294.

[60] A. Supong, P. C. Bhomick, U. B. Sinha, D. Sinha, A combined experimental and theoretical investigation of the adsorption of 4-Nitrophenol on activated biocarbon using DFT method, *Korean J. Chem. Eng.,* 36 (**2019**) 2023-2034.

[61] S. Kumar, S. Sharma, R. Karmaker, D. Sinha, DFT study on the structural, optical and electronic properties of platinum group doped graphene, *Mater. Today Commun.*, 26 (**2021**) 101755.

[62] G. Q. Blantocas, A. S. Alaboodi, A. baset H. Mekky, Synthesis of chitosan-TiO$_2$ antimicrobial composites via a 2-step process of electrospinning and plasma sputtering, *Arab. J. Sci. Eng.,* 43 **(2018)** 389-398.

[63] A. Bendjeddou, T. Abbaz, A. Gouasmia, D. Villemin, Molecular structure, HOMO-LUMO, MEP and Fukui function analysis of some TTF-donor substituted molecules using DFT (B3LYP) calculations, *Int. Res. J. Pure Appl. Chem.*, 12 **(2016)** 1-9.

[64] A. Bendjeddou, T. Abbaz, A. Gouasmia, D. Villemin, Quantum chemical studies on molecular structure and reactivity descriptors of some p-nitrophenyl tetrathiafulvalenes by density functional theory (DFT), *Acta Chim. Pharm. Indica*., 6 **(2016)** 32-44.

CHAPTER 3

EXPERIMENTAL AND THEORETICAL INSIGHT INTO THE ADSORPTION OF 2,4-DICHLOROPHENOL ON LOW-COST BAMBOO SHEATH ACTIVATED CARBON

This chapter deals with the development of cost-effective adsorbent as bamboo sheath activated carbon (BSAC) for removal of 2,4-dichlorophenol (DCP) from wastewater. Several analytical methods such as FT-IR, BET Surface Area Analyzer, SEM, XRD were used to examine the prepared BSAC. The batch experiments were carried out under varying initial concentration, adsorbent dosage, temperature, contact time, and pH (2-12) to understand the effects of different operating parameters on the removal efficiency for DCP from wastewater. The adsorption kinetics was well described by pseudo second order adsorption kinetics model with R^2 value of 0.99. Thermodynamic data indicated a negative $\Delta G°$ (spontaneous) and positive $\Delta H°$ process (endothermic). Theoretical studies using DFT (Density functional theory) simulations suggested that various interactions for DCP adsorption are possible on functionalized activated carbon surfaces such as (-CHO, -CO-, -CCO, -OH and -COOH). This study suggested that the bamboo sheath biomass of *Dendrocalamus hamiltonii* can be utilized to produce activated carbon (AC) for removing DCP from wastewater.

The text of this chapter has been published as:

3.1. Introduction

Organic pollutants are hazardous compounds that have negative health and environmental effects. Among these organic pollutants, phenolic compounds are the most common contaminants found in wastewaters and drinking water [1,2]. Phenolic derivative such as 2,4-dichlorophenol (DCP) is a non-biodegradable organic contaminant that has been widely used in pesticides, herbicides, germicides, in the manufacturing of plastics, dyes, antioxidants, paper, and in the petrochemical industries, etc. [3,4]. DCP compounds are known or believed to be carcinogenic, and they can induce mouth ulcers, central nervous system (CNS) paralysis, hemolytic anemia, protein denaturation, tissue erosion, damage to the liver, pancreas, and kidney, and are toxic to most aquatic organisms [5,6]. There are several techniques for removing phenolic compounds from water solution, including dichlorination [7], ozonation [8], catalytic wet oxidation [9], photocatalytic degradation utilizing TiO_2 [10], solvent extraction [11], ultrasound-assisted magnetic adsorption [12], and adsorption [13]. However, the removal of organic pollutants by activated carbon adsorption is a well-established and broadly used technique for the treatment of domestic and industrial effluents [14-16].

Activated carbon (AC) is a unique adsorbent because of its large surface area, high adsorption capacity, pore structure, and reusability [17,18]. It is used to remove pollutants from wastewater including harmful chemicals such as pesticides, dyes, organic compounds, medications, heavy metals, and other contaminants [19,20]. Although AC has a high adsorption capability for organic contaminants, using commercial AC makes the entire process more expensive [18]. Therefore, it is necessary to synthesize highly efficient and cost-effective AC and can easily be synthesized from readily accessible bio-waste material available around us.

Over the years many researchers have developed low-cost activated carbons utilizing fruit, paper, and textile waste [21]. For example, AC generated from guava seed (*Psidium guajava*) was used to remove chlorinated phenol from an aqueous medium [22], while AC derived from pistachio shells was employed for the removal of phenol and chlorinated phenol [23], Pongener *et al.* [24] reported the synthesis of AC from *Manihot esculenta* biomass and assessed its potential for fluoride removal from an aqueous medium, Li *et al*. [25] also proposed a high value-added AC prepared from waste vinasse for efficient removal of cationic dyes. Krishnaiah *et al.* [26] reported that chlorinated phenol could be removed using AC derived from papaya (*Carica Papaya*) seeds. Rashtbari *et al.* [12] presented an environmentally friendly and green pomegranate peel AC coated with nanoparticles for Cephalexin adsorption. The ultrasound-assisted magnetic adsorption of 2,4-dichlorophenol using GO-Fe_3O_4 adsorbent has been studied

by Azari *et al*. [27]. In this present work, efforts have been undertaken to produce a new and less expensive AC derived from locally available bamboo sheath biomass as source material, and the adsorptive ability of the produced bamboo sheath activated carbon (BSAC) was performed for removal of DCP from aqueous medium.

Several studies are done to understand the adsorption interactions between pollutants and the functional group present on the AC surface. Shen *et al*. [28] studied the hydrogen sulfide (H_2S) interactions with the active sites of zigzag and armchair AC surfaces. They found that the adsorption of H_2S on zigzag edge sites AC provides stronger force to attract H_2S than the armchair edge sites. Supong *et al*. [29,30] investigated the interaction of 4-Nitrophenol and Bisphenol A with AC surfaces containing various functional groups (-OH, -COOH, and -CHO). Among these, -COOH functionalized AC interacted most strongly with 4-Nitrophenol and Bisphenol A. Jan *et al*. [31] investigated four different adsorption configurations of azo dye on AC surfaces containing different surface functional groups (-COOH, -OH, -CH$_2$ or -CH$_3$, -C=C, -C=O, -SO$_3$, and -NO$_2$). It was observed that dye put horizontally over the AC formed four intermolecular H-bonds and show more effectiveness than the others. Unfortunately, the detailed adsorption interactions between DCP molecules and the surface of AC remain unclear. Therefore, using the density functional theory (DFT) approach the adsorption interaction of DCP with the surface of AC can be elucidated and would aid in understanding the bonding and reactivity of DCP adsorption on the carbon surface.

Therefore, keeping this in mind, the present study aimed to prepare activated carbon from locally available waste material bamboo sheaths. The prepared activated carbon was characterized using different analytical techniques and further used for the removal of DCP from water. Batch mode adsorption studies were conducted and the obtained experimental data were fitted to various isotherm and kinetic models. Further, a DFT study was planned to examine and understand the possible interactions occurring between 2,4-dichlorophenol and the surface of AC during the adsorption process.

The novelty of the present work lies in the utilization of a waste bamboo sheath biomass to prepare a low-cost activated carbon for the effective removal of toxic 2,4-dichlorophenol from an aqueous solution. In addition, theoretical calculations using DFT provided an understanding of the possible interaction of 2,4-dichlorophenol with the activated carbon. DFT studies also provided an insight into the effect of a different functional group such as -OH, -CHO, -CO-, -CCO, and -COOH on the adsorption process. Such studies would help in selecting the appropriate chemical activating agent to modify the carbon surface to enhance the adsorption

property of the carbon. The experimental and theoretical insight into the adsorption of 2,4-dichlorophenol on low-cost bamboo sheath activated carbon is shown in Figure 3.1.
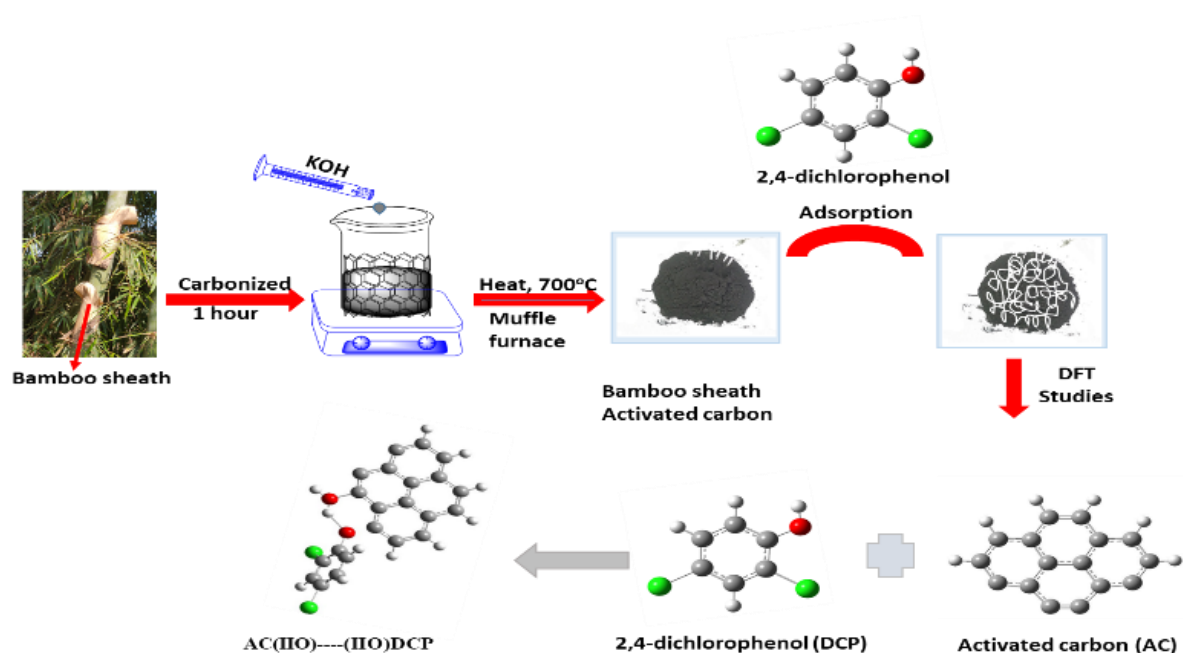
Figure 3.1. Schematic representation for preparation of bamboo sheath activated carbon.

3.2. Materials and methods

3.2.1. Materials

2,4-dichlorophenol ($C_6H_4Cl_2O$) was purchased from Himedia. The molecular structure of 2,4-dichlorophenol is presented in Figure 3.2. Stock solution of 1000 mg/L of the adsorbate was prepared and subsequently diluted to prepare varying concentrations of the working solutions. The raw material bamboo sheath of *Dendrocalamus hamiltonii* utilized for this experiment was obtained from the vicinity of Nagaland University, Lumami campus (26°28'29" N, 94°50'58" E). All other chemicals, such as HCl, and KOH, of analytical grade, were purchased by Sigma Aldrich and utilized without further purification. All the aqueous solution for the experiments were prepared using distilled water and the pH measurement was done using Eutech pH 700 digital pH meter. Incubator shaker (Make; IKA Model; KS4000 i control) was used to shake the solution. The biomass was carbonized and activated using Muffle furnace (Make; EIE instruments pvt. ltd Model; EIE-1501).
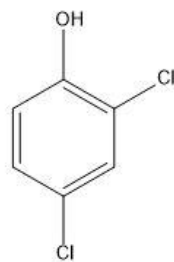
Figure 3.2. Molecular structure of 2,4-dichlorophenol.

3.2.2. Preparation of bamboo sheath activated carbon (BSAC)

Bamboo sheath biomass (*Dendrocalamus hamiltonii*) was manually cut into pieces, then thoroughly cleaned with water and dried for 12 hours at 110 °C in an oven. After that, a muffle furnace was used to carbonize the oven-dried bamboo sheath for one hour at 400 °C; the carbonized carbon was crushed into a powder form. To activate the carbonized powder, KOH (potassium hydroxide) was utilized as an activating agent. 20 g potassium hydroxide (KOH) was dissolved in 250 mL distilled water for this activation method. Mixing powder carbonized char with KOH solution resulted in a 1:2 impregnation ratio. The mixture was then agitated for an hour before being dried for 24 hours at 105 °C in an oven to ensure that the mixture sample was completely dry. The impregnated dry carbonized char was then pyrolyzed in a muffle furnace for 1 hour at 700 °C. After cooling to room temperature, the activated carbon samples were collected and rinsed with distilled water and 0.1 M hydrochloric (HCl) acid until the pH remained constant. After drying the activated carbon samples at 105 °C, bamboo sheath activated carbon (BSAC) was obtained.

3.2.3. Characterizations of BSAC

Several analytical methods were used to examine the prepared BSAC. A Fourier Transform Infrared (FT-IR) spectrometer (Model: Spectrum Two, Made: Perkin Elmer) was used to record the functional groups present on the BSAC surface. BET Surface Area Analyzer (Model: Autosorb iQ MP-AG (2 STAT) Anton Paar) was used to investigated the total surface area and total pore volume by N_2 adsorption-desorption isotherm studies along with the Barrett-Joyner-Halenda model (BJH) pore size distribution of activated carbon. The surface topography of activated carbon was investigated using Scanning Electron Microscope (SEM) (Model: JSM 6390LV, made by JEOL, Japan). The phase structure and degree of graphitization of the BSAC were determined by Powder X-ray diffraction analysis (XRD) (Rigaku, Model: Micromax-007HF).

3.2.4. Adsorption study

The batch adsorption approach was used to study BSAC adsorption studies for the removal of DCP from wastewater. The influence of important operational variables such as BSAC dosage, initial DCP concentration, contact time, temperature, and pH on removal efficiency was investigated. A 250 mL Erlenmeyer flask was filled with 50 mL DCP solution at varying initial concentrations and the requisite BSAC dose in each experiment. After that, the mixtures were then shaken for a fixed time at 180 rpm in a rotary shaker at 298 K. After filtering the solution, the residual DCP solution was determined by using UV-Visible spectroscopy (Lambda 365, Perkin Elmer) at 284 nm absorbance. Each set of adsorption investigations was performed in triplicate, with the average of the three measurements given. The following equation was used to calculate DCP adsorption capacity (q_e) and removal efficiency (R%):

$$q_e = \frac{(C_0 - C_e)}{M} \times V \tag{3.1}$$

$$R\% = \frac{C_0 - C_e}{C_e} \tag{3.2}$$

where the quantity of DCP adsorbed per unit mass at equilibrium is represented by q_e (mg/g), the initial DCP concentration is represented by C_0 (mg/L), the equilibrium concentration is represented by C_e (mg/L), the mass of the BSAC is represented by M (g), and the volume of the solution is represented by V (L).

3.2.5. Adsorption isotherm

For the study of adsorption isotherms, DCP solutions having varied concentrations (30 to 120 mg/L) were stirred with an activated carbon dosage of 0.35 g at 30 °C until equilibrium was obtained. The adsorption process has been examined by matching the data from the experiment to the three most generally used Langmuir, Freundlich, and Temkin isotherms models [32,33]. The linear forms of the Langmuir isotherm, Freundlich isotherm, and Temkin isotherm models are represented by equations given below.

$$\frac{C_e}{q_e} = \frac{1}{q_m} C_e + \frac{1}{q_m K_L} \tag{3.3}$$

$$log\ q_e = log\ K_F\ + \frac{1}{n} log\ C_e \qquad\qquad (3.4)$$

$$q_e = \frac{RT}{b_T} ln\ C_e + \frac{RT}{b_T} ln\ A_T \qquad\qquad (3.5)$$

where the equilibrium adsorption capacity of activated carbon is represented by q_e (mg/g), the equilibrium DCP concentration is represented by C_e (mg/L), the maximum adsorption capacity is represented by q_m (mg/g), Langmuir isotherm constant is represented by K_L (L/mg), Freundlich constant is represented by K_F (mg/g) (L/mg)$^{1/n}$, Freundlich adsorption intensity is represented by *n,* the adsorption heat constant is represented by b_T (kJ/mol), Temkin constant is represented by A_T (L/mg), Temperature is represented by T (298 K) and the universal gas constant is represented by R (8.314 J/mol K).

3.2.6. Adsorption kinetic

The kinetic adsorption investigation gives important information for understanding DCP adsorption dynamics. Pseudo first order kinetic and pseudo second order kinetic models were examined in this work by assessing the absorption of the DCP by the BSAC at various time intervals. Equations 3.6 and 3.7 provide the linear forms of the pseudo first order kinetic and pseudo second order kinetic models [17,33], respectively.

$$log(q_e - q_t) = log\ q_e - \frac{k_1}{2.303} t \qquad\qquad (3.6)$$

$$\frac{t}{q_t} = \frac{1}{k_2 q_e^2} + \frac{1}{q_e} t \qquad\qquad (3.7)$$

where the adsorption capacity at equilibrium is represented by q_e (mg/g), at the time (*t*) the adsorption capacity of BSAC is represented by q_t (mg/g), pseudo first-order rate constant k_1 is represented by (1/min), and pseudo second-order rate constant is represented by k_2 (g/mg min).

3.2.7. Chi-squared test

A chi-squared test (χ^2) is a statistical hypothesis that is used to examine if the calculated and experimental data differ significantly. The chi-squared test (χ^2) was employed in this work to

examine the fitness of the isotherm and kinetic adsorption models to the experimental result. Equation 3.8 is the mathematical formula for chi-square analysis [34].

$$\chi^2 \sum_{i=1}^{n} = \frac{\left(q_{e(exp)} - q_{e(cal)}\right)^2}{q_{e(cal)}} \tag{3.8}$$

The calculated data using various isotherm and kinetic models agree with the experimental result in a small χ^2 value. However, the variation between calculated and experimental data will result in a high χ^2 value. As a result, it is essential to use χ^2 to evaluate the data and select the best-fitting adsorption isotherm and kinetic models for the DCP on the adsorbents.

3.3. Theoretical study of 2,4-dichlorophenol DCP adsorption onto BSAC

3.3.1. Computational methodology

To understand the potential interaction between DCP and activated carbon, theoretical simulations using the density functional theory (DFT) approach were employed. For optimizing the electronic ground state of all the structures, Gauss View 05 was used. The energy calculations and geometry optimizations were carried out with the Gaussian 09W software package and the B3LYP hybrid functional at the theoretical level of 6-31g in water with a dielectric constant ($\varepsilon = 80$). The adsorption energy of DCP on AC surface was calculated from equation 3.9:

$$E_{Ads} = E_{ab} - (E_a + E_b) \tag{3.9}$$

where E_a denotes the total energy of the DCP molecule, E_b denotes the total energy of the AC, and E_{ab} denotes the total energy of the DCP and AC in equilibrium. In general, if E_{Ads} is lower than -30 kJ/mol, interactions are regarded to be physisorption; if E_{Ads} is larger than -50 kJ/mol, the interactions are termed chemisorption. Furthermore, a greater negative E_{Ads} value indicates more adsorption [29].

3.3.2. Activated carbon modelling

To investigate the possible adsorption interaction between the surfaces of AC and the adsorbate DCP, an appropriate structure for the AC surfaces must be established. Several researchers have

considered different models for theoretical investigations of AC surfaces such as carbonaceous surfaces [35], carbon nanotubes [36], nano-graphene sheets [37], benzene ring cluster models [28], platelet models [38], and activated carbon with a fullerene-like structure [39]. Some researchers have also found that the responsiveness of AC surfaces with active sites is mostly determined by the cluster model's form rather than its size [40]. Thus, for this research, a model of an armchair made up of four fused benzene ring clusters containing armchair edge sites was employed to replicate the AC surface. In the model of the armchair, one side of the carbon atoms was left unsaturated to provide an effective active site, whereas the rest sections were all ended with H-atoms. It has been well known that the availability of oxygenated-functionals onto AC has a major impact on its adsorptive characteristics. As a result, functional groups with oxygenated AC surface, -CCO, -CO-, -OH, -COOH, and -CHO were applied to the model of AC active site, to investigate the impact of these functional groups on the DCP adsorption mechanism. Figure 3.3 shows the AC surface optimized cluster models used in this research. Pristine armchair (AC-P), activated carbon with a function of -CCO i.e. (AC-CO), activated carbon with a function of -CO- i.e. (AC-O), activated carbon with a function of -OH i.e. (AC-OH), activated carbon with a function of -CHO i.e. (AC-CHO), and activated carbon with a function of -COOH i.e. (AC-COOH) were the names given to the various clusters.

(a)   (b)   (c)

(d)   (e)   (f)
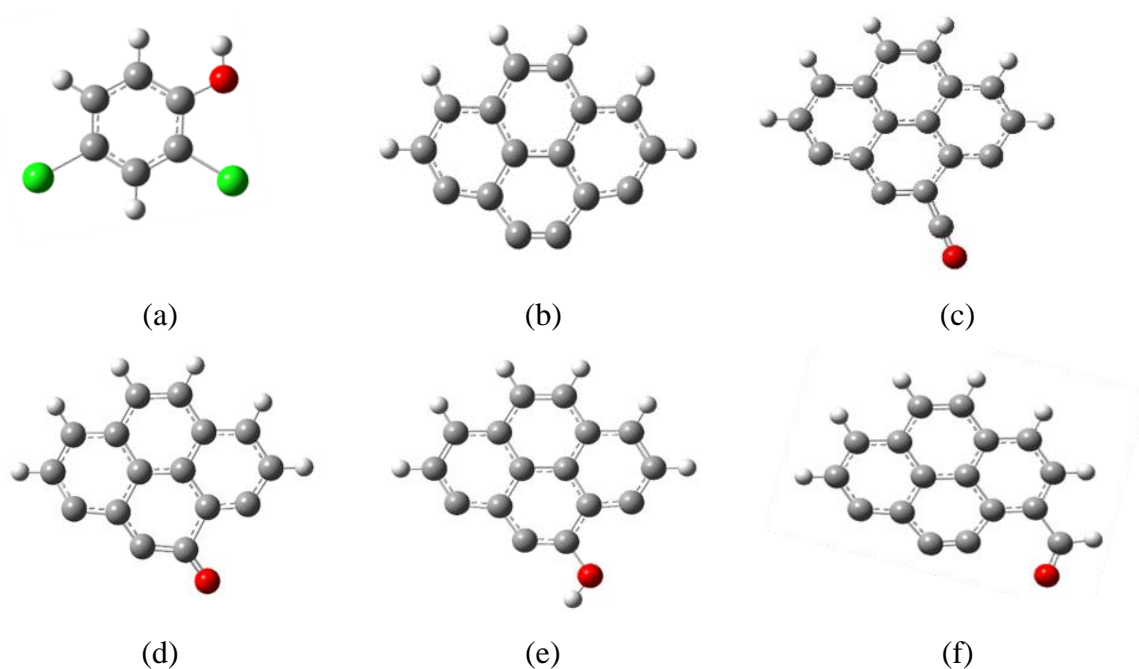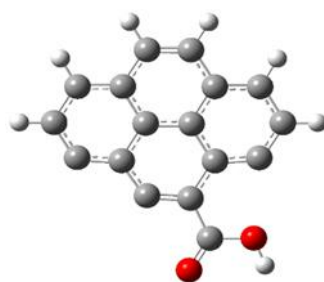
(g)

Figure 3.3. The optimized models of (a) DCP (b) AC-P (c) AC-CO (d) AC-O (e) AC-OH (f) AC-CHO (g) AC-COOH.

3.4. Results and discussion

3.4.1. Characterization of BSAC

FT-IR spectrum in Figure 3.4 reveals information about the presence of various functional groups on the BSAC surface. The O-H stretching vibration of alcohol, carboxylic acid, or water might be attributed to the bands between 3380 and 3690 cm^{-1}. The appearance of a peak around 3010 cm^{-1}was attributed to aromatic C-H stretching vibration. The peaks observed at 2943 cm^{-1} and 2860 cm^{-1} might be due to aldehyde C-H stretching [41]. The presence of CH$_2$ and CH$_3$ bending might explain the bands found between 1559 cm^{-1} and 1440 cm^{-1}. The bands around 1208 cm^{-1} region could be assigned to alkoxy C-O stretching. The presence of C-O stretch in alcohol, aldehyde, and carboxylic acid might explain the broad bands between 1700 and 1750 cm^{-1} [6]. The alkane C=C bending vibrations may be seen at the peak around 964 cm^{-1}.
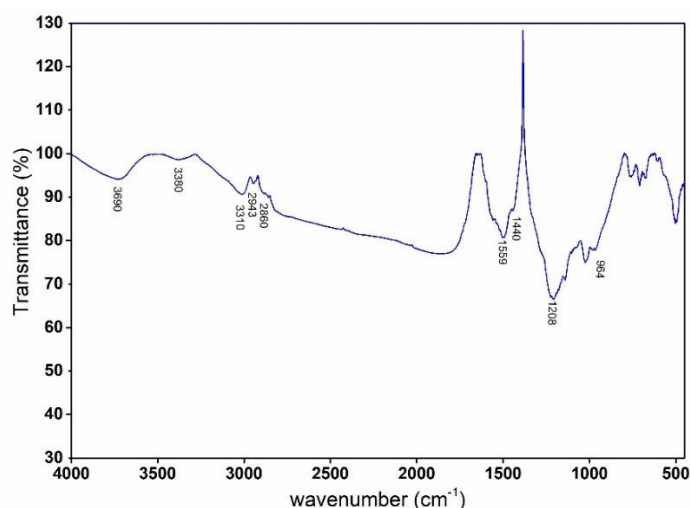
Figure 3.4. FT-IR spectra of bamboo sheath activated carbon (BSAC).

69

Figure 3.5 depicts the N_2 adsorption/desorption isotherm and pore-size distribution of the BSAC. The isotherm is observed to be type IV, indicating that mesoporous materials can form. The BET surface area of BSAC is 287.005 m^2g^{-1}, and the total pore volume is 0.020 cm^3g^{-1}. The pore size distributions of BSAC were estimated and confirmed the existence of mesopores with a range of pore diameter of 2 to 50 nm using the BHJ from the desorption branches of the isotherms, as seen from the figure, the pore size distribution of BSAC was primarily narrow, with an average diameter of 3.409 nm.

(a)   (b)
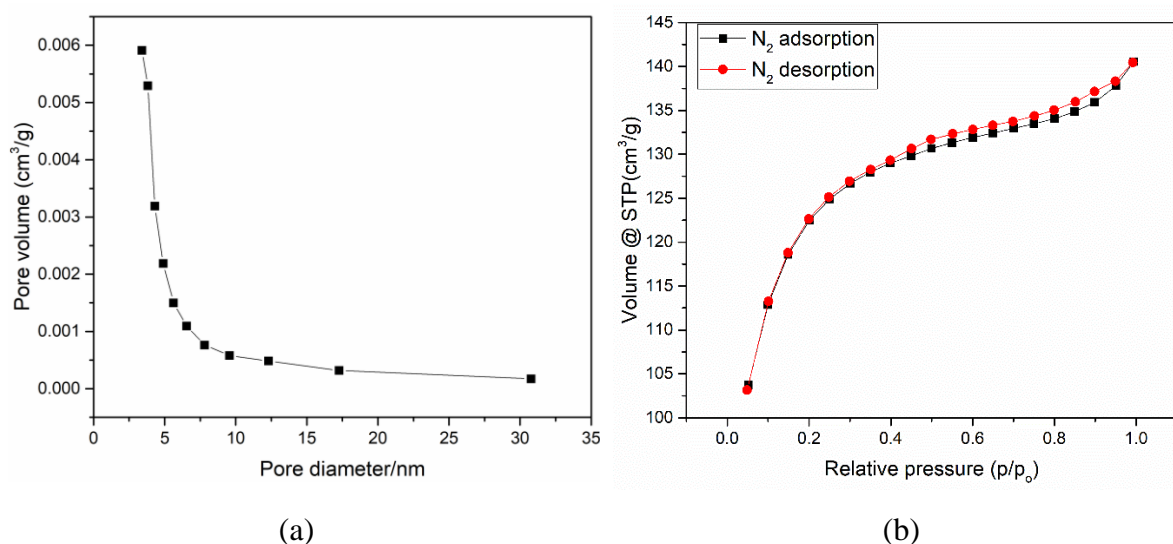
Figure 3.5. (a) Pore size distribution, (b) N_2 adsorption desorption/isotherm studies of BSAC.

SEM analysis revealed important details regarding the surface structure of BSAC. Figure 3.6 shows a micrograph of BSAC that shows cylindrical pores of various shapes and sizes distributed all over the surface of BSAC. It can be observed that BSAC pores have sizes ranging from 10-30 μm. The BSAC sample shows an irregular surface structure, which might be due to the combination of chemical activation and heat treatment.
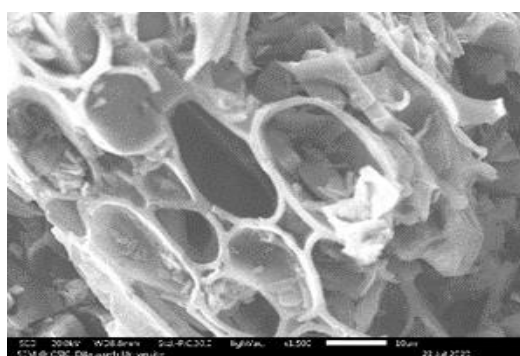
Figure 3.6. SEM image of bamboo sheath activated carbon (BSAC).

The surface crystalline structure of BSAC is analyzed using an XRD pattern (Figure 3.7). The distinct diffraction peaks at the interval 20-26° indicate the formation of graphitic carbon with miller indices (0 0 2) [42]. The characteristic peak at 43° with miller indices (1 0 0) refers to aromatic carbon crystallites (JCPDS 00-025-0284).
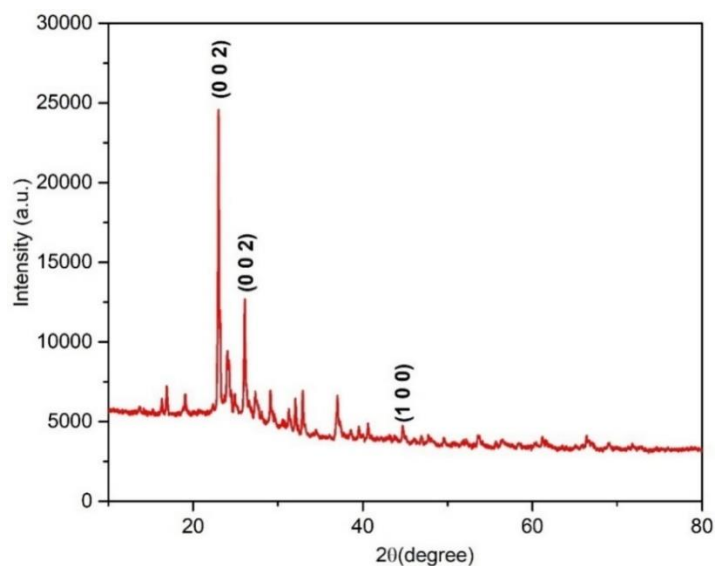
Figure 3.7. XRD patterns of bamboo sheath activated carbon (BSAC).

3.4.2. Batch adsorption study

The impact of adsorbent dose, initial DCP concentration, contact time, temperature, and pH were investigated using the batch adsorption method. Figure 3.8 shows the efficiency of DCP removal as a function of activated carbon dose.

(a)   (b)

(c)

(d)

(e)
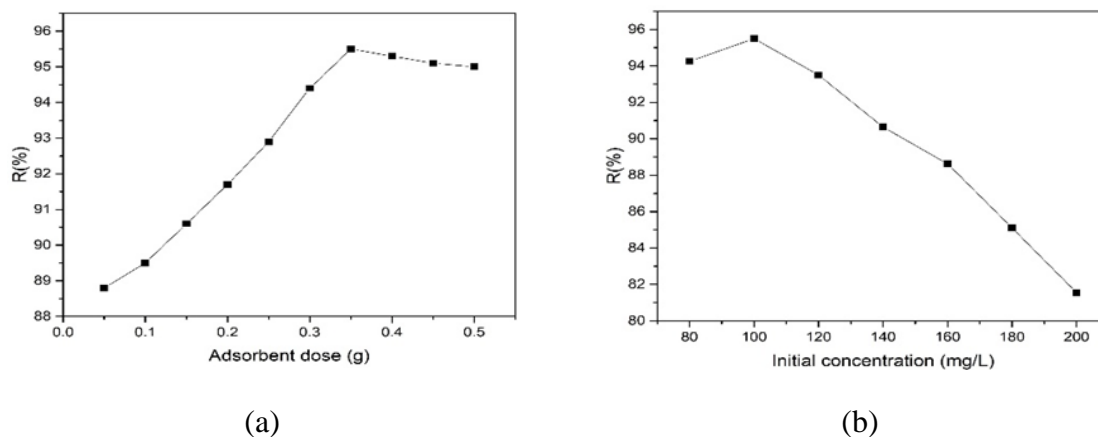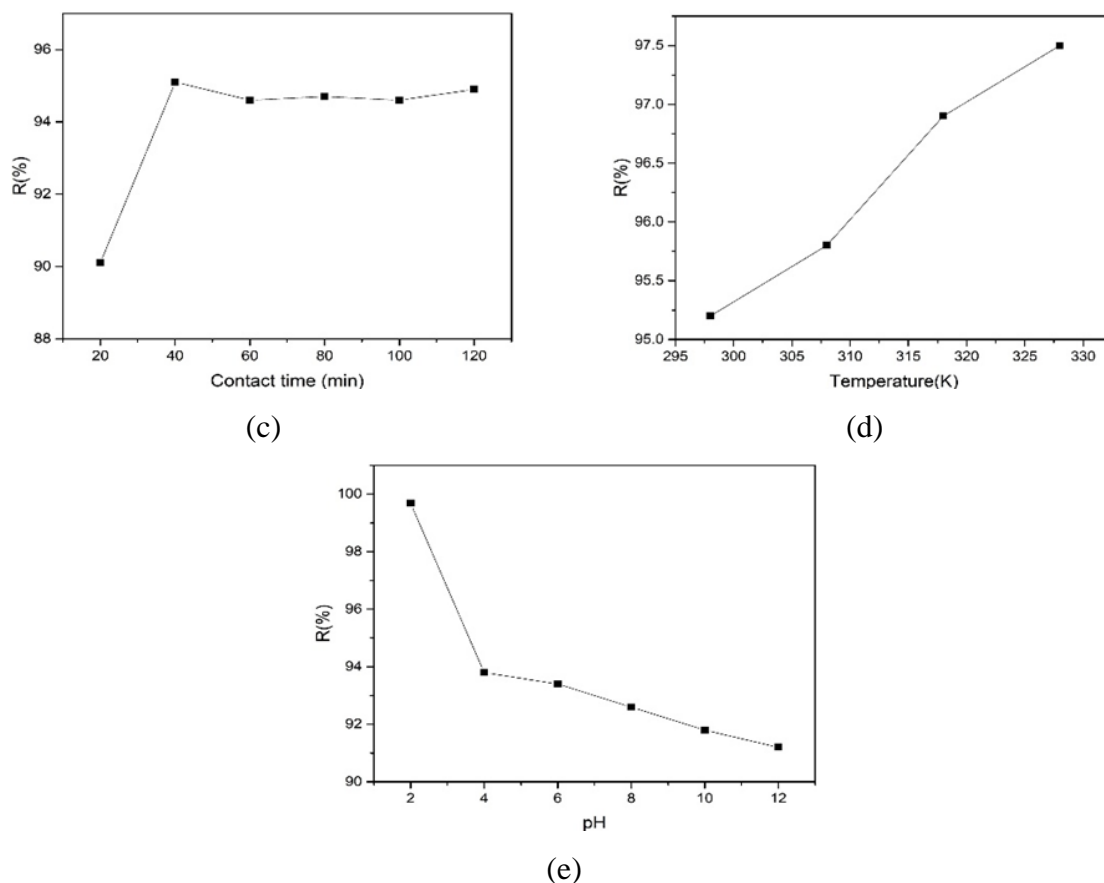
Figure 3.8. (a) Effect of adsorbent dose on DCP adsorption (b) Effect of initial concentration on DCP adsorption (c) Effect of contact time on DCP adsorption (d) Effect of temperature on DCP adsorption and (e) Effect of pH on DCP adsorption.

3.4.2.1. Effect of BSAC dose on DCP adsorption

Figure 3.8 (a) shows the effect of BSAC dose on DCP removal. It can be seen that the removal percentage of DCP concentration increases from 88.8 % to 95.5 % with an increase in BSAC dosage from 0.05 g to 0.35 g and remained nearly constant above the dose of 0.35 g. The initial increase in percentage removal might be due to the adsorbent's increased availability of adsorption sites, which allowed the DCP to penetrate the adsorption sites more easily [42]. However, at doses greater than 0.35 g, the percent removal remained nearly constant even after increasing the adsorbent doses which might be possible due to aggregation [43]. Therefore 0.35 g of BSAC dose was chosen as the optimum dosage for subsequent experiments.

3.4.2.2. Effect of initial concentration on DCP adsorption

DCP removal by BSAC was investigated at a constant BSAC dosage (0.35 g), 25 °C tempera-

ture, and pH 6.6 by varying the DCP concentrations in the range between 80 mg/L to 200 mg/L. A plot of adsorption removal efficiency vs the initial DCP concentration is presented in Figure 3.8 (b) and it can be seen that the highest percentage removal efficiency was achieved at a concentration of 100 mg/L. The greater removal % at lower DCP concentrations might be due to the adsorbent's surface having more adsorption sites than the amount of DCP molecules in the solution. But, the decrease in removal efficiency at concentrations greater than 100 mg/L could be attributed to the adsorbent's restricted number of active sites [29]. As a result, the optimum concentration is taken to be 100 mg/L for all following tests.

3.4.2.3. Effect of contact time on DCP adsorption

DCP removal by BSAC was investigated at different time intervals ranging from 20 to 120 minutes at a fixed adsorbent dose (0.35 g), and DCP concentration (100 mg/L), respectively. Figure 3.8 (c) shows a graph of the BSAC's removal % efficiency vs contact time. The result indicates that the uptake of DCP concentration initially increased rapidly with the increased contact time and reaches the maximum at 40 minutes and thereafter, increase in contact duration did not affect DCP adsorption rate, and 40 minutes was considered near to equilibration [44,45]. As a result, a 40 minutes contact time was chosen as the best time for further adsorption investigations.

3.4.2.4. Effect of temperature on DCP adsorption

In the adsorption process, the temperature is one of the most important variables. The effect of temperature on DCP removal by BSAC was investigated at four different temperatures (298, 308, 318, and 328 K), keeping the other parameters at optimum value (0.35 g adsorbent dose, 100 mg/L DCP concentration, and 40 minutes contact time). Figure 3.8 (d) shows a plot of % removal against temperature. It has been observed that the percentage of DCP removed increased with increasing temperature, reaching a maximum of 97.5 percent at 328 K [46].

3.4.2.5. Effect of solution pH on DCP adsorption

The effect of pH on the adsorption efficiency of DCP onto BSAC was determined by the variation of pH ranging from 2 to 12 at an optimum condition (adsorbent dose of 0.35 g, 100 mg/L DCP concentration, and 40 minutes contact time). The solution pH was adjusted to 2 to 12 using 1 M NaOH or 1 M HCl. Figure 3.8 (e) shows that the percentage removal of DCP decreases (99.7 % to 91.2 %) with an increase in the pH of the solution from 2 to 12. Meanwhile, the BSAC's pHzpc (zero point charge) was determined to be 5.2, suggesting that at lower pH

(pH<pH$_{zpc}$), the surface of the BSAC acquires a positive (+ve) charge, resulting in electrostatic interaction with negative (-ve) charge DCP concentration. At higher pH (pH>pH$_{zpc}$), on the other hand, the BSAC surface becomes negatively charged, resulting in less DCP adsorption on the carbon. Figure 3.8 (e) clearly shows that when the pH rises, the adsorbent's removal effectiveness diminishes.

3.4.3. Adsorption isotherms studies

Studies of adsorption isotherms are essential for comprehending the nature of adsorption process. The adsorptive behavior of DCP onto the BSAC was evaluated by models of Langmuir Freundlich, and Temkin isotherms shown in Figure 3.9.

      (a)   (b)   (c)
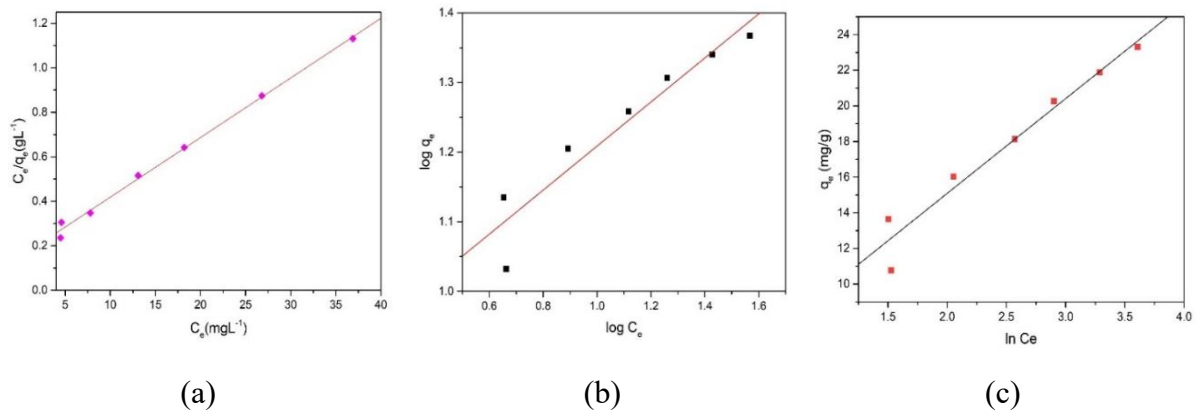
Figure 3.9. (a) Langmuir isotherm model (b) Freundlich isotherm model and (c) Temkin isotherm model.

The adsorption isotherm characteristics for DCP adsorption onto BSAC are shown in Table 3.1. According to the chi-squared test ($\chi^2 = 0.00055$) and R^2 value (0.9949), the Langmuir isotherm model best suited the experimental adsorption data, indicating that DCP adsorption on the BSAC proceeded via monolayer adsorption. The strong correlation factor ($R^2 = 0.99$), the dimensionless separation value $R_L = 0.75621$, and the q_m (maximum adsorption capacity) of 37.29 mg/g indicate that DCP adsorption on the BSAC is favorable. The Freundlich model provided the value of $K_F = 1.1245$, and the value of $n = 3.164$ was determined to be greater than 1. The smaller R^2 value ($R^2 = 0.889$) suggests that the model is unable to adequately explain the DCP adsorption process on prepared BSAC. The Temkin isotherm model was used to calculate the b_T (Temkin constant) corresponding to the adsorption heat, and its value was 0.465 kJ/mol. The value of $R^2 = 0.94$, indicating that Temkin's concept is unable to provide a complete description of the DCP adsorption process on prepared BSAC.

Table 3.1. Adsorption isotherm parameters for adsorption of DCP on BSAC.

Isotherm	Parameters	
Langmuir	q_m	37.29951
	K_L	0.00403
	R_L	0.75621
	R^2	0.9949
	χ^2	0.00055
Freundlich	$1/n$	0.316
	n	3.164
	K_F	1.1245
	R^2	0.88983
	χ^2	0.00158
Temkin	b_T	0.465
	A_T	2.31059
	R^2	0.94791
	χ^2	1.06663

3.4.4. Adsorption kinetic studies

Two adsorption kinetic models, Pseudo first order and Pseudo second order were studied to describe the adsorption kinetics mechanism. The pseudo first order kinetic model gives a simple kinetic evaluation of the adsorption of adsorbate from a liquid phase to a solid phase and describes the physisorptive nature of the adsorption process [47]. While, the pseudo second order model is based on adsorption equilibrium capacity and describes the chemosorptive behavior of the adsorption process [48]. Figure 3.10 shows the kinetic graphs obtained, with their plot parameters presented in Table 3.2. As evidenced by the plot, the pseudo first order model has a large disparity between the experimental and calculated (q_e) values, suggesting the model's poor applicability. The experimental (q_e) value in the Pseudo second order kinetic model, on the other hand, was found to be similar to the calculated (q_e) value. Furthermore, the pseudo second order kinetics model had the lowest chi-squared value (8.21×10^{-4}) and the maximum R^2 value (0.99), indicating that it is the best-fitted for DCP adsorption. As a result of the kinetics investigations, it can be stated that chemisorption regulates the total rate of DCP adsorption.

(a)   (b)
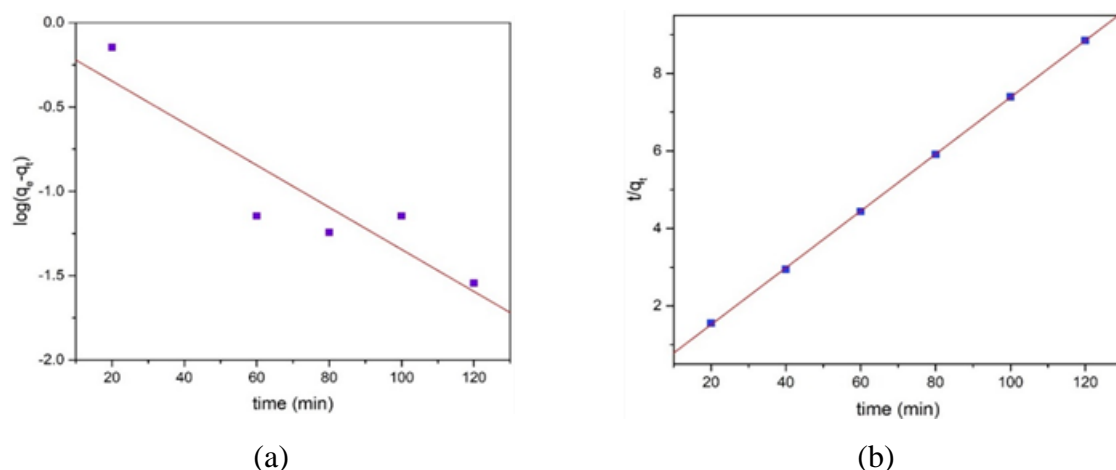
Figure 3.10. Adsorption kinetic plots of (a) Pseudo first order and (b) Pseudo second order model for adsorption of DCP on BSAC.

Table 3.2. Adsorption kinetic parameters for adsorption of DCP on BSAC.

Pseudo first order							Pseudo second order		
$q_{e\,(exp)}$	$q_{e\,(cal)}$	k_1	R^2	χ^2	$q_{e\,(exp)}$	$q_{e\,(cal)}$	k_2	R^2	χ^2
13.58	0.8009	0.028	0.768	6.47×10^{-2}	13.58	13.63	0.105	0.999	8.21×10^{-4}

3.4.5. Thermodynamic study

The thermodynamics parameters for adsorption of DCP on BSAC were determined at different temperatures ranging from 298 to 328 K. The thermodynamic parameters like entropy ($\Delta S°$) and enthalpy ($\Delta H°$) change were determined using the intercept and slope of the plot of *ln K_d* vs *1/T* (Figure 3.11) of equation 10, however, the Gibbs free energy change ($\Delta G°$) at various temperatures was determined by equation 3.11. The $\Delta H°$, $\Delta S°$ and $\Delta G°$ values for the adsorption are given in Table 3.3.

$$ lnK_d = \frac{\Delta S^o}{R} - \frac{\Delta H^o}{RT} \tag{3.10} $$

$$ \Delta G^o = -RTlnK_d \tag{3.11} $$

The value of $\Delta G°$ (kJ/mol) is negative (-1.2867 at 298 K; -1.8581 at 303 K; -2.4294 at 318 K; -3.0008 at 328 K) signifying that the adsorption process is feasible and spontaneous. The calculated ΔH^o value is found to be positive (15.73 kJ/mol), signifying that the adsorption of

DCP on BSAC is endothermic. The positive value of $\Delta S°$ (0.057 kJ/mol K) corresponds to the adsorption system's randomness.

Table 3.3. Thermodynamic parameters for adsorption of DCP on BSAC.

Temperature	ΔG^o (kJ/mol)	ΔH^o (kJ/mol)	ΔS^o (kJ/mol K)
298	-1.2867	15.73	0.057
308	-1.8581		
318	-2.4294		
328	-3.0008		
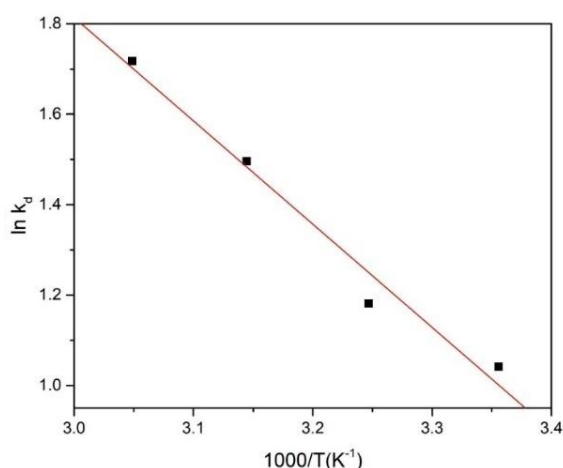
Figure 3.11. Van't Hoff plot for the thermodynamic study of DCP adsorption onto BSAC.

3.4.6. Theoretical calculations

An essential method of interaction in the adsorption process is the creation of hydrogen bonds between DCP and functionalized AC [49]. Therefore, the use of computational technique such as DFT calculations in this study is to elucidate the effect of the hydrogen bond interaction of DCP on AC surfaces. The adsorption processes of pure AC and functionalized AC with DCP through the creation of the hydrogen bond were studied using an armchair model. Thus, an attempt has been made to understand the possible interaction of the -OH group of DCP with the pristine AC and oxygenated surface functional groups (-CCO, -CO-, -CHO, -COOH, and -OH) of AC via hydrogen bond formation. Figure 3.11 represents the optimized structures of AC surface and DCP interactions and the adsorption energies and bond distance obtained for the different interactions are listed in Table 3.4.

(a)

(b)

(c)

(d)

(e)

(f)

(g)
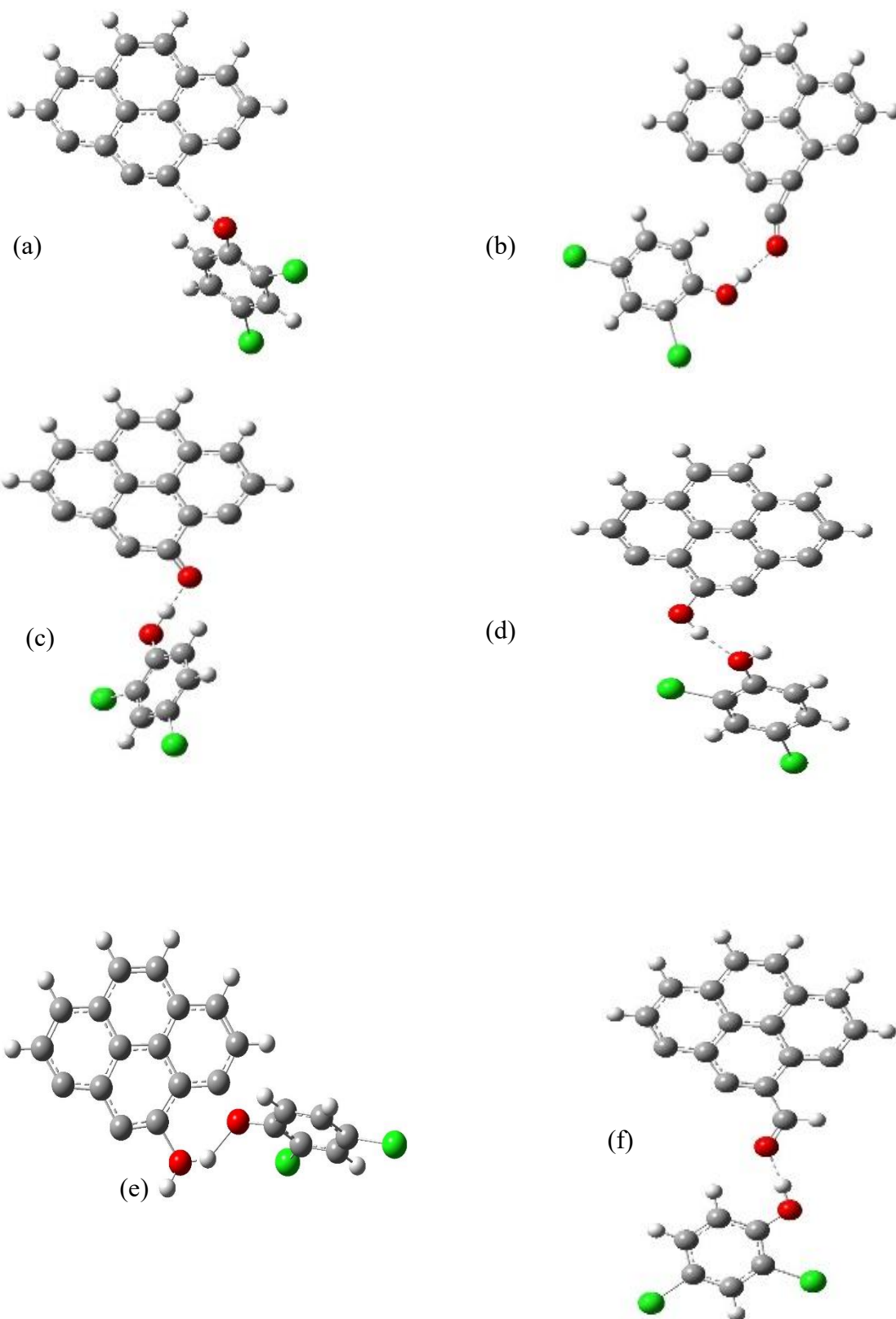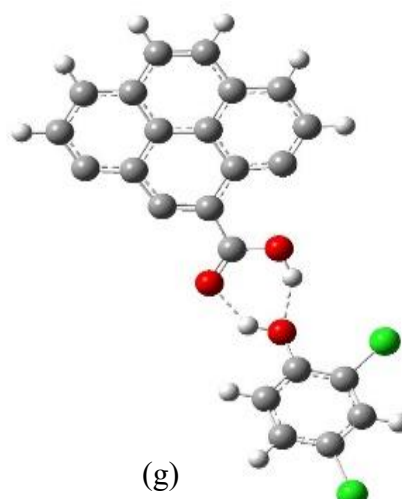
Figure 3.12. Optimized interaction structures of activated carbon and DCP interactions (a) (DCP)H----C(AC) (b) (DCP)OH----OC(AC) (c) (DCP)OH----O(AC) (d) (DCP)HO----HO(AC) (e) (DCP)OH----OH(AC) (f) (DCP)OH----OHC(AC) (g) (DCP)OH----HOOC(AC).

Table 3.4. Adsorption energies and bond distance between DCP and AC.

System	Mode of interaction	Adsorption energy (kJ/mol)	Bond length (Å)
DCP+AC	(DCP)OH----C(AC)	-23.49	1.83 (H_{DCP}----C_{AC})
DCP+(AC)O	(DCP)OH----O(AC)	-52.92	1.55 (H_{DCP}----O_{AC})
DCP+(AC)CO	(DCP)OH----OC(AC)	-97.68	1.68 (H_{DCP}----O_{AC})
DCP+(AC)OH	(DCP)HO----HO(AC)	-29.14	1.77 (O_{DCP}----H_{AC})
	(DCP)OH----OH(AC)	-103.44	1.007 (H_{DCP}--O_{AC})
DCP+(AC)CHO	(DCP)OH----OHC (AC)	-42.40	1.66 (H_{DCP}----C_{AC})
DCP+(AC)COOH	(DCP)OH----HOOC(AC)	-46.12	1.77 (O_{DCP}----$H_{AC-COOH}$)
			1.75 (H_{DCP}----$O_{AC-COOH}$)

3.4.6.1. DCP adsorption on pristine activated carbon

The formation of a bond between a carbon atom at the armchair edge site and the -OH group of DCP was used to investigate the possible interaction of AC-P with DCP. Figure 3.12 (a) shows the optimized structure of AC-P and DCP interaction and the formation of a bond is represented as (DCP)OH----C(AC). The C-C bond lengths of the armchair edge sites attached to the hydrogen atom of DCP stretched from 1.42 Å to 1.45 Å and 1.24 Å to 1.25 Å on DCP adsorption. The weaker bond lengths of the armchair AC is because the electron cloud shifts in the direction of the adsorption site, i.e. the (DCP)OH----C(AC) bond. Furthermore, the

adsorption energy for the (DCP)OH----C(AC) system was found to be -23.49 kJ/mol, indicating that the adsorptive interaction between AC and DCP is favorable.

3.4.6.2. DCP adsorption on activated carbon with the function of -CCO

The adsorptive interactions of DCP and activated carbon with the function of -CCO was studied i.e. (DCP)OH----OC(AC). As seen from Figure 3.12 (b) the optimized interaction structures of (DCP)OH----OC(AC), and Table 3.4 lists the lengths of their corresponding bonds. The adsorption energy of (DCP)OH----OC(AC) interactions corresponded to - 97.68 kJ/mol and their H_{DCP}-O_{ACCO} bond length of (DCP)OH----OC(AC) mode of interaction was 1.68 Å. The negative adsorption energies of (DCP)OH----OC(AC) indicate that it is favorable in the process of adsorption.

3.4.6.3. DCP adsorption on activated carbon with the function of -CO-

The interaction of -CO- functionalized activated carbon (AC-O) with the -OH group of DCP results in the bond formation of OH_{DCP}----O_{AC}. Figure 3.12 (c) shows the (DCP)OH----O(AC) interaction structure that was optimized. The O-H bond length of DCP increases from 0.97Å to 1.02 Å and the C=O bond length of AC-O from 1.25 Å to 1.29Å. Thus, the C=O bond of -CO- functionalized activated carbon and the O-H bond of DCP become weaker, which might be attributed to the electron cloud being displaced more in the direction of the adsorption site. The adsorption energy of (DCP)OH----O(AC) was calculated to be -52.92 kJ/mol. As a result, all these findings suggest that DCP adsorption on -CO- functionalized activated carbon is advantageous.

3.4.6.4. DCP adsorption on activated carbon with the function of -OH

The adsorption of DCP onto the OH-functionalized AC surface was investigated using two types of interactions: (DCP)HO----HO(AC) shown in Figure 3.12 (d) and (DCP)OH----OH(AC) shown in Figure 3.12 (e) represent the optimized interaction structures of (DCP)HO----HO(AC) and (DCP)OH----OH(AC) respectively, with the appropriate bond lengths listed in Table 3.4. The adsorption energies of (DCP)HO----HO(AC) and (DCP)OH----OH(AC) interactions were found to be -29.14 kJ/mol and -103.44 kJ/mol. The bond length of the O_{DCP}-H_{AC} mode of interaction corresponded to 1.77Å while the bond length of H_{DCP}-O_{AC} corresponded to 1.00 Å. The shorter bond length of the H_{DCP}-O_{AC} system is shorter and the greater negative value of adsorption energy implies that the (DCP)OH----OH(AC) mode of interaction is more preferable to the (DCP)HO----HO(AC) form.

3.4.6.5. DCP adsorption on activated carbon with the function of -CHO

To understand the adsorption of DCP adsorption on activated carbon with the function of -CHO i.e. (AC-CHO), the DCP interacts with AC-CHO via forming hydrogen bonds between its Hydrogen atom of DCP and an oxygen atom of AC-CHO, as presented in Figure 3.12 (f). The adsorption energy of (DCP)OH----OCH-(AC) corresponding to -42.40 kJ/mol suggests that the DCP adsorption on -CHO functionalized activated carbon (AC-CHO) is favorable.

3.4.6.6. DCP Adsorption on activated carbon with the function of -COOH

The adsorption interaction of DCP on activated carbon with the function of -COOH i.e. (AC-COOH) occurred via the formation of two H-bonds between DCP and AC-COOH. The H-atom of AC-COOH formed a hydrogen bond with the O-atom of the DCP ($H_{AC-COOH}$ ----O_{DCP}) at the same time as additional hydrogen bonds formed between the H-atom of DCP and O-atom of AC-COOH and (H_{DCP}----$O_{AC-COOH}$). The optimized structures are shown in Figure 3.12 (g). The O_{DCP}---$H_{AC-COOH}$ and H_{DCP}----$O_{AC-COOH}$ adsorption energy were determined to be -46.12 kJ/mol, with a bond length of 1.77 Å and 1.75 Å respectively. As a result of these findings, it appears that DCP adsorption on activated carbon with a function of -COOH is preferred.

3.4.7. Relative adsorption energies of DCP on bamboo sheath activated carbon

A relative investigation of the adsorption interaction of DCP onto surface functional groups of activated carbon was determined by considering their relative adsorption energies. Different optimized configurations of adsorbate and adsorbent are given in Figure 3.13. Among the various functional group found on the AC surface, AC with functions of –CCO, -CO-, -OH, -CHO, and –COOH i.e. (AC-CO), (AC-O), (AC-OH), (AC-CHO) and (AC-COOH) were considered in this study. The interaction of the H-atom (from HO group) of DCP with the oxygen atom of OH-AC i.e. (DCP)OH----OH(AC) was shown with the highest negative adsorption energy in comparison to HOC-AC, HOOC-AC, OC-AC, and O-AC. Thus, the results confirmed that the introduction of hydroxyl groups on the surface of activated carbon improved the binding of DCP and strengthen the hydrogen bond with the AC surface as compared to all the other HO-AC, HOC-AC, HOOC-AC, OC-AC, and O-AC. In the sequence shown below, the relative adsorption energies and stability of the various forms of interactions decreased.

(DCP)OH----OH(AC)>(DCP)OH----OC(AC)>(DCP)OH----O(AC)>(DCP)OH----HOOC(AC)>(DCP)OH----OHC(A)>(DCP)HO----HO(AC)
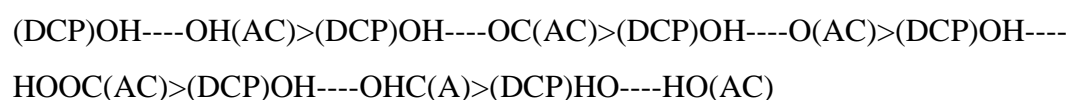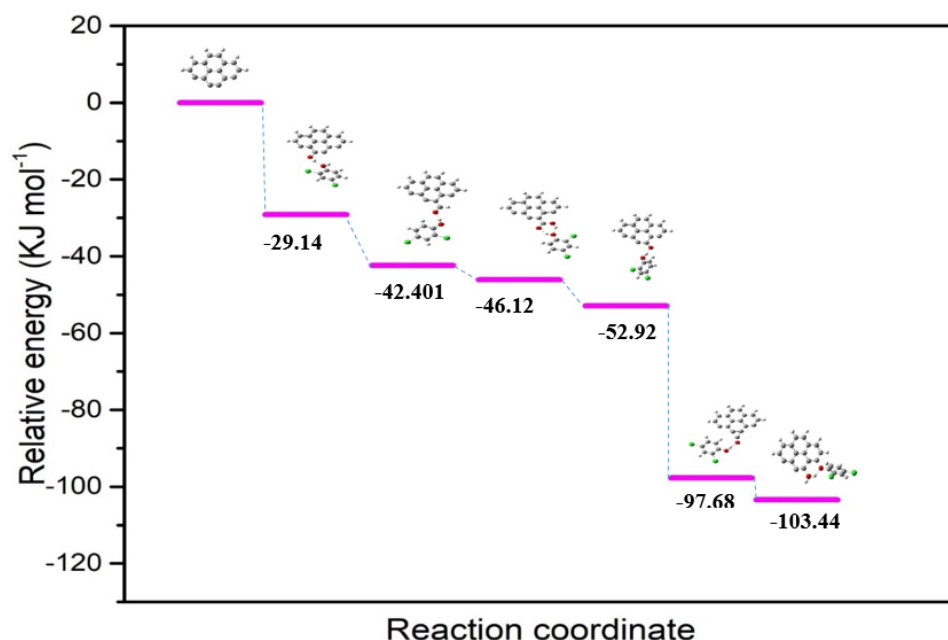
Figure 3. 13. Relative energy diagram of DCP adsorption on functionalized activated carbon surfaces.

3.4.8. Comparative study of bamboo sheath activated carbon with other adsorbents

To understand the relative effectiveness of the produced BSAC for DCP removal from aqueous solution, a comparative study of the prepared activated carbon with various other adsorbents in the literature was made. The bamboo sheath activated carbon's maximum adsorption capacity (q_m), as determined by the Langmuir isotherm, was compared to the q_m of various other adsorbents described in the literature. Table 3.5 shows the results of the comparison, and it is observed that the current activated carbon has a better adsorption capacity for 2,4-dichlorophenol than other adsorbents in the literature. As a result, waste bamboo sheath activated carbon could be used as a good optional adsorbent for removing DCP chemicals from waste water.

Table 3.5. Comparative study of adsorption capacity of various adsorbents.

Adsorbate	Adsorbent	Adsorption capacity (mg/g)	Reference
2,4-dichlorophenol	Bamboo sheath	37.29	Present case
	Plantain peels	14.25	[50]
	Palm pith carbon	19.16	[51]
	Coconut coir pith	19.12	[52]

Maize cob carbon	17.94	[53]
Oil palm empty fruit bunches	27.25	[15]
Phanerochaete chrysosporium biomass	11.62	[54]
Grapefruit Peel-derived carbon material	22.09	[55]
Rice straw	36.85	[56]
Guava seed (*Psidium Guajava*)	20.9	[22]

3.4.9. Cost analysis

Cost estimate is a key aspect in determining the efficacy of the method used. The whole approximate cost of producing 250 g of BSAC was estimated, which included the prices of electricity, raw material, water, HCl, and KOH. The approximate cost analysis and the comparative cost studies are given in Table 3.6 and Table 3.7 respectively. The approximate cost for the production of 250 g BSAC was found to be ₹ 478. This cost was found to be lower than those commercially available carbon considered for the present study, indicating that the bamboo sheath activated carbon could be used as an economical adsorbent in various environmental applications.

Table 3.6. Cost estimates for production of 250 g BSAC.

Materials	Consumption (approx.)	Cost (approx.)
KOH	500 g	₹ 420
HCl	200 ml of 0.1 M HCl	₹1 (307/500 ml)
Raw precursor	1.5 kg	₹0
Electricity	14 kWh	₹42
Water	50 L	₹15
Total Cost/250 g (in Rupees)		₹478

*1 dollar ($) =Approx.74.37. Rupees (₹)

Table 3.7. Comparative cost of BSAC with some commercially available activated carbon.

Brand	Cost/250 g
Activated carbon (Merck)	₹7,059.60
Activated charcoal (Merck)	₹9,179.70

Activated charcoal, NORIT(R) SA 2, Thermo Scientific™	₹ 4,434.00
Activated charcoal, NORIT(R) A SUPRA, Thermo Scientific™	₹ 20,117.085
Activated charcoal DARCO® (Merck)	₹5361.30
Charcoal activated (Merck)	₹8,760.00
Activated Charcoal Norit®(Sigma-Aldrich)	₹4,761.90
BSAC (present case)	₹478

3.6. Conclusion

Waste bamboo sheath is inexpensive, indigenous and easily available in large quantity. Based on the experimental and theoretical investigations of the present work BSAC proved to be one of the powerful precursors capable of removing DCP from aqueous solutions. The SEM image revealed that the synthesized carbon has cylindrical pores with sizes ranging from 10 to 30 μm, and the XRD data confirmed that the synthesized carbon contains graphite-like micro crystallites. The batch adsorption suggested a maximum DCP removal efficiency of 95.5 % under optimum conditions. The data obtained for the adsorption process was found to be best fitted in Langmuir isotherm model, indicating a monolayer coverage of the adsorbent with a q_m of 37.29 mg/g. The pseudo second order kinetic model described better adsorption kinetics with R^2 value of 0.99 indicating that the adsorption process was a chemisorption. The thermodynamic studies suggested that the adsorption process is endothermic, temperature-dependent, and spontaneous. DFT simulations also revealed that DCP adsorbs well on activated carbon. The -OH group interacts most strongly with DCP among the several functional groups (-CHO, -CO-, -CCO, -COOH) utilized to functionalize activated carbon. These findings imply that functionalizing activated carbon with -OH group may improve its interaction with DCP, resulting in improved adsorption. The results obtained along with the free and wide availability of waste bamboo sheath proves that it could be used as a potential raw material for the preparation of low-cost and effective AC. The synthesized BSAC shows great potential as adsorbents in the treatment of wastewater. In addition, theoretical investigations could provide critical insights into the interaction of AC surface and the adsorbate which can help in the design and development of AC with improved adsorption properties.

References

[1]   M. Ahmaruzzaman, Adsorption of phenolic compounds on low-cost adsorbents: a review, *Adv. Colloid Interface Sci.*, 143 **(2008)** 48-67.

[2]   A. Dąbrowski, P. Podkościelny, Z. Hubicki, M. Barczak, Adsorption of phenolic compounds by activated carbon - a critical review, *Chemosphere*, 58 **(2005)** 1049-1070.

[3]   M. Sathishkumar, K. Vijayaraghavan, A.R. Binupriya, A.M. Stephan, J.G. Choi, S.E. Yun, Porogen effect on characteristics of banana pith carbon and the sorption of dichlorophenols, *J. Colloid Interface Sci.*, 320 **(2008)** 22-29.

[4]   N. N. M. Zain, N. K. A. Bakar, S. Mohamad, N. Saleh, Optimization of a greener method for removal phenol species by cloud point extraction and spectrophotometry, *Spectrochim. Acta A Mol. Biomol. Spectrosc.*, 118 **(2014)** 1121-1128.

[5]   M. Akhtar, M. I. Bhanger, S. Iqbal, S. M. Hasany, Sorption potential of rice husk for the removal of 2,4-dichlorophenol from aqueous solutions : kinetic and thermodynamic investigations, *J. Hazard. Mater.*, 128 **(2006)** 44-52.

[6]   K. P. Singh, A. Malik, S. Sinha, P. Ojha, Liquid-phase adsorption of phenols using activated carbons derived from agricultural waste material, *J. Hazard. Mater.*, 150 **(2008)** 626-641.

[7]   C. Wu, L. Zhou, Y. Zhou, C. Zhou, S. Xia, B.E. Rittmann, Dechlorination of 2 , 4-dichlorophenol in a hydrogen-based membrane palladium-film reactor : performance , mechanisms and model development, *Water Res.*, 188 **(2021)** 116465.

[8]   S. Contreras, M. Rodriguez, F. Al Momani, C. Sans, S. Esplugas, Contribution of the ozonation pre-treatment to the biodegradation of aqueous solutions of 2,4-dichlorophenol, *Water Res.*, 37 **(2005)** 3164-3171.

[9]   A. S. Oliveira, J. A. Baeza, B. S. De Miera, L. Calvo, J. J. Rodriguez, M. A. Gilarranz, Aqueous phase reforming coupled to catalytic wet air oxidation for the removal and valorisation of phenolic compounds in wastewater, *J. Environ. Manage.*, 274 **(2020)** 111199.

[10]   S. Esplugas, B. Bayarri, J. Gime, Photocatalytic degradation of 2 , 4-dichlorophenol by TiO$_2$/UV: kinetics , actinometries and models, *Catalysis Today*, 101 **(2005)** 227-236.\

[11]   P. Taylor, J. Liu, J. Xie, Z. Ren, W. Zhang, Treatment solvent extraction of phenol with cumene from wastewater, *Desalin. Water.*, 51 **(2013)** 3826-3831.

[12]   Y. Rashtbari, S. Hazrati, A. Azari, S. Afshin, M. Fazlzadeh, M. Vosoughi, A novel, eco-friendly and green synthesis of PPAC-ZnO and PPAC-nZVI nanocomposite using pomegranate peel: cephalexin adsorption experiments, mechanisms, isotherms and kinetics, *Adv. Powder Technol.*, 31 **(2020)** 1612-1623.

[13]   A. Supong, P. C. Bhomick, R. Karmaker, S. L. Ezung, L. Jamir, U. B. Sinha, D. Sinha, Experimental and theoretical insight into the adsorption of phenol and 2,4-dinitrophenol

onto *Tithonia diversifolia* activated carbon, *Appl. Surf. Sci.*, 529 **(2020)** 147046.

[14] U. Mahapatra, A. Chatterjee, C. Das, A. Kumar, Environmental technology & innovation adsorptive removal of hexavalent chromium and methylene blue from simulated solution by activated carbon synthesized from natural rubber industry biosludge, *Environ. Technol. Innov.*, 22 **(2021)** 101427.

[15] Z. Alam, S. A. Muyibi, J. Toramae, Statistical optimization of adsorption processes for removal of 2 , 4-dichlorophenol by activated carbon derived from oil palm empty fruit bunches, *J. Environ. Sci.*, 19 **(2007)** 674-677.

[16] J. B. Castro, P. R. Bonelli, E. G. Cerrella, A. L. Cukierman, Phosphoric acid activation of agricultural residues and bagasse from sugar aane : influence of the experimental conditions on adsorption characteristics of activated carbons, *Ind. Eng. Chem. Res.*, 2000, 39 **(2000)** 4166-4172.

[17] T. C. Egbosiuba, A. S. Abdulkareem, A. S. Kovo, E. A. Afolabi, J. O. Tijani, M. Auta, W. D Roos, Ultrasonic enhanced adsorption of methylene blue onto the optimized surface area of activated carbon: adsorption isotherm, kinetics and thermodynamics, *Chem. Eng. Res. Des.*, 153 **(2020)** 315-336.

[18] P. C. Bhomick, A. Supong, M. Baruah, C. Pongener, Pine cone biomass as an efficient precursor for the synthesis of activated biocarbon for adsorption of anionic dye from aqueous solution : Isotherm , kinetic , thermodynamic and regeneration studies, *Sustain. Chem. Pharm.*, 10 **(2018)** 41-49.

[19] A. Bhatnagar, W. Hogland, M. Marques, M. Sillanpää, An overview of the modification methods of activated carbon for its water treatment applications, *J. Chem. Eng.*, 219 **(2013)** 499-511.

[20] J. Saleem, U. Bin Shahid, M. Hijab, H. Mackey, G. Mckay, Production and applications of activated carbons as adsorbents from olive stones, *Biomass Conv. Bioref.*, 9 **(2019)** 775-802.

[21] R. Mustafa, E. Asmatulu, Preparation of activated carbon using fruit , paper and clothing wastes for wastewater treatment, *J. Water Process Eng.*, 35 **(2020)** 101239.

[22] S. M. Anisuzzaman, C. G. Joseph, A. Bono, E. Suali, S. Abang, L. M. Fai, Removal of chlorinated phenol from aqueous media by guava seed (*Psidium guajava*) tailored activated carbon, *Water Resour. Ind.*, 16 **(2016)** 29-36.

[23] R. Tseng, K. Wu, F. Wu, R. Juang, Kinetic studies on the adsorption of phenol , 4-chlorophenol , and 2,4-dichlorophenol from water using activated carbons, *J. Environ. Manage.*, 91 **(2010)** 2208-2214.

[24] C. Pongener, P. C. Bhomick, A. Supong, M. Baruah, U. B. Sinha, D. Sinha, Adsorption of Fluoride onto activated carbon synthesized from *Manihot esculenta* biomass-Equilibrium, kinetic and thermodynamic studies, *J. Environ. Chem. Eng.*, 6 **(2018)** 2382-2389.

[25] L. Li, M. Wu, C. Song, L. Liu, W. Gong, Y. Ding, J. Yao, Efficient removal of cationic dyes via activated carbon with ultrahigh specific surface derived from vinasse wastes, *Bioresour. Technol.*, 322 **(2021)** 124540.

[26] D. Krishnaiah, C. G. Joseph, S. M. Anisuzzaman, W. M. A. W. Daud, M. Sundang, Y.C. Leow, Removal of chlorinated phenol from aqueous solution utilizing activated carbon derived from papaya (*Carica papaya*) seeds, *Korean J. Chem. Eng.*, 34 **(2017)** 1377-1384.

[27] A. Azari, M. Yeganeh, M. Gholami, M. Salari, The superior adsorption capacity of 2,4-dinitrophenol under ultrasound-assisted magnetic adsorption system: Modeling and process optimization by central composite design, *J. Hazard. Mater.*, 418 **(2021)** 126348.

[28] F. Shen, J. Liu, Z. Zhang, Y. Dong, C. Gu, Density functional study of hydrogen sul fi de adsorption mechanism on activated carbon, *Fuel Process. Technol.*, 171 **(2018)** 258-264.

[29] A. Supong, P. C. Bhomick, U. B. Sinha, D. Sinha, A combined experimental and theoretical investigation of the adsorption of 4-Nitrophenol on activated biocarbon using DFT method, *Korean J Chem Eng.*, 36 **(2019)** 2023-2034.

[30] A. Supong, P. C. Bhomick, M. Baruah, C. Pongener, U. B. Sinha, D. Sinha, Adsorptive removal of Bisphenol A by biomass activated carbon and insights into the adsorption mechanism through density functional theory calculations, *Sustain. Chem. Pharm.*, 13 **(2019)** 100159.

[31] S. U. Jan, A. Ahmad, A. A. Khan, S. Melhi, I. Ahmad, G. Sun, C. Chen, R. Ahmad, Removal of azo dye from aqueous solution by a low-cost activated carbon prepared from coal : adsorption kinetics , isotherms study , and DFT simulation, *Environ. Sci. Pollut. Res.*, 28 **(2020)** 10234-10247.

[32] J. Wang, H. Feng, H. Yu, Analysis of adsorption characteristics of 2,4-dichlorophenol from aqueous solutions by activated carbon fiber, *J. Hazard. Mater.*, 144 **(2007)** 200-207.

[33] Z. N. Garba, A. A. Rahim, Evaluation of optimal activated carbon from an agricultural waste for the removal of para-chlorophenol and 2,4-dichlorophenol, *Process Saf. Environ. Prot.*, 102 **(2016)** 54-63.

[34] A. Jumasiah, T.G. Chuah, J. Gimbon, T. S. Y. Choong, I. Azni, Adsorption of basic dye onto palm kernel shell activated carbon: Sorption equilibrium and kinetics studies, *Desalination*, 186 **(2005)** 57-64.

[35] P. He, J. Wu, X. Jiang, W. Pan, J. Ren, Effect of SO_3 on elemental mercury adsorption on a carbonaceous surface, *Appl. Surf. Sci.*, 258 **(2012)** 8853–8860.

[36] K. Gharbavi, H. Badehian, Structural and electronic properties of armchair (7, 7) carbon nanotubes using DFT, *Comput. Mater. Sci.*, 82 **(2014)** 159-164.

[37] S. Banerjee, D. Bhattacharyya, Electronic properties of nano-graphene sheets calculated using quantum chemical DFT, *Comput. Mater. Sci.*, 44 **(2008)** 41-45.

[38] J. C. Liu, P. A. Monson, Molecular modeling of adsorption in activated carbon : comparison of monte carlo simulations with experiment, *Adsorption*, 11 (**2005**) 5-13.

[39] L. M. Cam, L. Van Khu, N. N. Ha, Theoretical study on the adsorption of phenol on activated carbon using density functional theory, *J. Mol. Model.*, 19 (**2013**) 4395-4402.

[40] B. Padak, J. Wilcox, Understanding mercury binding on activated carbon, *Carbon N. Y.*, 47 (**2009**) 2855-2864.

[41] Y. Chen, Y. Zhu, Z. Wang, Y. Li, L. Wang, L. Ding, X. Gao, Y. Ma, Y. Guo, Application studies of activated carbon derived from rice husks produced by chemical-thermal process-a review, *Adv. Colloid Interface Sci.*, 163 (**2011**) 39-52.

[42] M. Radhika, K. Palanivelu, Adsorptive removal of chlorophenols from aqueous solution by low cost adsorbent-kinetics and isotherm analysis, *J. Hazard. Mater.*, 138 (**2006**) 116-124.

[43] N. Marhaini, B. Latip, K. Gopal, M. Suwaibatu, N. Munira, Removal of 2,4-dichlorophenol from wastewater by an efficient adsorbent of magnetic activated carbon, *Sep. Sci. Technol.*, 56 (**2020**) 252-265.

[44] M. Shirzad-siboni, S. Jafari, M. Farrokhi, J.K. Yang, Removal of phenol from aqueous solutions by activated red mud: equilibrium and kinetics studies, *Environ. Eng. Res.*, 18 (**2013**) 247-252.

[45] L. S. Maia, I. C. Andressa, S. Emanuel, S. C. Francisco, M. Monticelli, F. R. Pinhati, D.R. Mulinari, Activated carbon from palm fibres used as an adsorbent for methylene blue removal, *J. Polym. Environ.*, 29 (**2021**) 1162-1175.

[46] T. Dula, K. Siraj, S.A. Kitte, Adsorption of hexavalent chromium from aqueous solution using chemically activated carbon prepared from locally available waste of bamboo (*Oxytenanthera abyssinica*), *ISRN Environ. Chem.*, 2014 (**2014**) 1-9.

[47] K. Lagergren, About the theory of so-called adsorption of soluble substances, *Sven. Vetensk. Handingarl*, 24 (**1898**) 1-39.

[48] Y. S. Ho, G. McKay, Pseudo-second order model for sorption processes, *Process Biochem.*, 34 (**1999**) 451-465.

[49] D. Cortés-arriagada, L. Sanhueza, M. Santander-nelli, Modeling the physisorption of bisphenol A on graphene and graphene oxide, *J. Mol. Model.*, 19 (**2013**) 3569-3580.

[50] S. E. Agarry, C. N. Owabor, A. O. Ajani, Modified plantain peel as cellulose- based low-cost adsorbent for the removal of 2 , 6-dichlorophenol from aqueous solution : adsorption isotherms , kinetic modeling , and thermodynamic studies, *Chem. Eng. Commun.*, 200 (**2013**) 1121-1147.

[51] M. Sathishkumar, Kinetic and isothermal studies on liquid-phase adsorption of 2 , 4-dichlorophenol by palm pith carbon, *Bioresour. Technol.*, 98 (**2007**) 866-873.

[52] C. Namasivayam, D. Kavitha, Adsorptive removal of 2,4-dichlorophenol from aqueous solution by low-cost carbon from an agricultural solid waste : coconut coir pith from an agricultural solid waste, *Sep. Sci. Technol.*, 39 **(2010)** 1407-1425.

[53] M. Sathishkumar, A. R. Binupriya, D. Kavitha, R. Selvakumar, R. Jayabalan, J. G. Choi, S. E. Yun, Adsorption potential of maize cob carbon for 2,4-dichlorophenol removal from aqueous solutions: equilibrium, kinetics and thermodynamics modeling, *J. Chem. Eng.*, 147 **(2009)** 265-271.

[54] J. Wu, H. Yu, Biosorption of 2,4-dichlorophenol from aqueous solution by *Phanerochaete chrysosporium* biomass: isotherms, kinetics and thermodynamics, *J. Hazard. Mater.*, 137 **(2006)** 498-508.

[55] S. Batool, M. Idrees, M. Ahmad, M. Ahmad, Q. Hussain, Design and characterization of a biomass template/SnO_2 nanocomposite for enhanced adsorption of 2,4-dichlorophenol, *Environ. Res.*, 181 **(2019)** 108955.

[56] W. Liu, D. Ren, J. Wu, Z. Wang, S. Zhang, Adsorption behavior of 2,4-DCP by rice straw biochar modified with CTAB, *Environ. Technol.*, 42 **(2021)** 3797-3806.

CHAPTER 4

PHOTOCATALYTIC DEGRADATION OF THE ORGANOPHOSPHORUS INSECTICIDE CHLORPYRIFOS IN AQUEOUS SUSPENSIONS USING A NOVEL ACTIVATED CARBON ZrO₂-ZnO NANOCOMPOSITE UNDER UV LIGHT

This chapter deals with the photocatalytic degradation of the organophosphorus insecticide Chlorpyrifos in aqueous suspensions using *Schima wallichii* activated carbon supported on Zirconium dioxide-Zinc oxide (SWAC/ZrO₂-ZnO) nanocomposite in UV light. Analytical techniques such as XRD, FT-IR, TEM-SEAD, XPS, PL and BET analyzer were used to characterize the SWAC/ZrO₂-ZnO nanocomposite. SWAC/ZrO₂-ZnO nanocomposite has a BET surface area of 223.387 m^2g^{-1} and a total pore volume of 0.1845 cm^3g^{-1}. The chlorpyrifos photocatalytic degradation followed pseudo-first-order rate kinetics with a half-life period ($t_{1/2}$) of 7.088 mins and K_{ap} (apparent rate constant) of 0.09778 min^{-1}. The mechanism of composite formation was explained using DFT investigations, which demonstrated a favourable immobilization of ZrO₂-ZnO on SWAC. Chemical descriptors gained from DFT investigations, such as HOMO-LUMO energy, ionisation energy, dipole moment, chemical softness, and chemical hardness, supported an understanding of the relative efficiency and reactivity of ZrO₂-ZnO and SWAC/ZrO₂-ZnO towards chlorpyrifos degradation.

4.1. Introduction

Pesticides are substances designed to control pests. However, their widespread use in industrial and agricultural activities has become a matter of concern as the discharges from these sources contaminate water systems. Chlorpyrifos (CPs) is a common organophosphate insecticide used in agriculture to boost production and protect crops from insects and pests. The presence of chlorpyrifos in water can cause skin irritation, headaches, nausea, respiratory failure, stomach cramps, and even death in humans [1,2]. Therefore, developing a new and efficient method of wastewater treatment is necessary to remove the organic pollutants from the aqueous medium. Several novel approaches for chlorpyrifos-containing wastewater treatment have been suggested to date. These involve the application of electrochemical degradation [3], ionising radiation [4], biodegradation [5] batch adsorption [6], and photocatalytic degradation [7]. Out of various approaches, the development of the photocatalytic technique is one of the most potential processes for the degradation of organic contaminants due to its ease of use, high efficiency, lack of secondary pollution, and low cost [8]. This method takes place in presence of light wherein the semiconductor materials absorb the energy of a photon $\geq E_g$ (bandgap) and promotes an electron from the valence band to the conduction band. This allows for the creation of an electron in the conduction band and a positive hole in the valence band. Thus, the electron behaves as a reductant and the positive hole as an oxidant in the photocatalytic method [9].

Some of the metal oxide nanoparticle photocatalysts employed for the degradation or removal of organic compounds in aqueous media are ZnS (Zinc sulfide), TiO_2 (Titanium dioxide), ZnO (Zinc oxide), WO_3 (Tungsten trioxide), CuO (Copper oxide), and ZrO_2 (Zirconium dioxide) [10,11]. Under UV radiation, these metal oxides degrade the organic compounds, transforming them into harmless end products through various steps. Out of these, ZnO has been extensively studied because of its superior photocatalytic activity, stability, non-toxicity, and low cost [12]. However, ZnO has disadvantages such as photocorrosion and instability when exposed to light. Furthermore, a high recombination rate of photogenerated holes and electrons renders the photocatalytic process ineffective [13]. As a result, ongoing attempts are being made to increase the photocatalytic activity of ZnO by coupling or doping with metal/metal oxides. The well-known metal oxide zirconium dioxide (ZrO_2) has high thermal stability, excellent corrosion resistance, a high dielectric constant, and a wide band gap energy of ~5.0 eV [14]. Although the ZrO_2 band gap value is insufficient for degradation studies, its monoclinic phase and composite form help to improve photocatalytic activity. Further presence of ZrO_2 in ZnO/ZrO_2 complexes increases the generation of *OH radicals which is also responsible for the increase

in photoactivity. Therefore, the presence of ZrO_2 can strengthen the thermo-mechanical and chemical stability of ZnO. Simultaneously, the presence of ZnO can reduce the band gap of ZrO_2 [15]. In addition, ZnO undergoes dissolution at lower pH, but when coupled with ZrO_2 it can improve the dissolution resistance at lower pH as reported [16].

Numerous researchers have concluded that incorporating an adsorbent and a photocatalyst system improves the removal percentage of organic pollutants [17,18]. Activated carbon (AC) is a type of co-adsorbent widely utilized as key support for the photocatalyst in the treatment of wastewater through photocatalytic degradation [20]. AC having high adsorption capacity is more preferable as an adsorbent support system for photocatalyst as it can easily absorb organic pollutant molecules close to the photocatalytic sites during the adsorption-degradation process. [21]. Metal oxides nanoparticles with AC show an excellent adsorbent which provides a large number of active sites that can interact chemically with the adsorbents thereby enhancing chemisorption [22]. However, earlier reported combinations were based on single photocatalyst systems rather than multiple heterojunctions, which might significantly enhance photocatalytic performance through electron-hole separation and better light absorption. Thus, in the present work, we report a novel nanocomposite that integrates AC with ZrO_2-ZnO photocatalyst.

Quantum chemical approaches have now shown to be a viable means of understanding the quantitative structure-activity connection and providing a theoretical foundation for the fast selection of highly competent materials [23]. Density functional theory (DFT) is one such quantum mechanical modeling approach used to study the electronic structure, properties, reactivity, and stability of atoms and molecules [24]. Employing these approaches, several researchers have succeeded in anticipating the theoretical reasoning of the reactivity and interaction features of nanomaterials [25]. Therefore, the current work strives to provide a theoretical basis to explain the reactivity of the AC nanocomposite toward CPs degradation.

The goal of this research was to investigate the photodegradation of CPs in aqueous solutions utilizing ZrO_2-ZnO nanoparticles as a catalyst supported on *Schima wallichii* fruits activated carbon. Theoretical investigations were utilized to support experimental data and to study the reactivity towards CPs degradation using water as the solvent medium. The schematic representation for preparation of activated Carbon/ZrO_2-ZnO Nanocomposite under UV light is shown in the Figure 4.1
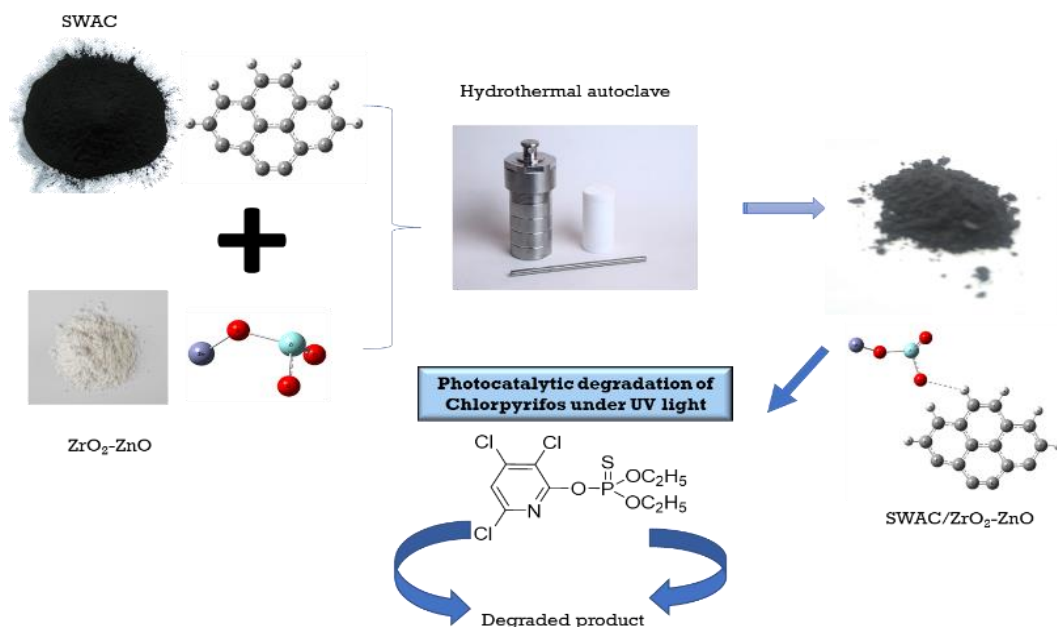
Figure 4.1. Schematic representation for preparation of activated Carbon/ZrO_2-ZnO nanocomposite under UV-light.

4.2. Materials and methods

4.2.1. Materials

Zinc acetate (Zn $(CH_3COO)_2 \cdot H_2O$), Zirconium dioxide (ZrO_2) and other chemicals such as HCl, NaOH, and KOH were utilized in the present study and were purchased from Sigma-Aldrich. Co., India. Tricel (20 % Chlorpyrifos) was purchased from Sumitomo Chemical India Ltd. The raw material *Schima wallichii* fruit utilized for this experiment was obtained directly from Nagaland University, Lumami Campus (26°28'29" N, 94°50'58" E).

4.2.2. Synthesis of *Schima wallichii* activated carbon (SWAC)

Synthesis of activated carbon was done using *Schima wallichii* biomass and KOH as an activating agent. *Schima wallichii* activated carbon is referred to as SWAC in all further discussions in this paper. In a typical preparation, the collected *Schima wallichii* biomass was properly cleaned with double-distilled water and oven-dried. Dried samples were carbonized by employing a muffle furnace at 600 °C for 1 hour under static conditions in a self-generated atmosphere followed by grinding the carbonized sample into a powder form and sieved before KOH activation. For activation, an aqueous solution of KOH was prepared by dissolving 20 g of KOH in double-distilled water. The impregnation was carried out by mixing KOH solution and 10 g carbonized sample in a ratio of 2:1 [26]. The mixture was then stirred for about 1 hour

and oven-dried at 105 °C for 24. The mixture was further pyrolyzed in a muffle furnace at 700 °C for 1 hour under static conditions in a self-generated atmosphere for the activation process. Afterward, the sample was then washed with 0.1 M NaOH and 0.1 M HCl followed by doubled-distilled water until the residual solution attained a neutral pH. The prepared sample was dried in an oven and stored in containers for further analysis.

4.2.3. Preparation of ZrO$_2$-ZnO nanocomposite

To prepare a ZrO$_2$-ZnO nanocomposite, 2.2 g of Zn (CH$_3$COO)$_2 \cdot$H$_2$O and 0.5 g of ZrO$_2$ were added to 100 mL double-distilled water while vigorously stirred for 30 mins at room temperature. The pH of the mixture was adjusted by adding 2M NH$_4$OH solution until the pH reached 9. The mixture solution was then sonicated for 30 mins to attain a homogenous mixture [26]. The mixture was then subjected to a stainless Teflon-lined autoclave for the hydrothermal process in an oven at the temperature of 160 °C for ~12 hours. The product was centrifuged, filtered, and washed multiple times with double-distilled water. Finally, after drying in an oven at 60 °C overnight. ZrO$_2$-ZnO nanocomposite was obtained.

4.2.4. Synthesis of SWAC/ZrO$_2$-ZnO nanocomposite

For the synthesis of SWAC/ZrO$_2$-ZnO nanocomposite, the mixture of 0.5 g of ZrO$_2$-ZnO nanocomposite and 1 g of the prepared SWAC were dispersed in 100 ml double-distilled water, and the mixture was agitated for 30 mins at room temperature. Afterward, the precursor mixture was sonicated for about 30 mins to attain a homogenous mixture. The SWAC/ZrO$_2$-ZnO nanocomposite was further subjected to a Teflon-lined autoclave for ~12 hours at 160 °C in an oven. Once the hydrothermal process was done, the solution was centrifuged washed with double-distilled water several times, and dried in an oven at 65 °C for 24 hours. The synthesized SWAC/ZrO$_2$-ZnO nanocomposite was further characterized and its application for the degradation of chlorpyrifos was investigated.

4.2.5. Characterization of the SWAC/ZrO$_2$-ZnO

Characterization of SWAC/ZrO$_2$-ZnO nanocomposite was done using different analytical techniques. The structure of the SWAC/ZrO$_2$-ZnO nanocomposite was assessed using a powder X-ray Diffraction (XRD) spectrum (Make: Rigaku Model: Smartlab, Japan). Fourier Transform Infra-Red (FT-IR) spectrometer (Model: Spectrum Two, Made: Perkin Elmer) was used to identify the functional groups on the surface of the SWAC/ZrO$_2$-ZnO nanocomposite. The morphologies and surface texture of the SWAC/ZrO$_2$-ZnO nanocomposite were studied using a Transmission Electron Microscopy (TEM) (Model: JEM-2100, Made: JEOL, JAPAN),

BET Surface Area Analyzer (Model: Autosorb iQ MP-AG (2 STAT) Anton Paar) was used to investigated the total surface area and total pore volume by N_2 adsorption-desorption isotherm studies along with the Barrett-Joyner-Halenda model (BJH) pore size distribution of activated carbon. EDX analysis for investigating elemental composition. Surface chemical states have been investigated using XPS. A Horiba Fluoromax 8-4CP spectrofluorometer with a 150 W Xenon Lamp was used to study photoluminescence (PL) spectra. The zero-point charge (pH_{pzc}) of the SWAC/ZrO_2-ZnO nanocomposite samples was investigated using the batch equilibrium method [27].

4.2.6. Photocatalysis

The photocatalytic degradation of CPs was carried out with the use of an ultraviolet light-assisted photocatalytic device, and details of the photocatalysis experiments are described below.

4.2.6.1. Photocatalytic device

In this work, photocatalytic degradation of CPs was carried out inside a photocatalytic reactor as described in Chapter 2. On top of a magnetic stirrer, a 250 mL Pyrex glass jar containing 50 mL CPs solution was placed, and a dose of SWAC/ ZrO_2-ZnO was stirred with the solution at the reactor's bottom. An Ultraviolet light (mercury lamp, 450W) with a maximum wavelength of 325 nm was placed 10 cm distance from the reaction mixture. A magnetic stirrer was installed directly under the double jacketed glass vessel to ensure that the reaction system was properly mixed. To keep the reactor temperature at 25 °C, a constant flow of water was employed throughout the reaction system. In addition, a reactor exhaust fan was installed to ensure that air was constantly circulated.

4.2.6.2. Photocatalytic degradation

The photocatalytic degradation was performed by utilizing a continuous flow of water at room temperature throughout the reaction process. A stock solution of 1000 ppm was first prepared by dissolving 1 g (5 mL of 20 % of chlorpyrifos) of CPs in 1000 ml double-distilled water. Furthermore, 100 ppm, 150 ppm, and 200 ppm were prepared by diluting the stock solution to the appropriate concentration. In the present work, the required amount of AC/ZrO_2-ZnO nanocomposite was dispersed in a 50 ml aqueous solution of varied CPs concentrations by vigorous stirring under dark conditions for 30 minutes to achieve adsorption-desorption equilibrium. Later, the UV light was switched on to start the photocatalytic reaction, and then

after 10 minute's intervals, 3 mL of sample was withdrawn and centrifuged for 10 minutes. The concentration of residual CPs was determined using a UV-Vis (PerkinElmer UV/Vis -365) spectrophotometer at λ_{max} of 221 nm. The following equations was used to calculate the degradation efficiency (R%) of CPs concentration.

$$R\% = \frac{C_o - C_e}{C_o} \times 100 \tag{4.1}$$

where, C_o (mg/L) is the initial concentration of CPs, and C_e (mg/L) is the equilibrium concentration of CPs.

4.2.7. Computational studies

To further understand the reactivity of the SWAC/ZrO$_2$-ZnO nanocomposite, theoretical investigations using density functional theory (DFT) were performed. To investigate any potential interactions between the activated carbon surfaces and the ZrO$_2$-ZnO catalyst, an appropriate structure for the activated carbon surfaces must be designed. According to reports, the carbon surfaces are made up of graphite clusters with 12-25 carbon atoms (3–7 carbon rings) [26, 29-31]. All the structures in this study were built using the Gauss View 05 software package, which was subsequently optimized using the Gaussian 09W software. The computations were carried out by B3LYP (Beck's three-parameter hybrid, functional correlation of Lee-Yang-Parr hybrid functional method), 6-31G/LanL2DZ basis set in water with a dielectric constant ($\varepsilon = 80$) to change the molecule geometry, lower the system's energy, and to achieve more stable conformation [31,32]. Quantum chemical parameters such as η (chemical hardness), H (HOMO-LUMO energy gap), μ (chemical potential), S (chemical softness), and ω (electrophilicity index) were used to comprehend the chemical reactivity of SWAC/ZrO$_2$-ZnO nanocomposite.

4.2.7.1. HOMO-LUMO energy gap

The chemical reactivity of a molecule is determined by the HOMO-LUMO energy gap (H); thus, a high value of the HOMO-LUMO energy gap signifies that the molecule is less reactive and more stable. Equation 4.2 gives the HOMO–LUMO energy gap [33].

$$H = E_{LUMO} - E_{HOMO} \tag{4.2}$$

where E_{LUMO} represents the energy of the lowest unoccupied molecular orbital, whereas E_{HOMO} represents the energy of the highest occupied molecular orbital.

4.2.7.2. Chemical hardness (η) and chemical softness (S)

The concepts of hardness (η) and softness (S) are important in understanding the behavior of chemical systems. The molecular stability increases as hardness increases and thereby its reactivity decreases. The chemical hardness (η) of a molecule is given by equation 4.3. The molecular stability increases as its softness decreases and thereby its reactivity increases. Equation 4.4 gives the chemical softness (S) of a molecule [34].

$$\eta = \frac{E_{LUMO} - E_{HOMO}}{2} \tag{4.3}$$

$$S = \frac{1}{2\eta} \tag{4.4}$$

4.2.7.3. Chemical potential and electronegativity

The reactivity of a molecule is determined by chemical potential (μ) and electronegativity (X) which are represented by the equations (4.5) and (4.6) respectively [35].

$$\mu = \frac{E_{HOMO} + E_{LUMO}}{2} \tag{4.5}$$

$$X = \frac{-(E_{HOMO} + E_{LUMO})}{2} \tag{4.6}$$

4.2.7.4. Electrophilicity index

The electrophilicity index (ω) is a measurement of energy loss caused by maximum electron flow between donor and acceptor. The higher the electrophilicity index, the molecule becomes more reactive. Electrophilicity index is calculated using equation 4.7 [36].

$$\omega = \frac{\mu^2}{2\eta} \tag{4.7}$$

when ω *is* greater than 1.5 eV, it has a high electrophilicity, ω less than 0.8 eV is considered marginal, and when ω is greater than0.8 and less than 1.5 eV is considered moderate.

4.3. Results and discussion

4.3.1. Characterization of the synthesized SWAC/ZrO$_2$-ZnO nanocomposite

FT-IR analysis confirmed the surface functionalities of the SWAC/ZrO$_2$-ZnO nanocomposite (Figure 4.2). Comparisons with previous reports, the wide bands are similar compared to ACs obtained from many different biomass sources having functional groups [38-49]. Peaks at 3432cm^{-1} and 3690 cm^{-1} have been ascribed to O-H stretching vibrations of water, alcohol, or carboxylic acid, and the band is comparable to previous reports [38,42-49]. The peaks at 3020 cm^{-1} appear similar to previous findings and might be due to the presence of aromatic C-H stretch vibration [43-44]. Aliphatic C-H stretching vibration may be responsible for the bands at 2946 cm^{-1} and 2852 cm^{-1} having similar to those reported in earlier reports [38, 43,45,48]. The presence of C-O stretch in alcohol, aldehyde, and carboxylic acid might explain the broad bands between 1700 and 1750 cm^{-1} that are similar to previous results [44-48]. The C=C aromatic peak was observed around 1562 cm^{-1} [38,44-48]. The transmittance at 1039 cm^{-1} and 1208 cm^{-1} was attributed to C-O stretching in alcohol, carboxylic acid, phenol, ester, or ester group derivatives being similar to those reported in earlier reports [38-39, 42-49]. The Zr-O vibrational mode is represented by the peak at 744 cm^{-1}. The Zn-O and Zn-O-Zr stretching vibrations are represented by the band at 528 cm^{-1} and 619 cm^{-1} respectively [40,41].
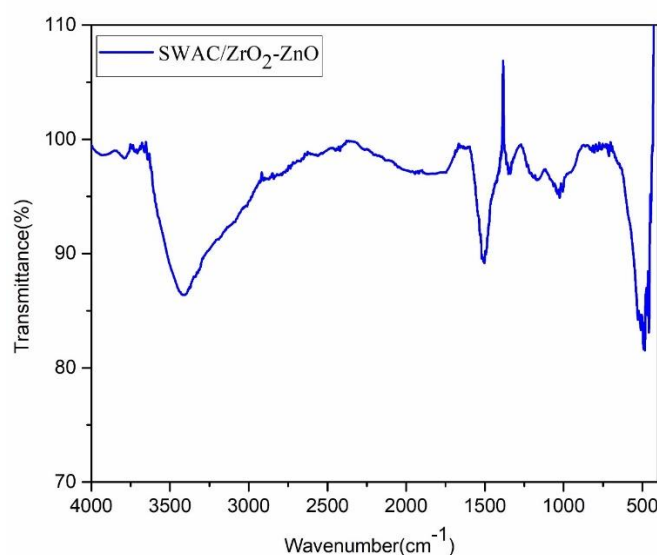
Figure 4.2. FT-IR spectra of SWAC/ZrO$_2$-ZnO nanocomposite.

The crystal structure of the synthesized SWAC/ZrO$_2$-ZnO nanocomposite was investigated using an XRD pattern, as shown in Figure 4.3. The peak at 2θ = 22.9° resembles the

characteristic of disordered aromatic carbon structure with miller indices (0 0 2), the intensity peak at 2θ= ~26° and ~44.17° corresponding to (1 0 0) and (1 0 1) planes of hexagonal graphitized carbon (JCPDS 00-025-0284). The presence of hexagonal zincite crystalline structure of ZnO is confirmed by the 2θ peaks at 34.43°, 57.16°, and 72.67°, with miller indices of (0 0 2), (1 1 0), and (0 0 4), respectively (JCPDS 01-075-1526). Furthermore, an X-ray diffractogram of commercial zirconia reveals the presence of a monoclinic phase, whereas an X-Ray Diffractogram of hydrothermally treated zirconia reveals cubic and tetragonal phases [50]. The ZrO_2 peaks were found at $2\theta = 30.1°$ corresponding to the cubic phase (1 1 1) (JCPDS 01-089-9069) [50], 50.3°, and ~60° lattice planes (1 1 2), and (1 0 3) correlate to tetragonal ZrO_2 (JCPDS No. 01-079-1764). As a result, the Debye-Scherer equation was used to calculate the average crystalline size of SWAC/ZrO_2-ZnO nanocomposite, which was found to be ~39.41 nm.
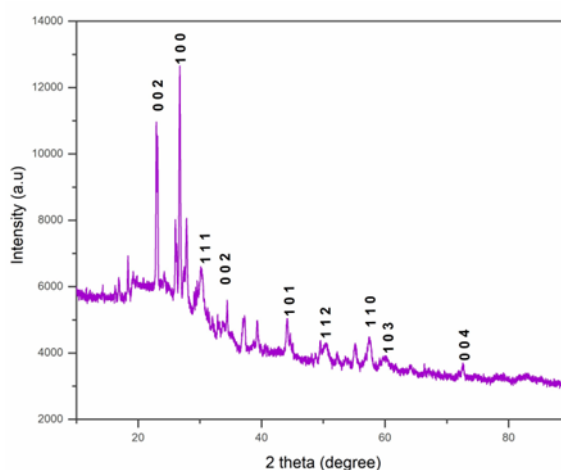
Figure 4.3. (a) XRD analysis of synthesized SWAC/ZrO_2-ZnO nanocomposite.

TEM investigations revealed the presence of an amorphous SWAC/ZrO_2-ZnO-thick layer. Simultaneously, irregularly shaped nanoparticles with crystallites ranging in size from a few nanometers to several nanometers emerge on the surface of other particles as shown in Figure 4.4 [51]. Thus, the particle size of synthesized SWAC/ZrO_2-ZnO was formed in the range of 21- 44 nm.
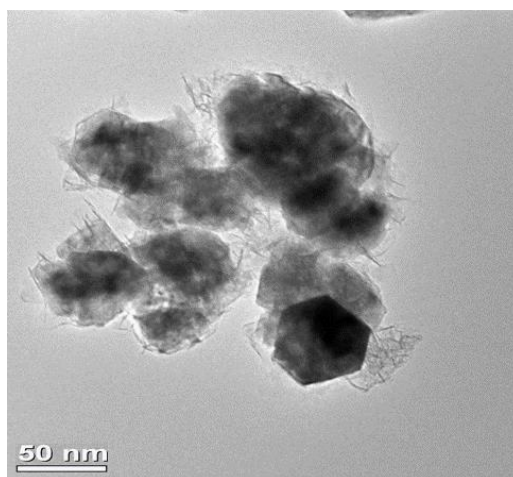
Figure 4.4. TEM analysis of synthesized SWAC/ZrO$_2$-ZnO nanocomposite.

The SAED (Selected Area Electron Diffractions) pattern as shown in Figure 4 (c) suggests that the material is polycrystalline. The defused character of the material indicates its decreased crystallinity, which is predicted owing to the integration of ZrO$_2$-ZnO nanocomposite particles inside the activated carbon envelop. The SAED patterns show spotty rings whose interplanar distances match with those of XRD crystal planes of hexagonal graphitized carbon (1 0 1), hexagonal zincite ZnO (0 0 2), and (0 0 4), and tetragonal ZrO$_2$ (1 1 2) as shown in Figure 4.5 [32,45].
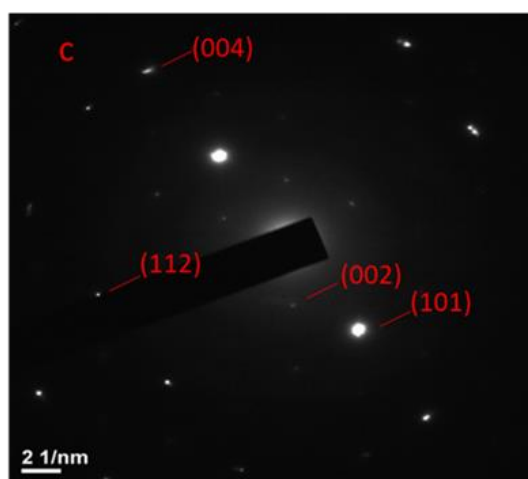
Figure 4.5. SAED analysis of synthesized SWAC/ZrO$_2$-ZnO nanocomposite.

The XPS analysis was used to ascertain the chemical state of C, O, Zn and Zr contained on the surface of synthesized SWAC/ZrO$_2$-ZnO nanocomposite. As shown in Figure 4.6, C, O, Zn, and Zr elements coexist on the nanocomposite's surface, with matching peaks at 284 eV (C 1s),

532 eV (O 1s), 1024 eV (Zn 2p 3/2), 1044 eV, (Zn 2p) and 184 eV (Zr 3d), respectively. The XPS spectra suggested the formation of a SWAC/ZrO$_2$-ZnO nanocomposite [52,53].
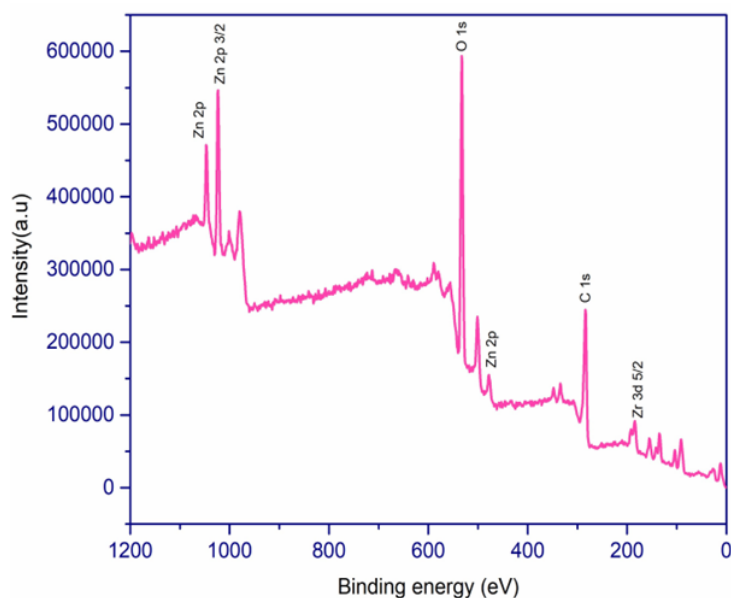
Figure 4.6. XPS analysis of synthesized SWAC/ZrO$_2$-ZnO nanocomposite.

Figure 4.7 shows the PL (Photoluminescence) spectra of pure ZnO and the synthesized SWAC/ZrO$_2$-ZnO composite. The recombination of electron hole pairs and the emission of photons are involved in photoluminescence. As photocatalytic efficiency increases, photoluminescence intensity and electron hole recombination efficiency decrease [21,54]. As seen in Figure 4.3 (e), ZnO has the highest PL intensity, suggesting the highest rate of electron-hole recombination. The PL intensity reduces after the formation of the SWAC/ZrO$_2$-ZnO nanocomposite, showing that the electron-hole recombination rate lowers, implying that the SWAC/ZrO$_2$-ZnO nanocomposite has higher photocatalytic efficiency.
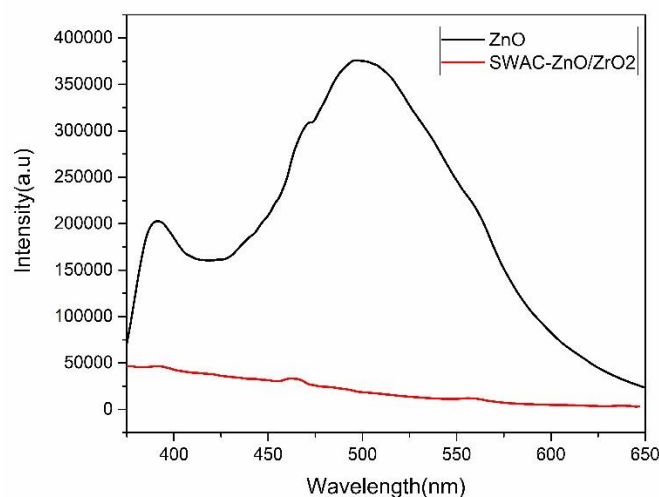
Figure 4.7. Photoluminescence analysis of synthesized SWAC/ZrO$_2$-ZnO nanocomposite.

EDX was used to further investigate the elemental compositions of the prepared SWAC/ZrO2-ZnO nanocomposite (Figure 4.8). The EDX graph revealed that the prepared SWAC/ZrO2-ZnO nanocomposite contains 98.05 % carbon, 0.15 % oxygen, 0.58 % Zr and 1.21 % Zn. The presence of C, O, Zr and Zn peaks in the EDX graph is due to the use of carbon, Zirconium dioxide and Zinc acetate in the preparation of the SWAC/ZrO2-ZnO nanocomposite.

Element	Weight %	Atomic %
O	0.15	0.60
C	98.05	96.22
Zr	0.58	0.41
Zn	1.21	2.77
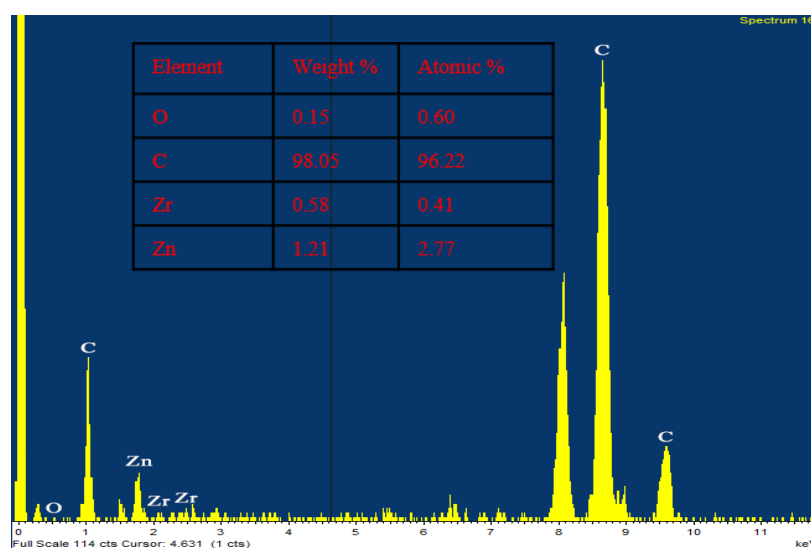
Figure 4.8. EDX spectra of SWAC/ZrO$_2$-ZnO nanocomposite.

To investigate the surface area and porosity of the SWAC/ZrO$_2$-ZnO nanocomposite, N$_2$ adsorption/desorption isotherm studies were performed along with the Barrett-Joyner-Halenda model (BJH) pore size distribution. The N$_2$ adsorption/desorption isotherm of the SWAC/ZrO$_2$-ZnO nanocomposite is depicted in Figure 4.9 (b) (It presented a physisorption isotherm of type

I and IV. The presence of micropores in the SWAC/ZrO_2-ZnO sample was demonstrated by a high adsorption limit at low relative pressure (p/p_o 0.99). The formation of a large number of mesopores in the SWAC/ZrO_2-ZnO nanocomposite was demonstrated by the H4 type hysteresis loop at a relative pressure p/p_o range of 0.4 to 1.0, which results from mesopores filling and emptying by capillary condensation. SWAC/ZrO_2-ZnO nanocomposite has a BET surface area of 223.387 m^2g^{-1} and a total pore volume of 0.1845 cm^3g^{-1}. From the desorption branches of the isotherms, the pore size distributions were calculated using the BHJ as shown in Figure 4.9 (a), the pore size distribution of SWAC/ZrO_2-ZnO was primarily narrow, with an average diameter of 3.81 nm.
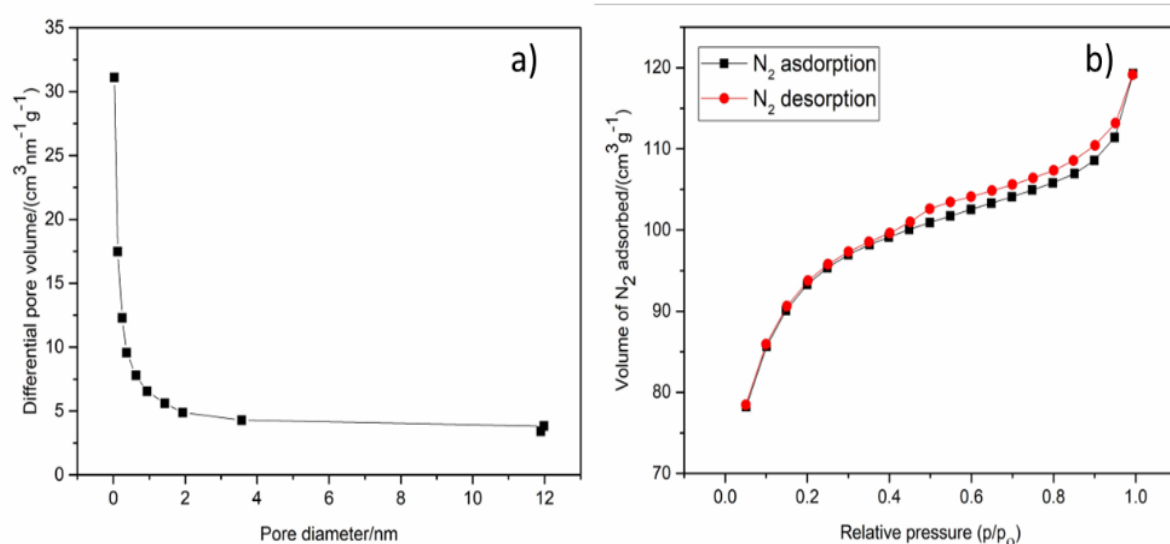
Figure 4.9. (a) Pore size distribution and (b) N_2 adsorption/desorption isotherm studies of the SWAC/ZrO_2-ZnO nanocomposite.

4.3.2. Photocatalytic activity

4.3.2.1. Effect of SWAC/ZrO_2-ZnO nanocomposite dosage

The photocatalytic activity of the synthesized SWAC/ZrO_2-ZnO nanocomposite for the degradation of CPs solutions was investigated at various doses (0.01-0.10 g) and for various concentrations (100 ppm, 150 ppm, and 200 ppm). For all CPs concentrations, the percentage of CPs degradation increased with the increase of nanocomposite doses till 0.05g (Figure 4.10). Under UV light irradiation for 50 minutes, the maximum percentage of degradation (97 %) was achieved for 100 ppm CPs concentration at the dosage of 0.05g SWAC/ZrO2-ZnO nanocomposite.

As the catalyst loading increases, the number of active sites in the solution increases, while UV light penetration reduces due to the high particle concentration, resulting in lower CPs degradation. Similar studies on other catalysts have been reported in the literature [8,55-56]. Thus, for further studies, 0.05 g of the SWAC/ZrO$_2$-ZnO nanocomposite was taken to be the optimal dosage for CPs degradation process.
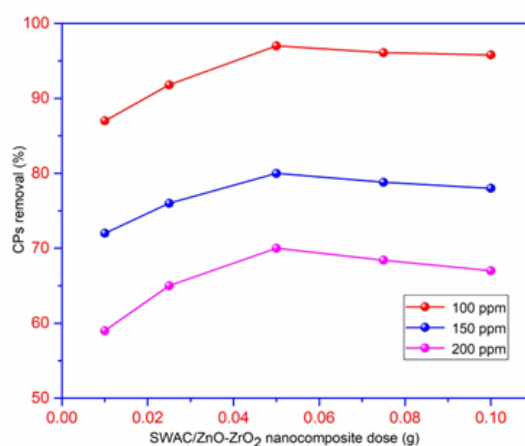
Figure 4.10. (a) Effect of SWAC/ZrO$_2$-ZnO nanocomposite dosage in the degradation of CPs solution.

4.3.2.2. Effect of pH on CPs concentration

To determine the optimal pH for CPs degradation, the experiment was carried out at different pH ranges from 2 to 10 with an initial CPs concentration of 100 ppm, nanocomposite dose of 0.05 g, UV light irradiation time of 50 mins, and temperature of 298 K. Figure 4.11 shows the photodegradation of CPs increases with an increase in pH from 2 to 6 and decreased thereafter in a basic medium. The pH$_{zpc}$ (zero point charge) of SWAC/ZrO$_2$-ZnO nanocomposite was found to be 6.8, which signifies that, the surface of the SWAC/ZrO$_2$-ZnO nanocomposite is negatively charged above this pH and positively charged below this pH. Therefore, at lower pH, a positively charged photocatalyst surface is likely to have a higher electrostatic attraction affinity towards oppositely charged CPs solution. In basic conditions, hydroxyl radicals behave as weak acids, forming less reactive $^-$O ions upon reaction with $^-$OH ions. Furthermore, at basic pH, the breakdown of H$_2$O$_2$ to H$_2$O and O$_2$ occurs more quickly, resulting in decreased photocatalytic activity. Similar studies on other catalysts have been reported in the literature [9,56-57]. Therefore, at lower pH, a positively charged photocatalyst surface is likely to have a higher electrostatic attraction affinity towards oppositely charged CPs solution. As a result, the optimal pH for CPs photodegradation was found to be pH 6.0.
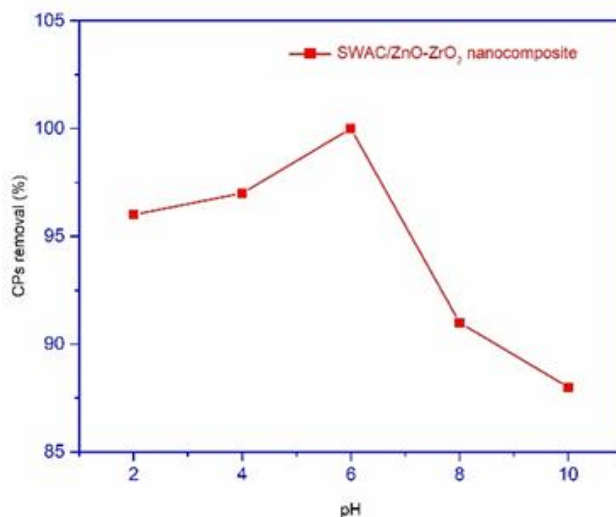
Figure 4.11. Effect of pH in the degradation of CPs solution.

4.3.2.3. Effect of initial CPs concentration and light irradiation time

The effect of initial concentration on the rate of CPs degradation was studied at varied CPs concentrations (100, 150, and 200 ppm) at the optimal dosage of 0.05 g SWAC/ZrO$_2$-ZnO nanocomposite and pH=6). A graph of CPs removal % Vs time is shown in Figure 4.12. After 50 minutes of UV light irradiation, 100 % degradation of CPs was observed for a 100 ppm solution. On the other hand, the removal percentage for 150 ppm and 200 ppm concentrations of CPs, was reduced to 80 percent and 70 percent, respectively. As a result, for all subsequent experiments, the optimal concentration is determined to be 100 ppm.
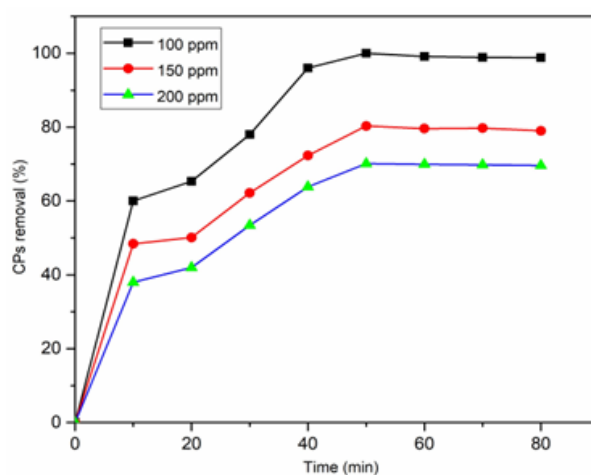
Figure 4.12. Effect of initial CPs concentration and light irradiation time in the degradation of CPs solution.

In addition, the lesser availability of hydroxyl radical species in the reaction media might explain why the CPs degrades more slowly. Photocatalytic degradation is started by reactive hydroxyl radicals produced as a result of light exposure, and the degradation process occurs mostly on the nanocomposite's surface. When the CPs concentration increases, light particles become trapped between the CPs particles and are unable to reach the nanocomposite surface [55]. As a result, the formation of reactive hydroxyl radicals decreases, and the breakdown of CPs decreases.

4.3.2.4. Effect of temperature

The effect of temperature on the degradation of CPs was examined at 301, 303, 308, and 311 K while maintaining the other parameters constant (dosage of 0.05 g SWAC/ZrO_2-ZnO nanocomposite, 100 ppm CPs solution, and pH= 6 for 50 minutes). Figure 4.13 depicts a plot of percentage removal of CPs vs temperature. It was observed that with increases in temperature the removal percentage of CPs decreased [58].
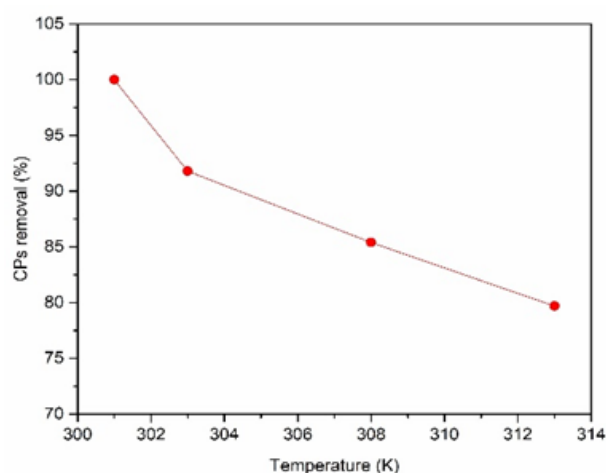
Figure 4.13. Effect of temperature in the degradation of CPs solution.

4.3.3. LC-MS analysis of CPs degradation

LC-MS spectra (Make: INKAR, Model: Expression-S) is utilized to identify the degraded products after the photocatalytic reaction. Figure 4.14 represents the spectra of the reaction mixture after 50 mins of UV irradiation. Based on the detected components from mass spectra, an effort has been made to understand the degradation process in detail shows the product obtain were given in the Table 4.1 shows the components that have been identified. The decomposition process of CPs proceeds in a similar way as reported in the literature [8,59]. Photodegradation occurs via a free radical process, and the possible mechanism is illustrated in Figure 4.15.
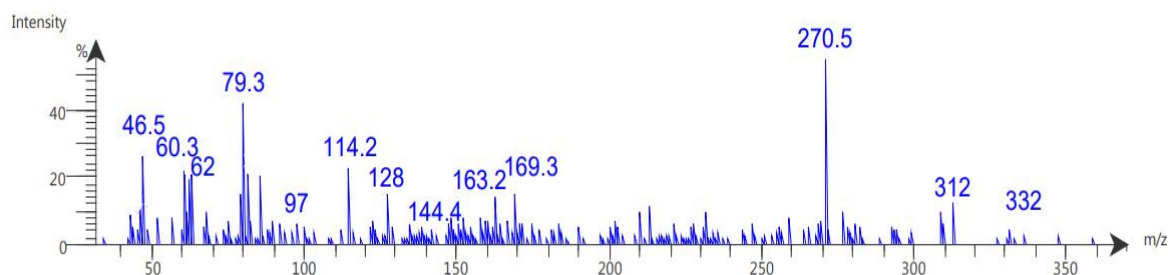
Figure 4.14. LC-MS spectra of the photolytic degradation products of CPs.

Table 4.1. LC-MS analysis of photodegraded chlorpyrifos.

Sl. No.	Photodegradation products	m/z	Probable structure
1	O-(5,6-dichloro-3-hydroxypyridin-2-yl) O,O-diethyl phosphorothioate	332	
2	O-(6-chloro-3,5-dihydroxypyridin-2-yl) O,O-diethyl phosphorothioate	312	
3	O-(5,6-dichloro-3-hydroxypyridin-2-yl) O,O-dihydrogen phosphorothioate	270.5	
4	O,O-diethyl O-hydrogen phosphorothioate	169.3	
5	5,6-dichloropyridin-3-ol	163.2	
6	2-chloropyridine-3,5-diol	144.4	
7	pyridine-2,3,5-triol	128	
8	Phosphorothioic O,O,O-acid	114.2	
9	phosphoric acid	97	
10	Pyridine	79.3	
11	2-aminoethan-1-ol	62	
12	acetic acid	60.3	
13	Ethanol	46.5	
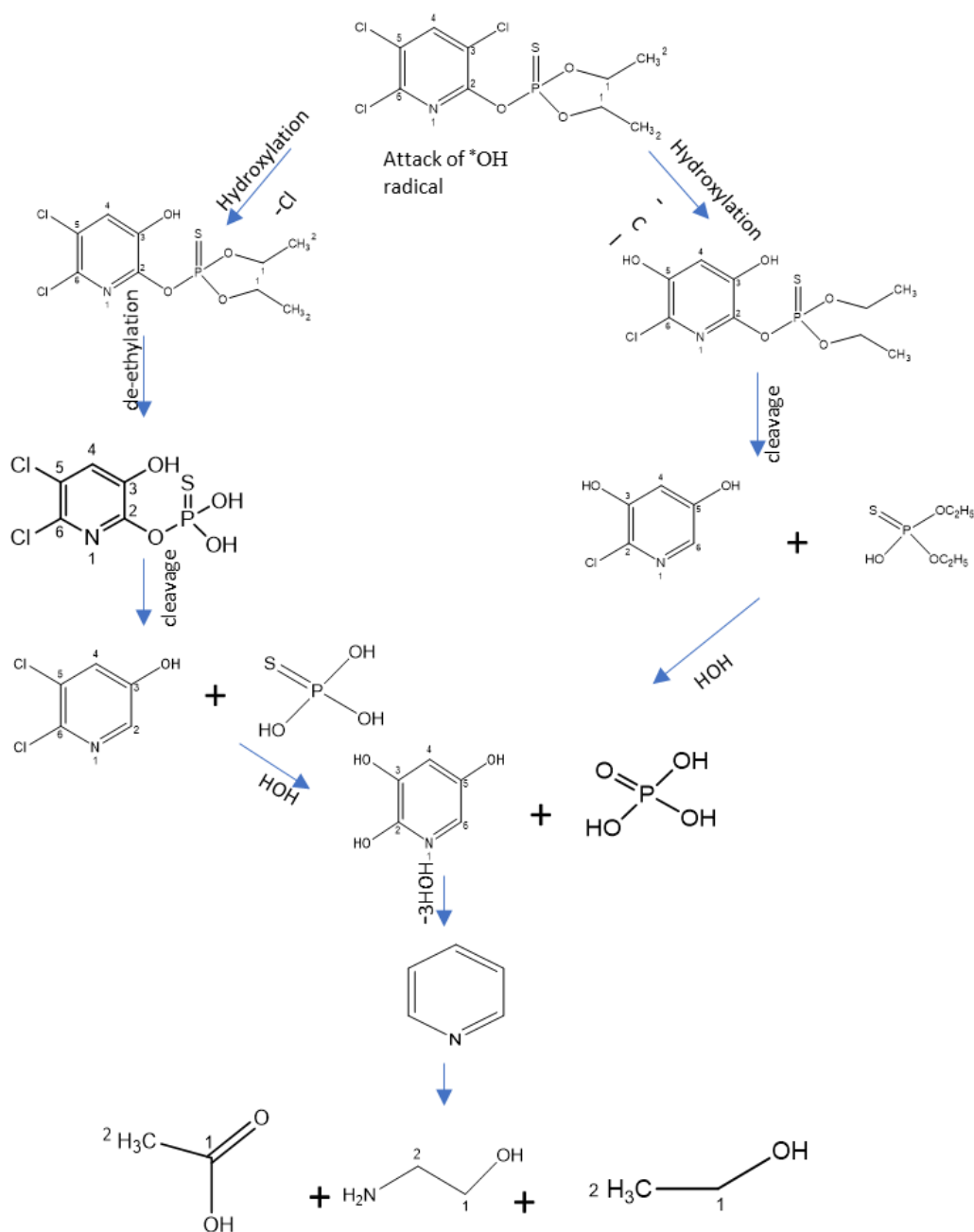
Figure 4.15. Photocatalytic degradation pathways of CPs using SWAC/ZrO$_2$-ZnO nanocomposite.

4.3.4. Photodegradation kinetics of chlorpyrifos

The kinetic studies were carried out at optimum conditions i.e., with 100 ppm CPs solutions (50 ml), pH at 6, irradiation time of 50 mins, and 0.05 g of SWAC/ZnO-ZrO$_2$ nanocomposite. The photocatalytic performance of the CPs concentration was determined by employing the Langmuir-Hinshelwood model [57]. The kinetics study was described using pseudo first-order rate and the half-life period. The equations are given as follows.

$$ln(Co/C) = k_{ap}t \qquad\qquad\qquad (4.8)$$

$$t_{1/2} = \frac{ln\,2}{k_{ap}} \qquad\qquad\qquad (4.9)$$

where C_o denotes the CPs initial concentration, C denotes the concentration at time t, K_{ap} denotes the apparent reaction rate constant, and $t_{1/2}$ denotes the half-life period.
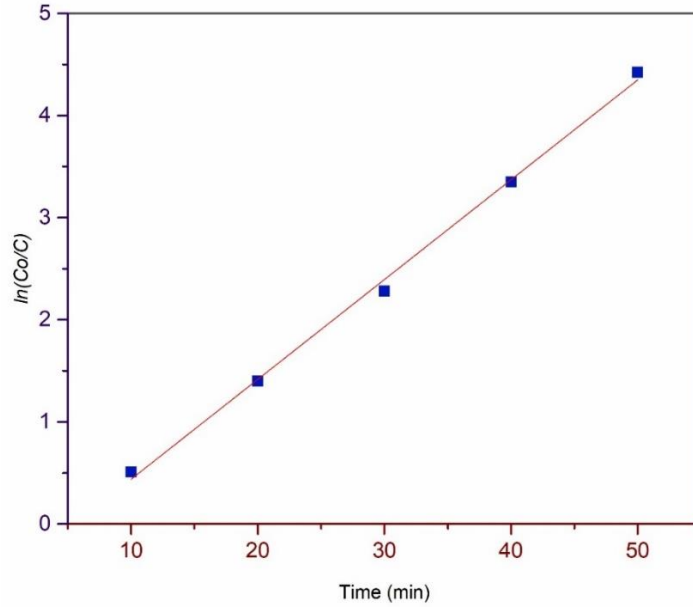
Figure 4.16. Pseudo first-order rate kinetics of CPs degradation loaded on SWAC/ZrO$_2$-ZnO nanocomposite.

For the SWAC/ZrO$_2$-ZnO nanocomposite, the linear plot of *ln (Co/C)* vs time shows a strong correlation coefficient (R^2 value: 0.99), indicating that the CPs degradation follows pseudo-first-order rate kinetics (Figure 4.16). The photocatalytic rate constant (K_{ap})value was derived from the slope of the curve to be0.09778 min^{-1} and $t_{1/2}$ was calculated using equation (12) to be 7.088 mins.

4.3.5. Catalyst efficiency for the degradation of CPs

The experiment was performed using different catalysts such as pristine ZrO$_2$, pristine ZnO, and prepared SWAC/ZrO$_2$-ZnO nanocomposite while maintaining all other parameters at optimum condition (dose of 0.05 g, initial CPs concentration of 100 ppm, and UV light irradiation time of 50 minutes).In all situations, the prepared SWAC/ZrO$_2$-ZnO nanocomposite catalysts surpass the pristine catalysts in terms of photocatalytic activity towards CPs

degradation (Figure 4.17). The decreasing order of photocatalytic efficiency towards CPs degradation are as follows: prepared SWAC/ZrO$_2$-ZnO (100 %)>pristine ZnO (65 %)>pristine ZrO$_2$ (54 %). This suggests that photocatalytic activity improved after ZnO was doped with ZrO$_2$ supported by activated carbon.
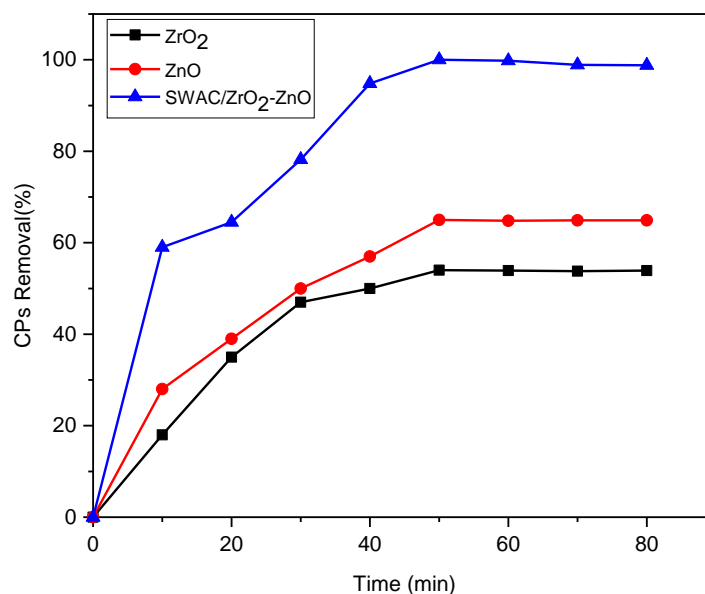
Figure 4.17. Photocatalytic activity test of CPs degradation by ZrO$_2$, ZnO and synthesized SWAC/ZrO$_2$-ZnO nanocomposite.

4.3.6. Effect of radical scavengers on photocatalytic degradation of CPs

The type and amount of reactive oxidation species produced by photo-generated electrons and holes are closely related to photocatalytic activity. Four scavengers were used to explore the reactive species in the photocatalytic reaction process to further detect the main reactive oxidative species in the photocatalytic process for elucidating the photocatalytic mechanism. Scavengers for hydroxyl radicals (*OH), holes (h$^+$), superoxide radicals (*O^{2-}), and electrons (e$^-$) were glycine, EDTA, BQ (p-benzoquinone), and CuSO$_4$ in this experiment. As demonstrated inFigure 4.18, the percentage removal decreases from 100 % to 54.0 % (Glycine), 66.7 % (EDTA), 77.3 % (CuSO$_4$), and 60.0 % (BQ). In the addition of four types of scavengers significantly reduces the photodegradation efficiency of the SWAC/ZrO$_2$-ZnO nanocomposite, indicating that *O^{2-}, h$^+$, e$^-$ and *OH may be the active species on the CPs degradation in the system. More importantly, the promoting effect of these reactive oxidation species decreases in the following order: hydroxyl radical (*OH)> superoxide radical (*O^{2-})> hole (h$^+$) > electron

(e⁻). These findings clearly show that the most important reactive oxidation species, $^*OH$, h^+, e^- and $^*O^{2-}$ are significantly increased in the SWAC/ZrO$_2$-ZnO nanocomposite.
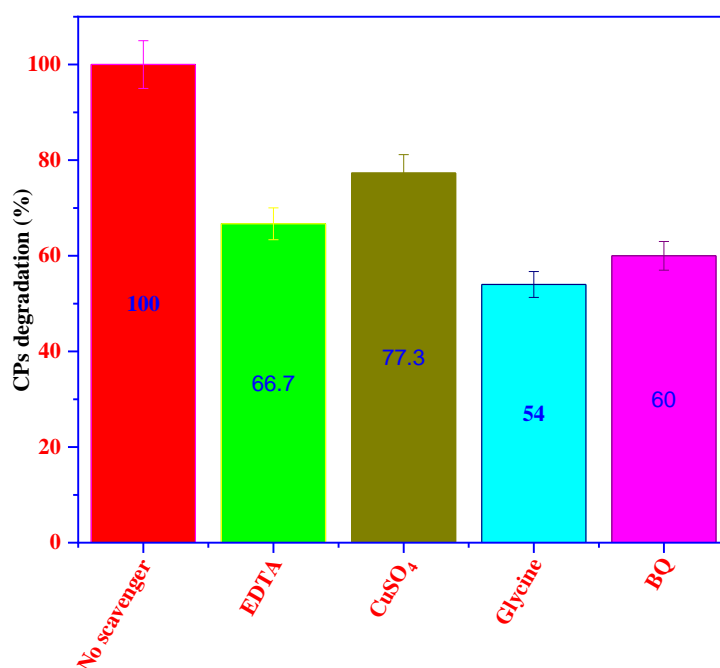
Figure 4.18. Photocatalytic degradation of CPs in the presence of different scavengers using SWAC/ZrO$_2$-ZnO nanocomposite.

4.3.7. Nanocomposite reusability and photostability

The reusability of the produced nanocomposite for photocatalytic CPs degradation was tested for six cycles. To reuse the nanocomposite, the nanocomposite remaining in the reaction medium was separated by centrifuging the solution after each photocatalytic reaction. The nanocomposite was then washed with double distilled water and oven dried. The dried nanocomposite was then employed for photocatalytic CPs degradation (Figure 4.19). The CPs degradation rate in the first cycle was 100 %, which decreased to 92.60 % in the second cycle, 88 % in the third cycle, 83 % in the fourth cycle and for the fifth cycle it degraded upto 74 %. With increasing usage, the degrading efficiency of the nanocomposite decreases significantly. This decrease in degradation efficiency might be attributed to a decrease in unoccupied adsorption sites on SWAC/ZrO$_2$-ZnO nanocomposite for CPs adsorption. It might also be owing to the release of photoactive substances from the SWAC/ZrO$_2$-ZnO nanocomposite during the recycling process. The degradation efficiency of the nanocomposite was found to be approximately 68 % in the sixth cycle, indicating that the SWAC/ZrO$_2$-ZnO nanocomposite still has outstanding utilisation capacity after numerous cycles.
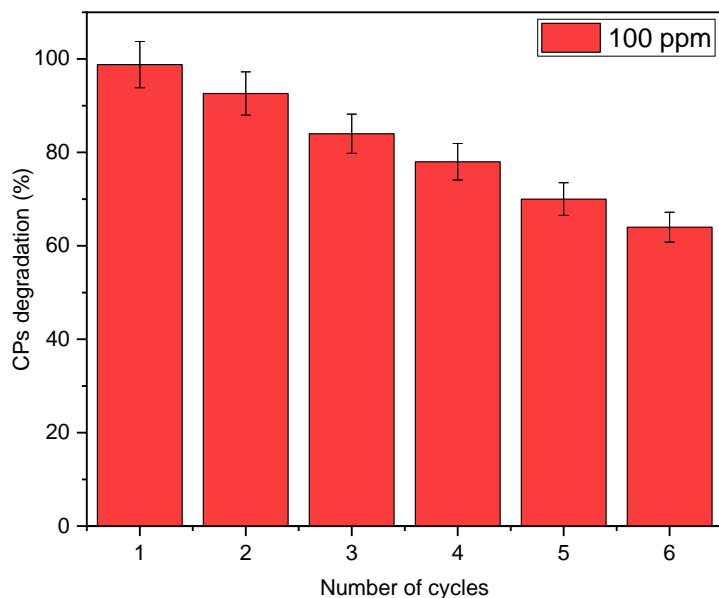
Figure 4.19. CPs degradation efficiency of SWAC/ZrO$_2$-ZnO nanocomposite upto six cycles.

4.3.8. Computational studies

Theoretical investigations were used to get insight into the reactivity of SWAC/ZrO$_2$-ZnO nanocomposite. For the current study, four fused benzene ring configurations were used to model SWAC [60]. SWAC was coupled with ZrO$_2$-ZnO through the formation of hydrogen bonding via O-linkage of the O-Zr-O bond in SWAC/ZrO$_2$-ZnO nanocomposite. The optimized molecular structures of ZrO$_2$-ZnO and SWAC/ZrO$_2$-ZnO composite, as well as their HOMO and LUMO structures, are shown in Figure 4.20.

Molecule	Optimize structures	HOMO	LUMO
ZrO$_2$-ZnO			
SWAC/ZrO$_2$-ZnO			

Figure 4.20. HOMO and LUMO molecular orbital of ZrO_2-ZnO and SWAC/ZrO_2-ZnO nanocomposite.

Table 4.2 shows the quantum chemical descriptors and calculated values of ZrO_2-ZnO and SWAC/ZrO_2-ZnO nanocomposite, including HOMO-LUMO band gap energies, ionization potentials, and dipole moment. The dipole moment increases from 19.0179 to 37.2082 Debye and the energy gap decreases from 0.05745 to 0.02364 eV when ZrO_2-ZnO is introduced into SWAC, as shown in the table. These modifications imply that the nanocomposite material produced is extremely reactive and has a favourable interaction.

Table 4.2. Calculated molecular properties of ZrO_2-ZnO and SWAC/ZrO_2-ZnO nanocomposite.

System	Dipole moment				Frontier orbital and energy gap		
	X	Y	Z	Total dipole moment (Debye)	HOMO (eV)	LUMO (eV)	Energy gap (eV)
ZrO_2-ZnO	-2.5874	-18.8411	0	19.0179	-0.14267	-0.08522	0.05745
SWAC/ZrO_2-ZnO	36.9314	3.1858	-3.2303	37.2082	-0.19174	-0.16810	0.02364

The HOMO-LUMO band gap energies of SWAC/ZrO_2-ZnO nanocomposite are compared to those of other Catalysts described in the literature in Table 4.3. According to the table, the HOMO-LUMO band gap energies of SWAC/ZrO_2-ZnO nanocomposite have a lower energy gap than other catalysts. As a result of these modifications, the nanocomposite material formed is extremely reactive and has a favourable interaction.

Table 4.3. Show the energy gap of different catalysts.

System	Energy gap (eV)	Reference
SWAC/ZrO_2-ZnO	0.02364	Present case

ZnBTC	2.3004	[61]
Mg(H₂BTC)₂(H₂O)₂	3.57	[62]
TiO₂-NP/PAC composite	0.02501	[23]
SWCNTs	1.16	[64]

The molecular chemical descriptors of ZrO₂-ZnO and SWAC/ZrO₂-ZnO nanocomposite are shown in Table 4.4. The chemical hardness (η) of SWAC/ZrO₂-ZnO was found to be lower than that of ZrO₂-ZnO. Moreover, The chemical softness (S) of SWAC/ZrO₂-ZnO nanocomposite is greater than ZrO₂-ZnO indicating that SWAC/ZrO₂-ZnO nanocomposite had a higher reactivity than ZrO₂-ZnO [52]. These results signify that by doping ZrO₂-ZnO nanoparticles into activated carbon, the reactivity of the nanocomposite increases. Also, SWAC/ZrO₂-ZnO possesses greater electronegativity value (X=0.17992 eV) and electrophilicity index (ω=1.3693 eV) than ZrO₂-ZnO (X= 0.11394 eV, ω= 0.0009 eV) suggesting that it is a better electron acceptor. Moreover, the μ value of the SWAC/ZrO₂-ZnO nanocomposite is lower than that of ZrO₂-ZnO, indicating that it is easier to gain electrons rather than to lose an electron.

As a result of this computational work, it is clear that incorporating ZrO₂-ZnO into SWAC improves its reactivity, which increases its effectiveness in removing CPs. Thus, these theoretical investigations help in the selection of highly effective materials for pollution removal by providing a theoretical concept of the reactivity of the materials.

Table 4.4. Molecular chemical descriptors of ZrO₂-ZnO and SWAC/ZrO₂-ZnO nanocomposite.

System	η (eV)	S (eV)	μ (eV)	ω (eV)	X (eV)
ZrO₂-ZnO	0.028725	14.406	-0.11394	0.0009	0.11394
SWAC/ZrO₂-ZnO	0.01182	42.301	-0.17992	1.3693	0.17992

4.3.9. Comparative study of SWAC/ZrO₂-ZnO nanocomposite with other nanocomposite materials

Table 4.5 presents a comparative study of SWAC/ZrO₂-ZnO nanocomposite with other nanocomposite materials described in the literature to comprehend the degradation efficiency

of CPs. This suggests that the SWAC/ZrO₂-ZnO nanocomposite has a relatively high activity under ideal circumstances and is a viable photocatalyst for the removal of CPs in water.

Table 4.5. Comparative study of chlorpyrifos removal percentage (%) with other nanocomposite materials.

Organic pollutant	Nanocomposite materials	Removal percentage (%)	Reference
Chlorpyrifos	SWAC/ZrO$_2$-ZnO nanocomposite	100	Present case
	CFGO/ZnO nanorod composite	99.4	[64]
	CuO/TiO$_2$/PANI nanocomposite	95	[56]
	CeO$_2$/TiO$_2$/SiO$_2$ nanocatalyst	90.8	[57]
	Fe: ZnO nanocomposite	93.5	[65]
	ZnS nanoparticles	85.29	[66]
	TiO$_2$/H$_2$O$_2$	74.38	[67]
	CoFe$_2$O$_4$@TiO$_2$/rGO nanocatalyst	89.9	[11]
	CuS/BSC heterojunction system	> 95%	[68]

4.4. Conclusions

In the present study, a novel SWAC/ZrO$_2$-ZnO nanocomposite was developed by effectively immobilizing a ZrO$_2$-ZnO photocatalyst on SWAC using a hydrothermal technique. FTIR, XRD, TEM-SEAD, XPS, LC-MS, and PL instruments were used to characterize SWAC/ZrO$_2$-ZnO nanocomposite. The XRD analysis showed that the SWAC/ZrO$_2$-ZnO nanocomposite crystal size was found to be 39.41 nm. The LC-MS analysis revealed that the CPs molecule had been fragmented into smaller m/z ratios. The insecticide chlorpyrifos (100 ppm) was degraded (100 %) with a 0.05 g dose of SWAC/ZrO$_2$-ZnO nanocomposite under UV light irradiation for 50 mins at pH 6. SWAC/ZrO$_2$-ZnO nanocomposite photodegradation of CPs follows pseudo first-order kinetics. Density functional theory (DFT) simulations also revealed the formation of hydrogen bonding via O-linkage of the O-Zr-O bond with SWAC to form chemically reactive SWAC/ZrO$_2$-ZnO nanocomposite. Thus, the SWAC/ZrO$_2$-ZnO nanocomposite could serve as a promising photocatalyst for the degradation of chlorpyrifos from an aqueous solution.

References

[1] S. Das, T. K. Adhya, Degradation of chlorpyrifos in tropical rice soils, *J. Environ. Manage.*, 152 (**2015**) 36-42.

[2] Z. Chishti, S. Hussain, K. R. Arshad, A. Khalid, M. Arshad, Microbial degradation of chlorpyrifos in liquid media and soil, *J. Environ. Manage.*, 114 (**2013**) 372-380.

[3] Y. Samet, L. Agengui, R. Abdelhédi, Electrochemical degradation of chlorpyrifos pesticide in aqueous solutions by anodic oxidation at boron-doped diamond electrodes, *Chem. Eng. J.*, 161 (**2010**) 167-172.

[4] M. N. Mori, H. Oikawa, M. H. O. Sampa, C. L. Duarte, Degradation of chlorpyrifos by ionizing radiation, *J. Radioanal. Nucl. Chem.*, 270 (**2006**) 99-102.

[5] K. Maya, R. S. Singh, S.N. Upadhyay, S. K. Dubey, Kinetic analysis reveals bacterial efficacy for biodegradation of chlorpyrifos and its hydrolyzing metabolite TCP, *Process Biochem.*, 46 (**2011**) 2130-2136.

[6] M. M. Jacob, M. Ponnuchamy, A. Kapoor, P. Sivaraman, Journal of Environmental Chemical Engineering Bagasse based biochar for the adsorptive removal of chlorpyrifos from contaminated water, *J. Environ. Chem. Eng.*, 8 (**2020**) 103904.

[7] M. Samy, M. G. Ibrahim, M. Gar Alalm, M. Fujii, K. E. Diab, M. ElKady, Innovative photocatalytic reactor for the degradation of chlorpyrifos using a coated composite of ZrV_2O_7 and graphene nano-platelets, *Chem. Eng. J.*, 395 (**2020**) 124974.

[8] D. Pathania, A. Sharma, S. Kumar, A. Kumar, Bio-synthesized Cu-ZnO hetro-nanostructure for catalytic degradation of organophosphate chlorpyrifos under solar illumination, *Chemosphere*, 277 (**2021**) 130315.

[9] E. S. Agorku, A.T. Kuvarega, B. B. Mamba, A. C. Pandey, A. K. Mishra, Enhanced visible-light photocatalytic activity of multi-elements-doped ZrO_2 for degradation of indigo carmine, *J. Rare Earths*, 33 (**2015**) 498-506.

[10] E. D. Sherly, J. J. Vijaya, N. C. S. Selvam, L. J. Kennedy, Microwave assisted combustion synthesis of coupled ZnO-ZrO_2 nanoparticles and their role in the photocatalytic degradation of 2,4-dichlorophenol, *Ceram. Int.*, 40 (**2014**) 5681-5691.

[11] V. K. Gupta, D. Pathania, P. Singh, B. S. Rathore, P. Chauhan, Cellulose acetate-zirconium (IV) phosphate nano-composite with enhanced photo-catalytic activity, *Carbohydrate Polymers*, 95 (**2013**) 434-440.

[12] T. A. Saleh, M. A. Gondal, Q. A. Drmosh, Z. H. Yamani, A. AL-yamani, Enhancement in photocatalytic activity for acetaldehyde removal by embedding ZnO nano particles on multiwall carbon nanotubes, *Chem. Eng. J.*, 166 (**2011**) 407-412.

[13] O. Benton, S. Apollo, B. Naidoo, A. Ochieng, Photodegradation of molasses wastewater using TiO_2-ZnO nanohybrid photocatalyst supported on activated carbon, *Chem. Eng. Commun.*, 203 (**2016**) 1443-1454.

[14] H. Anwer, J. W. Park, Synthesis and characterization of a heterojunction rGO/ZrO$_2$/Ag$_3$PO4 nanocomposite for degradation of organic contaminants, *J. Hazard. Mater.*, 358 **(2018)** 416-426.

[15] A. I. Vaizoğullar, ZnO/ZrO$_2$ composites: synthesis characterization and photocatalytic performance in the degradation of oxytetracycline antibiotic, *Mater. Technol.*, 34 **(2019)** 433-443.

[16] H. Wu, C. Lin, P. Shen, Structure and dissolution of CaO-ZrO$_2$-TiO$_2$-Al$_2$O$_3$-B$_2$O$_3$-SiO$_3$ glass, *J. Non-Cryst. Solids*, 209 **(1997)** 76-86.

[17] P. Muthirulan, M. Meenakshisundararam, N. Kannan, Beneficial role of ZnO photocatalyst supported with porous activated carbon for the mineralization of alizarin cyanin green dye in aqueous solution, *J. Adv. Res.*, 4 **(2013)** 479-484.

[18] M. Zbair, Z. Anfar, H. A. Ahsaine, N. El Alem, M. Ezahri, Acridine orange adsorption by zinc oxide/almond shell activated carbon composite: Operational factors, mechanism and performance optimization using central composite design and surface modeling, *J. Environ. Manage.*, 206 **(2018)** 383-397.

[19] X. Chen, X. Xu, J. Cui, C. Chen, X. Zhu, D. Sun, J. Qian, Visible-light driven degradation of tetracycline hydrochloride and 2,4-dichlorophenol by film-like N-carbon@N-ZnO catalyst with three dimensional interconnected nanofibrous structure, *J. Hazard. Mater.*, 392 **(2020)** 122331.

[20] J. Matos, J. Laine, J. M. Herrmann, Effect of the type of activated carbons on the photocatalytic degradation of aqueous organic pollutants by UV-irradiated titania, *J. Catal.*, 200 **(2001)** 10-20.

[21] M. Baruah, S. L. Ezung, A. Supong, P. C. Bhomick, S. Kumar, D. Sinha, Synthesis, characterization of novel Fe-doped TiO$_2$ activated carbon nanocomposite towards photocatalytic degradation of congo red, E. coli, and S. aureus, *Korean J. Chem. Eng.*, 38 **(2021)** 1277-1290.

[22] D. Mohanta, M. Ahmaruzzaman. Bio-inspired adsorption of arsenite and fluoride from aqueous solutions using activated carbon@SnO$_2$ nanocomposites: isotherms, kinetics, thermodynamics, cost estimation and regeneration studies. *J. Environ. Chem. Eng.*, 6 **(2018)** 356-366.

[23] M. Baruah, A. Supong, P. Chandra, B. Rituparna, K. Chubaakum, Batch sorption - photodegradation of Alizarin Red S using synthesized-TiO$_2$/activated carbon nanocomposite: an experimental study and computer modelling, *Nanotechnol. Environ. Eng.*, 5 **(2020)** 1-13.

[24] T. N. V. de Souza, S. M. L. de Carvalho, M. G. A. Vieira, M. G. C. da Silva, D. D. S. B. Brasil, Adsorption of basic dyes onto activated carbon: Experimental and theoretical investigation of chemical reactivity of basic dyes using DFT-based descriptors, *Appl. Surf. Sci.*, 448 **(2018)** 662-670.

[25] H. Ullah, A. A. Tahir, T. K. Mallick, Polypyrrole/TiO$_2$ composites for the application of photocatalysis, *Sensors Actuators B: Chem.*, 241 (**2017**) 1161-1169.

[26] A. Supong, P. C. Bhomick, M. Baruah, C. Pongener, U. B. Sinha, D. Sinha, Adsorptive removal of Bisphenol A by biomass activated carbon and insights into the adsorption mechanism through density functional theory calculations, *Sustain. Chem. Pharm.*, 13 (**2019**) 100159.

[27] A. Shokufeh, Structural and antibacterial properties of ZrO$_2$@ZnO core-shell by sonosynthesis methods, *Res. J. Chem. Environ.*, 19 (**2015**) 28-32.

[28] P. C. C. Faria, J. J. M. Órfão, M. F. R. Pereira, Adsorption of anionic and cationic dyes on activated carbons with different surface chemistries, *Water Res.*, 38 (**2004**) 2043-2052.

[29] B. Padak, J. Wilcox, Understanding mercury binding on activated carbon, *Carbon*, 47 (**2009**) 2855-2864.

[30] L. R. Radovic, The mechanism of CO$_2$ chemisorption on zigzag carbon active sites: A computational chemistry study, *Carbon*, 43 (**2005**) 907-915.

[31] J. R. PliegoJr, S. M. Resende, E. Humeres, Chemisorption of SO$_2$ on graphite surface: A theoretical ab initio and ideal lattice gas model study. *Chemical Physics*, 314 (**2005**) 127-133.

[32] S.L. Ezung, M. Baruah, A. Supong, S. Sharma, D. Sinha, Experimental and theoretical insight into the adsorption of 2,4-dichlorophenol on low-cost bamboo sheath activated carbon, *Sustain. Chem. Pharm.*, 26 (**2022**) 100643.

[33] S. Kumar, S. Sharma, R. Karmaker, D. Sinha, DFT study on the structural, optical and electronic properties of platinum group doped graphene, *Mater. Today Commun.*, 26 (**2021**) 101755.

[34] G. Q. Blantocas, A. S. Alaboodi, A. baset H. Mekky, Synthesis of Chitosan-TiO$_2$ Antimicrobial Composites via a 2-Step Process of Electrospinning and Plasma Sputtering, *Arab. J. Sci. Eng.*, 43 (**2018**) 389-398.

[35] A. Bendjeddou, T. Abbaz, A. Gouasmia, D. Villemin, Molecular structure, HOMO-LUMO, MEP and Fukui function analysis of some TTF-donor substituted molecules using DFT (B3LYP) calculations, *Int. Res. J. Pure Appl. Chem.*, 12 (**2016**) 1-9.

[36] A. Bendjeddou, T. Abbaz, A. Gouasmia, D. Villemin, Quantum chemical studies on molecular structure and reactivity descriptors of some p-nitrophenyl tetrathiafulvalenes by density functional theory (DFT), *Acta Chim. Pharm. Indica.*, 6 (**2016**) 32-44.

[37] S. Pratihar, S. Roy, Nucleophilicity and Site Selectivity of Commonly Used Arenes and Heteroarenes, *J. Org. Chem.*, 75 (**2010**) 4957-4963.

[38] A. Supong, P.C. Bhomick, U. B. Sinha, D. Sinha, A combined experimental and theoretical investigation of the adsorption of 4-Nitrophenol on activated biocarbon using DFT method, *Korean J. Chem. Eng.*, 36 (**2019**) 2023-2034.

[39] D. Angin, Production and characterization of activated carbon from sour cherry stones by zinc chloride, *Fuel*, 115 (**2014**) 804-811.

[40] M. M. Ibrahim, Photocatalytic activity of nanostructured ZnO-ZrO$_2$ binary oxide using fluorometric method, *Spectrochim. Acta A Mol. Biomol. Spectrosc*.,145 (**2015**) 487-492.

[41] M. Obaidullah, T. Furusawa, I. A. Siddiquey, N. M. Bahadur, M. Sato, N. Suzuki, A fast and facile microwave irradiation method for the synthesis of ZnO@ZrO$_2$ core-shell nanocomposites and the investigation of their optical properties, *Adv. Powder Technol.*, 29 (**2018**) 1804-1811.

[42] N. Nasseh, F. S. Arghavan, S. Rodriguez-Couto, A. H. Panahi, M. Esmati, T. J. A-Musawi, Preparation of activated carbon@ZnO composite and its application as a novel catalyst in catalytic ozonation process for metronidazole degradation, *Adv. Powder Technol.*, 31 (**2020**) 875-885.

[43] L. Gao and Y. Wei, Fabrication of a novel hydrophobic/ion-exchange mixed-mode adsorbent for the dispersive solid-phase extraction of chlorophenols from environmental water samples, Journal of Separation Science J. Sep. Sci. 39 (2016) 1-9.

[44] S. Joshi, B. P. Pokharel, Preparation and characterization of activated carbon from Lapsi (Choerospondias axillaris) seed stone by chemical activation with potassium hydroxide, *J. Inst. Eng. India Ser. D.*, 9 (**2013**) 79-88.

[45] X. Liu, C. He, X. Yu, Y. Bai, L. Ye, B. Wang, L. Zhang, Net-like porous activated carbon materials from shrimp shell by solution-processed carbonization and H$_3$PO$_4$ activation for methylene blue adsorption, *Powder Technol*., 326 (**2018**) 181-189.

[46] I. I. Gurten, M. Ozmak, E. Yagmur and Z. Aktas, Preparation and characterisation of activated carbon from waste tea using K$_2$CO$_3$ *Biomass Bioenergy*, 37 (**2012**) 73-81.

[47] A. Allwar, Characteristics of Pore Structures and Surface Chemistry of Activated Carbons by Physisorption, Ftir and Boehm Methods, *J. Appl. Chem.*, 2 (**2012**) 2278-5736.

[48] D. Krishnaiah, C. G. Joseph, S. M. Anisuzzaman, W. M. A. W. Daud, M. Sundang, Y. C. Leow, Removal of chlorinated phenol from aqueous solution utilizing activated carbon derived from papaya (Carica Papaya) seeds, Korean J. Chem. Eng., 34 (**2017**) 1377-1384.

[49] P. C. Bhomick, A. Supong, M. Baruah, C. Pongener, Pine Cone biomass as an efficient precursor for the synthesis of activated biocarbon for adsorption of anionic dye from aqueous solution: isotherm, kinetic, thermodynamic and regeneration studies, *Sustain. Chem. Pharm*., 10 (**2018**) 41-49.

[50] A. Behbahani, S. Rowshanzamir, A. Esmaeilifar, Hydrothermal synthesis of zirconia nanoparticles from commercial zirconia, *Procedia Eng.*, 42 (**2012**) 908-917.

[51] O. Długosz, K. Szostak, M. Banach, Photocatalytic properties of zirconium oxide-zinc oxide nanoparticles synthesised using microwave irradiation, *Appl. Nanosci*., 10 (**2020**) 941-954.

[52] K. Mishra, S. H. Kim, Y. R. Lee, Band-gap Narrowing of Highly Stable Heterogeneous ZrO_2-ZnO Nanocomposites for the Reductive Amination of Carbonyl Compounds with HCO_2H/Et_3N, *ChemSusChem.*, 12 (**2019**) 881-889.

[53] S. B. Khan, K. A. Alamry, H. M. Marwani, A. M. Asiri, M. M. Rahman, Synthesis and environmental applications of cellulose/ZrO_2 nanohybrid as a selective adsorbent for nickel ion, *Compos. B. Eng.*, 50 (**2013**) 253-258.

[54] R. Shen, J. Xie, P. Guo, L. Chen, X. Chen, X. Li, Bridging the g-C_3N_4 nanosheets and robust cus cocatalysts by metallic acetylene black interface mediators for active and durable photocatalytic h_2 production, *ACS Appl. Energy Mater.*, 1 (**2018**) 2232-2241.

[55] M. Baruah, S. L. Ezung, S. Sharma, U. B. Sinha, D. Sinha, Synthesis and characterization of Ni-doped TiO_2 activated carbon nanocomposite for the photocatalytic degradation of anthracene, *Inorg. Chem. Commun.*, 144 (**2022**) 109905.

[56] R. Nekooie, T. Shamspur, A. Mostafavi, Novel CuO/TiO_2/PANI nanocomposite: Preparation and photocatalytic investigation for chlorpyrifos degradation in water under visible light irradiation, *J. Photochem. Photobiol. A Chem.*, 407 (**2021**) 113038.

[57] R. Mansourian, S. M. Mousavi, S. Alizadeh, S. Sabbaghi, CeO_2/TiO_2/SiO_2 nanocatalyst for the photocatalytic and sonophotocatalytic degradation of chlorpyrifos, *Can. J. Chem. Eng.*, 100 (**2022**) 451-464.

[58] M. M. Jacob, M. Ponnuchamy, A. Kapoor, P. Sivaraman, Bagasse based biochar for the adsorptive removal of chlorpyrifos from contaminated water, *J. Environ. Chem. Eng.*, 8 (**2020**) 103904.

[59] A. Saljooqi, T. Shamspur, A. Mostafavi, Synthesis and photocatalytic activity of porous ZnO stabilized by TiO_2 and Fe_3O_4 nanoparticles: investigation of pesticide degradation reaction in water treatment, *Environ. Sci. Pollut. Res.*, 28 (**2021**) 9146-9156.

[60] P. He, J. Wu, X. Jiang, W. Pan, J. Ren, Effect of SO_3 on elemental mercury adsorption on a carbonaceous surface, *Appl. Surf. Sci.*, 258 (**2012**) 8853-8860.

[61] C. A. Anyama, B. I. Ita, A. A. Ayi, H. Louis, E. E. D. Okon, J. O. Ogar, C. O. Oseghale Experimental and density functional theory studies on a zinc(ii) coordination polymer constructed with 1,3,5-benzenetricarboxylic acid and the derived nanocomposites from activated carbon, *ACS Omega*, 6 (**2021**) 28967–28982.

[62] E. E. Ekpenyong, H. Louis, C. A. Anyama, J. O. Ogar1, P. M. Utsu, A. A. Ayi, Experimental and density functional theory studies on the adsorption behaviour of selected gas molecules on Mg(II) co-ordination polymer constructed with 1,3,5-benzenetricarboxylates, *J. Mol. Struct.*, 1220 (**2020**) 128641.

[63] M. A. daiem, A. A. Alotaibi, E. M. Alosime, B. Zaidi, N. Said, Structural-property relationship in activated carbon synthesized from rice straw for electronic application, *Pol. J. Environ. Stud.*, 5 (**2020**) 3535-3547.

[64] T. S. Anirudhan, F. Shainy, V. C. Sekhar, V. S. Athira, Highly efficient photocatalytic degradation of chlorpyrifos in aqueous solutions by nano hydroxyapatite modified CFGO/ZnO nanorod composite, *J. Photochem. Photobiol. A Chem.*, 418 **(2021)** 113333.

[65] S. H. Khan, B. Pathak, M. H. Fulekar, Synthesis, characterization and photocatalytic degradation of chlorpyrifos by novel Fe:ZnO nanocomposite material, *Nanotechnol. Environ. Eng.*, 3 **(2018)** 1-14.

[66] D. Ayodhya, G. Veerabhadram, Fabrication of Schiff base coordinated ZnS nanoparticles for enhanced photocatalytic degradation of chlorpyrifos pesticide and detection of heavy metal ions, *J. Mater.*, 5 **(2019)** 446-454.

[67] P. S. Thind, D. Kumari, S. John, TiO_2/H_2O_2 mediated UV photocatalysis of chlorpyrifos: optimization of process parameters using response surface methodology, *J. Environ. Chem. Eng.*, 6 **(2018)** 3602-3609.

[68] D. Majhi, Y. P. Bhoi, P. K. Samal, B. G. Mishra, Morphology controlled synthesis and photocatalytic study of novel $CuSBi_2O_2CO_3$ heterojunction system for chlorpyrifos degradation under visible light illumination, *Appl. Surf. Sci.*, 455 **(2018)** 891-902.

CHAPTER 5

PHOTOCATALYTIC DEGRADATION OF CHLORPYRIFOS USING Fe-DOPED ZnO/ACTIVATED CARBON NANOCOMPOSITE

This chapter discusses the synthesis of Iron-Zinc dioxide nanocomposite supported on activated carbon. The nanocomposite was produced using a hydrothermal process, and its physicochemical characterization was carried out using several analytical methods such as Transmission Electron Microscope (TEM), X-Ray Diffractometer (XRD), Fourier Transform Infra-Red (FT-IR), Photoluminescence (PL), and UV-Visible Diffuse Reflectance Spectroscopy (DRS). The photocatalyst was utilised to degrade chlorpyrifos (CPs) from an aqueous solution using visible light irradiation. The degrading performance of the catalyst was investigated by different catalyst doses, CPs concentrations and light irradiation time, and pH of the solution. The degradation products were examined using LC-MS. The effect of various interfering ions on photocatalytic degradation of CPs as well as the reusability of the nanocomposite were also studied.

5.1. Introduction

Over the last century, pesticides have played a pivotal role in increasing agricultural production and also used in urban households. This is because of their efficiency, affordability, and immediate toxicity [1]. However, it has been found that pesticides have negative impacts on species and can be harmful to human health [2-4]. For example, chlorpyrifos is an organophosphorus pesticide that is widely used to control insect and pest in various crops such as fruit, grain, vegetable, cotton as well as ornamental plants etc. The excessive use of chlorpyrifos can result in neurological disorders, growth abnormalities, brain cell replication, intracellular oxidative stress, and therefore interrupting normal cellular development and differentiation. Furthermore, exposure to chlorpyrifos during pregnancy may result in mental abnormalities in children. Pesticides containing chlorpyrifos are the most common pollutants in water sources, harming not only farmers but also spreading over long distances due to their prolonged durations [5,6]. As a result, removing chlorpyrifos from water systems is an urgent task [7]. Several techniques have been applied to remove chlorpyrifos pesticides from waste water. Among the different strategies available, photocatalysis has been found as the most effective and advantageous method for treating wastewater [8].

Semiconductor materials such as ZnS (Zinc sulfide), TiO_2 (Titanium dioxide), ZnO (Zinc oxide), WO_3 (Tungsten trioxide), CuO (Copper oxide), and ZrO_2 (Zirconium dioxide) are often used photocatalysts for the degradation of organic pollutants [9,10]. ZnO is well-known as one of the most cost-effective and ecologically friendly wide bandgap semiconductor materials with exceptional features, making it suitable for a wide range of applications such as organic pollutant photodegradation, optoelectronic devices, solar cells, and sensors [11-13]. However, only UV light which makes up around 5 % of the solar spectrum can activate ZnO. As a result, several efforts have been made to prepare ZnO photocatalyst that is active in visible light. It may be done by doping ZnO with anionic non-metals and transition metals. Among these, doping ZnO with transition metal cations has been suggested as a useful technique for improving photocatalytic properties of the catalyst under visible light. Numerous studies found that Fe doped ZnO nanocrystalline particles have superior photocatalytic activity than pure ZnO. It was assumed that Fe (III) cations could serve as shallow traps in the photocatalyst's lattice, reducing the rate at which electrons and holes recombined. The best photocatalytic activities might be obtained by doping iron at a very low level. In addition to its use as a photocatalyst, ZnO and its doped nanoparticles have also been considered as potential photocatalysts for degrading of organic pollutants [14,15]. Furthermore, difficulties with the

use of ZnO is aggregation in suspension, especially at high loadings, making it more difficult to separate and recover after use. Another drawback of ZnO particle is its photo instability in aqueous solution and high recombination rate of photogenerated electron-hole pairs, which significantly lowers the photocatalytic activity of pure photocatalysts [16,17]. Alumina, zeolite, silica gel, fibre optic cable, glass beads, quartz, stainless steels, clays, and activated carbon have all been studied as photocatalyst particle supports for these problems [18,19].

Activated carbon (AC) has been widely studied as a support for photocatalyst during photodegradation [20,21]. AC with a high adsorption capacity is desirable as an adsorbent support system for photocatalyst because it can readily absorb organic pollutant molecules close to the photocatalytic sites during the adsorption-degradation process [22]. Metal oxides nanoparticles with AC show an excellent adsorbent which provides a large number of active sites that can interact chemically with the adsorbents thereby enhancing chemisorption [23].

The purpose of this present work is to investigate the photodegradation of chlorpyrifos (insecticide) in aqueous solutions utilizing active Fe-ZnO nanoparticles as a catalyst supported by activated carbon under visible light.

5.2. Materials and methods

5.2.1. Materials

Zinc Oxide (ZnO), ferric nitrate hexahydrate (98 %), ammonia (25 %), and other chemicals such as HCl, NaOH, and KOH utilized in the present study were purchased from Sigma-Aldrich. Co., India. Tricel (20 % Chlorpyrifos) was purchased from Sumitomo Chemical India Ltd. The raw material *Schima wallichii* was used for this experiment was collected locally from Nagaland University, Lumami Campus (26°28'29" N, 94°50'58" E).

5.2.2. Synthesis of activated carbon

For the present study, *Schima wallichii* biomass were utilized for activated carbon preparation. The detailed preparation procedure and characterization of the activated carbon have already been discussed under section 4.2.2 of Chapter 4. The synthesized activated carbon is name as of *Schima wallichii* activated carbon (SWAC) for this study.

5.2.3. Synthesis of SWAC/Fe-ZnO nanocomposite

For the synthesis of SWAC/Fe-ZnO nanocomposite, 0.15 g of ZnO nanoparticle was slowly added to 1 g of 100 mL ferric nitrate solution and the solution was simultaneously stirred for 30 minutes. Thereafter, 0.3 g of the as-prepared SWAC was poured slowly into the above

mixture and the obtained solution was ultrasonicated for 1 h. Later, the sonicated mixture was shifted into a hydrothermal autoclave and kept at 150 ºC inside the oven for 24 h. After the hydrothermal treatment, the solution was washed appropriately with double refined water using a centrifuge machine so that the solution pH becomes neutral and finally the solution was dried at 65 ºC for 12 h. The schematic representation for preparation of activated Carbon/Fe-ZnO nanocomposite is shown in the Figure 5.1.
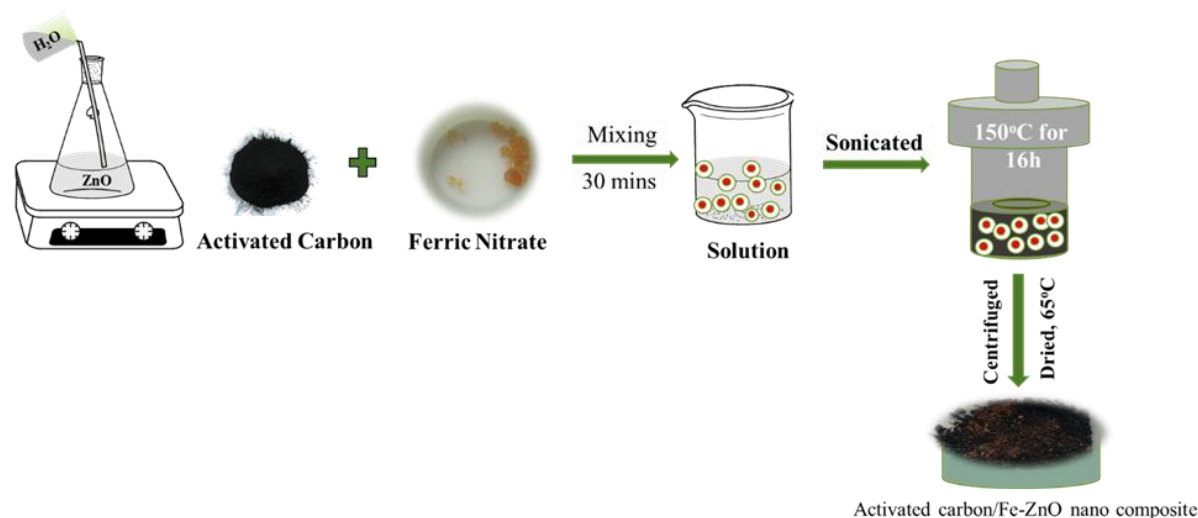

Figure 5.1. Schematic representation of the SWAC/Fe-ZnO nanocomposite preparation process.

5.2.4. Characterization of SWAC/Fe-ZnO nanocomposite

The synthesized SWAC/Fe-ZnO nanocomposite was characterized by several analytical techniques. The functional groups present on the SWAC/Fe-ZnO nanocomposite were identified using Fourier Transform Infra-Red (FT-IR) Spectrometer (Model: Spectrum Two, Made: Perkin Elmer). The crystalline phase of the SWAC/Fe-ZnO nanocomposite was obtained using an X-Ray Diffractometer (Make: Rigaku Model: Smartlab, Japan). The shape and size distribution of the samples were studied by Transmission Electron Microscopy (TEM) (Model: JEM-2100, Made: JEOL, JAPAN). A UV-Visible Diffuse Reflectance Spectrophotometer (Shimadzu UV-2600) was used to measure the bandgap energy of the SWAC/Fe-ZnO nanocomposite. Photoluminescence spectrophotometer (Horiba Fluoromax-4CP spectrofluorometer, 150 W Xenon Lamp) was used to obtain the Photoluminescence (PL) spectra. BET Surface Area Analyzer (Model: AutosorbiQ MP-AG (2 STAT) Anton Paar) was used to investigated the total surface area and total pore volume by N_2 adsorption/desorption

isotherm studies. The pore size distribution of the sample was obtained based on Barrett-Joyner-Halenda (BJH) model. The batch equilibrium method was used to determine the zero point charge (pH_{zpc}) of the nanocomposite sample [24] and the method has been described in Chapter 2 section 2.4.10.

5.2.5. Photocatalytic degradation experiment

The photocatalytic reaction of chlorpyrifos (CPs) was carried out in a photocatalytic reactor consisting of a black box (dimension: $63 \times 44 \times 44$ cm). A 250 mL Pyrex glass jar holding 50 mL of chlorpyrifos solution was placed above a magnetic stirrer, and an amount of SWAC/Fe-ZnO nanocomposite was mixed with the solution at the bottom of the reactor. A visible lamp with a maximum wavelength of 520 nm (High-pressure mercury lamp, 350 W) was placed at the top of the reactor, 10 cm away from the reaction mixture. The photocatalytic process was initiated by the use of visible radiation, which reached the SWAC/Fe-ZnO nanocomposite photocatalyst via the chlorpyriphos solution. A steady flow of water inside the reaction scheme was used to keep the reactor temperature at 25 °C. In addition, an exhaust fan was installed within the reactor to provide continuous air circulation.

For the degradation of CPs, a stock solution of 1000 ppm was first prepared by dissolving 1 g (5 mL of 20 % of chlorpyrifos) of CPs in 1000 mL double-distilled water. Furthermore, the required concentration was achieved by the dilution of stock solution to various concentrations 150 ppm, 200 ppm, and 250 ppm. For this study, SWAC/Fe-ZnO nanocomposite was mixed in a 50 mL CPs solution of varying concentrations (150, 200 and 250 ppm) by vigorously stirring the reaction mixture without exposure to light till 30 minutes so that adsorption-desorption equilibrium could be established within the reaction system. After equilibrium was established, the concentration of the dye was measured and this was taken as the initial concentration so that the adsorption of CPs due to the nanocomposite does not hinder the study of the overall photocatalytic effect. Then, the final concentration of the CPs solution was determined using a UV-Vis spectrophotometer at λ_{max} of 221 nm and the measurement of the test solution was withdrawn after every 10 minutes. The CPs degradation percentage (R%) was calculated by equation given below.

$$R\% = \frac{C_o - C_e}{C_o} \times 100 \hspace{4cm} (5.1)$$

where C_o and C_e are the concentrations of CPs before and after the photocatalytic treatment.

5.3. Results and discussions

5.3.1. Characterization of the synthesized Fe-ZnO /AC nanocomposite

The FT-IR spectra of SWAC/Fe-ZnO nanocomposite is shown in Figure 5.2. The existence of aromatic C-H stretch vibration might explain the peaks at 3127 cm^{-1} [25]. C-O stretching in phenol, alcohol, carboxylic acid, ester or ester group derivatives was ascribed to the transmittance at 1090 cm^{-1} [26]. The aromatic C=C is responsible for the peak at 1526 cm^{-1} [27]. The formation of the Fe-ZnO nanocomposite material is indicated by the peak obtained between 540 and 600 cm^{-1} [28]. The peaks at 568 cm^{-1} and 479 cm^{-1} correspond to the stretching vibrations of Fe-O and Zn-O, respectively [29,30].
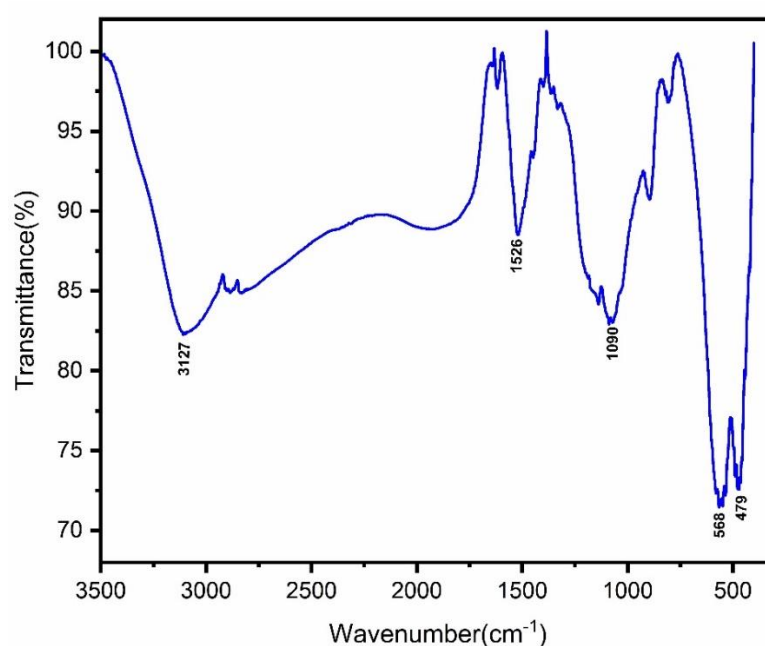
Figure 5.2. FT-IR spectrum of SWAC/Fe-ZnO nanocomposite.

The XRD patterns was used for detecting the crystalline phase of SWAC/Fe-ZnO nanocomposite (Figure 5.3). The intensity crystalline peak at 2θ= 26.5° corresponds to (1 0 0) planes of hexagonal graphitized carbon (JCPDS card no. 00-008-0415) [31]. The diffraction peaks obtained at 2θ value of 30.24° (1 0 0), 33.06° (0 0 2), 35.64° (1 0 1), 40.84° (2 2 2), 53.94° (4 2 2), and 62.44° (1 0 3) are related to the hexagonal wurtzite crystal structure of pure ZnO [32]. The observed diffraction peaks are well matched with the published literature [33,34] and standard JCPDS card no. 01-075-1533. Despite the addition of Fe to ZnO, all observed peaks were almost similar to pure ZnO, indicating that Fe-doping caused no structural

deformation in the ZnO lattice [35]. This demonstrates that Fe ions were successfully substituted in ZnO lattice sites. The crystallite sizes of the catalysts were calculated using Scherrer's formula, and the average crystal size was found to be 29.9 nm.
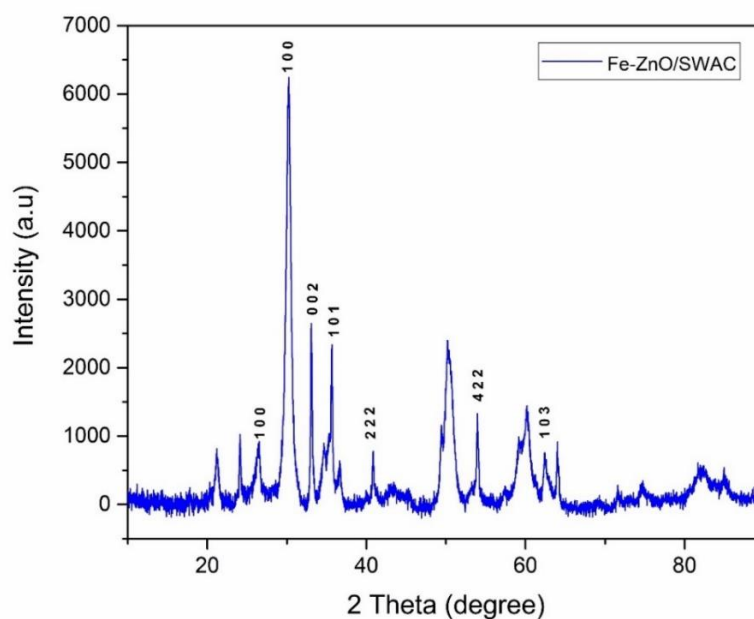

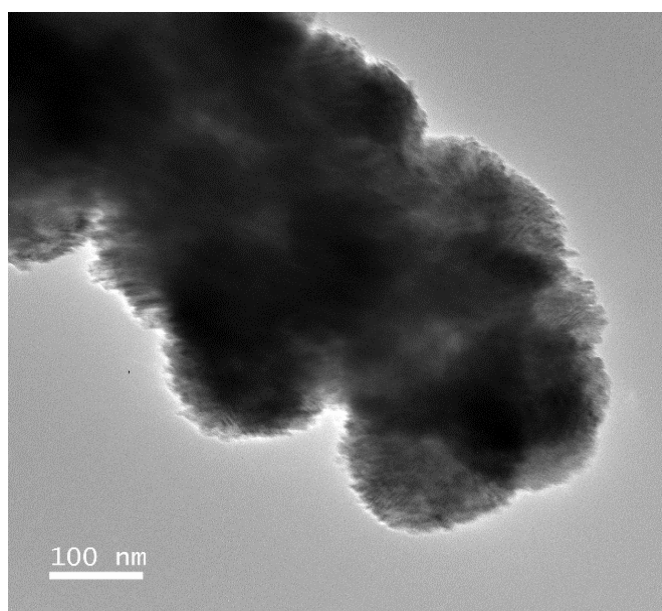**Figure 5.3.** XRD analysis of synthesized SWAC/Fe-ZnO nanocomposite.

Figure 5.4. Morphological (TEM) analysis of SWAC/Fe-ZnO nanocomposite.

Transmission Electron Microscope (TEM) was used to determine the morphology of SWAC/Fe-ZnO nanocomposite. The dark background in Figure 5.4 represents activated

carbon, and the light parts distributed on its surface are Fe-ZnO nanocomposite [36]. A nanorods like F-ZnO has a length ranging from 26 to 45 nm and diameters ranging from 1.9 to 10 nm were observed on the edges of activated carbon.

The optical band gap energy (E_g) of an SWAC/Fe-ZnO nanocomposite was determined using optical diffuse reflectance spectra (DRS). E_g value was calculated using the following Tauc's equation [37]:

$$\alpha h v = K \ (hv\text{-}E_g)^n \tag{5.2}$$

where E_g denotes optical bandgap, hv denotes photon energy, α denotes molar extinction coefficient, K is the proportionality constant, and n depends on the type of transition.

According to reported literature, the E_g value of ZnO is 3.2 eV [9,38] while the E_g values of the SWAC/Fe-ZnO nanocomposite is found to be 2.1 eV based on the Tauc plot curve shown in Figure 5.5. With the addition of Fe ions in the SWAC/Fe-ZnO nanocomposite, the E_g value of ZnO decreased from 3.2 to 2.1 eV which shifts the light absorption in the visible region.
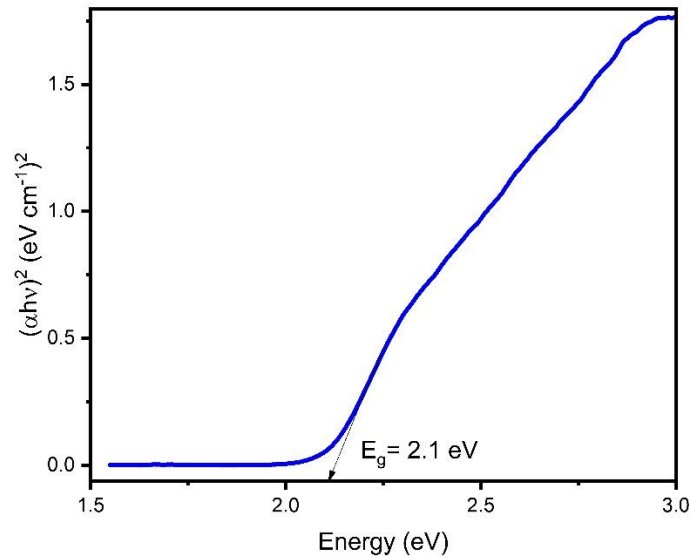
Figure 5.5. Tauc plot for calculating optical band gap of synthesized SWAC/Fe-ZnO nanocomposite.

Figure 5.6 shows Photoluminescence (PL) spectra of synthetic SWAC/Fe-ZnO nanocomposite and pure ZnO. Photoluminescence involves the recombination of electron hole pairs and the emission of photons. The intensity of photoluminescence and the effectiveness of electron hole recombination decrease as photocatalytic efficiency increases. As seen in Figure 5.6, ZnO has

the highest PL intensity, implying the highest rate of electron-hole recombination. Whereas the PL intensity decreases drastically after the SWAC/Fe-ZnO nanocomposite is formed, showing that the rate of electron-hole recombination is lowered. This suggest that the SWAC/Fe-ZnO nanocomposite has a higher photocatalytic efficiency as compared to ZnO.
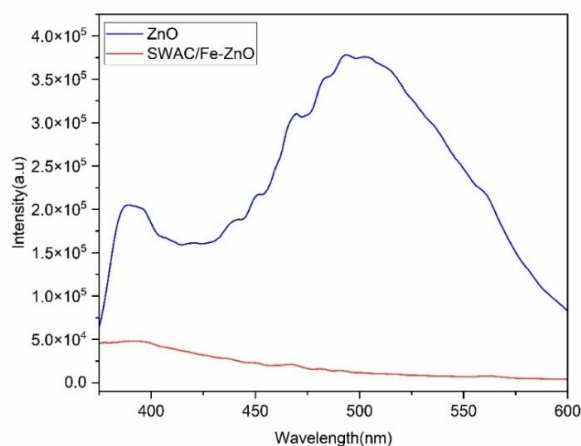
Figure 5.6. Photoluminescence analysis of synthesized SWAC/Fe-ZnO nanocomposite.

Figure 5.7 depicts the N_2 adsorption/desorption isotherm and pore-size distribution of the SWAC/Fe-ZnO. The isotherm is type IV, and the formation of a large number of mesopores in the SWAC/Fe-ZnO was demonstrated by the H4 type hysteresis loop, which occurs when mesopores fill and empty by capillary condensation at relative pressures p/p_o ranging from 0.4 to 1.0 [39]. The BET surface area of SWAC/Fe-ZnO is 3013.04 m^2g^{-1}, and the total pore volume is 2.18 cm^3g^{-1}. The pore size distributions of SWAC/Fe-ZnO were estimated and confirmed the presence of mesopores with pore diameters ranging from 2 to 50 nm.
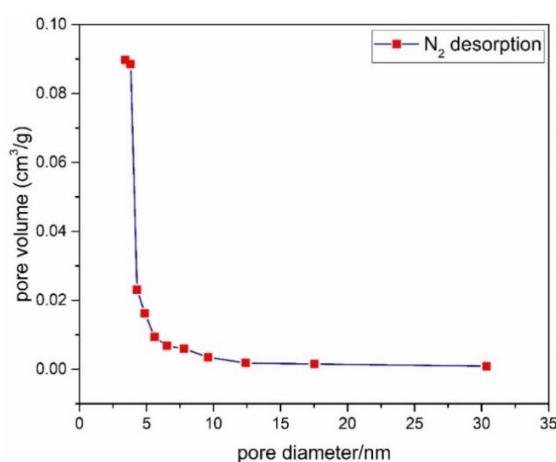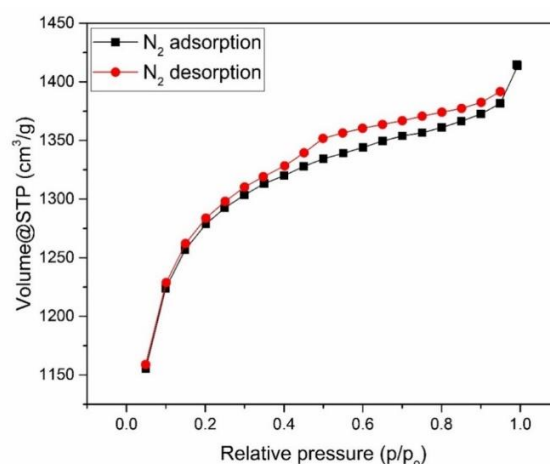
(a)   (b)

Figure 5.7. (a) Pore size distribution, (b) N$_2$ adsorption/desorption isotherm studies of SWAC/Fe-ZnO nanocomposite.

5.3.2. Photocatalytic Activity

5.3.2.1. Effect of SWAC/Fe-ZnO nanocomposite dosage

The photocatalytic activity of the SWAC/Fe-ZnO nanocomposite on the degradation of CPs solution was investigated using various nanocomposite doses (0.01- 0.10 g) for varied CPs solution concentrations (150, 200 and 250 ppm). It can be seen that for all the CPs concentration, the percentage of CPs degradation increased with increase the nanocomposite doses till 0.05 g (Figure 5.8). The highest percentage of degradation (96.4 %) was obtained for 150 ppm CPs concentration at the dose of 0.05 g SWAC/Fe-ZnO nanocomposite after 60 minutes of visible light irradiation.

For this outcome, there might be a number of possible reasons: (i) SWAC is added to the nanocomposite to improve its surface area, which enables more CPs molecules to assemble around the SWAC/Fe-ZnO nanocomposite; (ii) The addition of impurity Fe ions to the ZnO matrix causes a decrease in the recombination of electron-hole pairs. However, when the dosage exceeds 0.05 g, it acts as a recombination centre for the photogenerated electron-hole species, causing the nanocomposite's photocatalytic activity to decrease. One possible explanation is that as the nanocomposite dosage increases above a certain dose, visible light penetration through the reaction mixture decreases due to which less amount of nano catalyst gets excited and ultimately less electron/holes and hydroxyl radical were produced, resulting in decrease in CPs degradation efficiency [40]. Thus, for further studies, 0.05 g of the SWAC/Fe-ZnO nanocomposite dose was chosen to be the optimum dose for the CPs degrading process.
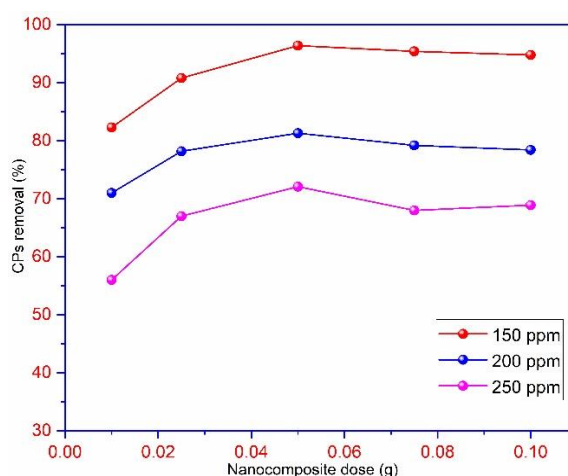
Figure 5.8. Effect of SWAC/Fe-ZnO nanocomposite loading in the degradation of CPs solution.

5.3.2.2. Effect of initial CPs concentration and light irradiation time

The effect of initial concentration on the rate of CPs degradation was investigated for different CPs concentrations (150, 200, and 250 ppm) at the optimal dosage of 0.05 g SWAC/Fe-ZnO nanocomposite and pH= 6). Figure 5.9 shows a graph of CPs removal percentage vs time. At 60 minutes, the maximum degradation of 96.08 % was recorded for a 150 ppm CPs solution. However, the removal percentage of CPs for 200 ppm and 250 ppm concentrations was decreased to 79.6 % and 69.9 %, respectively. Thus, for further studies, the optimum CPs concentration is chosen to be 150 ppm at contact time of 60 minutes.
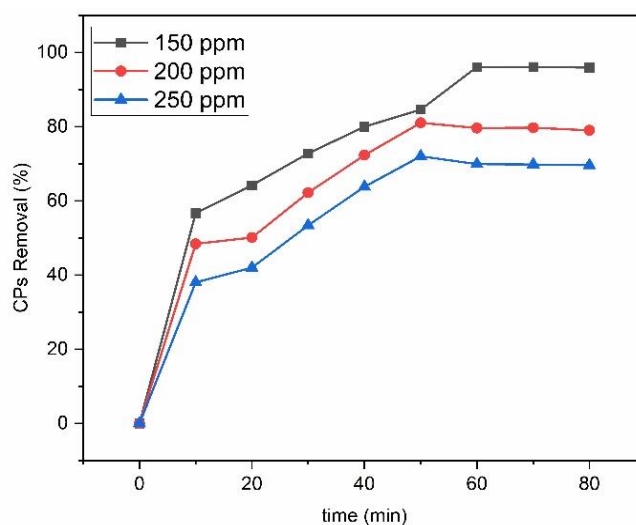
Figure 5.9. Effect of initial CPs concentration and light irradiation time in the degradation of CPs solution.

5.3.2.3. Effect of pH on CPs concentration

The pH of the solution plays an important role in the photocatalytic studies, as it controls the reaction during photodegradation and also affects the formation of hydroxyl radicals [41,42]. The effect of pH on the photocatalytic degradation of CPs was carried out at different pH ranges from 2 to 10 under optimum conditions (contact time = 60 min, CPs concentration = 150 ppm, and nanocomposite dosage = 0.05 g/L) shown in Figure 5.10. The pH of a solution alters the surface charge properties of the photocatalyst, which in turn affects the adsorption behaviour [43]. The pH_{zpc} (zero point charge) of SWAC/Fe-ZnO nanocomposite was determined to be

7.2, indicating that the surface of the SWAC/Fe-ZnO nanocomposite is negatively charged above this pH and positively charged below this pH.

The percentage of dye elimination increased with decreasing pH value and reached its maximum in acidic pH. At lower pH (pH<pH_{zpc}), the nanocomposite surface becomes positively charged, and hence has a higher electrostatic attraction affinity to interact with negatively charged CPs, resulting in maximum CPs degradation [44].
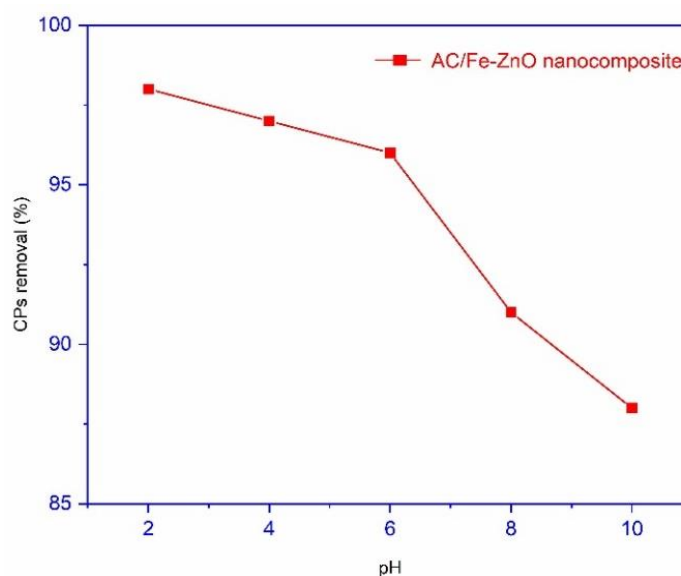
Figure 5.10. Effect of pH in the degradation of CPs solution.

5.3.3. LC-MS analysis of CPs degradation

To detect the degradation products after the photocatalytic process, LC-MS spectra (Make: INKAR, Model: Expression-S) was used. The spectra of the reaction mixture after 60 minutes of Visible light irradiation is shown in Figure 5.11. An attempt has been made to comprehend the degradation process in detail based on the observed components from mass spectra (Table 5.1). The decomposition of CPs proceeds in a manner similar to that described in the literature [45,46]. Figure 5.12 depicts a hypothetical mechanism for photodegradation through a free radical reaction.
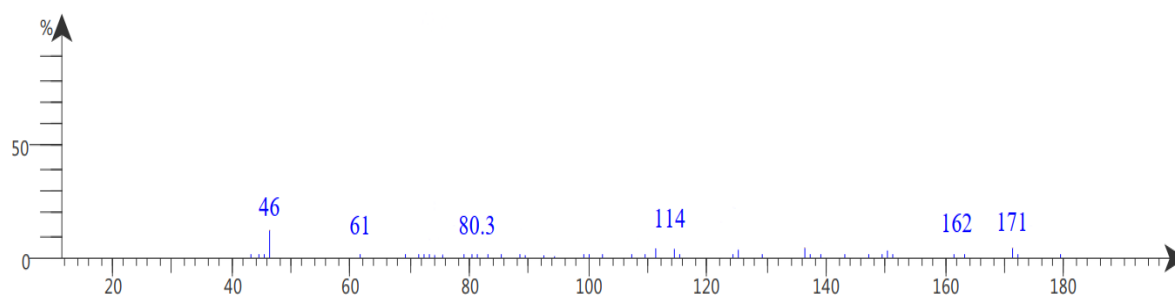
Figure 5.11. LC-MS spectra of the photocatalytic degradation products of chlorpyrifos.

Table 5.1. LC-MS analysis of photodegraded chlorpyrifos.

m/z value	Compound
350	O, O-diethyl O-(3,5,6-trichloropyridin-2-yl) phosphorothioate (M/Z of the Cps
171	O, O-diethyl O-hydrogen phosphorothioate
162	5,6-dichloropyridin-3-ol
114	Phosphorothioic O, O, O-acid
80.3	Pyridine
61	2-aminoethan-1-ol
46	Ethanol
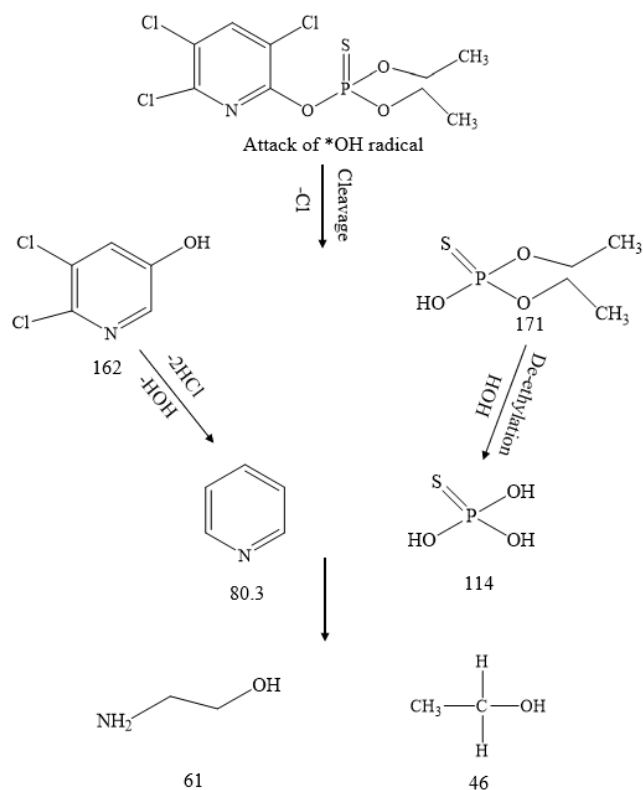
Figure 5.12. Schematic pathways for the degradation of chlorpyrifos.

5.3.4. Kinetic studies

The kinetic investigations were carried out under optimal circumstances, with 150 ppm CPs solutions (50 mL), pH at 2, irradiation time of 60 minutes, and 0.05 g of SWAC/Fe-ZnO nanocomposite. The photocatalytic performance of the CPs concentration was calculated using the Langmuir-Hinshelwood model [22]. The kinetic investigation was described using pseudo first-order rate and half-life period ($t_{1/2}$), for that the equations are given in Chapter 2 (equation 2.15 and equation 2.16.
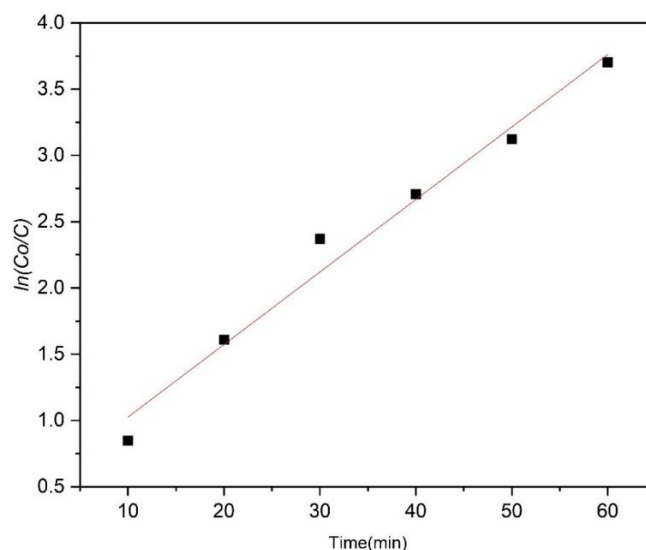
Figure 5.13. Pseudo first-order rate kinetic of CPs degradation loaded on SWAC/Fe- ZnO nanocomposite.

For the SWAC/Fe-ZnO nanocomposite, the linear plot of *ln (Co/C)* versus time exhibits a good correlation coefficient value ($R^2 = 0.97$), showing that the CPs degradation follows pseudo-first-order rate kinetics (Figure 5.13). Based on the slope of the curve, the photocatalytic rate constant (K_{ap}) value is found to be 0.055 min^{-1}, and $t_{1/2}$ is determined (using equation 2.16 of Chapter 2) to be 1.28 minutes.

5.3.5. Effect of radical scavengers on photocatalytic degradation of CPs

Photocatalytic activity is directly correlated with the type and quantity of reactive oxidation species generated by photogenerated electrons and holes. To further identify the main reactive oxidative species in the photocatalytic process for describing the photocatalytic mechanism, four scavengers were used to examine the reactive species in the photocatalytic reaction process. In this experiment, the scavengers used for hydroxyl radicals (*OH), holes (h$^+$), superoxide radicals (*O^{2-}), and electrons (e$^-$) were glycine, EDTA, BQ (p-benzoquinone), and CuSO$_4$. Figure 5.14 shows that the percentage elimination of CPs reduces from 98.0 % to 58.0 % (Glycine), 68.0 % (EDTA), 79.0 % (CuSO$_4$), and 62.0 % (BQ). The use of four different types of scavengers considerably affects the photodegradation effectiveness of the SWAC/Fe-ZnO nanocomposite, indicating the presence of active species like *O^{2-}, h$^+$, e$^-$, and *OH in the system. More interestingly, the promoting effect of these reactive oxidation species declines in the following order:

hydroxyl radical (*OH)> superoxide radical (*O^{2-})> hole (h$^+$) > electron (e$^-$)

134

Thus, from this result it can be clearly demonstrated that the presence of reactive oxidation species, $*OH$, h^+, e^-, and $*O^{2-}$, are greatly enhanced in the SWAC/Fe-ZnO nanocomposite.
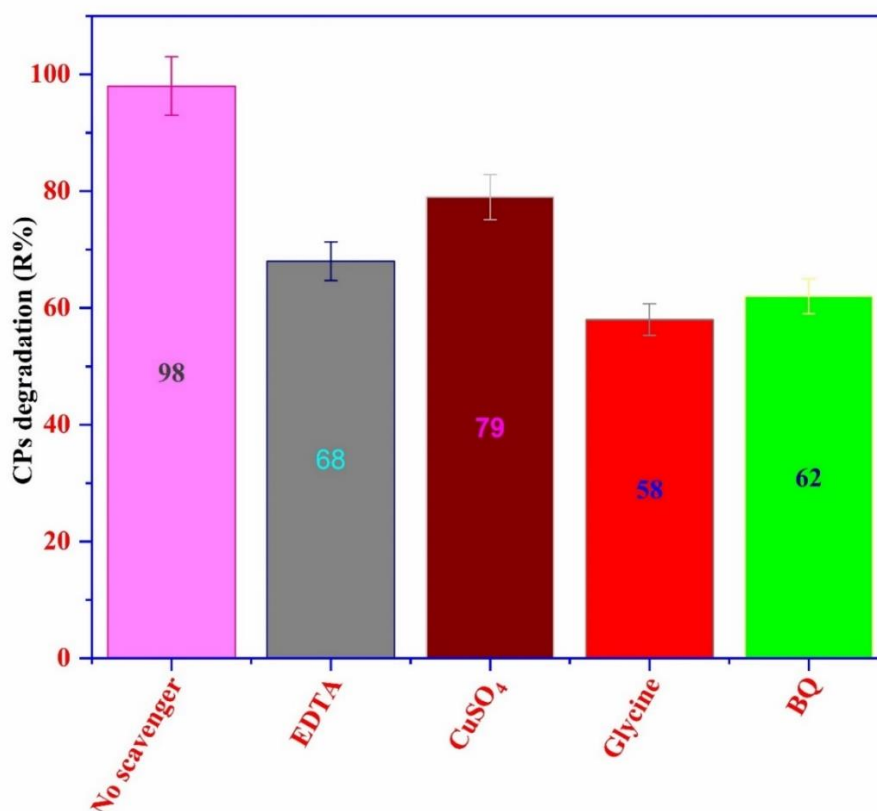
Figure 5.14. Photocatalytic degradation of CPs in the presence of different scavengers using SWAC/Fe-ZnO nanocomposite.

5.3.6. Nanocomposite reusability and photostability

The degrading efficiency of the SWAC/Fe-ZnO was investigated by recycling the catalyst for numerous cycles. To reuse catalyst, the nanocomposite residue was collected by centrifuging the solution after each photocatalytic reaction. After that, the nanocomposite was washed with double distilled water and dried in an oven. The dried catalyst was again used for photocatalytic CPs degradation (Figure 5.15). The rate of CPs degradation in the first cycle was 98 %; it then decreased to 91.6 % in the second cycle, 83.4 % in the third cycle, 78.5 % in the fourth cycle, and finally 71 % in the fifth cycle. This decrease in degradation efficiency might be due to a decrease in unoccupied adsorption sites on SWAC/Fe-ZnO nanocomposite for CPs adsorption in each cycle. In the sixth cycle, it was shown that the nanocomposite's degradation efficiency was around 62.7 %, signifying that even after several cycles of use, the SWAC/Fe-ZnO catalyst

was still showing a good catalytic activity. These results indicate that the regenerated SWAC/Fe-ZnO catalyst could be used for several times.
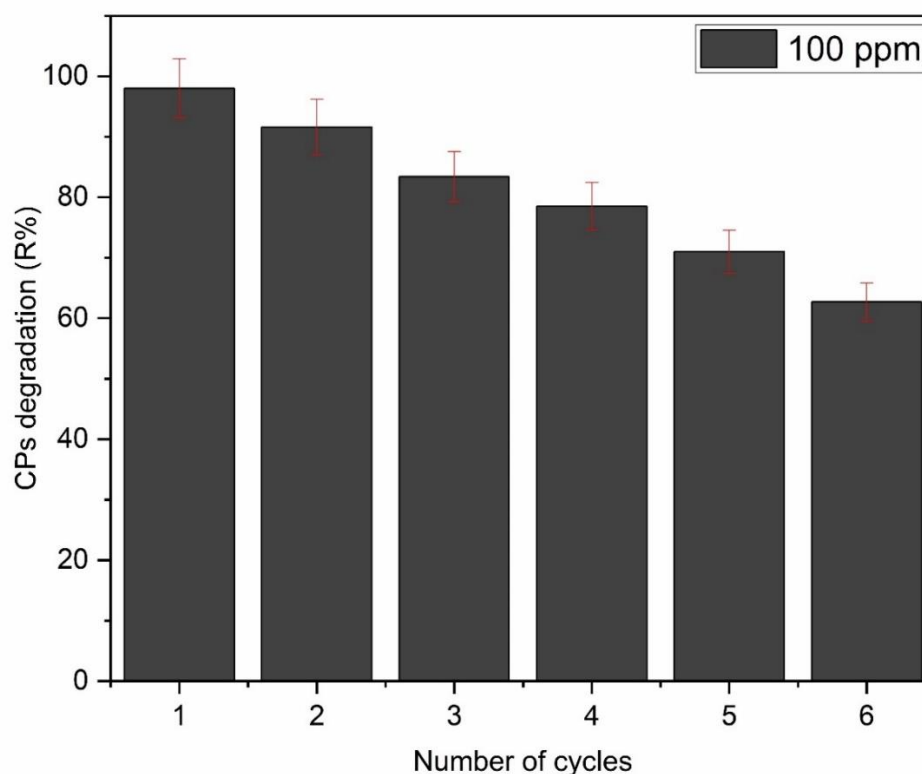
Figure 5.15. Chlorpyrifos degradation efficiency of SWAC/Fe-ZnO nanocomposite upto six cycles.

5.4. Conclusion

Fe-ZnO nanocomposite supported on activated carbon was synthesized using a hydrothermal method. The XRD analysis showed that the crystallite sizes of SWAC/Fe-ZnO nanocomposite was found to be 29.9 nm. BET Surface Area Analyzer was used to investigated the total surface area and total pore volume of SWAC/Fe-ZnO nanocomposite which was found to be 3013.04 m^2g^{-1} and 2.18 cm^3g^{-1}. From the UV-DRS spectra the band gap of Fe doped ZnO nanocomposite supported on activated carbon was found to be 2.1 eV. The SWAC/Fe-ZnO nanocomposite is effectively used for the removal of chlorpyrifos insecticide with a maximum degradation percentage of 98 % within 60 min for 150 ppm solution with 0.05 g of the catalyst. The photocatalytic degradation of chlorpyrifos followed the pseudo-first-order rate kinetics with an apparent rate constant of 0.055 min^{-1} and a half-life period of 1.26 min, according to the Langmuir-Hinshelwood model. The presence of interfering ions such as glycine, EDTA, copper

sulphate, and p-benzoquinone affects the degradation process of CPs by SWAC/Fe-ZnO nanocomposite, indicating that hydroxyl radicals are the dominant reactive species in the CPs degradation process. The SWAC/Fe-ZnO nanocomposite have excellent regeneration properties to be effective after the different cycle of use. Thus, SWAC/Fe-ZnO nanocomposite could serve as a promising photocatalyst for the degradation of chlorpyrifos from aqueous solution.

References

[1] M. S. Hossain, A. N. M. Fakhruddin, M. A. Z. Chowdhury, M. K. Alam, Degradation of chlorpyrifos, an organophosphorus insecticide in aqueous solution with gamma irradiation and natural sunlight, *J. Environ. Chem. Eng.*, 1 **(2013)** 270-274.

[2] S. Sharma, P. B. Singh, P. Chadha, H. S. Saini, Chlorpyrifos pollution: its effect on brain acetylcholinesterase activity in rat and treatment of polluted soil by indigenous Pseudomonas sp., *Environ. Sci. Pollut., Res.*, 24 **(2017)** 381-387.

[3] M. E. Yonar, Chlorpyrifos-induced biochemical changes in Cyprinus carpio: ameliorative effect of curcumin, *Ecotoxicol. Environ. Saf.*, 151 **(2018)** 49-54.

[4] H. Zheng, Q. Zhang, G. Liu, X. Luo, F. Li, Y. Zhang, Zhenyu Wang, Characteristics and mechanism of chloropyrifos and chlrpyrifos-methyl adsorption onto biochars: Influence of deashing and low molecular weight organic acid (LMWOA) aging co-existence, *Sci. Total Environ.*, 657 **(2019)** 953-962.

[5] A. A. Shorgoli, M. Shokri, Photocatalytic degradation of imidacloprid pesticide in aqueous solution by TiO_2 nanoparticles immobilized on the glass plate. *Chem. Eng. Commun.,* 204 **(2017)** 1061-1069.

[6] G. Rozsa, M. Nafradi, T. Alapi, K. Schrantz, L. Szabo, L. Wojnarovits, E. Takacs, A. Tungler, Photocatalytic, photolytic and radiolytic elimination of imidacloprid from aqueous solution: reaction mechanism, efficiency and economic considerations, *Appl. Catal. B Environ.,* 250 **(2019)** 429-439.

[7] K. A. Osman, A. Al-Humaid, K. Al-Redhaiman, R. A. El-Mergawi, Safety methods for chlorpyrifos removal from date fruits and its relation with sugars, phenolics and antioxidant capacity of fruits, *J. Food Sci. Technol.*, 51 **(2014)** 1762-1772.

[8] D. Pathania, A. Sharma, S. Kumar, A. Kumar, Bio-synthesized Cu-ZnO hetro-nanostructure for catalytic degradation of organophosphate chlorpyrifos under solar illumination, *Chemosphere*, 277 **(2021)** 130315.

[9] E. D. Sherly, J. J. Vijaya, N. C. S. Selvam, L. J. Kennedy, Microwave assisted combustion synthesis of coupled $ZnO-ZrO_2$ nanoparticles and their role in the photocatalytic degradation of 2,4-dichlorophenol, *Ceram. Int*., 40 **(2014)** 5681-5691.

[10] V. K. Gupta, D. Pathania, P. Singh, B. S. Rathore, P. Chauhan, Cellulose acetate-zirconium (IV) phosphate nano-composite with enhanced photo-catalytic activity, *Carbohydrate Polymers*, 95 **(2013)** 434-440.

[11] T. Khalafi, F. Buazar, K. Ghanemi, Phycosynthesis and enhanced photocatalytic activity of zinc oxide nanoparticles toward organosulfur pollutants. *Sci. Rep.*, 9 **(2019)** 6866-6876.

[12] J. Ai, C. Lin, W. Liao, C. Hu, T. Zhou, S. Luo, L. Cheng, Z. Chen, Y. Yang, Y. Zhang, W. Li, Shape-controlled synthesis of bare ZnO nanomaterials with improved photoactivity and photostability. *Mater. Sci. Technol*., 35 **(2019)** 336-348.

[13] C. Hariharan, Photocatalytic degradation of organic contaminants in water by ZnO nanoparticles: revisited, *Appl. Catal. A*, 304 (**2006**) 55-61.

[14] L. Sun, Y. Yao, L. Wang, Y. Mao, Z. Huang, D. Yao, W. Lu, W. Chen, Efficient removal of dyes using activated carbon fibers coupled with 8-hydroxyquinoline ferric as a reusable Fenton-like catalyst, *Chem Eng J.*, 240 (**2014**) 413-419.

[15] M. S. Haydar, Photodegradation of Alizarin Black S dye using zinc oxide. *J Environ Sci. Eng.*, 4 (**2015**) 395-400.

[16] S. S. Kumar, P. Venkateswarlu, V. R. Rao, G. N. Rao, Synthesis, characterization and optical properties of zinc oxide nanoparticles, *Int. Nano Lett.*, 3 (**2013**) 1-6.

[17] S. Mustapha, M. M. Ndamitso, A. S. Abdulkareem, J. O., Tijani, D. T. Shuaib, A. O. Ajala, A. K. Mohammed, Application of TiO_2 and ZnO nanoparticles immobilized on clay in wastewater treatment: a review, *Appl. Water Sci.*, 10 (**2020**) 1-36.

[18] A. Fernandez, G. Lassaletta, V. M. Jimenez, A. Justo, A. R. Gonzalez-Elipe, J. M. Herrmann, Preparation and characterization of TiO_2 photocatalysts supported on various rigid supports (glass, quartz and stainless steel): comparative studies of photocatalytic activity in water purification, *Appl. Catal. B*, 7 (**1995**) 49-63.

[19] X. Chen, S. S. Mao, Titanium dioxide nanomaterials: synthesis, properties, modifications, and applications, *Chem. Rev.*, 107 (**2007**) 2891-959.

[20] W. Zhou, P. Zhang, W. Liu, Anatase TiO_2 nanospindle/activated carbon (AC) composite photocatalysts with enhanced activity in removal of organic contaminant, *Int. J. Photoenergy*, 2012 (**2012**) 28-30.

[21] A. Subramani, K. Byrappa, S. Ananda, R. K. Lokanatha, M. Yoshimura, Photocatalytic degradation of indigo carmine dye using TiO_2 impregnated activated carbon, *Bull. Mater. Sci.*, 30 (**2007**) 37-41.

[22] M. Baruah, S. L. Ezung, A. Supong, P. C. Bhomick, S. Kumar, D. Sinha, Synthesis, characterization of novel Fe-doped TiO_2 activated carbon nanocomposite towards photocatalytic degradation of Congo red, *E. coli*, and *S. aureus*, *Korean J. Chem. Eng.*, 38 (**2021**) 1277-1290.

[23] D. Mohanta, Biosorption of arsenite and fluoride from aqueous solutions using activated carbon@SnO_2 nanocomposites: isotherms, kinetics, thermodynamics, cost estimation and regeneration studies, *J. Environ. Chem. Eng.*, 6 (**2018**) 356-366.

[24] B. M. Babic, S. K. Milonjic, M. J. Polovina, B. V. Kaludierovic, Point of zero charge and intrinsic equilibrium constants of activated carbon cloth, *Carbon N. Y.*, 37 (**1999**) 477-481.

[25] W. Zou, L. Gong, J. Huang, Z. Zhang, C. Sun, H. Zeng, Adsorption of hydrophobically modified polyacrylamide P(AM-NaAAC$_{16}$DMAAC) on model coal and clay surfaces and the effect on selective flocculation of fine coal, *Miner. Eng.*, 142 (**2019**) 105887.

[26] D. Shao, Q. Wei, Microwave-assisted rapid preparation of nano-ZnO/Ag composite functionalized polyester nonwoven membrane for improving its UV shielding and antibacterial Properties, *Materials*, 11 (**2018**) 1412.

[27] S. Joshi, B. P. Pokharel, preparation and characterization of activated carbon from Lapsi (Choerospondias axillaris) seed stone by chemical activation with potassium hydroxide, *J. Inst. Eng.*, 9 (**2013**) 79-88.

[28] S. H. Khan, B. Pathak, M. H. Fulekar, Synthesis, characterization and photocatalytic degradation of chlorpyrifos by novel Fe:ZnO nanocomposite material, *Nanotechnol. Environ. Eng.*, 3 (**2018**) 1-14.

[29] Y. Lei, J. Ding, P. Yu, G. He, Y. Chen, H. Chen, Low-temperature preparation of magnetically separable Fe$_3$O$_4$@ZnORGO for high-performance removal of methylene blue in visible light, *J. Alloys Compd.*, 821 (**2020**) 153366.

[30] M. Ma, Y. Zhang, W. Yu, H. Shen, H. Zhang, N. Gu, Preparation and characterization of magnetite nanoparticles coated by amino silane, *Colloids and Surfaces A: Physicochem. Eng. Aspects*, 212 (**2003**) 219-226.

[31] V. R. Posa, V. Annavaram, J. R. Koduru, V. R. Ammireddy, and A. R. Somala, Graphene-ZnO nanocomposite for highly efficient photocatalytic degradation of methyl orange dye under solar light irradiation, *Korean J. Chem. Eng.*, 33 (**2016**) 456-464.

[32] S. Lam, J. Sin, H. Zeng, H. Lin, H. Li, Y. Chai, M. Choong, A. R. Mohamed, Green synthesis of Fe-ZnO nanoparticles with improved sunlight photocatalytic performance for polyethylene film deterioration and bacterial inactivation *Mater. Sci. Semicond. Process.*, 123 (**2021**) 105574.

[33] A. Najafidoust, E. A. Asl, H. K. Hakki, M. Sarani, H. Bananifard, M. Sillanpaa, M. Etemadi, Sequential impregnation and sol-gel synthesis of Fe-ZnO over hydrophobic silica aerogel as a floating photocatalyst with highly enhanced photodecomposition of BTX compounds from water, *Solar Energy*, 225 (**2021**) 344-356.

[34] H. R. Mardani, M. Forouzani, M. Ziari, P. Biparva, Visible light photo-degradation of methylene blue over Fe or Cu promoted ZnO nanoparticles, *Spectrochim. Acta A Mol. Biomol. Spectrosc.*, 141 (**2015**) 27-33.

[35] T. Srinivasulu, K. Saritha, K. T. Ramakrishna Reddy, Synthesis and characterization of Fe-doped ZnO thin films deposited by chemical spray pyrolysis, *Mod. Electron. Mater.*, 3 (**2017**) 76-85.

[36] S. K. Mohamed, S. H. Hegazya, N. A. Abdelwahab, A. M. Ramadan, coupled adsorption-photocatalytic degradation of crystal violet under sunlight using chemically synthesized grafted sodium alginate/ZnO/graphene oxide composite, *Int. J. Biol. Macromol.*, 108 (**2018**) 1185-1198.

[37] P. R. Chowdhury, K. G. Bhattacharyya, Synthesis and characterization of Mn/Co/Ti LDH and its utilization as a photocatalyst in visible light assisted degradation of aqueous Rhodamine B, *RSC Adv.*, 6 **(2016)** 112016-112034.

[38] G. Chaitanya Lakshmi, S. Ananda, R. Somashekar, C. Ranganathaiah, Synthesis of ZnO/ZrO$_2$ nanocomposites by electrochemical method and photocatalytic degradation of fast green dye, paper dyeing and printing press effluent, *Int. J. Mater. Adv. Mater. Sci.*, 3 **(2012)** 221-237.

[39] M. Zbair, Z. Anfar, H. A. Ahsaine, N. El Alem, M. Ezahri, Acridine orange adsorption by zinc oxide/almond shell activated carbon composite: operational factors, mechanism and performance optimization using central composite design and surface modeling, *J. Environ. Manage.*, 206 **(2018)** 383-397.

[40] K. A. Isai, V. S. Shrivastava, Photocatalytic degradation of methylene blue using ZnO and 2 % Fe–ZnO semiconductor nanomaterials synthesized by sol-gel method: a comparative study, *SN Applied Sciences*, 1 **(2019)** 1247.

[41] M. Shanthi, V. Kuzhalosai, Photocatalytic degradation of an azo dye, Acid Red 27, in aqueous solution using nano ZnO, *Ind. J. Chem.*, 51 **(2012)** 428-434.

[42] S. Mohammadzadeh, M. E. Olya, A. M. Arabi, A. Shariati, N. M. R. Khosravi, Synthesis, characterization and application of ZnO-Ag as a nanophotocatalyst for organic compounds degradation, mechanism and economic study. *J. Environ. Sci.*, 35 **(2015)** 194-207.

[43] M. O. Fatehah, H. A. Aziz, S. Stoll, Stability of ZnO nanoparticles in solution, influence of pH, dissolution, aggregation and disaggregation effects. *J. Coll. Sci. Biotechnol.*, 3 **(2014)** 75-84.

[44] Z. Ghasemi, H. Younesi, A. A. Zinatizadeh, Kinetics and thermodynamics of photocatalytic degradation of organic pollutants in petroleum refinery wastewater over nano-TiO$_2$ supported on Fe-ZSM-5, *J. Taiwan Inst. Chem. Eng.*, 65 **(2016)** 357-366.

[45] D. Sud, P. Kaur, Heterogeneous photocatalytic degradation of selected organophosphate pesticides: a review, *Crit. Rev. Environ. Sci. Technol.*, 42 **(2012)** 2365-2407.

[46] D. Vaya, P. K. Surolia, Semiconductor based photocatalytic degradation of pesticides: an overview, *Technol. Innov.*, 20 **(2020)** 101128.

CHAPTER 6

2,4,6-TRICHLOROPHENOL ADSORPTION USING ACTIVATED CARBON: A DFT ANALYSIS OF THE ROLE OF FUNCTIONAL GROUPS ON THE CARBONACEOUS SURFACE

This chapter deals with density functional theory (DFT) simulations to explore the adsorptive behaviors of various oxygen and nitrogen containing functional groups present on activated carbon surface towards 2,4,6-trichlorophenol (TCP) molecules. The adsorption energy, molecular electrostatic potential, frontier molecular orbitals, and dipole moment of various configurations were investigated. The outcomes showed that the presence of carboxyl functionalized activated carbon improves the adsorption of TCP compared to amine, amide, hydroxyl, and carbonyl groups. Furthermore, the adsorption capacity is decreased when multiple functional groups are present next to each other. The results suggest that introducing functional groups on its surface can increase the carbon molecule's dipole moment, thereby improving its polarity and adsorption ability.

6.1. Introduction

Chlorinated phenols are one of the most influential families of poisonous non-biodegradable chemicals, and contamination by these compounds is considered a serious environmental concern. The US Environmental Protection Agency (EPA) has designated chlorophenols as a priority pollutant because of their toxicity and harmful effects on human health and the environment [1,2]. Among the chlorinated phenols, 2,4,6-trichlorophenol (TCP) is one of the chlorophenolic pollutants commonly found in wastewater [3-5]. Numerous industrial activities, including the manufacturing of pesticides, pulp bleaching, water chlorination, and dyes and plastics, result in the generation of wastewater containing 2,4,6-trichlorophenol (TCP) [6-8]. The continued use of these compounds in numerous applications causes an increase in the level of a contaminant in soil and water, which has an adverse effect on public health [9]. According to reports, TCP has negative effects on the nervous system of humans, such as gastrointestinal, respiratory, and cardiovascular problems [1,10-12]. Consequently, TCP-contaminated wastewater should be thoroughly treated before being discharged into the environment. Therefore, developing an effective approach for removing TCP from wastewater becomes essential.

There are several approaches that can be used to remove TCP, such as advanced oxidation, adsorption, solvent extraction, and biological degradation [13,14]. Out of these, adsorption on the surface of activated carbon (AC) is one of the most successful and convenient ways of removing organic and inorganic pollutants from wastewater [15,16]. Some of the pollutants that can be removed by ACs include heavy metals, volatile organic compounds (VOCs), dyes, pesticides, phenols etc. [17-20]. The most attractive attributes of ACs are their large pore size, high surface area, and capacity to adsorb numerous contaminants at the same time [21,22]. The pore structure and surface area of the AC are responsible for the physical qualities, whereas the functionals on the AC surface are primarily responsible for the chemical characteristics [23]. The functional groups on the AC surface are either generated from biomass during carbonization or modified by chemical agents during the activation process. AC surfaces can be modified by oxidation or by adding nitrogen-containing groups to produce nitrogen and oxygen enriched carbons. Oxygenated functional groups were mostly generated to the surface of the AC during the activation process using KOH, NaOH, and H_2SO_4. Alternatively, nitrogen enriched AC can be produced from ammonia, urea, and melamine solution in ethyl alcohol etc. [24]. The surface chemical characteristic of AC is a key component that determines its adsorption ability. It is mainly influenced by the type and number of functional groups on the

surface of AC. The most common oxygen containing functional groups on the surface of carbon material are hydroxyl, carboxyl, and carbonyl [25,26]. There have been many experimental studies on the removal of TCP using AC. However, there have been relatively few investigations into the adsorption processes and their effects on oxygen and nitrogen functional groups on the surface of AC. Therefore, it is necessary to further focus on the detailed adsorption mechanism of TCP interacting with various oxygen and nitrogen containing functional groups of AC on the surface.

In current times, research based on theoretical DFT simulations is regarded as one of the most potent techniques for predicting interaction processes between adsorbates and adsorbents in surface science [27,28]. Several investigations using DFT models have been made to comprehend the adsorption processes of organic pollutants on AC surfaces. For example, DFT analysis of Congo red dye adsorption on functionalized and pristine graphene has been reported by Achour *et al.* [29]. The electronic and molecular characteristics of adsorbates using DFT calculations to understand the behavior of atrazine adsorption on AC were done by Vieira *et al.* [30]. DFT studies using hydrogen bond lengths and associated thermodynamic parameters were also used to investigate the affinity of various oxygen functional groups on AC [31]. DFT simulations performed by Jan *et al.* [32] to examined the adsorption of azo dye on AC with different functionals groups, i.e., $-CH_2$ or $-CH_3$, $-C=O$, $-OH$, $-C=C$, $-NO_2$, and $-SO_3$, as well as a greater degree of substituted aromatic rings (H-Ar) and defect sites. Their observation suggested that the azo dye was found to form four intermolecular hydrogen bonds (H-bonds) with AC: H-bond 1 (NO-HO), H-bond 2 (OH-OC), H-bond 3 (SO-H-Ar), and H-bond 4 (SO-H-Ar), respectively. Supong *et al.* [23,33] reported the interactions of Bisphenol A and 4-Nitrophenol with AC surfaces having different functional groups (-COOH, -CHO, and -OH) using DFT calculation. Their study also revealed that the AC surface containing the carboxylic group had the strongest interactions with the Bisphenol A and 4-Nitrophenol. According to Yin *et al.* [34], phenol adsorption on activated carbon decreases with an increase in the concentration of oxygen functional groups. The effect of functionalized activated carbon on the adsorptive interaction of 2,4-dinitrophenol and 2,4-dichlorophenol has been examined in our earlier investigations using DFT studies [35,36]. The impact of oxygen and nitrogen functional groups on the adsorption of phenol was also examined by Liu *et al.* [37]. They observed that the presence of pyridine and carboxyl groups had the highest affinity for adsorbing phenol. DFT-based calculations were used to assess the effect of nitrogen-containing surface groups on AC on the adsorption of β-hexachlorocyclohexane and chlordecone. Their results indicate that

the functionalized AC with nitrogen-containing surface groups can be exploited as potential candidates for β-hexachlorocyclohexane and chlordecone removal from acidic water [38].

Most of the studies reported are on adsorption due to the presence of either Oxygen or Nitrogen functional groups on the carbon surface. However, in an ideal situation, different types of functional groups exist on the activated carbon surface. Thus, an attempt has been made in this chapter to analyze the interacting behaviors of TCP adsorption on AC surfaces containing oxygen and nitrogen functional group of AC surfaces. The impact of five primary functionals (amine, amide, hydroxyl, carboxyl, and carbonyl) on the adsorption of TCP was investigated, along with several forms of interacting processes.

The innovative aspect of this work is the application of DFT simulations to analyze the interaction of TCP with pristine and functionalized AC. New information on the impact of several oxygenated and nitrogenated functional groups, including amine, amide, hydroxyl, carboxyl, and carbonyl, on TCP adsorption is presented. There have been several studies published on the adsorption of TCP on AC, but very few on the interaction mechanism. The current work thus provides a novel insight into the interaction between activated carbon surface and TCP through the formation of hydrogen bonds using DFT. The findings of this research may provide guidelines for designing activated carbon with particular properties. The schematic diagram of AC surface interaction with TCP molecule is shown in Figure 6.1
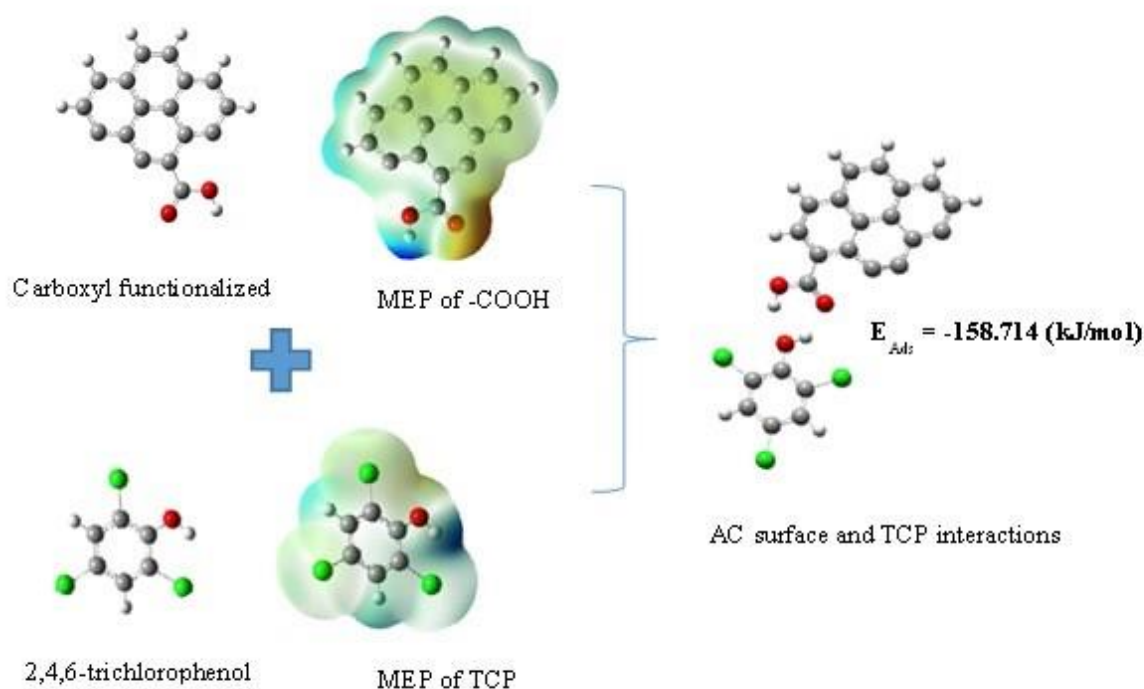

Figure 6.1. Schematic diagram of AC surface interaction with TCP molecule.

6.2. Materials and methods

In order to understand adsorption efficacy due to the presence of different functional groups on the carbon surface, a theoretical investigation employing the DFT method was conducted to study the chemical interactions between TCP and AC. In this study, the Gaussian 16 software package was used to carry out DFT simulations. The structure of the calculation model is optimized using B3LYP, which is commonly utilized in quantum chemical calculations. The chosen functional contained empirical dispersion components, which account for non-local interactions such as van der Waals interactions between adsorbate and surface. The convergence criterion was set to software defaults. The geometry optimization and single-point energy calculations were performed using the 6-31G (d,p) basis set for the H, C, N, O, and Cl atoms. This level of combination between B3LYP and 6-31G (d,p) has been recognized as an appropriate balance between accuracy and calculation time [17,39,40]. Each structure was generated using Gauss View 6 and was completely optimized to its electronic ground state. The following formula is used to calculate the absorption energy of the AC surface and TCP molecule.

$$E_{Ads} = E_{TCP+AC} - (E_{TCP} + E_{AC}) \tag{6.1}$$

where E_{Ads} is the adsorption energy, E_{TCP} is the total energy of TCP molecule, E_{AC} is the total energy of AC, and E_{TCP+AC} is the total energy of the TCP/AC combination in an equilibrium state. Stronger adsorption is correlated with a larger negative value of E_{Ads}. Normally, interactions are considered physisorption if E_{Ads} are less than -30 kJ/mol and chemisorption if E_{Ads} are greater than -50 kJ/mol. Generally, a higher negative value of adsorption energy implies easier adsorption [20,41].

A suitable structure for the AC surfaces must be constructed in order to examine any potential adsorption interactions between the surfaces of AC and the adsorbate TCP. According to reports, the structure of the carbon surfaces consists of clusters of graphite with 12-25 carbon atoms (3-7 carbon rings) [42-46]. Cluster models with four to seven fused benzene rings were also employed to simulate the surface of the activated carbon and it was found that the reactivity of active sites was significantly dependent on their local form rather than the size of the cluster [33,44,47]. Thus, an arm-chair model was employed in this study to simulate the activated carbon surface. This model consists of four fused benzene rings with unsaturated upper side carbon atoms representing the active site. The remaining carbon atoms on the lower side were

terminated with hydrogen atoms. This model, which had an active site-unsaturated carbon, was regarded as pristine activated carbon. The effect of oxygenated and nitrogenated functionals on the adsorption process was investigated by examining two nitrogen and three oxygen containing functional groups, namely amine, amide, hydroxyl, carboxyl, and carbonyl attached to the active site of the arm-chair model. All the activated carbon models are shown in Figure 6.2, together with the optimized structure of TCP. The models were termed pristine activated carbon (AC), amine-functionalized activated carbon (AC-NH$_2$), amide functionalized activated carbon (AC-CONH$_2$), hydroxyl functionalized activated carbon (AC-OH), carboxyl functionalized activated carbon (AC-COOH), and carbonyl functionalized activated carbon (AC-CHO) and multiple functionalized activated carbon (AC-(CHO+OH+COOH) and AC-(NH$_2$+CONH$_2$+COOH).

(a)   (b)   (c)

(d)   (e)   (f)
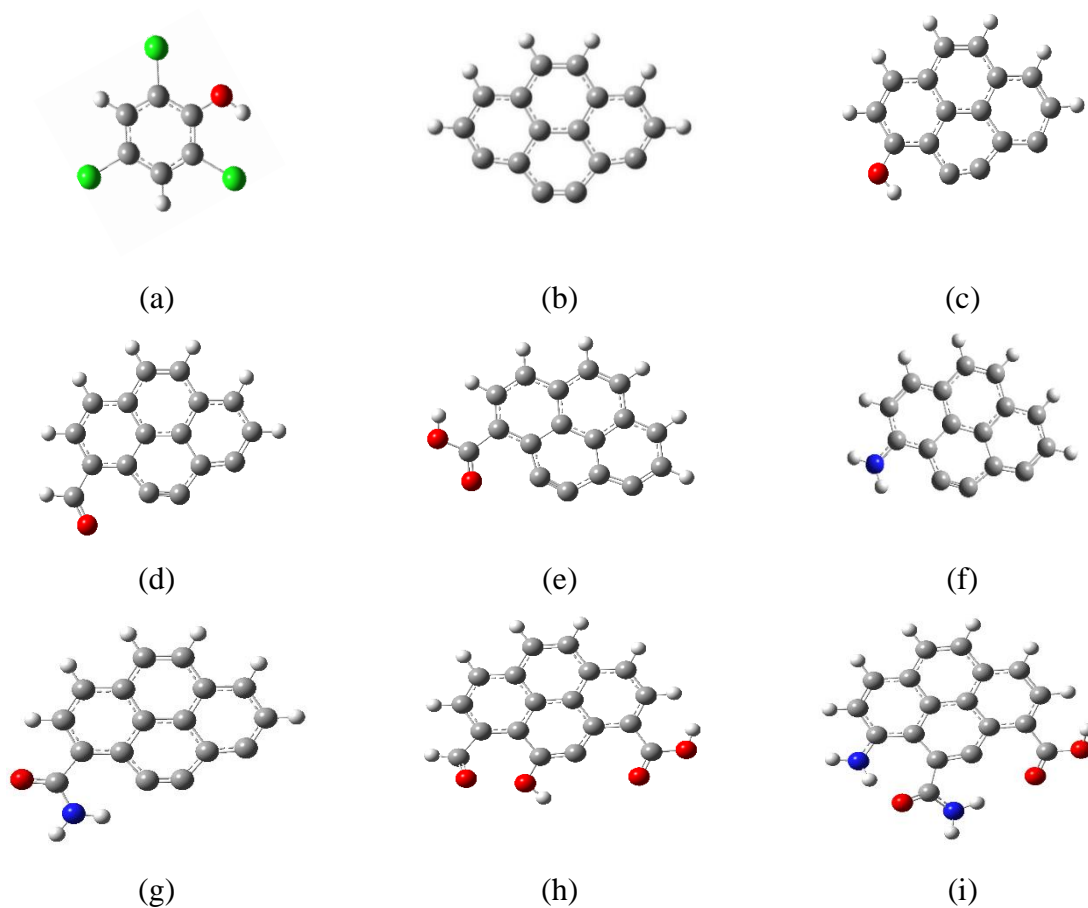
(g)   (h)   (i)

Figure 6.2. The optimized model of (a) TCP (b) AC-P (c) AC-OH (d) AC-CHO (e) AC-COOH (f) AC-NH$_2$ (g) AC-CONH$_2$ (h) AC-(CHO+OH+COOH) (i) AC-(NH$_2$+CONH$_2$+COOH).

6.3. Results and discussion

6.3.1. Theoretical calculations

The purpose of the DFT calculations in this work is to understand the interaction of the TCP molecule interaction with AC surfaces having different functional groups. The formation of hydrogen bonds between chlorophenol pollutants and functionalized AC is considered to be an essential mode of interaction in the adsorption process [36]. An armchair model was used to study the adsorption processes of pure AC and functionalized AC with TCP through the formation of a hydrogen bond. Thus, an effort has been made to comprehend the potential bond formation between the -OH group of TCP with oxygenated and nitrogenated surface functional groups (-OH, -CHO, -COOH, -NH$_2$, -CONH$_2$, -(CHO+OH+COOH) and -(NH$_2$+CONH$_2$+COOH)) of AC. Accordingly, the optimized structure between the interaction of TCP and AC surfaces with different functional groups is shown in Figure 6.3. From these structures, it can be seen that except for pristine AC, TCP prefers to bind to the functionalized AC through hydrogen atoms. Whereas, in the case of pristine AC, it prefers to attach to the AC through Cl rather than hydrogen. This may be attributed to the fact that AC forms a more stable complex with TCP through Cl linkage rather than H linkage.
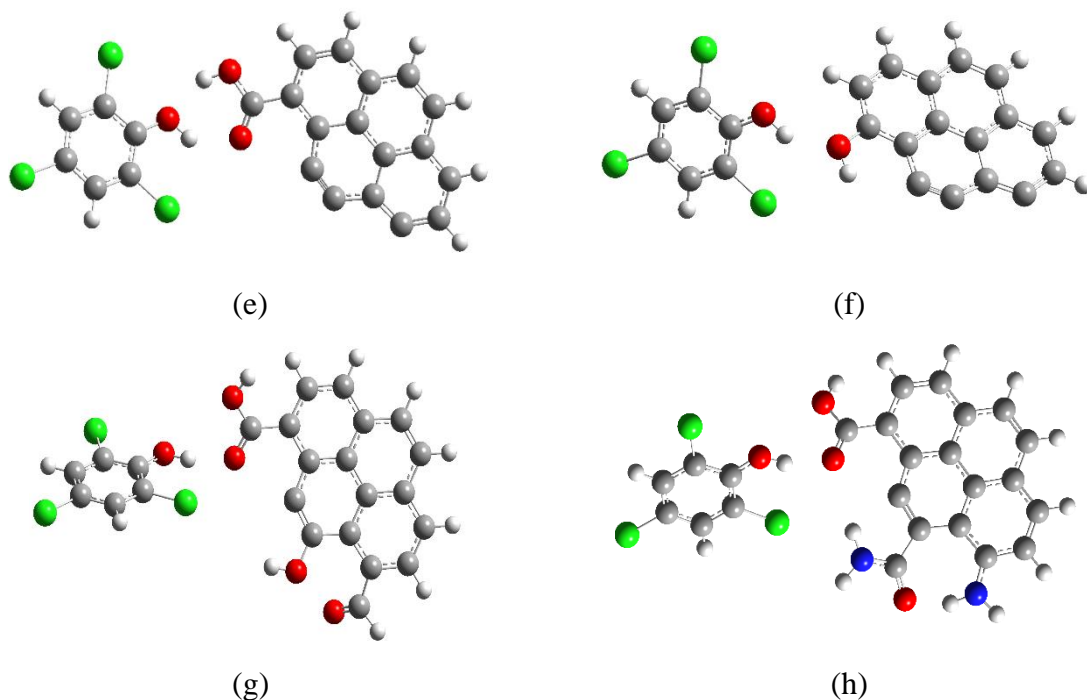

(a)

(b)

(c)

(d)
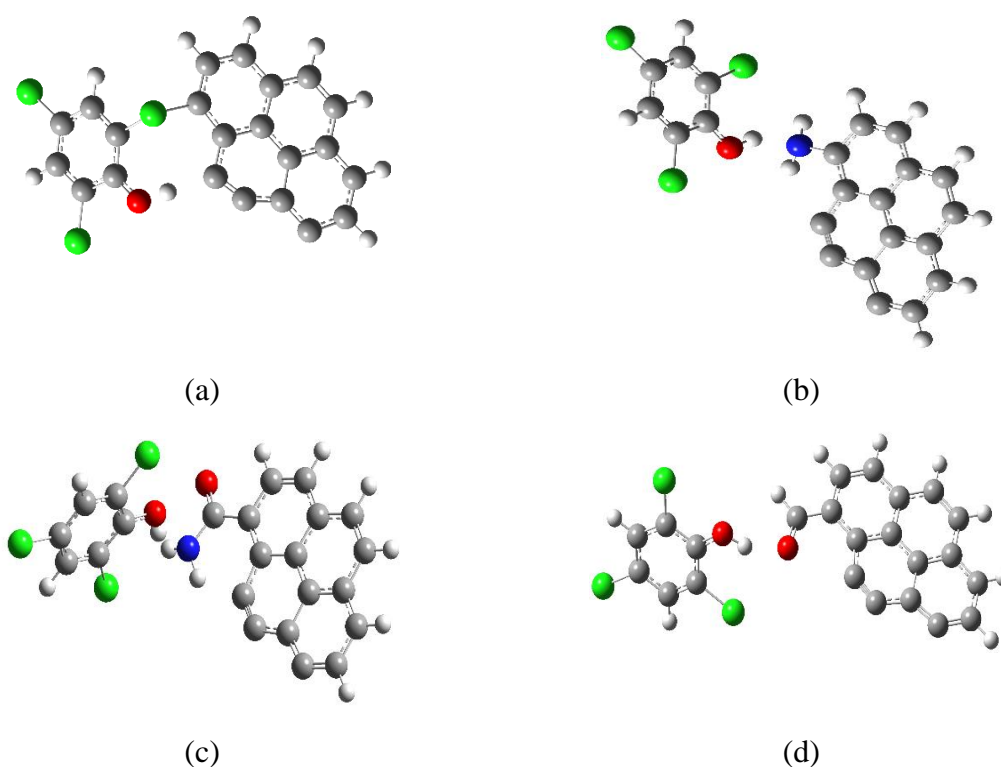
Figure 6.3. Optimized interaction structures of AC surface and TCP interactions (a) AC+TCP (b) AC-NH$_2$+TCP (c) AC-CONH$_2$+TCP (d) AC-CHO+TCP (e) AC-COOH+TCP (f) AC-OH+TCP (g) AC-(COOH+OH+CHO) +TCP (h) AC-(COOH+CONH$_2$+NH$_2$) +TCP.

6.3.2. Adsorption energy analysis

The feasibility of adsorption of adsorbates onto adsorbents can be described with the help of adsorption energy. Generally, chemisorption is characterized by adsorption energy between -960 and -50 kJ/mol, whereas, for physisorption, the adsorption energy is between -30 and -10 kJ/mol [48]. Therefore, an analysis of adsorption energy is a handy way to ascertain the nature of adsorption and the effect of different functional groups on the adsorption of TCP onto AC. Table 6.1 lists TCP's adsorption energies and bond distance with different functional groups. The computed results show that the adsorption energy between functional group-modified AC and TCP ranges between -12 and -158 kJ/mol. Physisorption is the mutual attraction between adsorbents and adsorbates through weak van der Waals forces. Conversely, chemisorption generally involves rearrangement of atoms, redistribution of electronic charges or cleavage, or formation of chemical bonds between adsorbate and adsorbent.

Table 6.1. Adsorption energies of TCP with different functional groups.

| System	E_{Ads} (kJ/mol)
AC+TCP	-90.443
AC-NH$_2$+TCP	-23.369
AC-CONH$_2$+TCP	-12.468
AC-CHO+TCP	-71.316
AC-COOH+TCP	-158.714
AC-OH+TCP	-122.219
AC-(CHO+OH+COOH)+TCP	-27.042
AC-(NH$_2$+CONH$_2$+COOH)+TCP	-27.654

Table 6.1 presented the computed adsorption energy values of AC and functionalized AC with TCP. The presence of functional groups have varying effects on TCP adsorption. Among them, the presence of -NH$_2$, -CONH$_2$, and -CHO groups are found to increase the adsorption energy hence the positive AC. Therefore, the presence of these functional groups on the surface of AC would cause a decrease in the adsorption capacity of the AC. On the other hand, the presence of -OH and -COOH on AC's surface decreases the adsorption energy thereby enhances its adsorption ability towards TCP. Further, TCP gets attached to AC functionalized with -NH$_2$, -CONH$_2$ and -CHO groups through physisorption since physisorption is characterized by adsorption energies between -30 and -10 kJ/mol. On the other hand, chemisorption operates between pristine AC, AC functionalized with -CHO, -COOH, -OH, with TCP. When multiple functional groups are present adjacent to one another and exist at the same time, it is found that the adsorption energy is lower than that of single oxygen containing functional groups and higher than that of nitrogen containing functional groups.

(a)   (b)

(c)

(d)

(e)

(f)
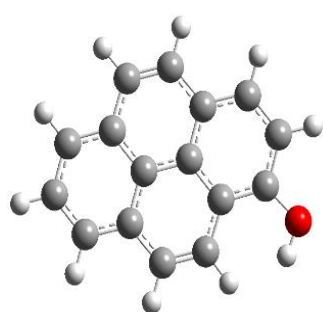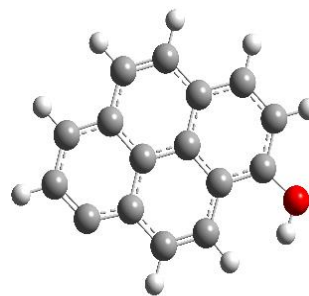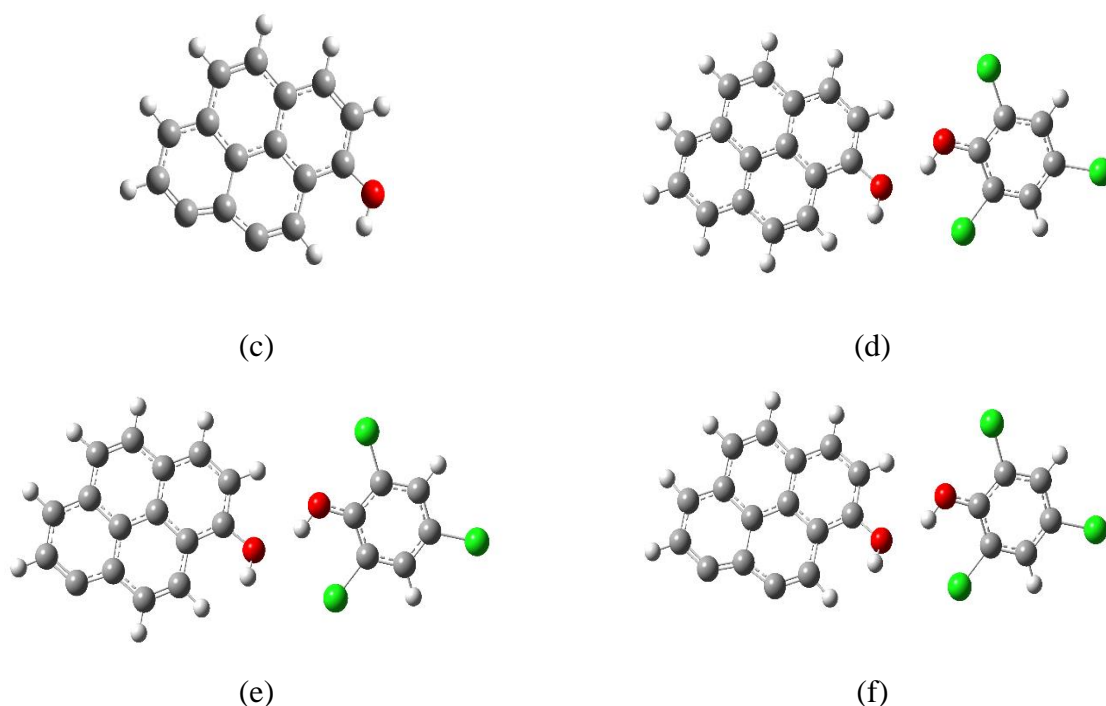
Figure 6.4. Optimized structure of (a) AC-(OH+H+H+H), (b) AC-(OH+H+H), (c) AC-(OH+H), (d) interaction structure of AC-(OH+H+H+H) and TCP, (e) interaction structure of AC-(OH+H+H) and TCP, (f) interaction structure of AC-(OH+H) and TCP.

To examine how the removal of unsaturated centers affects the interaction energy, three activated carbon models were constructed: AC-(OH+H+H+H), AC-(OH+H+H), and AC-(OH+H). The adsorption energy of TCP with AC-(OH+H+H+H), AC-(OH+H+H), and AC-(OH+H) were found to be around -19 kJ/mol. These results indicate that the number of unsaturated centers for a substituted AC has minimal effects on interaction energy. The results obtained are presented in the Table 6.2.

Table 6.2. The adsorption energy of TCP with AC-(OH+H+H+H), AC-(OH+H+H), and AC-(OH+H).

System	E_{Ads} (kJ/mol)
TCP with AC-(OH+H+H+H)	-19.26
TCP with AC-(OH+H+H)	-19.13
TCP with AC-(OH+H)	-19.21

The optimised AC-(OH+H+H+H), AC-(OH+H+H), and AC-(OH+H) structures are presented in Figures 6.4 (a), (b), (c) and their possible interaction with TCP are given in Figure 6.4 (d), (e), (f) respectively.
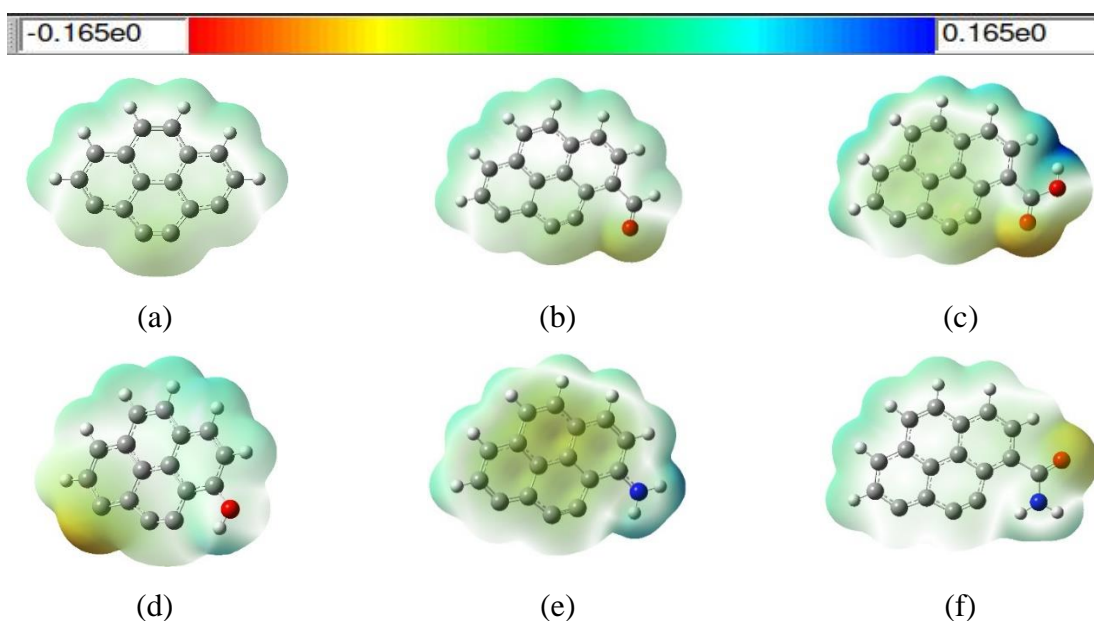
6.3.3. Molecular electrostatic potential study

Molecular electrostatic potential (MEP) is widely employed to examine relative electron density in a system. An analysis of MEP provides information regarding possible reactive sites, enabling one to predict the complexes that may be formed. Furthermore, it also gives the insight to understand the shift in electron density caused by the functional groups. MEP diagrams of AC and functionalized AC, along with a color bar to indicate the charge density, is depicted in Figure 6.5. The positively charged portion on the MEP diagram is shown in blue, while the negatively charged portion is shown in red or orange. Since the TCP in the aqueous solution has a positive charge, its electrostatic potential diagram in Figure 6.5 (g) is entirely blue. The hydrogen atoms in the carbonyl, carboxyl, hydroxyl, amine, and amide groups are also represented in blue as shown in Figure 6.5 (b), (c), (d), (e), (f), (g), and (h) demonstrating their positively charged character. The negatively charged region easily attracts the positively charged TCP in the carbon structure. In other words, the red or orange region of the carbon structure has a tendency to absorb TCP.
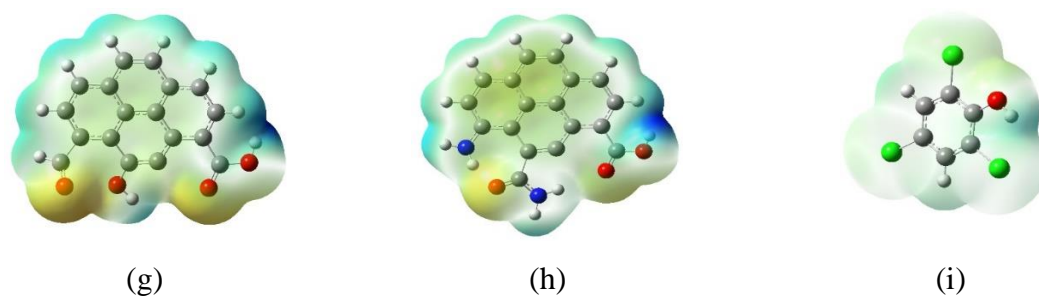

(a)   (b)   (c)

(d)   (e)   (f)

(g)   (h)   (i)

Figure 6.5. Molecular electrostatic potential maps of different carbon structures.

6.3.4. Frontier molecular orbitals and dipole moment study

The tendency of a system to lose or gain electrons depends on its HOMO-LUMO energy level. Lower HOMO energy indicates that it is difficult for the system to lose electrons. Therefore, lower HOMO energy represents higher ionization potential. On the other hand, a low LUMO energy level signifies that it is easier for the systems to capture electrons. The HOMO-LUMO energy gap is calculated using the equation.

$$E_{gap} = E_{LUMO} - E_{HOMO} \tag{6.2}$$

where E_{gap}, E_{LUMO}, and E_{HOMO} represent the HOMO-LUMO energy gap, LUMO energy level, and HOMO energy level, respectively. E_{gap} symbolizes the reactivity of systems. A higher E_{gap} value reflects a lesser electron transition ability and hence greater stability. Table 6.3 represents E_{HOMO}, E_{LUMO}, and E_{gap} values. The E_{gap} value of AC is found to be 0.0299 eV. It is clear from Table 6.3 that the addition of functional groups alters the E_{gap} value by varying degrees. It is found that the presence of -CONH$_2$, -CHO, and -NH$_2$ functional groups increases the E_{gap} of AC, thereby reducing its reactivity and increasing its stability. Whereas, introduction of -COOH and -OH groups lower the E_{gap} value indicating an increase in reactivity and decrease in stability. The E_{gap} value is found to decrease in the following order:

$$-CONH_2 > -CHO > -OH > -NH_2 > -COOH$$
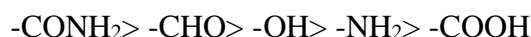
Further, the presence of multiple functional groups is also found to increase the energy gap as compared to pristine AC.

Table 6.3. Represents E_{HOMO}, E_{LUMO}, and E_{gap} values of pristine AC and functionalized.

System	HOMO	LUMO	Energy gap
AC	-0.1914	-0.1614	0.0299
AC-CHO	-0.2217	-0.0926	0.1290
AC-COOH	-0.2918	-0.2799	0.0119
AC-OH	-0.1820	-0.0827	0.0992
AC-NH$_2$	-0.2951	-0.2211	0.0740
AC-CONH$_2$	-0.2203	-0.0889	0.1313
AC-(CHO+OH+COOH)	-0.29562	-0.24355	0.0520
AC-(NH$_2$+CONH$_2$+COOH)	-0.28641	-0.23279	0.0536

Dipole moment is associated with the spatial configuration and polarity of systems. A higher dipole moment implies greater polarity of the system under study. Carbon materials like activated carbon are nonpolar and thus insoluble in water. They exhibit greater adsorption characteristics for nonpolar organic materials in aqueous media. The polarity of AC may be improved by the introduction of functional groups on its surface, thereby enhancing its adsorption properties.

Table 6.4. The dipole moment values of AC and functionalized AC.

System	Dipole moment (Debye)
AC	5.699
AC-CHO	7.858
AC-COOH	5.598
AC-OH	9.429
AC-NH$_2$	3.573
AC-CONH$_2$	5.986
AC-(CHO+OH+COOH)	10.041
AC-(NH$_2$+CONH$_2$+COOH)	9.153

Table 6.4 lists the dipole moment values of AC and functionalized AC. It is evident from the data in Table 6.4 that the presence of a functional group changes the dipole moment of AC. The introduction of -COOH and -NH$_2$ groups decreases the dipole moment, whereas the presence of -CONH$_2$, -CHO, and -OH groups increases the total dipole moment. The variation in dipole

moment is attributed to the nature of functional groups. For instance, the introduction of the -NH_2 group decreases the dipole moment of AC by 2.162 Debye, whereas, the presence of -OH group increases the dipole moment of AC by 3.730 Debye. The influence of single functionalization on the dipole moment decreases in the following order:

$$-OH> -CHO> -CONH_2> -COOH> -NH_2$$

For AC containing multiple functional groups, dipole moment values are found to be greater than that of pristine AC and single functionalized AC, except the -OH group.

6.4. Conclusion

In this study, DFT with B3LYP/6-31G (d,p) method was used to examine the influence of oxygen and nitrogen-containing groups on AC's surface towards TCP adsorption. The study was carried out to comprehend and assist the development of better adsorbents for TCP removal. From the present study, the following conclusions are made.

- Adsorption energy analysis reveal that TCP adsorption on AC's surface is highly sensitive towards the functional groups present on the carbon surface.

- It is found that the presence of -NH_2, -$CONH_2$, and -CHO groups decreases the adsorption efficiency of AC for TCP. On the other hand, presence of -COOH and -OH groups increases the adsorption abilities of AC for TCP removal.

- The presence of multiple functional groups adjacent to each other lowers the adsorption capacity.

- MEP analysis indicates that introducing functional groups causes a redistribution of electronic charge.

- The energy gap (E_{gap}) value is found to decrease in the following order:

  AC-$CONH_2$> AC-CHO>AC-OH> AC-NH_2> AC-COOH

- The influence of single functionalization on the dipole moment decreases in the following order:

  AC-OH> AC-CHO> AC-$CONH_2$>AC-COOH> AC-NH_2

From these results, it can be concluded that the adsorption capability of AC towards TCP adsorption is improved due to the presence of oxygen containing groups (except -CHO) and decreases due to the presence of nitrogen containing groups. Multiple functional group present on the carbon surface also decreases the adsorption capacity towards TCP.

References

[1] I. A. W. Tan, A. L. Ahmad, B. H. Hameed, Preparation of activated carbon from coconut husk: Optimization study on removal of 2,4,6-trichlorophenol using response surface methodology, *J. Hazard. Mater.,* 153 (**2008**) 709-717.

[2] S. Ghezali, A. Mahdad-Benzerdjeb, M. Ameri, A. Z. Bouyakoub, Adsorption of 2,4,6-trichlorophenol on bentonite modified with benzyldimethyltetradecylammonium chloride. Chem. Int., 4 (2019) 24-32.

[3] G. Liu, H. Tang, J. Fan, Z. Xie, T. He, R. Shi, B. Liao, Removal of 2,4,6-trichlorophenol from water by Eupatorium adenophorum biochar-loaded nano-iron/nickel. *Bioresour. Technol*., 289 (**2019**) 121734.

[4] C. E. Enyoh, B. O. Isiuku, 2,4,6-Trichlorophenol (TCP) removal from aqueous solution using Canna indica L.: kinetic, isotherm and thermodynamic studies. *Chem. Ecol.,* 37 (**2021**) 64-82.

[5] U. I. Gaya, A. H. Abdullah, M. Z. Hussein, Z. Zainal, Photocatalytic removal of 2,4,6-trichlorophenol from water exploiting commercial ZnO powder. *Desalination,* 263 (**2010**) 176-182.

[6] S. Mubarik, A. Saeed, M. M. Athar, M. Iqbal, Characterization and mechanism of the adsorptive removal of 2,4,6-trichlorophenol by biochar prepared from sugarcane baggase. *J. Ind. Eng. Chem*., 33 (**2016**) 115-121.

[7] J. Zhang, C. Wang, M. Xiang, Y. Huang, L. Jin, Z. Yang, H. Li, $Fe@Fe_2O_3$ core-shell nanowires compounding humic acid enhanced catalysis removal 2,4,6-trichlorophenol: Performance and mechanism. *Chem. Eng. J*., 428 (**2022**) 131779.

[8] N. S. Kumar, M. Asif, A. M. Poulose, M. Suguna, M. I. Al-Hazza, Equilibrium and kinetic studies of biosorptive removal of 2,4,6-trichlorophenol from aqueous solutions using untreated agro-waste pine cone biomass, *Processes,* 7 (**2019**) 757.

[9] S. Chaliha, K. G. Bhattacharyya, Wet oxidative method for removal of 2,4,6-trichlorophenol in water using Fe(III), Co(II), Ni(II) supported MCM41 catalysts. *J. Hazard. Mater.,*150 (**2008**) 728-736.

[10] N. Taghavi, A. A. Amooey, A. Amouei, H. Tashakkorian, Imidazole-modified clinoptilolite as an efficient adsorbent for removal of 2,4,6- trichlorophenol: fabrication, characterization, kinetic and isotherm studies. *Microchem. J.,*169 *(***2021**) 106561.

[11] B. H. Hameed, I. A. W. Tan, A. L. Ahmad, Adsorption isotherm, kinetic modeling and mechanism of 2,4,6-trichlorophenol on coconut husk-based activated carbon. *Chem. Eng. J.,*144 (**2008**) 235-244.

[12] Z. U. Zango, Z. N. Garba, N. H. H. Abu Bakar, W. L. Tan, Adsorption studies of Cu^{2+}-Hal nanocomposites for the removal of 2,4,6-trichlorophenol. *Appl. Clay Sci.,*132–133 (**2016**) 68-78.

[13] A. C. Oladipo, A. C. Tella, H. S. Clayton, V. T. Olayemi, O. B. Akpor, T. O. Dembaremba, A. S. Ogunlaja, G. J. Clarkson, R. I. Walton, A zinc-based coordination polymer as adsorbent for removal of trichlorophenol from aqueous solution: Synthesis, sorption and DFT studies. *J. Mol. Struct.,* 1247 (**2022**) 131274.

[14] J. Fan, J. Zhang, C. Zhang, L. Ren, Q. Shi, Adsorption of 2,4,6-trichlorophenol from aqueous solution onto activated carbon derived from loosestrife. *Desalination,* 267 (**2011**) 139-146.

[15] B. I. Olu-Owolabi, A. H. Alabi, P. N. Diagboya, E. I. Unuabonah, R. A. Düring, Adsorptive removal of 2,4,6-trichlorophenol in aqueous solution using calcined kaolinite-biomass composites. *J. Environ. Manage.,* 192 (**2017**) 94-99.

[16] D. Krishnaiah, S. M. Anisuzzaman, A. Bono, R. Sarbatly, Adsorption of 2,4,6-trichlorophenol (TCP) onto activated carbon. *J. King Saud. Univ. Sci*., 25 (**2013**) 251-255.

[17] Q. Yin, L. Si, R. Wang, Z. Zhao, H. Li, Z. Wen, DFT study on the effect of functional groups of carbonaceous surface on ammonium adsorption from water. *Chemosphere,* 287 (**2022**) 132294.

[18] R. Mustafa, E. Asmatulu, Preparation of activated carbon using fruit, paper and clothing wastes for wastewater treatment. *J. Water Process Eng.,* 35 (**2020**) 101239.

[19] B. H. Hameed, I. A. W. Tan, A. L. Ahmad, Preparation of oil palm empty fruit bunch-based activated carbon for removal of 2,4,6-trichlorophenol: Optimization using response surface methodology. *J. Hazard. Mater.,* 164 (**2009**) 1316-1324.

[20] K. Zhou, W. Ma, Z. Zeng, X. Ma, X. Xu, Y. Guo, H. Li, L. Li, Experimental and DFT study on the adsorption of VOCs on activated carbon/metal oxides composites. *Chem. Eng. J.,* 372 (**2019**) 1122-1133.

[21] Z. Aksu, J. Yener, A comparative adsorption/biosorption study of mono-chlorinated phenols onto various sorbents. *Waste Manag*., 21 (**2001**) 695-702.

[22] Q. S. Liu, T. Zheng, P. Wang, L. Guo, Preparation and characterization of activated carbon from bamboo by microwave-induced phosphoric acid activation. *Ind. Crops Prod*., 31 (**2010**) 233-238.

[23] A. Supong, U. B. Sinha, D. Sinha, Density functional theory calculations of the effect of oxygenated functionals on activated carbon towards cresol adsorption. *Surfaces*, 5 (**2022**) 280-289.

[24] M. Seredych, D. Hulicova-Jurcakova, G. Q. Lu, T. J. Bandosz, Surface functional groups of carbons and the effects of their chemical character, density and accessibility to ions on electrochemical performance. *Carbon*, 46 (**2008**) 1475-1488.

[25] K. László, P. Podkościelny, A. Dąbrowski, Heterogeneity of polymer-based active carbons in adsorption of aqueous solutions of phenol and 2,3,4-trichlorophenol. *Langmuir*, 19 (**2003**) 5287-5294.

[26] K. László, A. Szucs, Surface characterization of polyethyleneterephthalate (PET) based activated carbon and the effect of pH on its adsorption capacity from aqueous phenol and 2,3,4-trichlorophenol solutions. *Carbon,* 39 (**2001**) 1945-1953.

[27] W. Qu, F. Shen, H. Zu, S. Liu, J. Yang, Y. Hu, Z. Yang, H. Li, Density functional theory studies of the adsorption and interactions between selenium species and mercury on activated carbon. *Energy and Fuels*, 34 (**2020**) 9779-9786.

[28] A. M. Tolmachev, D. A. Firsov, T. A. Kuznetsova, K. M Anuchin, DFT modeling of the adsorption of benzene, methanol, and ethanol molecules in activated carbon nanopores. *Prot. Met. Phys. Chem. Surfaces*, 45 (**2009**) 163-168.

[29] Y. Achour, L. Bahsis, E. H. Ablouh, H. Yazid, M. R. Laamari, M. El Haddad, insight into adsorption mechanism of congo red dye onto bombax buonopozense bark activated-carbon using central composite design and DFT studies. *Surfaces and Interfaces,* 23 (**2021**) 100977.

[30] W. T. Vieira, M. D. Bispo, S. De Melo Farias, A. D. S. V. De Almeida, T. L. Da Silva, M. G. A. Vieira, J. I. Soletti, T. L. Balliano, Activated carbon from macauba endocarp (*Acrocomia aculeate*) for removal of atrazine: experimental and theoretical investigation using descriptors based on DFT. *J. Environ. Chem. Eng*., 9 (**2021**) 105155.

[31] I. Efremenko, M. Sheintuch, Predicting solute adsorption on activated carbon: phenol. *Langmuir*, 22 (**2006**) 3614-3621.

[32] S. U. Jan, A. Ahmad, A. A. Khan, S. Melhi, I. Ahmad, G. Sun, C. Chen, R. Ahmad, Removal of azo dye from aqueous solution by a low-cost activated carbon prepared from coal: adsorption kinetics, isotherms study, and DFT simulation. *Environ. Sci. Pollut. Res.,* 28 (**2021**) 10234-10247.

[33] A. Supong, P. C. Bhomick, M. Baruah, C. Pongener, U.B. Sinha, D. Sinha, Adsorptive removal of Bisphenol A by biomass activated carbon and insights into the adsorption mechanism through density functional theory calculations. *Sustain. Chem. Pharm.,* 13 (**2019**) 100159.

[34] C. Yin, M. Ng, B. Goh, M. Saunders, N. Hill, Z. Jiang, J. Balach, H. El-Harbawi, Probing the interactions of phenol with oxygenated functional groups on curved fullerene-like sheets in activated carbon. *Phys. Chem. Chem. Phys*., 18 (**2016**) 3700-3705.

[35] A. Supong, P. C. Bhomick, R. Karmaker, S. L. Ezung, L. Jamir, U.B. Sinha, D. Sinha, Experimental and theoretical insight into the adsorption of phenol and 2,4-dinitrophenol onto *Tithonia diversifolia* activated carbon. *Appl. Surf. Sci.,* 529 (**2020**) 147046.

[36] S. L. Ezung, M. Baruah, A. Supong, S. Sharma, D. Sinha, Experimental and theoretical insight into the adsorption of 2,4-dichlorophenol on low-cost bamboo sheath activated carbon. *Sustain. Chem. Pharm.,* 26 (**2022**) 100643.

[37] X. Liu, Y. Han, Y. Cheng, G. Xu, Microwave-assisted ammonia modification of activated carbon for effective removal of phenol from wastewater: DFT and experiment study. *Appl. Surf. Sci.,* 518 (**2020**) 146258.

[38] K. Melchor-Rodríguez, C. Carmenate-Rodríguez, A. Ferino-Pérez, S. Gaspard, U. J. Jáuregui-Haza, Role of basic surface groups of activated carbon in chlordecone and β-hexachlorocyclohexane adsorption: a molecular modelling study, *Molecules,* 26 (**2021**) 6969.

[39] A. Spaltro, M. N. Pila, D. D. Colasurdo, E. Noseda Grau, G. Román, S. Simonetti, D. L. Ruiz, Removal of paracetamol from aqueous solution by activated carbon and silica. Experimental and computational study. *J. Contam. Hydrol.,* 236 (**2021**) 103739.

[40] C. Dang, F. Sun, H. Jiang, T. Huang, W. Liu, X. Chen, H. Ji, Pre-accumulation and in-situ destruction of diclofenac by a photo-regenerable activated carbon fiber supported titanate nanotubes composite material: Intermediates, DFT calculation, and ecotoxicity. *J. Hazard. Mater.,* 400 (**2020**) 123225.

[41] M. S. Abdelbassit, S. A. Popoola, T. A. Saleh, H. H. Abdallah, A. A. Al-Saadi, K. R. Alhooshan, DFT and kinetic evaluation of chloromethane removal using cost-effective activated Carbon. *Arab. J. Sci. Eng.,* 45 (**2020**) 4705-4716.

[42] N. Chen, R. T. Yang, Ab initio molecular orbital calculation on graphite: Selection of molecular system and model chemistry. *Carbon,* 36 (**1998**) 1061-1070.

[43] S. T. Perry, E. M. Hambly, T. H. Fletcher, M. S. Solum, R. J. Pugmire, Solid-state ^{13}C NMR characterization of matched tars and chars from rapid coal devolatilization. *Proc. Combust. Inst.,* 28 (**2000**) 2313-2319.

[44] B. Padak, J. Wilcox, Understanding mercury binding on activated carbon. *Carbon,* 47 (**2009**) 2855-2864.

[45] L. R Radovic, The mechanism of CO_2 chemisorption on zigzag carbon active sites: A computational chemistry study. *Carbon*, 43 (**2005**) 907-915.

[46] J. R Pliego Jr, S. M. Resende, E. Humeres, Chemisorption of SO_2 on graphite surface: A theoretical ab initio and ideal lattice gas model study. *Chemical Physics,* 314 (**2005**) 127-133.

[47] L. M. Cam, L.V. Khu, N. N. Ha, Theoretical study on the adsorption of phenol on activated carbon using density functional theory. *J. Mol. Model,* 19 (**2013**) 4395-4402.

[48] Q. Yin, L. Si, R. Wang, Z. Zhao, H. Li, Influence of the defect of carbonaceous surface on ammonium adsorption: a DFT study. *Fuel,* 325 (**2022**) 124873.

CHAPTER 7

SUMMARY AND CONCLUSION

This chapter presents the overall summary and conclusions of the thesis. The future scope of the work is also highlighted in this chapter.

Biomass materials of bamboo sheath of *Dendrocalamus hamiltonii* and *Schima wallichii* were used as a potential precursor for the preparation of activated carbon (namely BSAC and SWAC). The synthesized activated carbon was then applied for the adsorption of 2,4-dichlorophenol. further the prepared activated carbon nanocomposite was used for the synthesis of activated carbon nanocomposite for the study of chlorpyriphos degradation from wastewater. Also, density functional theory study was used to understand the removal mechanism of activated carbon for organic pollutants such as 2,4,6-trichlorophenol. A summary of the overall thesis work is presented below:

1. Waste bamboo sheath is inexpensive, indigenous and easily available in large quantity. Based on the experimental and theoretical investigations of the present work BSAC proved to be a very good precursors capable of removing DCP from aqueous solutions. The SEM image revealed that the synthesized carbon has cylindrical pores with sizes ranging from 10 to 30 μm, and the XRD data confirmed that the synthesized carbon contains graphite-like micro crystallites. The batch adsorption suggested a maximum DCP removal efficiency of 95.5 % under optimum conditions. The data obtained for the adsorption process was found to be best fitted in Langmuir isotherm model, indicating a monolayer coverage of the adsorbent with a q_m of 37.29 mg/g. The pseudo second order kinetic model described better adsorption kinetics with R^2 value of 0.99 indicating that the adsorption process was a chemisorption. The thermodynamic studies suggested that the adsorption process is endothermic, temperature-dependent, and spontaneous. DFT simulations also revealed that DCP adsorbs well on activated carbon. The -OH group interacts most strongly with DCP among the several functional groups (-CHO, -CO-, -CCO, -COOH) utilized to functionalize activated carbon. These findings imply that functionalizing activated carbon with -OH group may improve its interaction with DCP, resulting in improved adsorption. The results obtained from the present study indicates that waste bamboo sheath could be used as a potential raw material for the preparation of low-cost and effective AC. In addition, theoretical investigations could provide critical insights into the interaction of AC surface and the adsorbate which can help in the design and development of AC with improved adsorption properties.

2. A novel SWAC/ZrO$_2$-ZnO nanocomposite was developed by effectively immobilizing a ZrO$_2$-ZnO photocatalyst on SWAC using a hydrothermal technique. FT-IR, XRD, TEM-SEAD, XPS, LC-MS, and PL instruments were used to characterize SWAC/ZrO$_2$-ZnO nanocomposite. The XRD analysis showed that the SWAC/ZrO$_2$-ZnO nanocomposite crystal size was found to be 39.41 nm. The LC-MS analysis revealed that the CPs molecule had been

fragmented into smaller m/z ratios. The insecticide chlorpyrifos (100 ppm) was degraded (100 %) with a 0.05 g dose of SWAC/ZrO$_2$-ZnO nanocomposite under UV-light irradiation for 50 mins at pH 6. SWAC/ZrO$_2$-ZnO nanocomposite photodegradation of CPs follows pseudo first-order kinetics. Density functional theory (DFT) simulations also revealed the formation of hydrogen bonding via O-linkage of the O-Zr-O bond with SWAC to form chemically reactive SWAC/ZrO$_2$-ZnO nanocomposite.

3. Fe-ZnO nanocomposite supported on activated carbon was synthesized using a hydrothermal method. The XRD analysis showed that the SWAC/Fe-ZnO nanocomposite crystallite sizes was found to be 29.9 nm. BET surface area analyzer was used to investigated the total surface area and total pore volume of SWAC/Fe-ZnO nanocomposite and found to be 3013.04 m^{2}g^{-1} and 2.18 cm^{3}g^{-1}. From the UV-DRS spectra the band gap of Fe doped ZnO nanocomposite supported on activated carbon was found to be 2.1 eV. The SWAC/Fe-ZnO nanocomposite is effectively used for the removal of chlorpyrifos insecticide with a maximum degradation percentage of 98 % within 60 min for 150 ppm solution. The photocatalytic degradation of chlorpyrifos followed the pseudo-first-order rate kinetics with an apparent rate constant of 0.055 min^{-1} and a half-life period of 1.26 min, according to the Langmuir-Hinshelwood model. The presence of interfering ions such as glycine, EDTA, copper sulphate, and p-benzoquinone affects mostly the degradation of CPs by SWAC/ Fe-ZnO nanocomposite, indicating that hydroxyl radicals are the dominant reactive species in the CR degradation process. The SWAC/ Fe-ZnO nanocomposite have excellent regeneration properties and it could degrade around 62.7 % of CPs at the sixth cycle of use. Thus, SWAC/Fe-ZnO nanocomposite could serve as a promising photocatalyst for the degradation of chlorpyrifos from a waste water.

4. In this study, density functional theory with B3LYP/6-31G (d,p) method was used to examine the influence of oxygen and nitrogen-containing groups on AC's surface towards TCP (2,4,6-trichlorophenol) adsorption. From the present study, the following conclusions are made.

- Adsorption energy analysis reveal that TCP adsorption on AC's surface is highly sensitive towards the functional groups present on the carbon surface.

- It is found that the presence of -NH$_2$, -CONH$_2$, and -CHO groups decreases the adsorption efficiency of AC for TCP. On the other hand, presence of -COOH and -OH groups increase the adsorption abilities of AC for TCP removal.

- The presence of multiple functional groups adjacent to each other lowers the adsorption capacity.

- MEP analysis indicates that introducing functional groups causes a redistribution of electronic charge.
- The energy gap (E_{gap}) value is found to decrease in the following order:
  $AC\text{-}CONH_2 > AC\text{-}CHO > AC\text{-}OH > AC\text{-}NH_2 > AC\text{-}COOH$
- The influence of single functionalization on the dipole moment decreases in the following order:
  $AC\text{-}OH > AC\text{-}CHO > AC\text{-}CONH_2 > AC\text{-}COOH > AC\text{-}NH_2$

From these results, it can be concluded that the adsorption capability of AC towards TCP adsorption is improved due to the presence of oxygen containing groups (except -CHO) and decreases due to the presence of nitrogen containing groups. Multiple functional group present on the carbon surface also decreases the adsorption capacity towards TCP.

Thus, it can be concluded from the current thesis work that activated carbon was successfully produced using cost-effective and widely available biomass sources. The synthetized activated carbon has a high potential for use as adsorbents in wastewater treatment. Also, the catalyst based on activated carbon nanocomposite materials has the potential to be an effective photocatalyst for the degradation of chlorpyrifos from wastewater. Furthermore, theoretical studies may give critical insights into the interaction of the activated carbon surface and the adsorbate, assisting in the design and development of activated carbon with improved adsorption properties.

Future Prospective

Based on the results obtained from the present study, a future study can be planned. Given below are some of the future prospective:

- ➢ The activated carbon surface can be further modified using various methods to enhance its adsorption efficiency or to increase its affinity for a specific contaminant.
- ➢ The synthesized carbons can be studied for their efficiency in removing inorganic contaminants such as heavy and trace metals from water samples.
- ➢ Developing new visible-light hybrid photocatalyst by coupling ZnO with other metal oxides such as Ni-O, Fe_2O_3, CaO, Cu_2O and supporting them on activated carbon to apply them in photo electrochemical water splitting reactions, photodegradation of herbicides, insecticides, and saturated hydrocarbon.
- ➢ The photocatalytic performance could be enhanced to degrade more water contaminants, and the technique can also be used on an industrial scale.

➤ Density functional theory simulations can be used to examine the functionalized activated carbon surface towards pollutants adsorption. This type of study helps in the creation of better adsorbents for pollutants removal.

NAGALAND ![logo] UNIVERSITY

(A Central University Estd. By the Act of Parliament No. 35 of 1989)
Headquarters: Lumami-798627, Nagaland, India
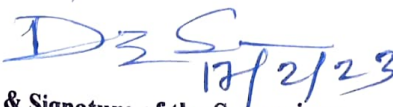
Ph.D. Thesis Certificate on Plagiarism check

Name of the Research Scholar	Soremo L Ezung
Ph.D. Registration Number	790/2017
Title of Ph.D. thesis	Activated Carbon/Carbon Nanocomposite Materials for Adsorption and Catalytic Oxidation of Organic Pollutants: An Experimental and Theoretical Study
Name & Institutional Address of the Supervisor	Prof. Dipak Sinha Department of Chemistry, Nagaland University, Lumami
Name of the Department and School	Department of Chemistry, School of Sciences
Date of submission	10/02/2023
Date of plagiarism check	02/04/2023
Percentage of similarity detected by the **URKUND** software	4%

1. I hereby declare that/certify that the Ph.D. thesis submitted by me is complete in all respect as per the guidelines of Nagaland University (NU) for this purpose. I also certify that the Thesis (soft copy) has been checked for plagiarism using **URKUND** similarity checked software. It is also certified that the contents of the electronic version of the thesis re the same as the final hardcopy of the thesis. Copy of the report generated by the **URKUND** software is also enclosed.

(SOREMO L EZUNG)
(Name & Signature of the Scholar)

Place: LUMAMI

Date: 17/2/23

17/2/23

Name & Signature of the Supervisor:
With Seal

Prof. Dipak Sinha
Department of Chemistry
Nagaland University

![Ouriginal by Turnitin logo]

Document Information

Analyzed document	Soremo Ph.D Thesis.docx (D157813426)
Submitted	2023-02-04 10:47:00
Submitted by	Dipak Sinha
Submitter email	dipaksinha@gmail.com
Similarity	4%
Analysis address	dipaksinha.naga@analysis.urkund.com

Sources included in the report

W	URL: https://www.sciencedirect.com/science/article/abs/pii/S0013935119301951 Fetched: 2023-01-11 12:02:06	4
W	URL: https://link.springer.com/10.1007/s41204-020-00071-3 Fetched: 2021-04-07 11:07:23	29
W	URL: https://pdfs.semanticscholar.org/c6e2/7f59ca98e076be932821558cfb0e3843765a.pdf Fetched: 2023-02-04 08:23:26	1
W	URL: https://www.mdpi.com/2073-4344/11/12/1520 Fetched: 2023-02-04 07:56:23	2
W	URL: https://link.springer.com/article/10.1007/s10971-022-05936-4 Fetched: 2023-02-04 07:56:22	2
W	URL: https://www.mdpi.com/2073-4441/14/23/3899/pdf Fetched: 2023-01-12 09:49:35	3
W	URL: https://www.ncbi.nlm.nih.gov/pmc/articles/PMC7180850/ Fetched: 2020-06-04 08:51:43	3
W	URL: https://www.nature.com/articles/s41467-019-09072-6 Fetched: 2020-07-15 14:03:52	1
W	URL: https://www.intechopen.com/chapters/67999 Fetched: 2021-10-08 12:25:35	2
W	URL: https://mdpi-res.com/d_attachment/crystals/crystals-11-01502/article_deploy/crystals-11-01502.... Fetched: 2023-02-04 07:55:54	2
W	URL: https://www.sciencedirect.com/science/article/abs/pii/S0925838821008318 Fetched: 2023-02-04 07:48:28	1

CURRICULUM VITAE

Name in Full	**SOREMO L EZUNG**
Date of Birth	21st November 1991
Address of Correspondence	Department of Chemistry
	Nagaland University
	Lumami Campus-798627
	Zunheboto, Nagaland
Email ID	lothasoremo@gmail.com

Academic qualifications

Exam Passed	Board/ University	Year of Passing	Division	Percentage of marks	Subjects
B.Sc.	Nagaland University	2013	1st Div	69.78 %	Chemistry (Honors)
M.Sc.	North Maharashtra University	2015	1st Div	66.80 %	Chemistry (Industrial chemistry)

Areas of Research Interest

- Development of biomass-based materials for removal of organic, inorganic and biological pollutants from water
- Synthesis and characterization of metal oxide nano materials and composite for wastewater treatment
- Activated carbon and its composite for various environmental applications
- Adsorption/Photocatalysis studies
- Computation studies using Density functional studies on adsorption/ photocatalysis studies

Research Publications

1. **Soremo L. Ezung**, Mridushmita Baruah, Aola Supong, Shisak Sharma, Dipak Sinha, Experimental and theoretical insight into the adsorption of 2,4-dichlorophenol on low-cost bamboo sheath activated carbon, *Sustainable Chemistry and Pharmacy*, 26 (2022) 100643.

2. **Soremo L. Ezung**, Mridushmita Baruah, Suraj Kumar, Shisak Sharma and Dipak Sinha, Photocatalytic degradation of the organophosphorus insecticide chlorpyrifos in aqueous suspensions using a novel activated Carbon ZrO_2-ZnO Nanocomposite under UV light, *Korean Journal of Chemical Engineering*. (Accepted)

3. Mridushmita Baruah, Aola Supong, **Soremo Likongthung Ezung**, Parimal Chandra Bhomick, Suraj Kumar, Dipak Sinha, Synthesis, characterization of novel Fe-doped TiO_2 activated carbon nanocomposite towards photocatalytic degradation of Congo red, *E. coli, S. aureus*, *Korean Journal of Chemical Engineering*. 38 (2021) 1277-1290.

4. Synthesis and characterization of Ni-doped TiO_2 activated carbon nanocomposite for the photocatalytic degradation of anthracene, Mridushmita Baruah, **Soremo L. Ezung**, Shisak Sharma, Dipak Sinha, *Inorganic Chemistry Communications*. 144 (2022) 109905.

5. Aola Supong, Parimal Chandra Bhomick, Rituparna Karmaker, **Soremo L. Ezung**, Latonglila Jamir, Upasana Bora Sinha, Dipak Sinha, Experimental and theoretical insight into the adsorption of phenol and 2, 4-dinitrophenol onto *Tithonia diversifolia* activated carbon, *Applied Surface Science*. 529 (2020) 147046.

6. Shisak Sharma, **Soremo L. Ezung**, Aola Supong, Mridushmita Baruah, Suraj Kumar, Raplang Steven Umdor, Dipak Sinha, Activated carbon adsorbent derived from waste biomass,"*Croton caudatus*" for efficient removal of 2-chlorophenol from aqueous solution: Kinetics, isotherm, thermodynamics and DFT simulation, *Chemical Engineering Research and Design*. 190 (2023) 777-792.

7. **Soremo. L. Ezung**, M. Baruah, S. Kumar, S. Sharma, D. Sinha, Photocatalytic degradation of chlorpyrifos using Fe-doped ZnO/activated carbon nanocomposite, *Environmental Nanotechnology, Monitoring and Management*. (Communicated).

8. **Soremo. L. Ezung**, M. Baruah, S. Kumar, S. Sharma, D. Sinha, 2,4,6-trichlorophenol adsorption using activated carbon: A DFT analysis of the role of functional groups on the carbonaceous surface, *Computational and Theoretical Chemistry*. (Communicated).

Seminars/Workshops Attended

➢ Poster presentation at "**National seminar on Chemistry in interdisciplinary research**", organized by Department of Chemistry, Nagaland university, March 16th -17th 2017.

➢ Attended a short-term course on **"Analytical techniques for physical, Chemical and Bioinspired materials"** organized by Department of science and humanities, NIT Nagaland, Chümoukedima, Dimapur, July 23rd-27th 2018.

➢ Presented paper at **"National seminar on Chemistry in interdisciplinary research"**, organized by Department of Chemistry, Nagaland university, November 09th-10th 2018.

➢ Presented Paper at the "**National e-Seminar on Chemistry in emerging trends of Interdisciplinary Research (NeSCETIR)"**, organized by Department of Chemistry,

Nagaland University, Lumami, 18th-20th November 2020.

➢ Participated in IPR awareness/training program on **"National Intellectual Property Awareness Mission (NIPAM)"** organized by RGNIIPM IPR Training Institute in co-ordination with IPR cell, Nagaland university on March 4th 2022.

➢ Participated in Two-day Workshop on **"Quality Enhancement in Research"** organized by IQAC, Nagaland University during the period 22nd-23rd March 2021.